

# THE EVOLUTION OF AGN AND THEIR HOST GALAXIES

By

ELENI KALFOUNTZOU

A thesis submitted to the University of Hertfordshire  
in partial fulfilment of the requirements of the degree of  
Doctor of Philosophy

July 2015

© Eleni Kalfountzou, 2016.

Typeset in L<sup>A</sup>T<sub>E</sub>X 2<sub>ε</sub>.

# Abstract

Active galaxies have been in the forefront of astronomic research since their first discovery, at least 50 years ago (e.g. Schmidt, 1963; Matthews & Sandage, 1963). The putative supermassive black hole (SMBH) at their center characterizes their properties and regulates the evolution of these objects. In this thesis, I study the ‘demographics’ and ‘ecology’ of active galactic nuclei (AGN) in the context of their evolution and the interaction with their environments (mainly their host galaxy).

The number density of AGN has been found to peak at  $1 < z < 3$  (e.g. Ueda et al., 2003; Hasinger et al., 2005; Richards et al., 2005; Aird et al., 2010), similar to the star formation history (e.g. Silverman et al., 2008a; Aird et al., 2010). However, when taking into account obscuration, faint AGN are found to peak at lower redshift ( $z \leq 2$ ) than that of bright AGN ( $z \approx 2 - 3$ ; e.g. Hasinger et al., 2005; Hopkins et al., 2007; Xue et al., 2011). This qualitative behaviour is also broadly seen in star-forming galaxies (e.g. Cowie et al., 1996) and is often referred to as ‘cosmic downsizing’, although this term has developed a number of usages with respect to galaxies (e.g. Bundy et al., 2006; Cimatti et al., 2006; Faber et al., 2007; Fontanot et al., 2009). Though this behaviour is well established up to  $z \approx 3$ , the nature of how and when the initial seed of these AGNs were formed remains an open question.

For this study, I use *Chandra* surveys to study some of the most distant AGN in the Universe ( $z > 3$ ). The combination of two different size and depth *Chandra* surveys (*Chandra*-COSMOS and ChaMP) provides me with the largest to-date  $z > 3$  AGN sample, over a wide range of rest-frame 2-10 keV luminosities [ $\log(L_X/\text{erg s}^{-1}) = 43.3 - 46.0$ ] and obscuration ( $N_H = 10^{20} - 10^{23} \text{ cm}^{-2}$ ). I find strong evidence about a strong decline in number density of X-ray AGN above  $z \approx 3$ , and also the association of this decline with a luminosity-dependent density evolution (LDDE; e.g. Gilli et al., 2007). Especially at high redshifts, the different evolution models predict quite different numbers of AGNs. The large size and the wide X-ray luminosity range of this sample reduces the uncertainties of previous studies at similar redshifts making it possible to distinguish between the different models and suggest that observations appear to favour the LDDE model.

The observed AGN downsizing behaviour seen via the measured X-ray luminosity function (XLF) could arise due to changes in the mass of the typical active SMBH and/or changes in the typical accretion rate. But how does the growth of SMBHs over cosmic time influence

its environment? A powerful way to address this question is to compare the host galaxy properties over a wide range of AGN and accretion rate types.

Radio-jets are one of the most prominent constituents of AGN as they can interact directly with the host galaxy. Although AGN with radio jets are rare (they make up to 10 per cent of the total AGN population) radio galaxies make up over 30 per cent of the massive galaxy population and it is likely that all massive galaxies go through a radio-loud phase, as the activity is expected to be cyclical (e.g [Best et al., 2005](#)). It is therefore, important to investigate the impact of radio jets on the host galaxy and particularly the star formation. The method I follow focuses on the comparison of the host galaxy properties between optically selected quasar samples, with and without strong radio emission associated with powerful radio-jets, matched in AGN luminosity. *Herschel* far-infrared observations are used to trace the star formation in the host galaxy, providing minimal AGN contamination. In my first approach, I have constructed a sample of radio-loud and radio-quiet quasars from the Faint Images Radio Sky at Twenty-one centimetres (FIRST) and the Sloan Digital Sky Survey Data Release 7 (SDSS DR7), over the H-ATLAS Phase 1 Area ( $9^h$ ,  $12^h$  and  $14.5^h$ ). The main result of this work is that RLQs at lower AGN luminosities tend to have on average higher FIR and  $250\text{-}\mu\text{m}$  luminosity with respect to RQQs matched in AGN luminosity and redshift. However, evolution effects could be strong as the quasars in this sample cover a wide range of redshifts ( $0.4 < z < 5$ ). Therefore, I follow a second approach with the advantage of a QSO sample selection at a single redshift epoch, decomposing the evolution effects from the AGN/star-formation study. The results indicate that radio-jets in powerful QSOs can both suppress and enhance the star formation in their host galaxies. These findings are consistent with a galaxy mass and jet-power dependence model. Then we expect more massive galaxies to have more star-formation for a given jet-power because their star-formation is more enhanced by the jet.

Although radio-jets are the best candidates for a direct AGN impact to the host galaxy, many models refer to an AGN feedback associated with energetic AGN winds and outflows which are expected to suppress the star formation in powerful AGN when compared to the overall galaxy population. My results do not suggest star formation is suppressed in the hosts of optically selected QSOs at  $z \approx 1$ , with more than 30 per cent of them being associated with strong star formation rates ( $\text{SFR} \approx 350 M_{\odot} \text{ yr}^{-1}$ ). Although different interpretations are possible, this result can be explained through periods of enhanced AGN activity and star-forming bursts, possibly through major mergers.

However, optical QSOs comprise only a small fraction of the total AGN population. Even if the ‘unified model’ predicts that the host galaxy properties should not be affected by the viewing angle (type-1 vs. type-2 AGN), several studies have shown results supporting a scenario departing from the basic model. Investigating star formation in the hosts of  $24 \mu\text{m}$  selected type-1&2 AGN, I found that the type-2 AGNs display on average higher

star-formation rate than type-1 AGNs. This result is in agreement with previous studies suggesting an undergoing transition between a hidden growth phase and an unobscured AGN phase.

*... To my family!*

# Acknowledgements

Keeping a record of everyone who helped me during my PhD years seems challenging. So first, I have to start with the obvious... money! Money makes the world go round and I would like to thank the University of Hertfordshire for providing me with a PhD scholarship to go around the world.

As behind every PhD thesis there is a supervisor, my greatest regards go to Dr. Jason Stevens. Dr. Stevens has been a great mentor, always there to share with me his experience, comments, and worthwhile ideas, yet allowing me to work independently. Working with Dr. Stevens, I never felt like a PhD student, but like a PhD researcher.

Additionally, I would like to thank Prof. Matt Jarvis and Prof. Martin Hardcastle for sharing their vast knowledge on extragalactic astronomy, and collaborating with me on multiple projects.

Moving further (and when I say further I mean to the United States), I would like to thank the advisers during my predoctoral at CfA - Dr. Martin Elvis and Dr. Francesca Civano. Working at CfA with Dr. Elvis was an incredible experience - especially for someone studying QSOs! As expected, each and every meeting with him was like loading dozens of papers to your hard-drive. However, meetings with Martin would not have been so straightforward without before filtering my initial ideas with Francesca. That's why I should thank Francesca for introducing me to the X-ray and Cambridge world when I first moved there.

But working at CfA was a great opportunity given to me by Dr. Markos Trichas. It all started over seven years ago when I met Markos as my bachelor thesis advisor who turned out to be a good friend and an even better career manager. Markos is responsible for many of the opportunities that have come my way in the last few years. Always there to share his experience and advice me although, I think I can hear him right now complaining that I never listen...

Next, I would like to thank my colleagues and friends during these years. Particularly, my colleagues at UH with some special thanks to Hanifa for her amazing song! I want to thank Gulay and Emrah, Dimitris and Maria (I should start worrying about spending time with married couples). I have amazing memories with all of you, whether it be dinners, talking about radio-jets and drinking beers, playing guitar, fighting about Greek yogurt, being such great flatmates, or interrupting me while working for some much needed breaks. Moving to

the other side of the Atlantic, I want to sincerely thank the people I met there throughout this great year; Valia (just for everything, my mum would be very proud for you) and the Italian gang (E ora, con l'aiuto del sole vincerò!).

But, when colleagues are too professionals to complain about your PhD and your family doesn't know what your PhD is about who should you call? *Eva!* Apart from her friendship the last 15 years, the massive fun and the fights about politics she has always been there to listen me complain about weird results, scripts that didn't work, moving countries, moving houses. If you ask her she would say that she knows everything about AGN... and I think she might does!

Finally, I would like to thank my family with a short story. My mum, as a math geek, used to help me with my math courses at school. For this reason, every time I was getting a good mark she used to say that half of that belonged to her. So, mum, dad, Stellaki and grandma (my number one fan), half of this thesis definitely belongs to you. There are no words to express my gratitude, so, I will only say that without you and your support I would not be here.

*Thank you all!*

# Contents

<b>Abstract</b>	<b>iii</b>
<b>Acknowledgements</b>	<b>vii</b>
<b>List of Figures</b>	<b>xii</b>
<b>List of Tables</b>	<b>xiv</b>
<b>List of Abbreviations</b>	<b>xv</b>
<b>Refereed Publications</b>	<b>xvii</b>
<b>1 Introduction</b>	<b>1</b>
1.1 The Global Picture . . . . .	2
1.2 Finding AGN . . . . .	3
1.3 AGN Phenomenology . . . . .	5
1.3.1 Unification of AGN . . . . .	7
1.3.2 Seyfert unification scheme . . . . .	9
1.3.3 Radio-loud – radio-quiet AGN unification . . . . .	11
1.4 AGN demographics and evolution . . . . .	14
1.5 The host galaxies of distant AGNs . . . . .	18
1.5.1 Where the distant AGNs live? . . . . .	22
1.5.2 Probing the AGN/Star-Formation connection . . . . .	23
1.6 Layout of PhD Thesis . . . . .	27
<b>2 The largest X-ray-selected sample of <math>z &gt; 3</math> AGNs: C-COSMOS and ChaMP</b>	<b>28</b>
2.1 Introduction . . . . .	29
2.2 Sample selection . . . . .	30
2.2.1 The C-COSMOS sample . . . . .	30
2.2.2 The ChaMP sample . . . . .	33
2.3 The C-COSMOS & ChaMP $z > 3$ AGN Sample . . . . .	39
2.3.1 Optical Types . . . . .	40

2.3.2	X-ray Types . . . . .	43
2.3.3	X-ray/Optical flux ratio . . . . .	44
2.3.4	Comparison of optical and X-ray types . . . . .	46
2.4	The logN-logS of the $z > 3$ AGN . . . . .	48
2.5	2-10 keV Comoving space density . . . . .	53
2.5.1	Type-1 vs Type-2 AGN . . . . .	56
2.6	Summary . . . . .	57
<b>3</b>	<b><i>Herschel</i>-ATLAS: Far-infrared properties of radio-loud and radio-quiet quasars</b>	<b>60</b>
3.1	Unveiling the role of jets to the AGN/star-formation connection . . . . .	61
3.1.1	Radio-loud and radio-quiet quasars . . . . .	63
3.1.2	This work . . . . .	64
3.2	Sample definition and measurements . . . . .	64
3.2.1	The data . . . . .	64
3.2.2	<i>Herschel</i> flux measurements and stacked fluxes . . . . .	69
3.2.3	Luminosity calculation . . . . .	70
3.3	Synchrotron contamination . . . . .	71
3.4	Far-infrared properties . . . . .	75
3.4.1	Stacking . . . . .	76
3.4.2	FIR luminosity . . . . .	80
3.4.3	Dust temperature and mass . . . . .	80
3.4.4	250- $\mu$ m luminosity . . . . .	81
3.4.5	Two-Temperature model . . . . .	83
3.4.6	Star-formation rate . . . . .	84
3.5	Discussion . . . . .	87
3.5.1	Star-formation excess . . . . .	87
3.5.2	Host galaxy and dust properties . . . . .	89
3.6	Conclusions . . . . .	90
<b>4</b>	<b>The star formation rate of <math>z \sim 1</math> AGN</b>	<b>92</b>
4.1	Decoupling the evolution effects . . . . .	93
4.2	Data . . . . .	94
4.2.1	Sample selection . . . . .	94
4.2.2	<i>Herschel</i> photometry . . . . .	97
4.2.3	SMA photometry . . . . .	98
4.3	The black hole and host galaxy properties . . . . .	102
4.3.1	Stellar mass and black hole mass . . . . .	102
4.3.2	Accretion rate . . . . .	104
4.3.3	FIR emission in RLQs, RQs and RGs . . . . .	105

4.3.4	The FIR colours of RLQs, RQQs and RGs . . . . .	107
4.3.5	SED fitting . . . . .	110
4.3.6	FIR-radio correlation . . . . .	111
4.4	The star formation dependence on AGN activity . . . . .	115
4.5	The dependence of star formation on radio jets . . . . .	118
4.6	Star formation in RGs and RLQs . . . . .	122
4.7	Conclusions . . . . .	125
<b>5</b>	<b>HerMES: Far-Infrared properties of narrow emission line galaxies</b>	<b>127</b>
5.1	Introduction . . . . .	128
5.2	Sample & Observations . . . . .	129
5.2.1	The 24 $\mu$ m flux-limited sample . . . . .	129
5.2.2	Optical Spectral Modeling: The Emission Lines . . . . .	130
5.2.3	FIR Sample selection . . . . .	131
5.3	Spectral Energy Distributions . . . . .	133
5.4	Emission line Diagnostic Diagrams . . . . .	137
5.4.1	Adding SED information on the BPT diagrams . . . . .	139
5.5	Far-Infrared properties . . . . .	140
5.5.1	250 $\mu$ m emission in type-1 & 2 AGN . . . . .	140
5.5.2	Star-formation rate . . . . .	140
5.5.3	AGN contribution and FIR luminosity . . . . .	144
5.6	Conclusions . . . . .	145
<b>6</b>	<b>Conclusions and Future prospects</b>	<b>147</b>
6.1	The AGN/host galaxy interplay at the early Universe . . . . .	149
6.1.1	Predictions and first results . . . . .	151
6.2	The evolution from binary QSOs to QSOs . . . . .	152
6.3	What is the role of radio-jets in the hosts of X-ray AGN? . . . . .	156
<b>A</b>	<b>Appendix</b>	<b>160</b>
	<b>Bibliography</b>	<b>176</b>

# List of Figures

1.1	Schematic cross-section of the central engine and its close environment . . .	8
1.2	Quasar's structure. The four symmetric quadrants illustrate . . . . .	10
1.3	Mean absolute V-band magnitude versus mean redshift at three epochs . . .	14
1.4	Black hole mass plotted against the radio-loudness (left) . . . . .	14
1.5	Top: Comoving number density of AGNs, selected from multiple X-ray . .	17
1.6	$M_{BH} - \sigma$ relation for isolated galaxies from <a href="#">McConnell &amp; Ma (2013)</a> . . .	20
1.7	Schematic diagrams to illustrate the two main modes of AGN outflows . . .	21
1.8	Top: Mean $60\mu\text{m}$ (FIR) luminosity vs. AGN luminosity in 5 different redshift	25
2.1	Sky area vs. X-ray flux sensitivity curves for the C-COSMOS . . . . .	31
2.2	Schematic flow diagram of the high- $z$ sample selection. . . . .	32
2.3	Optical and infrared ChaMP survey completeness as a function of 0.5-2 keV	35
2.4	Observed AB magnitude distribution of all the $i$ -band, $K$ -band, and $3.6\mu\text{m}$	41
2.5	The hard X-ray luminosity (computed with $\Gamma = 1.8$ ) redshift plane for . . .	42
2.6	Hardness ratio versus redshift. . . . .	45
2.7	X-ray flux (soft-top, hard-bottom) vs. the $i$ -band magnitude . . . . .	47
2.8	The mean hardness ratio as a function of redshift . . . . .	49
2.9	The binned $\log N - \log S$ relation of the $z > 3$ and $z > 4$ QSOs . . . . .	51
2.10	The comoving space density in 3 different 2-10 keV X-ray luminosity ranges.	54
2.11	The X-ray comoving space density for type-1 and type-2 AGN . . . . .	58
3.1	Optical luminosity of the radio-loud and radio-quiet samples . . . . .	66
3.2	The median radio flux density as a function of redshift . . . . .	68
3.3	SED at radio and FIR wavelengths of RLQs . . . . .	72
3.4	FIR luminosity versus dust temperature . . . . .	79
3.5	Correlation between infrared luminosity at $250\mu\text{m}$ and redshift . . . . .	82
3.6	Weighted mean SFRs as a function of redshift . . . . .	86
4.1	Optical absolute magnitude density map vs. redshift for SDSS quasars . . .	95
4.2	325-MHz radio luminosity vs. redshift for our sample . . . . .	96
4.3	Spectral energy distribution at radio and FIR wavelengths . . . . .	100

4.4	Distributions of $M_{\text{BH}}$ , $L_{\text{bol}}$ and $\lambda_{\text{Edd}}$ . . . . .	103
4.5	The PACS and SPIRE mean flux densities . . . . .	106
4.6	SPIRE and PACS colour-colour diagrams of the AGN in our sample . . . . .	109
4.7	FIR luminosity versus dust temperature . . . . .	112
4.8	FIR luminosity ( $L_{\text{FIR}}$ ) vs. radio 350 MHz luminosity ( $L_{325\text{MHz}}$ ) . . . . .	114
4.9	FIR luminosity ( $L_{\text{FIR}}$ ) vs. bolometric luminosity ( $L_{\text{bol}}$ ) . . . . .	116
4.10	FIR luminosity ( $L_{\text{FIR}}$ ) vs. galaxy mass ( $M_{\text{gal}}$ ) . . . . .	119
4.11	SFR excess between RLQs and RQQs as a function of bolometric luminosity	120
4.12	Fraction of sSFR enhancement for RLQs and RGs as a function of $Q_{\text{jet}}/L_{\text{Edd}}$	124
5.1	A sample of rest frame spectra drawn from our sample . . . . .	132
5.2	Redshift distribution of all 567 spectroscopically identified sources . . . . .	134
5.3	Examples of best-fit SEDs . . . . .	137
5.4	Fractional contribution of AGN and starburst components . . . . .	138
5.5	BPT diagram for the 121 sources with available lines . . . . .	141
5.6	250- $\mu\text{m}$ flux density distribution for type-1 and type-2 AGN . . . . .	142
5.7	Weighted mean SFRs as a function of redshift . . . . .	143
5.8	Histograms showing the FIR luminosity distribution for the type-1&2 AGN	144
5.9	Fractional contribution of AGN and starburst components to FIR luminosity	146
6.1	$i$ -band magnitude vs. 850 $\mu\text{m}$ flux density for C-COSMOS sample. . . . .	151
6.2	850 $\mu\text{m}$ image for the four targets observed by SCUBA-2 . . . . .	152
6.3	Optical and X-ray images of the SDSSJ1254+0846 binary QSO . . . . .	153
6.4	Numerical simulation of a merger like SDSSJ1254+0846 . . . . .	155
6.5	Top: Lower ( $5\sigma$ ) radio flux 1.4 GHz limits vs. X-ray 2-10 keV flux limits .	159
A.1	Radio to FIR spectral energy distribution . . . . .	175

# List of Tables

2.1	Photometric redshift reliability and number of sources . . . . .	38
2.2	Comparison of optical and X-ray types . . . . .	48
3.1	The RLQs and RQQs FIR mean flux densities . . . . .	70
3.2	The K-S and M-W probabilities of RLQs and RQQs flux densities . . . . .	71
3.3	Estimated weighted-mean FIR properties . . . . .	77
3.4	The K-S and M-W probabilities that FIR estimations . . . . .	77
3.5	Mean FIR parameters for each bin . . . . .	78
4.1	The $z \sim 1$ sample mean flux densities in the PACS and SPIRE bandpasses .	107
A.1	Properties of the $z > 3$ AGN sample (Chapter 2). . . . .	162

# List of Abbreviations

A list of abbreviations often used in this work for easy reference.

AGN.....	Active Galactic Nucleus
BH.....	Black Hole
BLAGN.....	Broad-line AGN
SMBH.....	Super-massive Black Hole
QSOs.....	Quasi-stellar objects
RLQ.....	Radio-loud quasar
RQQ.....	Radio-quiet quasar
RLAGN.....	Radio-loud AGN
RQAGN.....	Radio-quiet AGN
RG.....	Radio galaxy
NLAGN.....	Narrow-line AGN
FIR.....	Far-Infrared
SFR.....	Star-formation rate
sSFR.....	Specific star-formation rate
SED.....	Spectral energy distribution
LDDE.....	Luminosity-dependent density evolution
LADE.....	Luminosity and density evolution
ISM.....	Inter-stellar medium
ChaMP.....	Chandra Multi-wavelength Project survey

- SDSS . . . . . Sloan Digital Sky Survey
- FIRST . . . . . Faint Images Radio Sky at Twenty-one centimetres
- ISM . . . . . Interstellar medium
- K-S . . . . . Kolmogorov-Smirnov
- GMRT . . . . . Giant Metrewave Radio Telescope

# Refereed Publications

- **Kalfountzou E.**, Civano F., Elvis M., Green P. J., *The Largest X-ray Selected Sample of  $z > 3$  AGN: C-COSMOS & ChaMP*, 2014, MNRAS, 445, 1430 ([arXiv:1408.6280](#))
- **Kalfountzou E.**, Stevens J. A., Jarvis M. J., Hardcastle M. J., Smith D. J. B., Bourne N., Dunne L., Ibar E., Eales S., Ivison R. J., Maddox S., Smith M. W. L., Valiante E., de Zotti G., *Herschel-ATLAS: far-infrared properties of radio-loud and radio-quiet quasars*, 2014, MNRAS, 442, 1181 ([arXiv:1404.5676](#))
- Trichas M., Green P. J., Constantin A., Aldcroft T., **Kalfountzou E.**, Sobolewska M., Hyde A. K., Zhou W., Kim D., Haggard D., Kelly B.C, *Empirical Links between XRB and AGN accretion using the complete  $z < 0.4$  spectroscopic CSC/SDSS Catalog*, 2013, ApJ, 778, 188 ([arXiv:1306.0594](#))
- **Kalfountzou E.**, Jarvis M. J., Bonfield D. G. and Hardcastle M. J., *Star formation in high- redshift quasars: excess [OII] emission in the radio-loud population*, 2012, MNRAS, 427, 2401 ([arXiv:1209.2329](#))
- **Kalfountzou E.**, Trichas M., Rowan-Robinson M., Clements D., Babbedge T. and Seiradakis J. H., *EFOSC2 spectroscopy of SWIRE-CDFS galaxies*, 2011, MNRAS, 413, 249 ([arXiv:1005.4353](#))

*Where are we going? Do not ask! Ascend, descend.  
There is no beginning and no end. Only this present moment exists, full of bitterness, full of sweetness, and I rejoice in it all.*

[The Saviors of God (1923)] - Nikos Kazantzakis

# 1

## Introduction

Active Galactic Nuclei (AGN) belong amongst the most fascinating objects in the Universe. Their study has been rapidly evolving with a seismic shift in our understanding of their role in shaping the evolution of the Universe. The term AGN refers to the central region of a galaxy, which outshines its host over the bigger part of the electromagnetic spectrum. In the heart of these objects, large amounts of energy are released due to the accretion of matter onto a supermassive black hole (SMBH). An accretion disk of hot gas surrounds the SMBH, but moving further out it is also surrounded by a donut-shaped torus of colder gas and dust. Although classes of AGN can be very diverse, they exhibit at least some common features.

Despite the large amounts of energy they release, AGN are no longer considered as relatively rare and exotic gravity-driven phenomena but they are thought to play a dominant role in the galaxy evolution and formation. The main evidence comes from:

1. the identification in nearby galaxies of the tight relationships between the black hole (BH) mass and the various properties of the host galaxy (e.g. [Kormendy & Richstone, 1995](#); [Magorrian et al., 1998](#); [Gebhardt et al., 2000a](#); [Merloni, 2004](#); [Beifiori et al., 2012](#)),
2. the requirement for several theoretical models and numerical simulations to implement outflows driven by the AGN, such as jets and winds, to regulate or suppress star formation in galaxies ('AGN feedback'; e.g. [Springel et al., 2005](#); [Di Matteo et al., 2005](#); [Croton et al., 2006](#); [Hopkins et al., 2006](#)).

Whilst a compelling picture has emerged, it is mainly constructed from indirect evidence while direct observational evidences are still scarce particularly in the distant Universe where the majority of the BH and galaxy growth has occurred. This section provides an overview of the observed properties of AGN across the electromagnetic spectrum, their evolution across cosmic time, the effects of their local environment and how all these parameters could affect their connection with the star formation.

## 1.1 The Global Picture

Observations show that a number of galaxies possess a very high concentration of luminosity in their nuclear regions. For this class of objects, the so called AGN, the luminosity of their nuclei lie in the range of  $10^{40} - 10^{47} \text{ erg s}^{-1}$  (e.g. Fabian, 1999). In the current paradigm, the primary source of this energy is believed to be the gravitational accretion of matter onto a SMBH (e.g. Rees, 1984; Fabian, 1999). The central SMBH gains mass by accreting some of the surrounding matter in an accretion disk. As material in the disk loses angular momentum and gravitational potential energy, it falls further into the disk and gives off substantial amounts of electromagnetic radiation. The total radiation in an AGN can sometimes outshine the entire stellar component of its host galaxy and while their emission covers almost the entire electromagnetic spectrum. Therefore, AGN can be found at the farthest reaches of the universe.

One of the most important questions about AGN concerns the nature of their emitted energy source. Despite the observed differences between the AGN types, the entire AGN class has one common property: a large amount of energy is released within a small volume. It became clear very early that the black hole paradigm explains best, in a natural way, many of the observed properties and is thus commonly preferred (e.g. Hoyle & Fowler, 1963; Salpeter, 1964; Rees, 1984). In this picture, the large amount of energy comes from the release of gravitational energy from accretion onto the black hole. The surrounding matter, driven by its gravitational pull, generates an accretion disc in which, matter spirals towards the black hole whilst losing its angular momentum. The potential energy of the matter into the accretion disk is converted in radiation by viscous forces. As a matter of fact, accretion of matter in the strong gravitational field of these objects is the most efficient process. The accretion luminosity is a function of the radiative efficiency  $\epsilon$  given by:

$$L_{acc} = \epsilon \dot{M} c^2 \quad (1.1)$$

where  $\dot{M}$  is the accretion rate and  $c$  the speed of light. The radiative efficiency for accretion of matter onto a black hole is, however, with  $\epsilon \sim 0.1$  much higher than for nuclear fusion. Even though, there are studies suggesting the radiative efficiency might be higher, up to

$\epsilon \sim 0.4$ , for rapidly rotating black holes (e.g. [Elvis et al., 2002](#); [Wang et al., 2006](#)).

As an example, in order to fuel a luminous AGN with  $L \sim 10^{46}$  erg s $^{-1}$ , a mass accretion rate of  $2 M_{\odot} \text{ yr}^{-1}$  is required. It is clear that the luminosity of an AGN primarily depends on the mass accretion rate, with in turn depends on the mass of the central black hole and the efficiency for the conversion of gravitational energy into radiation. However, assuming a standard accretion disc models with a geometrically thin disc, the luminosity emitted from an object with mass  $M_{\text{BH}}$  has a physical upper limit, the Eddington limit

$$L_{\text{Edd}} \simeq 1.3 \times 10^{38} (M_{\text{BH}}/M_{\odot}) \text{ erg s}^{-1}, \quad (1.2)$$

at which the radiation pressure from accretion of the infalling matter balances the gravitational force of the black hole. The ratio between the bolometric and Eddington luminosities is referred as the Eddington ratio,  $\lambda = L_{\text{b}}/L_{\text{Edd}}$ . Luminosities and accretion rates higher than the Eddington limit in so-called super-Eddington accretion are possible in different disc models (e.g. [Shakura & Sunyaev, 1973](#); [Dotan & Shaviv, 2011](#); [Sądowski et al., 2011](#)).

## 1.2 Finding AGN

The exploration of how the BH growth can be triggered in time and space requires the identification of AGN over a wide range of redshifts and cosmic environments. Extensive optical surveys have provided the easiest way to identify AGN in the local Universe ([Kauffmann et al., 2003](#); [Heckman et al., 2004](#); [Ho, 2008](#)). Since the AGN narrow emission line region ( $\approx 10 - 1000$  pc) lies outside of the central dusty circumnuclear material (see Section 1.3.1), optical spectroscopic observations are able to identify even heavily obscured AGNs (e.g. due to the putative obscuring torus; [Antonucci, 1993](#)), though they may be affected by dust in the host galaxy. Multi-wavelength radio, mid-IR and X-ray observations further extend our understanding of the role of AGNs within the formation and evolution of galaxies with an almost complete census of AGN activity down to a given sensitivity limit (i.e., lower-luminosity AGNs can still be unidentified), even in the presence of star-forming dust in the host galaxy (e.g. [Goulding & Alexander, 2009](#); [Nardini et al., 2010](#)). However, if the obscuration level towards the central region is extremely high due to the presence of dust in the host galaxy (e.g. Arp 220; [Clements et al., 2002](#); [Iwasawa et al., 2005](#); [Downes & Eckart, 2007](#)), even intrinsically luminous AGN might be completely obscured and remain unidentified.

At high redshifts, although optical spectroscopy remains effective at identifying distant AGN (e.g. [Steidel et al., 2002](#); [Trichas et al., 2009](#); [Kalfountzou et al., 2011](#)), the number of identified AGN can be quite limited since the emission-line AGN diagnostics move out of

the optical bands at  $z > 0.4$ . Recently, various techniques have been employed to overcome these limitations extending the utility of optical spectroscopy for AGN identification out to  $z \approx 1$  (e.g. [Juneau et al., 2011](#); [Trouille et al., 2011](#)). Nevertheless, X-ray observations remain the most efficient and effective way to find a substantial fraction of the most heavily obscured distant AGNs, almost unaffected by the presence of obscuration (e.g. [Tozzi et al., 2006](#); [Gilli et al., 2007](#)) with a minimal weak contamination from star formation (e.g. [Alexander et al., 2011](#); [Comastri et al., 2011](#)). Despite the significant advances, even  $> 10$  keV X-ray observations (e.g. *Nuclear Spectroscopic Telescope Array*; *NuSTAR*, [Harrison et al., 2013](#)) are relatively insensitive to extreme amounts of absorption (i.e., the most Compton-thick AGNs with  $N_{\text{H}} > 3 \times 10^{24} \text{ cm}^{-2}$ ). Fortunately, some of these objects, where absorption is so high that not even X-ray photons can escape, can be recognized as AGNs by their infrared and radio emission (e.g. [Lacy et al., 2004](#); [Stern et al., 2005](#); [Hickox et al., 2007](#)) since:

1. the intrinsic emission from the AGN heats the obscuring dust and is re-emitted at infrared wavelengths and
2. any core or jet emission from the AGN produced at radio frequencies can easily pass through the absorbing material.

However, infrared and radio emission due to both AGN and star formation activity often co-exist, making it challenging to decompose the two components (e.g. [Polletta et al., 2007](#); [Mullaney et al., 2011a](#)). The bulk of a galaxy's light is emitted at ultra-violet (UV) to submillimetre wavelengths ( $\approx 0.1 - 1000 \mu\text{m}$ ; e.g. [Kennicutt & Evans, 2012](#)) and is primarily due to the radiation produced by stars and AGN activity, when present. The intrinsic emission from these stellar populations dominates in the UV - near-infrared (NIR) bands and can be described by a black-body radiation model over a range of masses and ages ([Kurucz, 1979](#)). These models are typically sensitive to the presence of dust, particularly in dusty star-forming regions, which are generally optically thick to short-wavelength UV-NIR radiation. Consequently, observations at far-infrared (FIR) wavelengths are among the most useful tools to efficiently measure the emission from young and forming stars since the emitted starlight will heat the dust and then thermally re-radiated as FIR emission ( $\lambda \approx 30 - 300 \mu\text{m}$ ; typical temperatures of  $T \approx 10 - 100$  K). Therefore, galaxies which are currently undergoing an intense burst of star formation emit most of their light at FIR wavelengths, while quiescent galaxy emission is produced at UV-NIR wavelengths.

Since the accretion disk is hotter than young stars, the dust is typically heated to higher temperatures ( $\approx 100 - 1000$  K) and therefore the majority of the infrared emission from the AGN is shifted to shorter NIR - mid-infrared (MIR) wavelengths than that from star formation ( $\approx 3 - 30 \mu\text{m}$ ; e.g. [Netzer et al., 2007](#); [Mullaney et al., 2011a](#)). Consequently, for many AGN studies, the FIR emission is taken as a measurement of the star formation rate

(SFR). However, in order to provide the most accurate SFR constraints it is necessary to decompose the infrared emission into the AGN and star-formation components, which is essential for reliable SFR measurements from intrinsically luminous AGNs (e.g. [Netzer et al., 2007](#); [Mullaney et al., 2011a](#); [Delvecchio et al., 2014](#)). The following sections explore the multi-wavelength process of AGN activity using observations at X-ray, optical, IR, and radio wavelengths. I investigate the evolution of AGN with redshift, the connection between AGN and radio-jet activity with star formation, and the role of environment.

### 1.3 AGN Phenomenology

AGN show a great variety of classes and definitions. In the following a brief excursion going through most AGN classes is given. Although many properties of AGN distribute relatively continuously, I will also consider the question to which extent these classes are really distinct and different or if AGN can be variable or may even one class of object evolve into another class on certain periods of their time life.

**Seyfert galaxies** are a class of active galaxies characterized by a very bright and star-like core, high nuclear surface brightness and strong emission lines in their optical spectrum ([Khachikian & Weedman, 1974](#)). About 3 to 5 per cent of all galaxies are Seyfert galaxies ([Maiolino & Rieke, 1995](#); [Maia et al., 2003](#)). Almost all these sources are hosted in spiral galaxies and they belong to the radio-quiet AGN family, i.e. they are either radio-undetected or radio-quiet. The Seyfert galaxies are classified according to the presence of ‘broad lines’ in their optical spectrum. In type-1 Seyfert galaxies (Sy1s) broad emission lines are observed due to gas with density of  $\sim 10^9 - 10^{12}$  atoms  $\text{cm}^{-3}$  and typical moving speed on the order of a few thousand  $\text{km s}^{-1}$ . Additionally, narrow forbidden emission lines with velocities of a few hundreds of kilometers per second can be also observed in their spectra. In the case of type-2 Seyfert galaxies (Sy2s) only narrow emission lines are found. There are, however, Seyferts with intermediate properties between the two types and even observed evolutionary pictures in which Sy1s evolve into Sy2s, or *vice versa*, on scales of a few months (e.g. NGC 4151; [Penston & Perez, 1984](#)).

**Low-Ionization Nuclear Emission Line Region** galaxies (LINERs; [Heckman, 1980](#)) are very similar to Sy2s. The difference in the optical spectra is that these galaxies show weaker continuum emission of LINER nuclei and stronger narrow low-ionization emission lines uncharacteristic of photoionization from normal stars ([Heckman, 1980](#)). LINERs are very common as they are detected in at least one third of nearby galaxies ([Ho et al., 1997](#)) and they may simply be very low-luminosity Seyferts or objects that include mechanisms of starburst-driven winds or shock-heated gas and cooling flows that play a major role in ionizing the gas ([Heckman, 1980](#); [Filippenko & Terlevich, 1992](#)). As [Heckman \(1980\)](#) and later [Keel \(1983\)](#) mentioned, these narrow-line regions are powered by the same type of source as Seyferts and therefore LINERs may represent the missing link between powerful

AGN and nearby ‘normal’ galaxies.

**Radio Galaxies** are also strong radio AGN emitters. These sources show similar spectral properties at optical wavelengths as the Seyferts and so they could be considered as their radio-loud analogues. Based on their optical spectra, the radio galaxies can as well be separated into Narrow Line Radio Galaxies (NLRGs) and Broad Line Radio Galaxies (BLRGs), depending on the full width at half maximum (FWHM) of their optical emission lines. Contrary to Seyferts, they are usually associated with (giant) elliptical galaxies.

The radio emission arises in two morphologically and spatially distinct components: the compact region and the extended region. Emission from both the compact and extended region is most likely synchrotron radiation from a population of relativistic particles being ejected from the central engine. Such collimated outflows are called jets. A further morphological classification is based on the morphology and the power of the jets. By comparing the distance with the total extent of the radio-emitting region, [Fanaroff & Riley \(1974\)](#) defined two subclasses of radio galaxies: radio galaxies with strong, symmetric jets and extended radio lobes that become fainter as one moves to the outer extremities of the lobes are classified as Fanaroff & Riley Type I (FR I) sources. On the other hand, when the radio lobes are collimated, ending in luminous hotspots that have steep radio spectra in the inner regions, these are classified as Fanaroff & Riley Type II (FR II) sources. [Fanaroff & Riley \(1974\)](#) suggested a separating luminosity at 178 MHz of  $2.5 \times 10^{26} \text{ W Hz}^{-1} \text{ sr}^{-1}$ , but the luminosity boundary between them is not very sharp, and as shown by [Ledlow & Owen \(1996\)](#) it depends on the host galaxy optical luminosity. The host galaxies of FR II are similar to the normal giant ellipticals, whereas FR I galaxies are usually larger, brighter and display flatter surface brightness profiles than normal ellipticals (e.g. [Owen & Laing, 1989](#)) but this may also depend on redshift (e.g. [Herbert et al., 2011](#)). FR II galaxies have more luminous optical emission lines (e.g. [Zirbel & Baum, 1995](#)) and are found in less rich environments compared to FR I galaxies depending on the redshift (e.g. [Hill & Lilly, 1991](#); [McLure & Dunlop, 2001](#); [Falder et al., 2010](#)).

**Quasars** are the most luminous AGN, which are typically very distant with their number density having a peak at  $1 < z < 3$  (e.g. [Fan et al., 2001](#); [Hasinger et al., 2005](#); [Richards et al., 2006a](#)). At these distances the host galaxy is no longer detectable, either because the nucleus outshines the host galaxy, or because its angular extension is well below the telescope’s angular resolution thus, quasars show a point-like appearance at optical wavelengths. The so-called quasi-stellar objects (QSOs) were first detected in the search for optical counterparts of unidentified radio sources (e.g. [Schmidt, 1963](#); [Matthews & Sandage, 1963](#)). Even though, the radio-loud quasars (RLQs) make only up to the 10 per cent of the total quasar population (e.g. [Ivezić et al., 2002](#)). The radio luminosity of the radio-loud objects at 5 GHz is about to 1 - 3 order of magnitude higher than their optical luminosity ([Sanders et al., 1989](#)).

**Blazars** constitute a subset of the AGN population with relativistic jets pointing in the direction of the observer. The general characteristics of Blazars that distinguish them from

the rest of the AGN are the smooth continuum at the IR/optical/UV regions from a stellar-like nucleus, their high optical polarization, the fast optical variability on timescales as short as hours and their strong and time-variable radio continuum. The special jet orientation can explain these characteristics. They contain two subclasses: the BL Lac objects and the optically violent variables (OVVs). BL Lac objects so no or weak emission lines thus, their optical spectra are clearly dominated by continuum emission (Strittmatter et al., 1972). The majority of blazars are hosted by giant elliptical galaxies.

### 1.3.1 Unification of AGN

In 1995, Urry & Padovani proposed an AGN unification scheme suggesting that the different types of AGN can be unified in a single theory. We could summarize the observed properties of AGN in three wide groups: luminosity, radio-loudness and emission line widths. Fig. 1.1 presents the current understanding of unification scheme in which the observed AGN type depends on the observer's viewing angle to the system. Radio jets are the only intrinsic property responsible for the presence of radio-loud and radio quiet AGN sub-classes, while most of the other AGN phenomenological differences arise simply from the different viewing angles.

The key elements of this unification model are the components of the AGN. The central engine is associated with a SMBH surrounded by an accretion disk which feeds the BH with gas. Material orbiting around the BH reaches its highest orbital speed velocities as it comes closer and closed to the BH. Due to the large velocity dispersion in the inner region of AGN, the emission lines, which are produced by photo-ionization by the continuum radiation from the central source, are broad. Thus, this inner region where fast-moving clouds orbit above the accretion disk is called Broad Line Region (BLR).

The original unification scheme (Antonucci, 1993) included a torus of gas and dust, large enough to completely obscure the central region in some directions (e.g. high inclination angles) and block the direct optical and UV emission to the BLR, even though some continuum and broad emission lines can be scattered into the line-of-sight by dust which is found throughout the region. Even further away from the BH, the emission comes from a region with much smaller velocity of clouds - the Narrow Line Region (NLR). Combined with the low gas density at these distances, the formation of forbidden lines is allowed while their profiles are narrower due to the smaller velocity spread. In some cases, the gravitational energy extracted by BH and accretion disk processes is radiated away as highly energetic photons or escapes in a jet. The direction of the relativistic jets is thought to align with the symmetry axis, but no preferential orientation relative to the rotation axis of the host galaxy is seen (e.g. Lyutikov et al., 2005; Lindner & Fragile, 2007).

As mentioned above, most of the properties of the different AGN types can be explained assuming a simple geometrical parameter associated with a 'donut'-shaped obscuring AGN

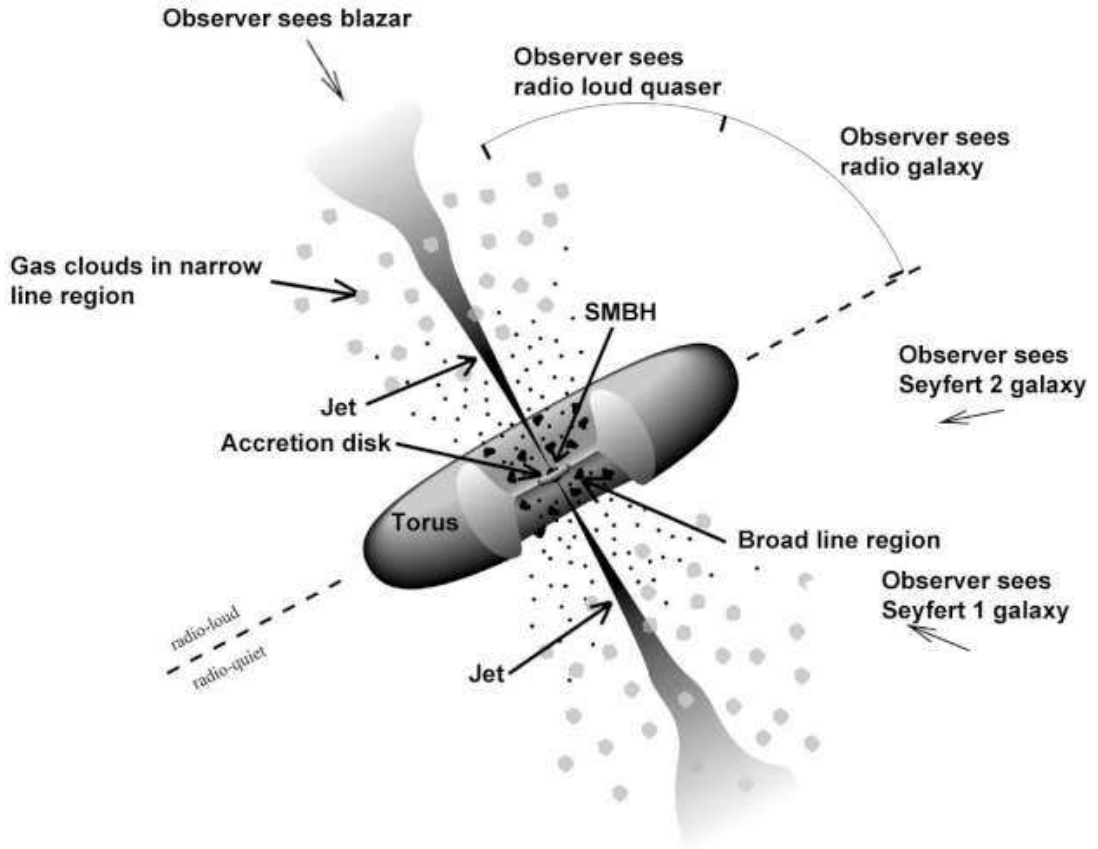


FIGURE 1.1: Schematic cross-section of the central engine and its close environment in the unified scheme (not to scale). In the unification model the different AGN classes are explained by different viewing angles of the same AGN model. The labels indicate the components of an AGN. Viewing angles are labelled with the AGN type. The separation in radio-loud and radio-quiet along the orbital plane is only used for illustration. The central super massive black hole is surrounded by an accretion disk of orbiting dust and gas. Depending on the radio-loudness of the source, a jet (or two back-to-back jets) of accelerated particles is present. Illustration after [Urry & Padovani, 1995](#).

torus and the relative position of the observer. For instance, the inclination of these systems can explain why only a fraction of AGN show broad lines in their spectra. If the obscuring torus is observed from the exact edge-on direction (inclination angle  $\theta = 90^\circ$ ), it can prevent the direct view of the inner AGN region and only the NLR can be seen while the BLR is obscured. As we move away from the edge-on axis (inclination angle decreases), the inner region becomes more apparent. Thus, the two types of Seyfert galaxies (type-1 and type-2) could be explained using the orientation parameter.

In a similar manner, RLQs are believed to have the same morphology as FR II radio galaxies. In the case of flat-spectrum radio-quasars (FSRQ), they are observed in small angles close to the line-of-sight which is nearly aligned to the axis of the jet. For the steep-spectrum radio-quasars (SSRQ), the line-of-sight is oriented to higher angles (until  $45^\circ$ ; e.g. [Barthel, 1989](#); [Padovani & Urry, 1992](#)). The most extreme case are the blazars, where the jet is pointed almost directly toward the observer. The relativistically boosted emission from

the jet can dominate all the other sources of radiation, and explains the feature-less spectra, as well as the short variability time scales. The BL Lac objects have been unified with FR I radio galaxies (e.g. [Schwartz & Ku, 1983](#)).

However, the traditional ‘donut’-shaped structure of the obscuring torus might be a simplified picture. The real distribution of the material could be associated with ways more complex structures (clumpy torus model; e.g. [Tristram et al., 2007](#); [Nenkova et al., 2008](#)) or even depend on AGN luminosity (e.g. [Elitzur & Shlosman, 2006](#); [Lawrence & Elvis, 2010](#); [Elitzur, 2012](#)). [Elvis \(2000\)](#) presented a more sophisticated model for the quasars’ structure (see [Fig. 1.2](#)) where an accelerating outflow ( $\sim 10^6$  K) with a funnel-shaped thin shell geometry rises vertically from a narrow range of radii on a disk in the BLR. This structure can explain the observed emission and absorption-line phenomena associated with both broad absorption line region, high-ionization ultraviolet narrow absorption lines and X-ray warm absorbers. The observed differences in high and low luminosity sources such as the UV and X-ray Baldwin and the greater prevalence of obscuration in low-luminosity AGNs could be explained by small luminosity-dependent changes in the outflow shape of the inner parts of the model.

Having treated AGN in general, what follows is a more detailed description of particular AGN sub-classes which are of direct relevance for this thesis. Special attention will be paid to the apparent type-1&2 AGN unification and radio-loudness dichotomy of quasars.

### 1.3.2 Seyfert unification scheme

The Seyfert unification scheme predicts that Sy1s and Sy2s galaxies are extracted from the same parent population and the observed differences are solely due to the differing orientations of the ‘donut’-shaped obscuring material around the nucleus (e.g. [Rowan-Robinson, 1977](#); [Lawrence & Elvis, 1982](#); [Antonucci, 1993](#)). Emission from the NLR is expected to be unaffected by the viewing angle while, on the contrary, emission from the BLR can be observed only if the line of sight does not intercept the torus. In type 2s, where the opening of the torus is edge-on, the BLR has been detected in polarised light due to scattering by free electrons and dust grains located above the torus opening. Spectropolarimetric observations provide direct evidence for the presence of polarized broad emission lines establishing that at least some of the Seyfert 2s harbor a type 1 Seyfert whose inner region is obscured from view (e.g. [Miller et al., 1991](#); [Heisler et al., 1997](#); [Moran et al., 2000](#); [Panessa & Bassani, 2002](#)). However, it is a matter of debate whether all Sy2s possess hidden type 1 nuclei.

Similarly to [Moran et al. \(2000\)](#), several other works have yielded results consistent with the predictions of the Seyfert unification scheme, e.g. stronger continuum emission in the case of Sy1s, with a systematic lack of ultraviolet and X-ray (soft and hard) emission in Sy2s compared to Sy1s galaxies ([Lawrence, 1987](#); [Mas-Hesse et al., 1994](#)), similar amount of molecular gas for both types ([Maiolino et al., 1997](#); [Curran, 2000](#)), (bi)conical morphology

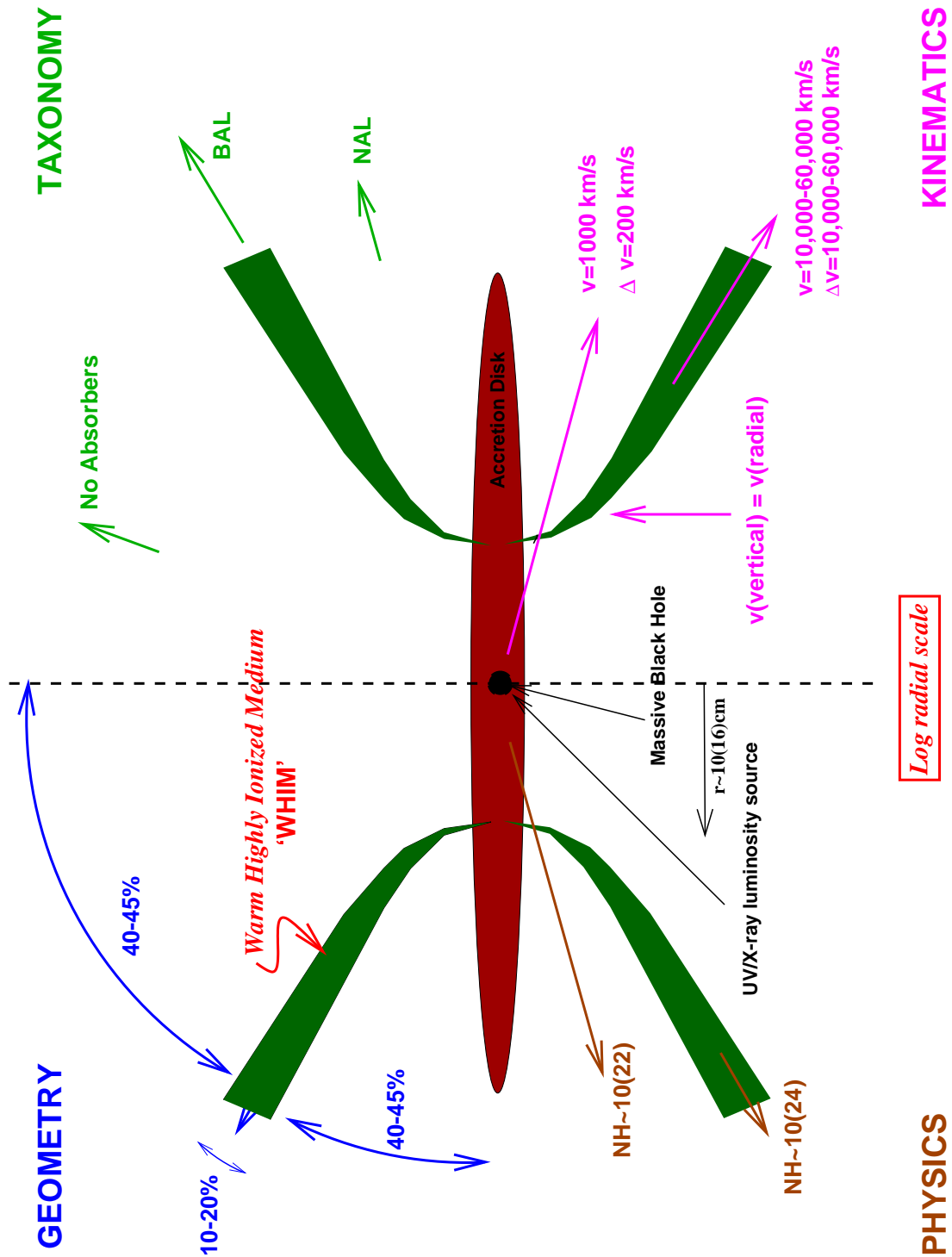


FIGURE 1.2: Quasar's structure. The four symmetric quadrants illustrate (clockwise from top left): the opening angles of the structure; the spectroscopic appearance to a distant observer at various angles; the outflow velocities a long different lines of sight; some representative radii (appropriate for the Seyfert 1 galaxy NGC 5548) and some typical column densities. Figure adapted from Elvis (2000).

of the NLR perhaps due to an obscuring torus (Mulchaey et al., 1996; Muñoz Marín et al., 2007), and no statistically significant difference in the nuclear radio properties of the two Seyfert subtypes (Lal et al., 2011).

While this unified scheme is simple and attractive, inconsistencies with its predictions remain, such as, the absence of hidden Seyfert 1 nuclei in a large fraction ( $\sim 50$  per cent) of Sy2s (e.g. Tran, 2001), the increase of the detected hidden broad-line regions (HBLRs) fraction with the radio power of AGN (e.g. Tran, 2003), Sy2s tend to have, on average, later Hubble types than Sy1s (e.g. Malkan et al., 1998), the lack or low X-ray absorption in some Sy2s (e.g. Panessa & Bassani, 2002; Caccianiga et al., 2004; Corral et al., 2005).

Although clear evidence favour the obscuration of the nuclei region due to the pc-scale torus presence, in agreement with the orientation-based unification model predictions, it is still a matter of debate whether an additional ingredient, associated with larger scales, must be considered (e.g. Maiolino & Rieke, 1995; Matt, 2000). Several recent studies have shown results that would imply significant departure from the default unified model, e.g. enhanced star formation in Sy1s (e.g. Page et al., 2004; Hatziminaoglou et al., 2010; Chen et al., 2015), more disturbed host galaxy morphology of dust-obscured quasars when compared to unobscured quasars (e.g. Lacy et al., 2007) and stronger clustering in Sy2s (e.g. Hickox et al., 2011; Donoso et al., 2014; DiPompeo et al., 2014). These results associate the high levels of nuclear obscuration with dusty starburst events due to major merger. Due to the powerful AGN activity and AGN winds, the dust can be later expelled implying an evolutionary link between type-1 (unobscured) and type-2 (obscured) AGN (e.g. Di Matteo et al., 2005; Hopkins et al., 2006; Somerville et al., 2008; Treister et al., 2009). However, other studies have found no significant difference between mean stellar masses and star-formation rates of obscured and unobscured X-ray-selected AGNs hosts (e.g. Mainieri et al., 2011; Rosario et al., 2012; Rovilos et al., 2012; Merloni et al., 2014).

Nonetheless, both AGN sample selection from flux limited surveys and measurements of star formation properties for AGN host galaxies still suffer from selection effects that are often different among various AGN populations. The test of the validation and limitation of the current unification models of AGN still continues with more improved and well defined samples.

### 1.3.3 Radio-loud – radio-quiet AGN unification

The radio-loudness dichotomy has been recognized for many years as constituting one of the major questions of intrinsic versus orientation differences in QSOs. The degree of radio-loudness is based on the radio emission generated by the core emission, jets and lobes and its correlation with the central engine. However, due to the large variety of definitions a unique classification is sometimes difficult.

Generally, two main parameters are used to estimate the radio-loudness of a QSO, either

the radio power at 5 GHz  $P_{5\text{GHz}}$  or the radio-to-optical flux density ratio  $R$ . [Kellermann et al. \(1989\)](#) originally defined the radio-loudness parameter  $R$  as the 5 GHz radio flux density to  $B$ -band (4000Å) flux ratio,  $R = \frac{S_{5\text{GHz}}}{S_{2500}}$ . Based on this definition, QSOs are often separated into two broad categories, the ‘radio-quiet’ (RQQs) and the ‘radio-loud’ (RLQs) quasars. The radio-loud sub-sample is usually categorized by  $R > 10$  (e.g. [Kellermann et al., 1989](#)) or  $P_{5\text{GHz}} > 10^{24} \text{W Hz}^{-1} \text{sr}^{-1}$  (e.g. [Miller et al., 1990](#)), or both (e.g. [Falcke et al., 1996](#); [Wold et al., 2001](#)), and makes only  $\sim 10$  per cent of the total population.

The radio-loudness parameter,  $R$ , was found to be bimodal where a luminosity gap separates the two populations ([Kellermann et al., 1989](#); [Miller et al., 1990](#); [Ivezić et al., 2002](#)). However, some studies found a class of radio-intermediate quasars which have radio luminosities that fill the gap ([Miller et al., 1993](#)). This group of sources was proposed to be the relativistically beamed radio-quiet (or radio-weak) quasars ([Falcke et al., 1996](#)). In contrast, [White et al. \(2000\)](#) found no bimodality in the  $R$  parameter distribution using quasars selected from the FIRST ([Becker et al., 1995](#)) survey (see also [Cirasuolo et al., 2003a,b](#); [Ivezić et al., 2004](#); [Barvainis et al., 2005](#)). However, it has been pointed out that the [White et al. \(2000\)](#) sample was biased by objects near the flux limit, a fact that could lead to spurious results. With their results, [Ivezić et al. \(2002\)](#), have suggested bimodality using FIRST and the large and unbiased SDSS catalogue ([York et al., 2000](#)). However, the detection limits of both surveys do not permit the detection of a significant number of RQQs and hence a secondary peak must exist due to the majority of undetected SDSS quasars in the FIRST survey ( $\sim 90$  per cent) and the weaker radio emission of typical RQQs compared to RLQs. More recently, [White et al. \(2007\)](#) using a sample  $\sim 40000$  quasars from SDSS DR3 catalog and a stacking analysis of FIRST for their radio-counterparts showed evidence for a shallow minimum between the RL and RQ groups of the radio-loudness distribution. However, again, optical selection effects at these flux levels may dominate the distribution.

Apart from the radio-loudness difference between the two QSO sub-samples, their spectral energy distribution along the other wavelength bands is broadly similar. Possible correlations of the radio-loud quasars fraction or radio luminosity with the optical luminosity (e.g. [Padovani, 1993](#); [Hooper et al., 1995](#); [Goldschmidt et al., 1999](#); [Impey & Petry, 2001](#)) or lack of correlations (e.g. [Stern et al., 2000](#); [Ivezić et al., 2002](#); [Cirasuolo et al., 2003a](#)) could indicate the physical differences of the two classes. The physical meaning of radio-loudness could lead to different physical properties between the two populations, such as different origin of radio emission (jet vs. corona; e.g. [Laor & Behar, 2008](#)), different BH masses (e.g. [McLure & Jarvis, 2004](#)), accretion rates (e.g. [Sikora et al., 2007](#)) and/or spins (e.g. [Blandford & Znajek, 1977](#); [Garofalo et al., 2010](#)), as well as host galaxy properties ([Sikora et al., 2007](#); [Lagos et al., 2009](#)) or could also be linked with dark matter halos and galaxy mergers (e.g. [Hughes & Blandford, 2003](#); [Lagos et al., 2009](#); [Garofalo et al., 2010](#)).

Several studies have reported a radio dichotomy dependence on the quasar’s environment (e.g. [Green & Yee, 1984](#)). While they confirmed the hypothesis that quasars tend to

lie in clusters, they have shown that low to moderate redshift RQQs are found in significantly less rich environments. More recent studies at higher redshifts agree with the fact that RLQs are found in overdense environments (e.g. McLure & Dunlop, 2001; Barr et al., 2003; Falder et al., 2010) but for RQQs there is as yet no clear consensus. While a number of studies suggest that RQQs are found in underdense regions, or at least regions less dense than RLQs (e.g. Ellingson et al., 1991; Smith et al., 2000; Hyvönen et al., 2007), other studies show that, at the very least, a significant fraction of RQQs is located in environments consistent with that of their radio-loud counterparts (e.g. Wold et al., 2001; McLure & Dunlop, 2001). Thus, the environment alone cannot provide the mechanism triggering radio activity.

An alternative handle on radio-loudness comes through studies of quasar host galaxies. Studies of the host galaxy morphology dependence on radio division have a long and chequered history. (Smith et al., 1986) argued that RLQs are predominantly hosted by luminous elliptical galaxies and RQQs are found in less bright spiral hosts. These early indications have been superseded by a picture in which RLQs indeed reside in luminous, massive elliptical galaxies but the morphology of the RQQ hosts may depend on the quasar luminosity. In that scene, although RQQ may reside in both early-type spirals and ellipticals at their bright end of the luminosity function (LF) are exclusively hosted in elliptical galaxies (e.g. Dunlop et al., 1993; McLure et al., 1999). At  $1 < z < 2$  redshifts, the hosts of RLQs appear 1 – 1.5 magnitudes more luminous than RQQs hosts with the same AGN luminosity (Kukula et al., 2001). At even higher redshifts the hosts have proved harder to detect making the picture less clear. Fig. 1.3 shows the results of Kukula et al. (2001) on the evolution of host luminosities of RLQ and RQQ at three cosmological epochs. As expected from the evolution of massive spheroids, RLQ host luminosity increases by a factor of 3 at redshift  $z \sim 2$ . In contrast to RLQ hosts and passive evolution, RQQ hosts appear to have the same absolute magnitude at all redshifts. The fact that the drop in RQQ host mass is not displayed by their radio-loud counterpart might be explained by a selection effect arising from the fact that radio-loudness criterion ensures a higher BH mass threshold in the case of RLQs.

An interesting result originally reported by (Franceschini et al., 1998) and since then has been the subject of many studies (Lacy et al., 2001; Nagar et al., 2002; Jarvis & McLure, 2002; McLure & Jarvis, 2004), is the correlation of BH mass and radio-loudness or radio luminosity. Many of these works have concluded that on average the BH mass of RLQS is more massive than that of RQQs by a factor of  $\sim 1.4$ . Fig. 1.4 shows the results of radio-loudness and BH mass correlation for RLQs and RQQs populations drawn from SDSS and NVSS/FIRST catalogues (McLure & Jarvis, 2004). The BH masses of RLQs were found to be confined to  $M_{\text{BH}} \geq 10^8 M_{\odot}$ . However, for a given BH mass the radio luminosity has a scatter of several orders of magnitude. On the other hand, several studies argue that RLQs with  $10^6 M_{\odot} < M_{\text{BH}} < 10^8 M_{\odot}$  rule out any correlation between BH mass and radio power giving evidence that radio dichotomy can not be explained just from BH mass parameter

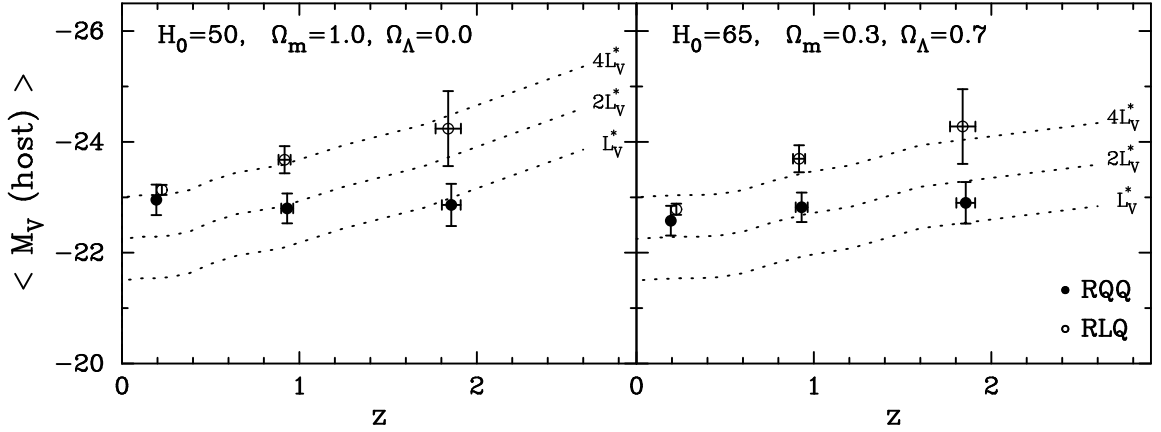


FIGURE 1.3: Mean absolute V-band magnitude versus mean redshift at three epochs for the host galaxies of RLQs (open circles) and RQQs (filled circles) for two different cosmologies. The dotted lines show the luminosity evolution of present day  $L^*$ ,  $2L^*$  and  $4L^*$  elliptical galaxies. Figure taken from [Kukula et al. \(2001\)](#).

([Oshlack et al., 2002](#); [Woo & Urry, 2002b,a](#); [Ho, 2002](#); [Urry, 2003](#)). Despite the lack of correlation, these studies also suggest the existence of a BH mass threshold which controls the onset of radio-loudness ([Laor, 2000](#); [Magliocchetti et al., 2004](#); [Metcalf & Magliocchetti, 2006](#)).

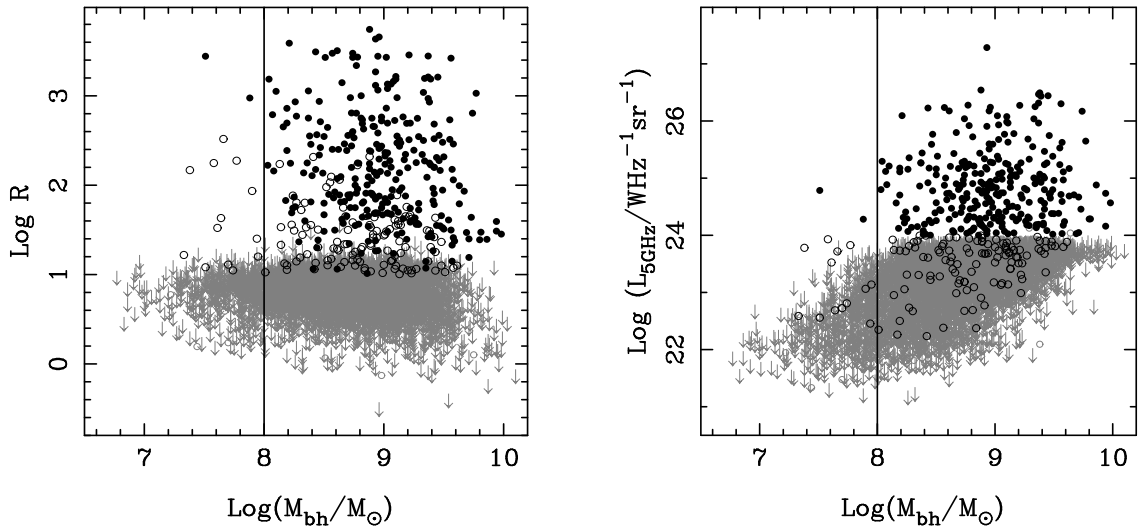


FIGURE 1.4: Black hole mass plotted against the radio-loudness (left) and against the radio luminosity at 5 GHz (right) for a sample of RLQs (filled black circles) and RQQs (grey arrows). RLQs with  $L_{5\text{GHz}} < 10^{24} \text{ W Hz}^{-1} \text{sr}^{-1}$  plotted as open black circles. Figure taken from [McLure & Dunlop \(2004\)](#).

## 1.4 AGN demographics and evolution

Since the early identification of AGN in the '60s ([Schmidt & Olsen, 1968](#)), their evolution as a function of cosmic time has been studied intensively. Ever since, the identification

of the relatively rare AGN systems was dominated by wide area optical and radio surveys. Due to the availability of large optical quasars surveys, it has become evident that the population of luminous quasars evolves strongly, being orders of magnitude more common at cosmic times corresponding to redshift  $z = 1 - 2$  than locally (e.g. Schmidt & Green, 1983; Boyle et al., 2000; Richards et al., 2006a). However, optical selection is heavily biased towards unobscured AGNs that are bright enough to dominate the combined spectrum over the host galaxy. Therefore, a complete study of AGN requires a comprehensive census of AGN including both unobscured and obscured AGNs down to a low luminosity level.

Currently, the most effective method to select distant AGNs is using X-ray observations which provide an almost unbiased selection and, since star-formation activity is comparatively weak at X-ray energies, can identify even low-luminosity systems. Thanks to deep X-ray observations at  $\leq 10$  keV performed by the *Chandra X-ray Observatory* (Chandra; Weisskopf et al., 2000), and the *X-ray Multi-Mirror Mission (XMM-Newton)* (Jansen et al., 2001) a large fraction of obscured systems, that are significantly less luminous up to 2 order of magnitude than typical quasars in wide-area surveys (e.g. SDSS; Ross et al., 2012), has been identified. Though the completeness of the most heavily obscured and high-redshift ( $z > 5$ ) AGN requires further improvements, the AGN samples are now fairly complete over a large redshift and luminosity range to allow fundamental questions about the evolution of AGN activity across cosmic time to be addressed.

A key finding, firstly introduced by observational studies, has revealed an ‘anti-hierarchical’ luminosity dependent trend in AGN evolution: the number density of luminous AGN peaks at higher redshifts than those of fainter AGN (e.g. Cowie et al., 2003; Hasinger et al., 2005; La Franca et al., 2005; Silverman et al., 2008a; Aird et al., 2010; Ueda et al., 2014). These findings are consistent with the downsizing behaviour observed also in optically and radio selected AGN (e.g. Richards et al., 2005; Hopkins et al., 2007; Croom et al., 2009; Ross et al., 2013), confirming the consistency of this phenomenon. While various signs of this downsizing phenomenon are now seen, precise measurements are still needed to efficiently reduce the large uncertainties as to the exact form of the X-ray luminosity function (XLF) and its evolution. Recent studies have proposed either luminosity-dependent density evolution (LDDE; e.g. Gilli et al., 2007; Ueda et al., 2014) or luminosity and density evolution (LADE; e.g., Aird et al., 2010) to describe the evolution of the XLF at both low and high redshifts. In LDDE scheme, the shape of the XLF changes with redshift, with a flattening of the faint-end slope as redshift increases. This evolution is broadly characterized by a shift in the peak of AGN space density towards lower redshifts for lower luminosity objects. In the latter (LADE), the shape of the XLF is constant over the whole redshift range, unlike the case of LDDE, but it undergoes strong luminosity evolution at  $z \leq 1.0$ , and overall negative density evolution toward increasing redshift Aird et al., 2010. While both models reproduce the down-sizing behavior, the number of AGN they predict, especially at high redshift ( $z > 3$ ), are quite different. Although the current X-ray data confirm the exponential decrease in the

AGN density above  $z \gtrsim 3$  (e.g. Silverman et al., 2008a; Brusa et al., 2009; Civano et al., 2011; Hiroi et al., 2012; Vito et al., 2013; Ueda et al., 2014), none of the previous works was able to sufficiently describe the shape of the XLF (e.g. LADE vs. LDDE) at high-redshifts, largely owing to the small samples and limited area coverage.

Unobscured AGNs ( $N_{\text{H}} \lesssim 10^{22} \text{ cm}^{-2}$ ) are found to trace the same evolution as obscured AGNs, although there is evidence that the fraction of obscured AGNs in the total (Compton-thin) AGNs increases toward higher redshift (e.g. Ballantyne et al., 2006; Treister & Urry, 2006; Hasinger, 2008). This trend would be consistent with a suggestion that distant AGNs contain nuclear regions that are more gas rich than lower-redshift AGNs. Although, deep X-ray surveys have provided the most effective method for the identification of complete samples of AGN, a significant fraction of the heavily obscured ( $N_{\text{H}} \gtrsim 10^{23} \text{ cm}^{-2}$ ), and Compton-thick ( $N_{\text{H}} \gtrsim 10^{24} \text{ cm}^{-2}$ ) AGN probably remains undetected (e.g. Alexander et al., 2008; Georgantopoulos et al., 2009; Comastri et al., 2011). The number density of these heavily obscured AGNs is estimated to be similar to the moderately obscured AGNs (e.g. Gilli et al., 2007) in order to fit the 30 keV peak in the cosmic X-ray background (CXRB), with  $\approx 25$  per cent at 6-8 keV and  $\approx 50$  per cent at  $\geq 8$  keV of them remaining unresolved (e.g. Worsley et al., 2004, 2005). Numerous attempts have been made to find AGN candidates that are undetected in the X-ray band, with the most successful methods have utilized radio and infrared observations. Each method has strengths in some areas and limitations in others, such as completeness and reliability, thus they are more efficient when used together to AGN candidates identification.

Apart from the observational constraints, a variety of theoretical models and simulations have been used to provide valuable insight into the physical nature of AGN evolution (e.g. Di Matteo et al., 2008; Hopkins et al., 2008; Fanidakis et al., 2012; Menci et al., 2013). Although, at present, small-scale physical mechanisms related to the BH accretion and formation are not sufficiently modeled due to the limited spatial and mass resolution, several state-of-the-art cosmological models have success in demonstrating the observed ‘anti-hierarchical’ trend in AGN evolution and SMBH growth providing a cosmological interpretation of the ‘downsizing’ effect. On the one hand, the cause of this trend may result from the exhaustion of the gas content in massive halos due to starburst events and feedback or from a drop of the rate of mergers, or even the combination of these physical mechanisms. On the other hand, less-luminous AGN evolve smoother as the gas content in low-mass galaxies evolves more mildly. Additionally, as luminous AGNs run out of fuel, their SMBHs are no longer rapidly growing and their luminosity fades, result to a significant fraction of the less-luminous sources that still appear as AGNs.

The integrated growth of SMBH is dominated by systems around the knee of the AGN luminosity function (e.g. Hopkins et al., 2007); AGNs with  $L_X = 10^{44} - 10^{45} \text{ erg s}^{-1}$  dominate SMBH power production at higher redshifts ( $z > 1.5$ ), while those with  $L_X =$

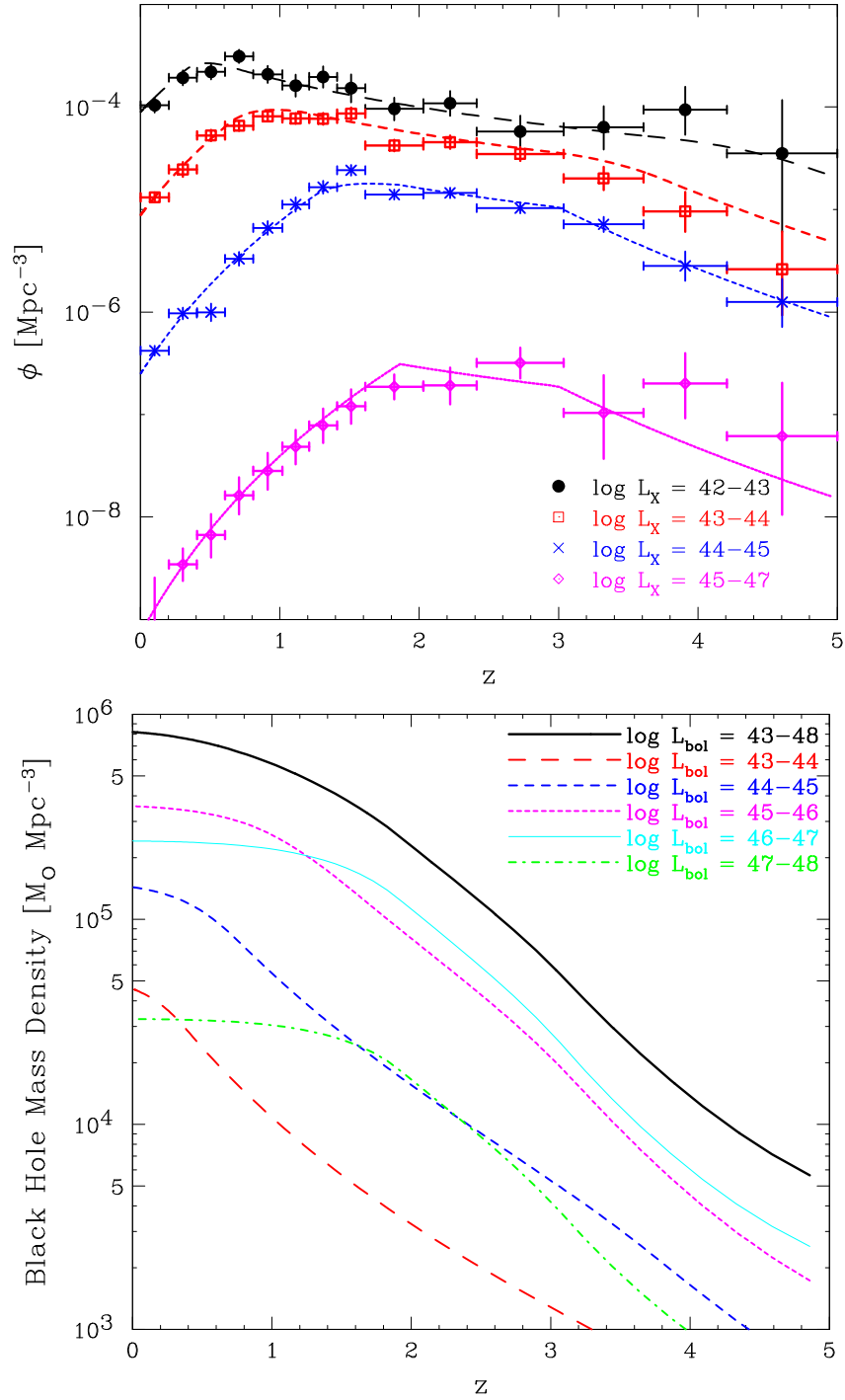


FIGURE 1.5: Top: Comoving number density of AGNs, selected from multiple X-ray surveys, plotted against redshift in different luminosity bins (as labelled; in units of  $\log[\text{erg s}^{-1}]$ ). The curves are the best-fit model, and the data points are calculated from either the soft or hard band sample. Note that the number density of luminous AGN peaks at higher redshifts than lower-luminosity AGN (i.e., AGN cosmic downsizing). Bottom: Comoving mass density of all SMBHs plotted against redshift (uppermost solid curve, black). Note the shift of the peak for AGNs with  $L_{\text{Bol}} < 10^{45} \text{ erg s}^{-1}$  (or  $L_X < 10^{43} \text{ erg s}^{-1}$ ). Taken from Ueda et al. (2014).

$10^{43} - 10^{44} \text{ erg s}^{-1}$  dominate at lower redshifts. Fig. 1.5 shows that the luminosity dependence of AGN evolution results in a shift of the SMBH mass density peak from  $z \sim 2$ , where AGNs with  $L_{\text{Bol}} = 10^{46} - 10^{47} \text{ erg s}^{-1}$  (or  $L_X = 10^{44} - 10^{45} \text{ erg s}^{-1}$ ) make the largest contribution, to lower redshifts (Ueda et al., 2014). Approximately, the integrated fractions of SMBH growth at  $z < 1$ ,  $z = 1 - 2$ , and  $z > 2$  are 35 – 50 per cent, 25 – 40 per cent, and 15 – 25 per cent, respectively (e.g. Marconi et al., 2004; Silverman et al., 2008a; Aird et al., 2010; Ueda et al., 2014). Two important AGN sub-populations for the growth of BHs and galaxies are optically selected quasars which contribute about  $\approx 40 - 50$  per cent (e.g. Di Matteo et al., 2003) to the integrated fractions of SMBH growth representing a rapid growth phase of massive BHs and, RLAGNs which contribute  $< 10$  per cent (e.g. Cattaneo & Best, 2009) but appear to have played a significant role in the formation and evolution of galaxies.

Although RLAGNs are a minority at all redshifts, the large amount of kinetic/mechanical energy produced by the jets and lobes can be transferred to the host galaxy or large-scale environment and prevent the gas cooling and star formation. Therefore, the radio luminosity functions associated with AGN activity are used to observationally constraint the volume-average heating rate from AGN (e.g. Croton et al., 2006; Lehmer et al., 2007; Smolčić et al., 2009; La Franca et al., 2010). Obtaining an estimate of the mechanical radio power has proven to be a difficult problem with a basic requirement of converting the synchrotron jet luminosity into a kinetic energy (e.g. Best et al., 2006; Heinz et al., 2007; Cavagnolo et al., 2010). On the basis of the current conversion factors, the kinetic energy density is predicted to be broadly flat over  $z \approx 0 - 4$ , with power density being completely dominated by low luminosity AGN at low redshifts, while the contribution from RLQs becomes significant at  $z \sim 2$  (e.g. Merloni & Heinz, 2008; Cattaneo & Best, 2009). There is evidence for a sharp (about a factor of five) decrease of the kinetic energy density at  $z < 0.5$ , which would indicate a weakening role of AGN activity towards  $z \approx 0$  (e.g. KÖrding et al., 2008; La Franca et al., 2010).

## 1.5 The host galaxies of distant AGNs

In the past 20 years astronomers discovered that almost every massive galaxy hosts a central galactic BH ( $M_{\text{BH}} \approx 10^5 - 10^{10} M_{\odot}$ ). The existence of SMBHs at the center of massive nearby galaxies has been confirmed mostly from the dynamics of stars and gas kinematics (e.g. Kormendy & Richstone, 1995). In the case of AGN, it has been possible to measure SMBH masses due to a technique known as reverberation mapping (e.g. Blandford & McKee, 1982; Peterson, 1993) which provides indirect BH mass estimates and kinematic studies which are known to provide the most reliable mass measurements (e.g. Kaspi et al., 2000). These measurements have lead astronomers to establish well-defined black hole mass scaling relations with host galaxy properties such as: stellar mass in the

spheroidal component (e.g. [Marconi & Hunt, 2003](#)), luminosity (e.g. [Magorrian et al., 1998](#)), velocity dispersion (e.g. [Gebhardt et al., 2000b](#); [Ferrarese & Merritt, 2000](#); [McConnell & Ma, 2013](#)) and mass of the dark matter halo (e.g. [Ferrarese, 2002](#)). The tightness of these relations suggests there may be a link between black hole formation and galaxy evolution.

Researchers, trying to understand the origin of this BH-spheroid mass link, have revealed the need of the presence of powerful phenomena such as gas-rich major mergers (e.g. [Sanders & Mirabel, 1996](#); [Hopkins et al., 2008](#)), galaxy interactions, minor merger or other secular processes such as galaxy bars, disk instabilities, and clumpy cloud accretion (e.g. [Silverman et al., 2011](#); [Bournaud et al., 2012](#); [Villforth et al., 2014](#)). These processes may be responsible for triggering both black hole feed via accretion of gas to the center of the galaxy and star formation. However, we note that there is evidence that the most luminous AGNs are preferentially triggered by major mergers, as also found for the most powerful star-forming galaxies (e.g. [Treister et al., 2012](#)), which could indicate that to reach the highest AGN luminosities - where the most massive BHs accreted the bulk of their mass - major mergers are required to drive sufficient quantities of gas into the central regions of galaxies. Fig. 1.6 shows a schematic example for the  $M_{BH} - \sigma$  relation with three possible evolutionary tracks for merging galaxies overlaid ([Medling et al., 2015](#)).

Black holes release huge amounts of energy to their surrounding systems. Assuming a sufficiently strong coupling between BH radiative/mechanical output and the surrounding gas, the SMBHs can potentially regulate the growth of their host galaxies through AGN feedback (e.g. [Springel et al., 2005](#); [Hopkins et al., 2010](#)). This assumption would be consistent with the existence of a correlation between the mass of stars in the bulge and the masses of the SMBHs. In particular, theory suggest that nuclear activity regulates host galaxy growth either by high velocity AGN-driven outflows that remove the gas from the galaxy and suppress the star formation and future black hole growth (e.g. [Hopkins et al., 2006](#); [Menci et al., 2006](#)), or by heating it (e.g. [Croton et al., 2006](#)). The feedback process from a growing SMBH can be split broadly into two types. Using the terminology of [Croton et al. \(2006\)](#), there is ‘quasar-mode’ feedback, which comprises wide-angle, sub-relativistic out-flows due to the efficient accretion of cold gas, and ‘radio-mode’ feedback, which are relativistic out-flows driven by radiation that punch their way out of the host galaxy and into the surrounding inter-galactic medium (IGM), often but not exclusively due to the relatively inefficient accretion of hot gas (see Fig. 1.7; [Alexander & Hickox, 2012](#)). It is important to note that this radio-mode is mechanical feedback from radio jets.

Quasar-mode feedback is considered to be driven by a wind created by the luminous accretion disk. The ignition of the nucleus in a star-forming galaxy heats-up and removes the inter-stellar medium (ISM) gas from its host galaxy, thus reducing or even stopping star formation (e.g. [Granato et al., 2001](#); [Croton et al., 2006](#); [Hopkins et al., 2010](#); [Page et al., 2012](#)). During this process, the flow of matter to the central SMBH can be reduced, lowering the accretion flow and eventually extinguishing the AGN. Once the gas cools down

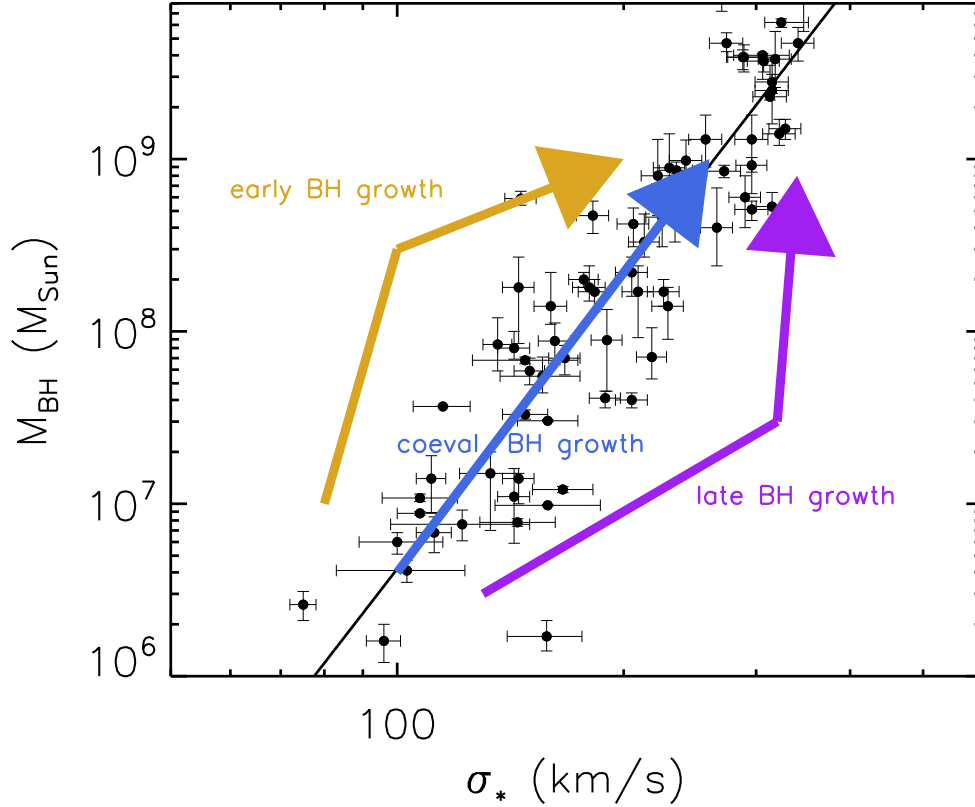


FIGURE 1.6:  $M_{BH} - \sigma$  relation for isolated galaxies from [McConnell & Ma \(2013\)](#) (black) with three possible evolutionary tracks for merging galaxies overlaid. If the black hole grows first or more quickly than the galaxy bulge, mergers would lie above the relation (as shown by the gold arrows). If the black hole growth lags the bulge growth and is responsible for curtailing evolution (e.g. quenching through AGN feedback), mergers would lie below the relation (as shown by the purple arrows). If instead the black hole and the bulge grow in lockstep, the mergers would remain on the relation (as shown by the blue arrow). Taken from [Medling et al. \(2015\)](#).

and starts to collapse into the nucleus again, a new AGN phase may begin and the cycle resumes. In recent years, much work has focused on observational evidence for AGN wind mainly through the presence of highly blue-shifted absorption and emission lines (e.g. [Boroson, 2005](#); [Davies et al., 2009](#); [Gofford et al., 2011](#); [Richards et al., 2011](#)). All these studies demonstrate that energetic winds are common in AGN. However, based on the exist data, it is not clear whether these winds have significant effects on the scale of the host galaxy since, many studies have shown that the winds are observed only along the line of sight and there are no direct constraints on the spatial distribution of the outflowing gas (e.g. [Tremonti et al., 2007](#); [Arav et al., 2008](#); [Dunn et al., 2010](#)). The emergence of integral-field unity (IFU) observations for spatially resolved spectroscopy of individual sources provide significant advantages over these challenges (e.g. [Feruglio et al., 2010](#); [Greene et al., 2011](#)). Observations reveal examples of powerful feedback in the form of AGN-driven outflows, but

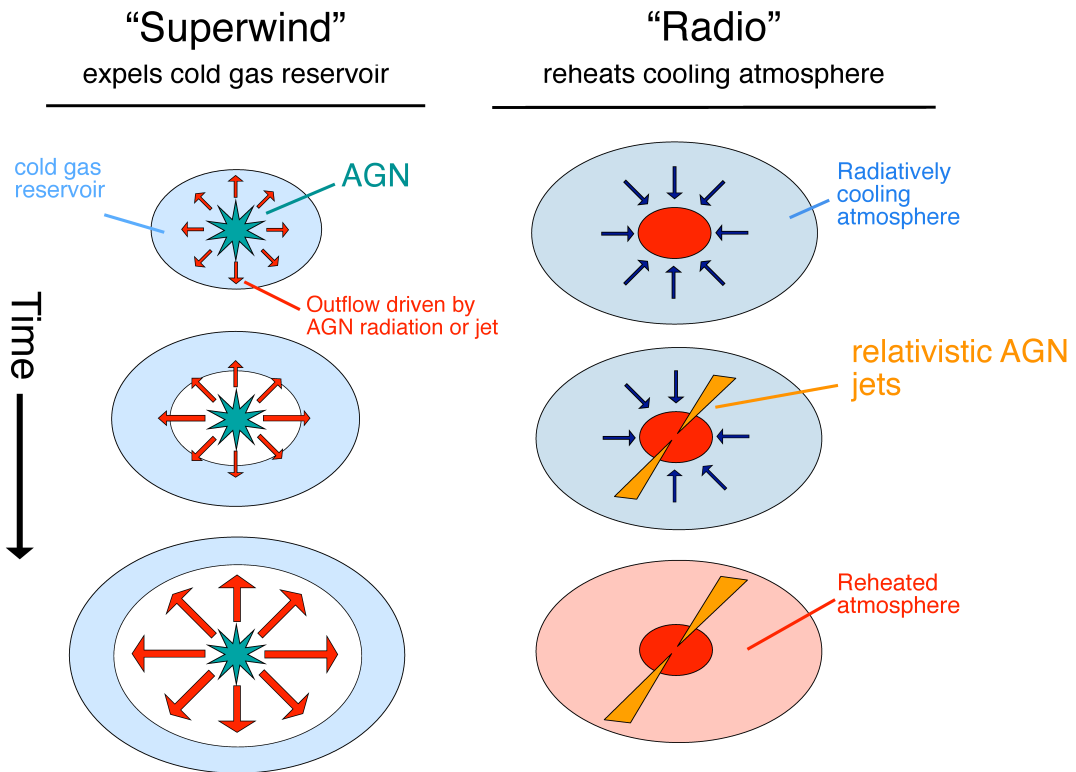


FIGURE 1.7: Schematic diagrams to illustrate the two main modes of AGN outflows: Quasar (superwind) mode outflows such as those found in luminous AGNs and radio mode outflows such as those found in low-excitation radio-loud AGNs. Figure taken from [Alexander & Hickox \(2012\)](#).

their overall prevalence and impact on the galaxy evolution remains to be determined.

Unlike AGN winds, direct observations show that jets can influence gas many tens of kpc from the centre of the parent host galaxy. Indeed, the brightest radio structures in AGN are often observed on kpc scales and are produced by the coupling of the AGN outflow to its environment. Although quasar-mode feedback might occur in all AGN, it is likely to be important only in powerful AGN, while lower AGN power radio sources are probably dominated by the radio-mode feedback. For most of the radio-loud AGN, the radio-mechanical power can exceed (by as much as  $\sim 1000$  times) the nuclear radiation (e.g. [Birzan et al., 2008](#); [Cavagnolo et al., 2010](#)). Radio AGN energy output, in the form of heating, can prevent hot gas from cooling and falling into a galaxy to form stars (e.g. [Croton et al., 2006](#)), especially in the more massive galaxies and at much smaller accretion rates than that of the quasar-mode feedback. The cooling of the hot gas onto the nuclei fuels sporadic AGN outbursts, which in turn heat the inflowing gas, perhaps stopping or reversing the inflow (e.g. [Best et al., 2005](#)).

Although on the basis of these feedback models, we would expect a suppression in the

star formation of the AGN, depending on how fast the star formation is suppressed, its signatures could be comparatively subtle (e.g. [Hopkins et al., 2006](#); [Harrison et al., 2012](#)). Sensitive SFR measurements for individual AGN but also their association with AGN luminosity and redshift are required to provide sufficient tests of the impact of AGN on star formation.

### 1.5.1 Where the distant AGNs live?

The general consensus is that the majority of distant X-ray AGNs are found to be hosted by massive galaxies with  $M_* \approx (0.3 - 3) \times 10^{11} M_\odot$  (e.g. [Alonso-Herrero et al., 2008](#); [Brusa et al., 2009](#); [Hickox et al., 2009](#)). AGN host galaxies down to the  $\approx 10^9 - 10^{10} M_\odot$  stellar mass regime are also identified although they appear to comprise a small fraction of the total X-ray AGN population (e.g. [Shi et al., 2008](#); [Xue et al., 2010](#)). RLAGNs predominantly inhabit the most massive elliptical galaxies with  $M_* \approx 10^{11} - 10^{12} M_\odot$  (e.g. [Tasse et al., 2008](#); [Floyd et al., 2010](#)). Radio-quiet, optically selected quasars are generally hosted by less-massive ellipticals and spirals, with a negligible disc component in most of the cases (e.g. [Dunlop et al., 2003](#); [Tasse et al., 2008](#); [Floyd et al., 2010](#)).

Galaxy colours are related to the star formation, dust, and metal-enrichment history of galaxies and thus provide information about their formation and evolution (e.g. [Strateva et al., 2001](#); [Baldry et al., 2004](#)). The colour-magnitude diagrams (CMD; plot of the rest-frame optical colours vs. absolute magnitude), are a common diagnostic to explore the role of AGNs in galaxy evolution. CMD analysis reveal a bimodality, i.e. a separation of galaxies into the ‘red sequence’ and ‘blue cloud’. In contrast, no colour bimodality appears to exist for X-ray AGN while it has been also found that they preferentially lie in the ‘green valley’ (e.g. [Nandra et al., 2007](#); [Silverman et al., 2008c](#); [Hickox et al., 2009](#)). By comparison, the radio AGNs are preferably found in the ‘red sequence’ of the CMD (e.g. [Tasse et al., 2008](#); [Hickox et al., 2009](#)), as expected for old massive galaxies, although it seems to depend on radio power and triggered mechanisms (e.g. [Hardcastle et al., 2006](#); [Kewley et al., 2006](#); [Smolčić et al., 2009](#)). IR-selected AGN inhabit slightly bluer, less luminous hosts than X-ray AGN (e.g. [Hickox et al., 2009](#)). A key result of the difference between the X-ray AGN and the optical galaxies color is a scenario in which AGN activity is the primary mechanism responsible for quenching star formation and the galaxy migration from the blue to the red sequence (e.g. [Nandra et al., 2007](#)). The large number of AGN found in the red sequence implies that strong, ongoing star formation is not mandatory in an active phase, as BH accretion persists even after the star-formation termination. However, it is possible that many of these AGN would be found in the ‘red sequence’ due to dust obscuration (e.g. [Donoso et al., 2014](#)).

Recent studies show that when the AGN and optical galaxy samples are matched in mass, there is no clear difference between the AGN and non-AGN galaxies on the CMD diagrams (e.g. [Silverman et al., 2009](#); [Xue et al., 2010](#); [Rosario et al., 2013](#)). The lack of a

significant difference suggests that X-ray AGNs do not reside in ‘special’ host-galaxy environments (but see also [Koss et al., 2011](#) for  $z \leq 0.05$ ). They additionally found that the AGN fraction is mostly independent of host-galaxy colour out to  $\approx 2 - 3$  (e.g. [Bundy et al., 2008](#); [Xue et al., 2010](#)), providing an estimate of the BH-growth duty cycle in typical massive galaxies ([Xue et al., 2010](#)). The fraction of massive galaxies hosting X-ray AGNs varies from  $\sim 10 - 20$  per cent for moderate-luminosity AGN ( $L_X \gtrsim 10^{42}$  erg s $^{-1}$ ) to  $< 5$  per cent for AGNs with  $L_X \gtrsim 10^{43}$  erg s $^{-1}$ , with some evidence for an increase with redshift (e.g. [Xue et al., 2010](#); [Georgakakis & Nandra, 2011](#)). The fraction of galaxies hosting RLAGN out to  $z \sim 1.3$  is essentially the same or slightly higher than that in the local Universe, indicating a relatively constant duty cycle of RLAGN activity (e.g. [Tasse et al., 2008](#); [Smolčić et al., 2009](#)).

X-ray AGN hosts show a broad range of morphologies out to at least  $z \approx 3$  between disk-dominated and bulge-dominated systems (e.g. [Grogin et al., 2005](#); [Gabor et al., 2009](#); [Georgakakis et al., 2009](#); [Kocevski et al., 2012](#); [Fan et al., 2014](#)). Although, the first evidence suggest a stronger association between AGN and bulge-dominated galaxies than normal galaxies (e.g. [Grogin et al., 2005](#)), these differences mostly disappeared when the samples were matched in mass (e.g. [Kocevski et al., 2012](#); [Fan et al., 2014](#); [Villforth et al., 2014](#)). Recently, [Rosario et al. \(2013\)](#) using a systematic morphological analysis of AGNs and galaxies mass-matched samples found evidence that X-ray selected AGN host galaxies are similar to inactive galaxies out to at  $z = 3$ .

### 1.5.2 Probing the AGN/Star-Formation connection

There are numerous evidence that support a global evolutionary connection between the star formation and AGN activity e.g. (1) the differential redshift evolution of the AGN luminosity function, or ‘AGN downsizing’ is also found for the star-forming galaxy population (e.g. [Hasinger et al., 2005](#); [Hopkins & Beacom, 2006](#); [Aird et al., 2010](#)), (2) the redshift distribution of the most strongly star-forming galaxies follows that of powerful AGN (e.g. [Willott et al., 2001](#); [Chapman et al., 2005](#); [Wardlow et al., 2011](#); [Miyaji et al., 2015](#)), (3) the star formation rate density as a function of redshift is broadly similar with the black hole accretion rate density (e.g. [Boyle & Terlevich, 1998](#); [Merloni, 2004](#); [Silverman et al., 2008a](#); [Aird et al., 2010](#); [Madau & Dickinson, 2014](#)) and (4) the tight correlation of the BH and stellar mass of the host galaxy bulge (e.g. [Magorrian et al., 1998](#); [McConnell & Ma, 2013](#); [Graham & Scott, 2013](#); [Kormendy & Bender, 2013](#)) with both ongoing AGN and star-formation activity. There are several examples of composite objects showing both AGN and star formation activity, in the literature (e.g. [Page et al., 2001, 2004](#); [Alexander et al., 2005](#)), particularly at  $z \approx 1$ , close to the peak of the AGN luminosity density in the Universe ([Barger et al., 2005](#); [Hasinger et al., 2005](#)). The AGN and star-formation histories show similar evolution up to  $z \approx 2$ , when the mass accretion history is scaled up by a factor  $\approx 5000$

(e.g. [Silverman et al., 2008a](#); [Aird et al., 2010](#)). However, at higher redshifts there are significant differences between the two evolution histories with the AGN slope being much steeper. As an example, at  $z \approx 6$  the star formation per unit volume is found to be 1 – 2 orders of magnitude higher than that of the mass accretion.

The first studies on the identification of the star-formation and accretion activity had attempted to determine the star-formation activity in AGN host galaxies using a broad variety of indicators such as optical colours or spectroscopy, mid-IR data and submillimetre observations (e.g. [Isaak et al., 2002](#); [Stevens et al., 2005](#); [Alexander et al., 2005](#); [Mullaney et al., 2010](#); [Lutz et al., 2010](#); [Kalfountzou et al., 2011](#)). These results suggested that, globally, the SFRs of AGNs of all classes are found to increase with redshift while the SFRs cover a wide range, up to  $\approx 5$  orders of magnitude for a fixed AGN luminosity (e.g. [Mullaney et al., 2010, 2011a](#); [Lutz et al., 2010](#); [Seymour et al., 2011](#)). The main drawbacks of these studies was the significant uncertainties in the estimation of the SFRs due to potential contamination from the AGN, underestimation of the SFR due to obscuration by dust and uncertain extrapolation from the observed wavelength to the total SFR.

These issues are best addressed by FIR observations which are shown to be dominated by emission from dust in the host galaxy, except in the most extreme cases (e.g. [Netzer et al., 2007](#); [Mullaney et al., 2011a](#)), and to be a proxy of its star formation activity that is largely uncontaminated by the AGN (e.g. [Hatziminaoglou et al., 2010](#)). Consequently, the launch of the *Herschel* Space Observatory ([Pilbratt et al., 2010](#)), with its high FIR sensitivity and wavelength coverage, offers a powerful way of measuring the instantaneous SFR with minimal AGN contamination (e.g. [Netzer et al., 2007](#); [Hatziminaoglou et al., 2010](#); [Mullaney et al., 2011b](#); [Bonfield et al., 2011](#); [Hardcastle et al., 2013](#)). Due to a large number of studies undertaken using *Herschel* observations, we have concluded that the average SFRs of the AGN host galaxies increase strongly with redshift from  $z < 0.1$  to  $z = 2 - 3$  (e.g. [Mullaney et al., 2011a](#); [Harrison et al., 2012](#); [Rosario et al., 2012](#); [Rovilos et al., 2012](#)). A similarly strong SFR increase is also seen in the overall star-forming galaxy population ( $\approx (1 + z)^4$ ; e.g. [Daddi et al., 2007](#); [Pannella et al., 2009](#); [Rodighiero et al., 2010](#); [Elbaz et al., 2011](#)). This good agreement probably suggests that both star formation and AGN activity are driven by the same fuel supplies.

Apart from the strong increase with redshift it is also found that, for both star-forming galaxies and AGN, this increase is independent of galaxy mass. Specifically, the specific star formation rate (sSFR) evolves strongly with redshift across all stellar masses, and is thought to be driven by the availability of a cold-gas supply (i.e., the distant galaxies are more gas rich than the nearby galaxies ([Daddi et al., 2010](#); [Genzel et al., 2010](#); [Tacconi et al., 2013](#))). The relatively tight relation between the galaxy stellar mass and its SFR is often referred to as the ‘main sequence’ of star formation, implying that galaxies spend most of their life in this stage of growth. Fig. 1.8 shows a comparison of sSFR between X-ray AGNs and star-forming galaxies out to  $z \approx 3$ .

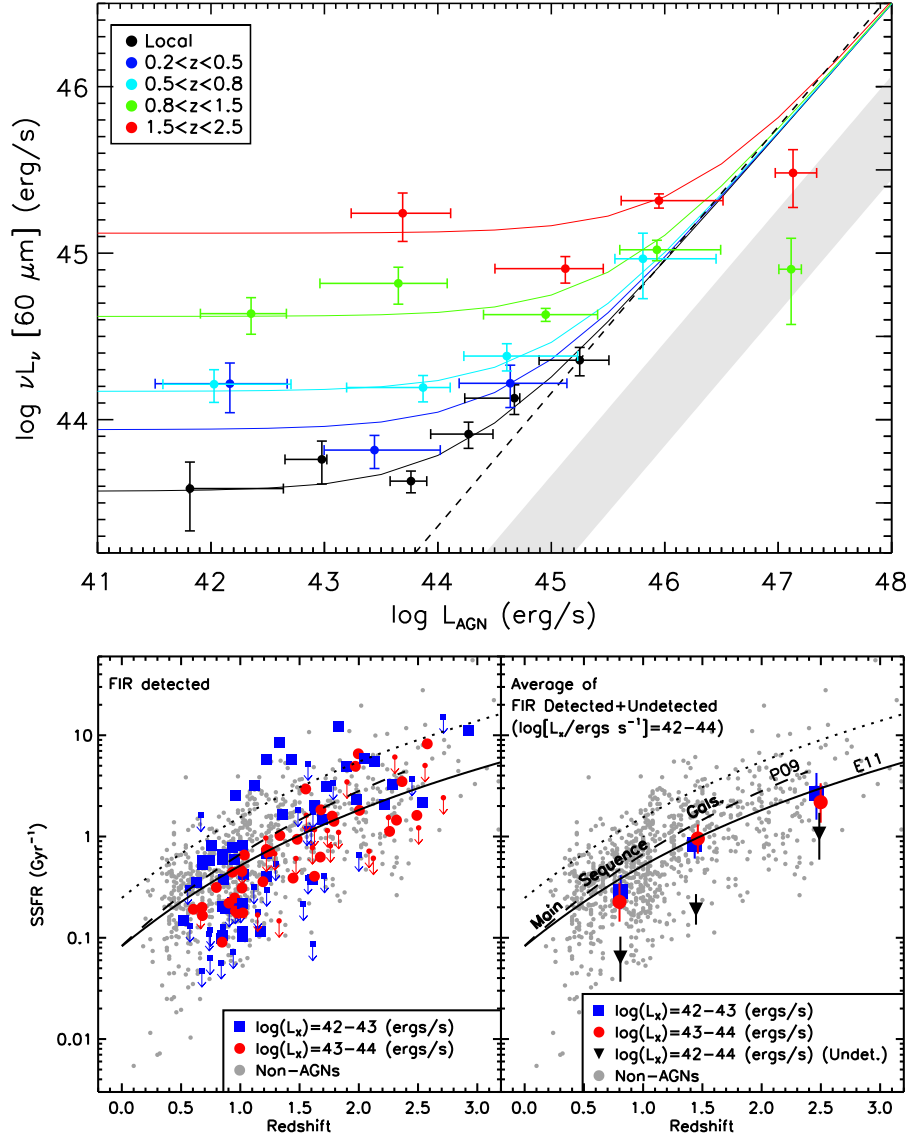


FIGURE 1.8: Top: Mean  $60\mu\text{m}$  (FIR) luminosity vs. AGN luminosity in 5 different redshift bins (as labelled) over  $z \approx 0 - 2.5$ , showing the observed relationship between AGN activity and star formation. The solid curves are functional fits to the mean measurements, based on a two-component model using a flat line (the constant value is determined by the mean SFR of low-luminosity AGN hosts and is unrelated to accretion activity) and a straight line with a positive non-zero slope. The dashed line is the correlation line shown by AGN-dominated systems in [Netzer \(2009\)](#), and the shaded region corresponds to the estimated  $1\sigma$  range exhibited by empirical pure-AGN SEDs (see Section 3.1 of [Rosario et al., 2012](#) for details).  $L_{\text{AGN}}$  corresponds to the bolometric AGN luminosity:  $L_X = 10^{42}$  and  $10^{44} \text{ erg s}^{-1}$  correspond to  $L_{\text{AGN}} = 5.7 \times 10^{42}$  and  $3.4 \times 10^{45} \text{ erg s}^{-1}$ , respectively. Bottom: Individually FIR-detected (left) and average (right) sSFR vs. redshift for X-ray AGNs with  $L_X = 10^{42} - 10^{44} \text{ erg s}^{-1}$  (as labelled) over  $z = 0.5 - 3$ . The AGNs are compared to FIR-detected star-forming galaxies not hosting AGN activity (non AGNs) and the tracks trace the evolution in sSFR found for star-forming galaxies with redshift, as defined by [Pannella et al. \(2009\)](#) and [Elbaz et al. \(2011\)](#). Overall, the X-ray AGNs broadly trace the evolution in SFR and sSFR found for the star-forming galaxy population. However, the observed relationship between the AGN and star-formation luminosity is complex and is probably, at least partially, driven by the different timescales of stability between star formation and AGN activity. Adapted from [Mullaney et al. \(2012a\)](#) and [Rosario et al. \(2012\)](#).

Although most studies agree on the strong increase of SFR with redshift, a broad range of results have been found regarding the dependence on AGN luminosity with researchers arguing that either the average SFR increases with both redshift and X-ray luminosity, increases only with redshift (similarly to moderate-luminosity AGN), or decreases with X-ray luminosity (e.g. [Harrison et al., 2012](#); [Page et al., 2012](#); [Rosario et al., 2012](#); [Rovilos et al., 2012](#)). Part of the disagreement between the different studies for high-luminosity AGNs possible arises from the facts that: (1) luminous AGNs are more rare than moderate-luminosity AGNs, limiting the statistics especially in small to moderate area surveys and (2) AGN contribution to the FIR wavelengths increases for luminous AGN reducing the reliability of the SFR measurements. Indeed, studies performed in large-area fields with good source statistics find that the average SFR of luminous AGNs is either constant with X-ray luminosity or increases with X-ray luminosity. The transition from a constant to a rising trend is found to be a function of redshift (e.g. [Harrison et al., 2012](#); [Rosario et al., 2012, 2013](#); Fig. 1.8).

In distant galaxies, the AGN fraction has been found to be driven by the star-formation rate. Recently, [Rafferty et al. \(2011\)](#) found that moderate-luminosity X-ray AGN ( $L_X > 10^{43} \text{ erg s}^{-1}$ ) are at least  $\sim 5 - 10$  times more common in systems with high star-formation ( $> 300 M_\odot \text{ yr}^{-1}$ ; equivalent to LIRGs) than in systems with lower star-formation rate ( $< 30 M_\odot \text{ yr}^{-1}$ ). At the highest star-formation rates ( $\sim 1000 M_\odot \text{ yr}^{-1}$ ; equivalent to ULIRGs) the AGN fraction rises to  $\approx 30$  per cent. These results are in agreement with previous studies ([Alexander et al., 2005](#); [Symeonidis et al., 2010](#)). The high AGN fraction at the highest SFRs indicates an intimate connection between BH growth and star-formation phases during periods of vigorous growth. However, the overall AGN fractions are generally consistent with those for intense star-forming galaxies in the local Universe (e.g., the fraction of nearby ULIRGs hosting AGNs with  $L_X > 10^{43} \text{ erg s}^{-1}$  is  $\approx 40$  per cent; [Alexander et al., 2008](#)), implying a constant ‘duty cycle’ of BH growth in star-forming galaxies over a wide range of redshift ( $z \approx 0 - 3$ ).

Although these results imply a general connection between observed AGN luminosities and the properties of AGN hosts, the observed correlations AGN and star-formation luminosity appear relatively weak or absent especially at lower and moderate-luminosity AGNs where the average SFR is flat across at least 2 orders of magnitude in AGN luminosity (Fig. 1.8). Several models (e.g. [Gabor & Bournaud, 2013](#); [Hickox et al., 2014](#); [Neistein & Netzer, 2014](#)) have explored the possibility that the lack of correlation is caused by significant AGN variability on timescales shorter ( $\lesssim \text{Myrs}$ ) than those characteristic of star formation which is assumed to be relatively stable over long periods (of order  $\approx 100 \text{ Myr}$ ). For instance, [Hickox et al. \(2014\)](#) constructed a simple model which assumes that the long-term growth rate of BHs is exactly proportional to the star formation rate in the host galaxy but it allows the observed AGN luminosity to vary over a wide dynamic range on short timescales on the basis of an assumed Eddington-ratio distribution. This model, and the other models referenced above, reproduce the broad trends seen between AGN activity and SFR

over galaxy evolution timescales and demonstrate how instantaneous luminosity of an AGN is a weak indicator of the average BH accretion rate on the timescales of the galaxy evolution processes that may be expected to drive the long-term growth of BHs (Hickox et al., 2014). However, it is not yet clear which model provides the best physical description of the observed trends and how additional parameters such as BH mass, AGN fueling and variability, Eddington limit would affect them. Further observational diagnostics and more sophisticated versions required to account for the joint distribution of BH masses and SFRs and provide greater diagnostic power.

## 1.6 Layout of PhD Thesis

This PhD thesis focuses on the parameters which would affect the AGN and their host galaxy evolution. As mentioned in Section 1.4, the evolution of AGN is well-determined out to  $z \approx 3$ . However, our knowledge at even higher redshifts is quite limited mainly due to the small number statistics. In **Chapter 2**, I present my results on the evolution of AGN at  $z > 3$  (up  $z \approx 7$ ) using the largest X-ray selected sample to date. Due to the large size of the sample, we are able to study also the evolution of both obscured and unobscured sub-populations, identifying for first time, the model that described best their evolutionary path at these high-redshifts. In the following Chapters [3-5], I present my works on the star formation of the host galaxies in particular AGN sub-classes. Specifically, as a follow-up of my Kalfountzou et al. (2012) work on radio-loud and radio-quiet quasars, in **Chapter 3** I present the FIR properties of the two populations investigating the effects of the radio-jets to the host galaxy and the star-formation. In **Chapter 4**, I focus on a well-defined sample at  $z \sim 1$  of optically selected quasars (radio-loud and radio-quiet), which span  $\sim 5$  orders of optical magnitude, and radio galaxies in order to decompose the evolution effects and compare the SFRs of the three populations to the presence of radio jets, their radio power and the AGN activity. In **Chapter 5**, I present my work on the FIR emission of type-1 and type-2 AGN associating my results to the AGN evolution and the unified model. Finally, in **Chapter 6** I focus on some of the key remaining questions which come out of my results and some future projects can be used to address them.

A cosmological model with  $\Omega_o = 0.3$ ,  $\lambda_o = 0.7$ , and a Hubble constant of  $70 \text{ km s}^{-1} \text{ Mpc}^{-1}$  is used throughout the thesis (Spergel et al., 2003). I follow the conversion in Kennicutt (1998) (which assumes a Salpeter, 1955 initial mass function) when deriving SFRs.

*We come from a dark abyss, we end in a dark abyss, and  
we call the luminous interval life.*

[The Fratricides (1964)] - Nikos Kazantzakis

# 2

## The largest X-ray-selected sample of $z > 3$ AGNs: C-COSMOS and ChaMP

This chapter is partly reproduced from the paper: *The largest X-ray-selected sample of  $z > 3$  AGNs: C-COSMOS and ChaMP*, **Kalfountzou E.**; Civano, F.; Elvis, M.; Trichas, M.; Green, P., 2014, MNRAS, 445, 1430

### Abstract

In this chapter I present results from an analysis of the largest high-redshift ( $z > 3$ ) X-ray-selected AGN sample to date, combining the *Chandra* Cosmological Evolution Survey and *Chandra* Multi-wavelength Project surveys and doubling the previous samples. The sample comprises 209 X-ray-detected AGNs, over a wide range of rest-frame 2-10 keV luminosities ( $L_X = 10^{43.3} - 10^{46.0}$  erg s $^{-1}$ ). X-ray hardness ratios show that  $\sim 39$  per cent of the sources are highly obscured,  $N_H > 10^{22}$  cm $^{-2}$ , in agreement with the  $\sim 37$  per cent of type-2 AGNs found in our sample based on their optical classification. It is found that  $\sim 26$  per cent of objects have mismatched optical and X-ray classifications. Utilizing the  $1/V_{max}$  method, I confirm that the comoving space density of all luminosity ranges of AGNs decreases with redshift above  $z > 3$  and up to  $z \sim 7$ . With a significant sample of  $z > 4$  AGNs ( $N = 27$ ), it is found that both source number counts in the 0.5-2 keV band and comoving space density are consistent with the expectation of a luminosity-dependent density evolution (LDDE) model at all redshifts, while they exclude the luminosity and density evolution (LADE) model. The measured comoving space density of type-1 and type-2 AGNs shows a constant ratio between the two types at  $z > 3$  as a function of redshift. Our results for both AGN types at these redshifts are consistent with expectations of the LDDE model.

## 2.1 Introduction

AGNs evolution at high redshifts, before their density peak, illuminates the role of AGN in the formation and co-evolution of galaxies and their SMBHs during the time of rapid SMBH growth. The so-called downsizing evolution has been revealed for both AGN (e.g. Ueda et al., 2003; Hasinger et al., 2005; Aird et al., 2010) and galaxies (e.g. Cowie et al., 1996; Kodama et al., 2004; Damen et al., 2009). Supporting this idea, X-ray surveys have shown that the number density of luminous AGN peaks at higher redshifts than less luminous ones (e.g. Ueda et al., 2003; Aird et al., 2010). This sort of cosmological co-evolution scenario is inferred from the tight correlation that exists locally between SMBH mass and galactic bulge properties (e.g. Magorrian et al., 1998; Ferrarese & Merritt, 2000; Gebhardt et al., 2000b; McConnell & Ma, 2013).

To elucidate the co-evolution of SMBHs and galaxies, the accretion activity in the Universe has to be studied both at high redshifts and for low luminosities. This requires large samples of AGNs spanning wide ranges of properties. While many optical surveys have investigated the space density of high-redshift AGNs (e.g. Richards et al., 2006a; Jiang et al., 2009; Willott et al., 2010; Glikman et al., 2011; Ikeda et al., 2011; Ross et al., 2013), the results are still controversial due to their inevitable incompleteness, especially at the faint luminosity end due to the host contamination, and the bias against obscured sources. As compared with optical surveys, X-ray observations are less contaminated by the host galaxy emission and include AGN populations with a wide range of neutral hydrogen column density.

For the investigation of absorption evolution (e.g. Ueda et al., 2003; Hasinger, 2008; Draper & Ballantyne, 2010), X-ray selected samples include all types of AGN (e.g. type-1/unobscured and type-2/obscured) and provide reduced obscuration bias in comparison with optically selected AGN. Although X-ray surveys have inferred the existence of an anticorrelation between the obscured AGN fraction and the luminosity, several of these studies have suggested that this fraction increases toward higher redshift from  $z = 0$  to  $z \sim 2$  with limited samples at  $z > 3$  (e.g. La Franca et al., 2005; Ballantyne et al., 2006; Treister & Urry, 2006; Ballantyne, 2008; Hiroi et al., 2012).

However, the evolution of AGN is still rife with uncertainty. On the basis of hard X-ray surveys, many studies agreed that the XLF of AGN is best described by a LDDE model (e.g. Ueda et al., 2003; Gilli et al., 2007; Silverman et al., 2008b; Ueda et al., 2014). Aird et al. (2010) preferred instead a LADE model. In LADE, the shift in the redshift peak of the AGN space density versus X-ray luminosity is much weaker than in LDDE models, yet gives a similarly good fit to their data. While the  $z < 2$  downsizing behaviour is common to both models, quite different numbers of AGNs are predicted at higher redshifts ( $z \geq 3$ ).

X-ray surveys (2-10 keV) are now sensitive enough to sample the bulk of the  $z > 3$  AGN population. Limited studies have been performed on high-redshift AGN exploiting

the deep X-ray surveys in the Cosmological Evolution Survey (COSMOS) field carried out with *XMMNewton* ( $N_{\text{AGN}} = 40$ ; Brusa et al., 2009) and *Chandra* ( $N_{\text{AGN}} = 81$ ; Civano et al., 2011), limited to 2-10 keV luminosities  $L_{2-10\text{keV}} > 10^{44.2} \text{ erg s}^{-1}$  and  $10^{43.5} \text{ erg s}^{-1}$ , respectively. A more recent study based on the 4 Ms *Chandra* Deep Field South (CDF-S; Xue et al., 2011) was able to investigate the evolution of  $z > 3$  AGN down to  $L_X \sim 10^{43} \text{ erg s}^{-1}$  ( $N_{\text{AGN}} = 34$ ; Vito et al., 2013). These results are consistent with a decline of the AGN space density at  $z > 3$ , but the shape of this decline remains highly uncertain at  $z > 4$ . To overcome these limitations, in this work we combined the two largest samples of  $z > 3$  X-ray-selected AGNs, both derived from *Chandra* X-ray Observatory (Weisskopf et al., 2002) surveys: the wide but shallow *Chandra* Multi-wavelength Project survey (ChAMP; Kim et al., 2007; Green et al., 2009), and the deeper but narrower *Chandra*-COSMOS survey (C-COSMOS; Elvis et al., 2009). This combination results in the largest X-ray selected AGN sample with  $N_{\text{AGN}} = 211$  at  $z > 3$  and  $N_{\text{AGN}} = 27$  at  $z > 4$ . At the same time, by combining two surveys with different flux limits, we are able to determine the density evolution of both low-luminosity ( $L_X < 10^{44} \text{ erg s}^{-1}$ ) and high-luminosity AGNs. Our sample includes both obscured and unobscured AGNs, and their separate evolution has been determined.

The chapter is structured as follows. In Section 2.2, I discuss the data sets used in this work and the selection of the high- $z$  sample. In Section 2.3, I present the optical and X-ray properties of the selected high- $z$  AGN sample, and I explain the AGN type classification using X-ray or optical data. In Sections 2.4 and 2.5, the number counts and space density of the sample are compared with model predictions. Section 2.6 summarizes the conclusions.

## 2.2 Sample selection

The high-redshift AGN sample used in this work has been selected from the C-COSMOS X-ray catalogue, combining the spectroscopic and photometric information available from the identification catalogue of X-ray C-COSMOS sources (Civano et al., 2011, 2012) and the ChAMP X-ray catalogue using only the 323 ChAMP obsids overlapping with Sloan Digital Sky Survey (SDSS; Richards et al., 2006a) DR5 imaging. In Fig. 2.1, I show the sky coverage (the area of a survey that is sensitive to sources above a given X-ray flux) using the observed soft band (0.5-2 keV) source detections for the two surveys, and their sum. This corresponds to 2-8 keV rest frame for  $z > 3$ . A schematic diagram of the sample selection with the detailed number of sources for each step is presented in Fig. 2.2.

### 2.2.1 The C-COSMOS sample

The C-COSMOS survey (Elvis et al., 2009; Civano et al., 2012) covers the central  $0.9 \text{ deg}^2$  of the COSMOS field up to a depth of 200 ks in the inner  $0.5 \text{ deg}^2$ , with the ACIS-I CCD imager (Garmire et al., 2003) on board *Chandra*. The C-COSMOS X-ray source

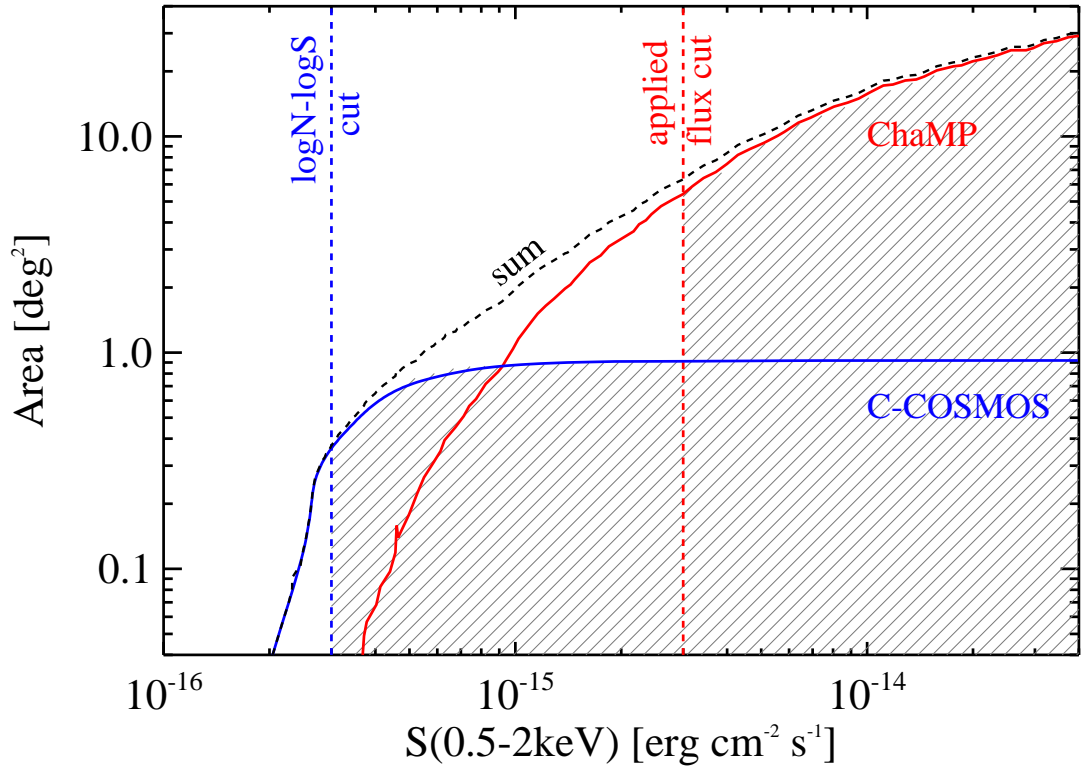
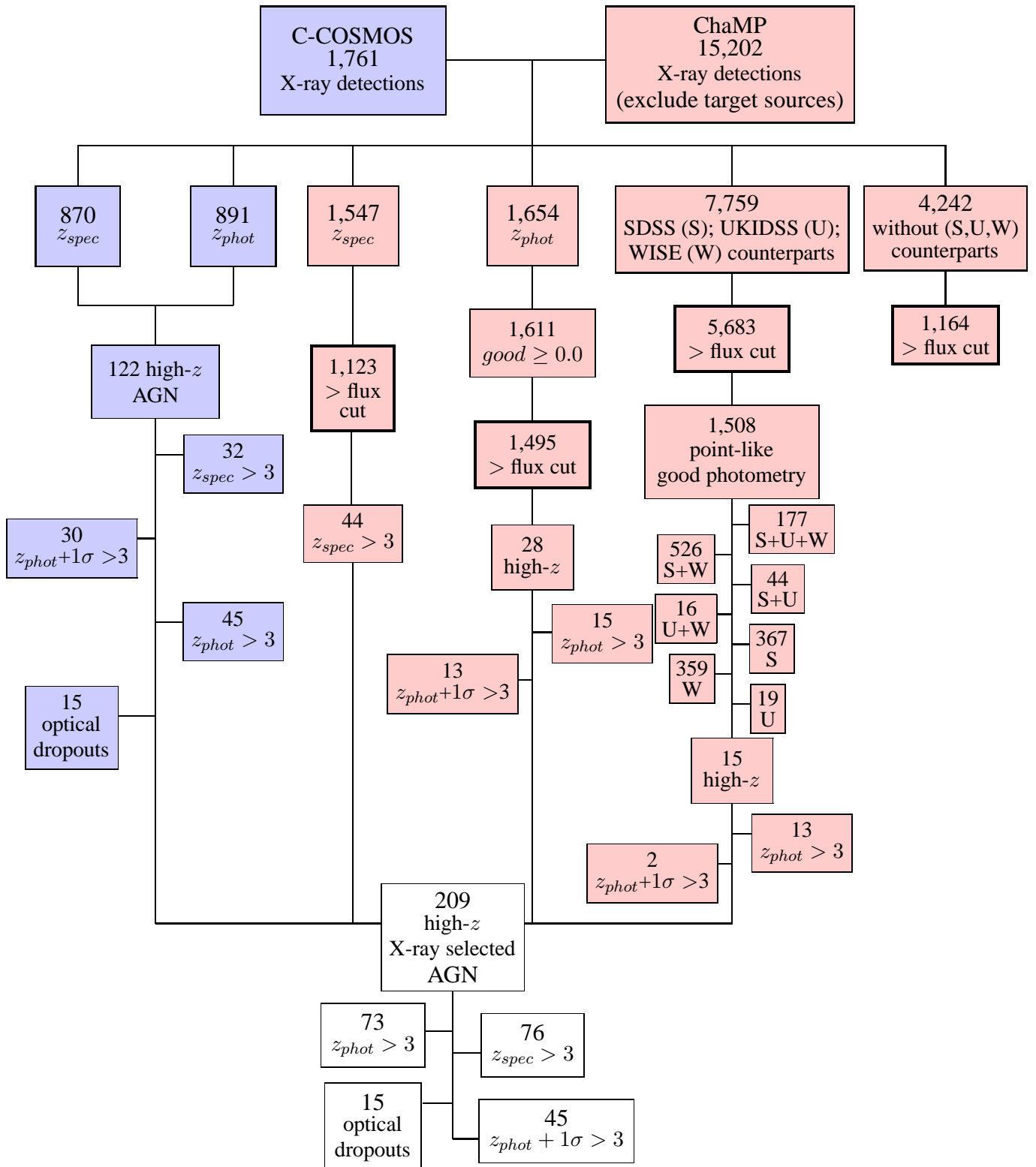


FIGURE 2.1: Sky area vs. X-ray flux sensitivity curves for the C-COSMOS (blue solid line) and ChaMP/SDSS (red solid line) samples and the total area (black dashed line). The vertical blue dashed line indicates the flux corresponding to 10 per cent of the total C-COSMOS area (see Section 2.4). The vertical red dashed line indicates the ChaMP X-ray flux limit with  $> 75$  per cent completeness from SDSS/UKIDSS/WISE (see Section 2.2.2). The total area, after the applied cuts, used for this work is represented by the shadowed grey area.

catalogue comprises 1761 point-like X-ray sources detected down to a maximum likelihood threshold  $\text{detml} = 10.8$  in at least one band. This likelihood threshold corresponds to a probability of  $\sim 5 \times 10^{-5}$  that a catalogue source is instead a background fluctuation (Puccetti et al., 2009). Given this likelihood threshold, the flux limit reached in the survey is  $5.7 \times 10^{-16} \text{ erg cm}^{-2} \text{ s}^{-1}$  in the full band (0.5-10 keV),  $1.9 \times 10^{-16} \text{ erg cm}^{-2} \text{ s}^{-1}$  in the soft band (0.5-2 keV) and  $7.3 \times 10^{-16} \text{ erg cm}^{-2} \text{ s}^{-1}$  in the hard band (2-10 keV).

The  $z > 3$  C-COSMOS sample, as presented by Civano et al. (2011), comprises 107 X-ray-detected sources with available spectroscopic (32) and photometric (45) redshifts plus 30 sources with a formal  $z_{\text{phot}} < 3$  but with a broad photometric redshift probability distribution, such that  $z_{\text{phot}} + 1\sigma_{\text{phot}} > 3$ . All of the spectroscopic C-COSMOS sources have a quality flag 3 (two sources) or 4 corresponding, respectively, to a secure redshift with two or more emission or absorption lines and a secure redshift with two or more emission or absorption lines with a good-quality, high S/N spectrum (see Lilly et al., 2007, 2009 for thorough explanation of quality flags). Tuned photometric redshifts for the C-COSMOS sources have

FIGURE 2.2: Schematic flow diagram of the high- $z$  sample selection.

been computed and presented in [Salvato et al. \(2011\)](#). Due to the large number of photometric bands and the sizeable spectroscopic training sample spanning a large range in redshift and luminosity the estimated photometric redshifts are expected to be quite robust at  $z > 2.5$  even at the fainter magnitudes ( $i_{AB} > 22.5$ ). The COSMOS photometric redshifts for X-ray-selected sources have an accuracy of  $\sigma_{\Delta z/(1+z_{spec})} = 0.015$  with a small fraction of outliers ( $< 6$  per cent), considering the sample as a whole at  $i < 22.5$ . At fainter magnitudes, the dispersion increases to  $\sigma_{\Delta z/(1+z_{spec})} = 0.035$  with  $\sim 15$  per cent outliers, still remarkably good for an AGN sample. For the  $z > 3$  C-COSMOS sample, an accuracy of  $\sigma_{\Delta z/(1+z_{spec})} = 0.014$  is achieved with only three catastrophic outliers ( $< 9$  per cent). The SEDs of the sources with photometric redshift larger than 3 have been visually inspected together with the photometric fitting and the probability distribution of all the possible solutions.

There are 91 sources selected in the 0.5-2 keV band, 14 in the 2-10 keV, and 4 in the 0.5-10 keV bands. There are 15 C-COSMOS sources without a counterpart in the optical bands, but with a  $K$ -band and IRAC (7), only IRAC (6) or no infrared detection (2). Given the small number of bands in which these objects are detected, no photometric redshift is available for them. In X-ray-selected samples, non-detection in the optical band has been often assumed to be a proxy for high redshift (e.g. [Koekemoer et al., 2004](#)), or for high obscuration, or a combination of both. 4 of the 15 sources have no detection in the soft band suggesting high obscuration, possibly combined with high redshift. More details about the sample selection can be found in [Civano et al. \(2011\)](#) and are also presented in [Fig. 2.2](#).

## 2.2.2 The ChaMP sample

The ChaMP is a wide-area non-continuous X-ray survey based on archival X-ray images of the high Galactic latitude ( $|b| > 20$  deg) sky observed with ACIS on *Chandra*. The flux levels (in  $\text{erg cm}^{-2} \text{s}^{-1}$  units) reached in the survey are  $9.4 \times 10^{-16} - 5.9 \times 10^{-11}$  in the full (0.5 – 8 keV),  $3.7 \times 10^{-16} - 2.5 \times 10^{-11}$  (0.5 – 2 keV) in the soft and  $1.7 \times 10^{-15} - 6.7 \times 10^{-11}$  (2 – 8 keV) in the hard band, respectively. The ChaMP survey includes a total of 392 fields, omitting pointings from dedicated serendipitous surveys like C-COSMOS, the *Chandra* Deep Fields, as well as fields with extended ( $> 3$  arcmin) bright optical or X-ray sources. The list of *Chandra* pointings avoids any overlapping observations by eliminating the observation with the shorter exposure time. The survey has detected a total of  $> 19\,000$  X-ray sources ([Kim et al., 2007](#); [Green et al., 2009](#)) over  $33 \text{ deg}^2$  with  $\sim 15\,350$  X-ray sources positionally matched to SDSS optical counterparts ([Green et al., 2009](#)).

The study of the X-ray-detected AGN properties requires accurate estimation of redshifts, luminosities and source classification thus, good quality spectra or, when not available, multiband photometry. Hence for our X-ray analysis we chose only the 323 fields over-lapping with SDSS DR5 imaging for which the sensitivity curve is given by [Green et al. \(2009\)](#), to determine accurate number counts. Optical spectroscopy of ChaMP X-ray sources

was described by [Trichas et al. \(2012\)](#), where redshifts and classifications for a total of 1569 *Chandra* sources are presented. Since the ChaMP is a *Chandra* archival survey, most ChaMP fields contain targeted sources selected by the targets PI, and those targets are likely to be biased towards special X-ray populations such as bright AGN. Of the targeted sources  $\sim 90$  per cent have a secure spectroscopic redshift with 33 of them residing at  $z > 3$  and 29 at  $z > 4$  (see [Trichas et al., 2012](#)). The high rate of high-redshift-detected sources clearly shows the strong selection biases that could affect our analysis if the targeted sources are included. Therefore, I exclude all targeted sources (153) to reduce bias in sample properties and source number counts.

For SDSS point sources with  $i < 21$  and without available spectroscopy, efficient photometric selection of quasars is possible using a nonparametric Bayesian classification based on kernel density estimation as described in [Richards et al. \(2009\)](#). To select high- $z$  candidates without available spectroscopic or photometric redshift, SDSS detection is required in at least the  $i$  and  $z$  bands, to detect Lyman dropouts (e.g. [Steidel et al., 1996](#)).

Searching the ChaMP catalogue for X-ray sources within 4 arcsec of the optical SDSS quasar coordinate (95 per cent of the matched sample has an X-ray/optical position difference of less than 3arcsec; see [Green et al., 2009](#)), yields 9727 unique matches ( $\sim 63$  per cent of the total ChaMP X-ray-selected sample). We additionally searched for cross-matches in the *Wide-field Infrared Survey Explorer* (*WISE*; [Wright et al., 2010](#)) and UKIRT (UK Infrared Telescope) Infrared Deep Sky Survey (UKIDSS; [Warren et al., 2000](#); [Hewett et al., 2006](#); [Maddox et al., 2008](#))<sup>1</sup>.

For a source to be included in the *WISE* All Sky Source Catalog ([Wright et al., 2010](#)), SNR  $> 5$  detection was required for one of the four photometric bands,  $W1$ ,  $W2$ ,  $W3$ ,  $W4$ , with central wavelengths of roughly 3.4, 4.6, 12, and 22  $\mu\text{m}$ , and angular resolutions of 6.1, 6.4, 6.5, and 12.0 arcsec. Because of the different spatial resolutions, 6.0 arcsec (*WISE*;  $W1$ ) and 1-2 arcsec (SDSS), I use 6 arcsec as the matching radius for *WISE* counterparts ([Wu et al., 2012](#)).

Similarly, I searched the UKIDSS Large Area Survey (LAS; [Lawrence et al., 2007](#)) Data Release 10 for NIR counterparts to ChaMP X-ray sources. The photometric system is described in [Hewett et al. \(2006\)](#), and the calibration is described in [Hodgkin et al. \(2009\)](#). I used the LAS YJHK source table, which contains only fields with coverage in every filter and merges the data from multiple detections of the same object. The X-ray source catalogues were then matched within 3 arcsec of the X-ray position separately to each UKIDSS band:  $Y$  (0.97-1.07  $\mu\text{m}$ ),  $J$  (1.17-1.33  $\mu\text{m}$ ),  $H$  (1.49-1.78  $\mu\text{m}$ ), and  $K$  (2.03-2.37  $\mu\text{m}$ ) recovering also the areas with coverage in a single UKIDSS band. The individual band lists were then

<sup>1</sup>The UKIDSS project is defined in [Lawrence et al. \(2007\)](#). UKIDSS uses the UKIRT Wide Field Camera (WFCAM; [Casali et al., 2007](#)) and a photometric system described in [Hewett et al. \(2006\)](#). The pipeline processing and science archive are described in [Hambly et al. \(2008\)](#).

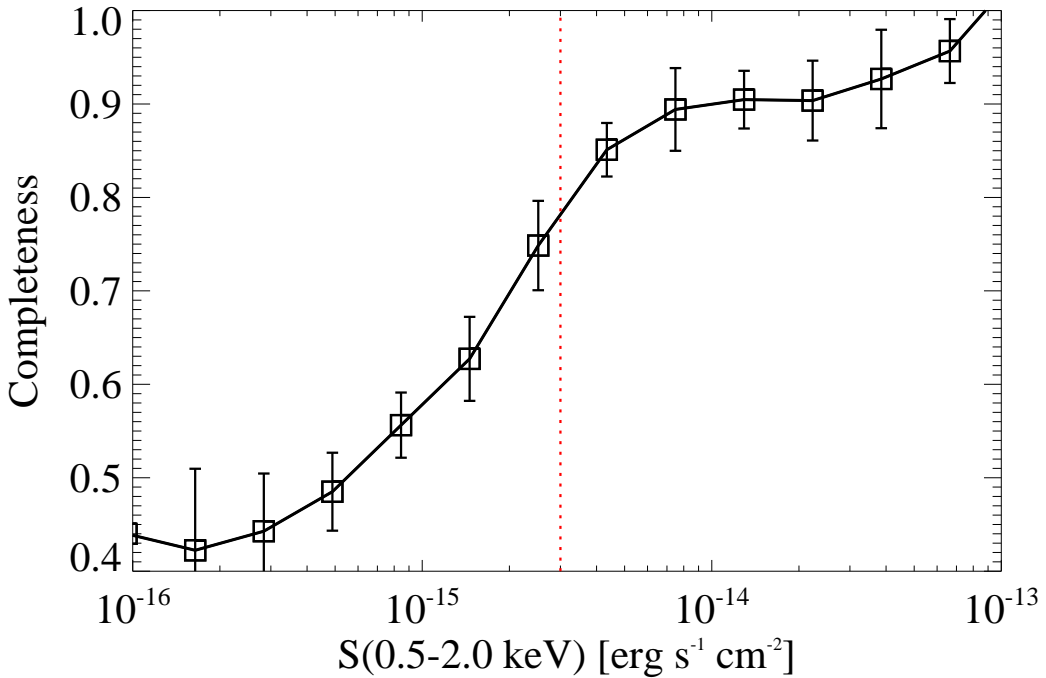


FIGURE 2.3: Optical and/or infrared ChaMP survey completeness as a function of 0.5-2 keV X-ray flux. The red dotted line indicates the ChaMP X-ray flux cut with  $> 75$  per cent completeness from SDSS/UKIDSS/*WISE*.

combined. For objects not detected in a UKIDSS band, I use the  $5\sigma$  detection limits provided in [Dye et al. \(2006\)](#) of  $Y = 20.23$ ,  $J = 19.52$ ,  $H = 18.73$ , and  $K = 18.06$ . Matching the ChaMP catalogue to *WISE* and UKIDSS, I find 1103 additional *WISE* and/or UKIDSS counterparts which do not have a SDSS counterpart (the detailed numbers are reported in [Fig. 2.2](#)).

In summary,  $\sim 70$  per cent of the total ChaMP X-ray sample have SDSS and UKIDSS/*WISE* photometry (9727 SDSS and/or *WISE* and/or UKIDSS and 1103 *WISE* and/or UKIDSS). The limited fraction of optical matches shows how optical counterparts of faint X-ray sources are fainter than the SDSS magnitude limit ( $i = 21.0$ ). SDSS quasars were identified to  $i < 19.1$  for spectroscopy by their UV-excess colours, with an extension for  $z > 3$  quasars to  $i = 20.2$  using *ugri* colour criteria ([Richards et al., 2002](#)).

Based on the X-ray limits, the identification completeness of ChaMP X-ray sources falls rapidly for objects with fainter optical counterparts. [Fig. 2.3](#) shows the optical (SDSS *i*-band counterparts) and infrared (*WISE* and UKIDSS counterparts) completeness of the X-ray-selected sample as a function of the soft (0.5-2 keV) X-ray flux. This incompleteness can severely bias determination of the number counts and space density, particularly at high redshifts (e.g. [Barger et al., 2005](#)).

To address this issue, I set a relatively high X-ray flux limit in ChaMP, where spectroscopic completeness is higher, and photometric coverage allows good photometric redshifts.

I use a soft flux limit for ChaMP at  $S_{0.5-2 \text{ keV}} > 3 \times 10^{-15} \text{ erg s}^{-1} \text{ cm}^{-2}$  as at these brighter fluxes the completeness is higher than 75 per cent (see Fig. 2.3). The completeness fraction as a function of flux has been taken into account for the estimation of the number counts and comoving space density (see Sections 2.4 and 2.5). For sources not detected in the soft band, the 0.5-2 keV flux has been computed by converting the 2-10 keV flux using  $\Gamma = 1.8$  (see Section 2.3.2). One of the main advantages of our compilation is that we do not miss the faint high-redshift population, since this is recovered by the C-COSMOS survey. In this way, the ChaMP sample is used for the determination of the bright end of the luminosity function at high redshifts.

### Spectroscopic redshifts

Secure spectroscopic redshifts have been compiled for a total of 1547 sources. I have used 1056 sources (excluding target sources) from existing ChaMP spectroscopy (Trichas et al., 2012) for the selected ChaMP fields. Additional spectroscopic redshifts are given in the SDSS-III ( $N = 91$ ; Noterdaeme et al., 2012) and SDSS-DR10 quasar catalogues ( $N = 145$ ; Pâris et al., 2014). I also searched the literature by cross-correlating optical positions with the NASA Extragalactic Database (NED), using a 2 arcsec match radius where I found 255 more sources with spectroscopic redshift.

The high-redshift spectroscopic sample consists of 44 sources with  $z > 3$ . All of these sources have a soft band X-ray detection, and only three sources lack a hard-band detection. Among them, there are seven sources with  $z > 4$  and one source with  $z = 6.016 \pm 0.005$  (Jiang et al., 2007). All but six of them have SDSS optical spectra with mean S/N  $> 4.5$  (none of them has S/N  $< 2.0$ ) with at least two broad emission lines (Ly $\alpha$  and CIV) significantly detected. For five of the remaining sources, redshifts have been obtained by Trichas et al. (2012) while for the source with the highest spectroscopic redshift ( $z = 6.016$ ) I have used the estimate from Jiang et al. (2007). For 30 sources of the ChaMP spectroscopic sample, there are available photometric redshifts derived by Richards et al. (2009) with an accuracy of  $\sigma_{\Delta z/(1+z_{spec})} = 0.013$  and only one catastrophic outlier.

### SDSS Photometric redshifts

For the sources without spectroscopic redshifts, I derived photometric redshifts. The criteria used in SDSS DR6 have now been refined to include objects redder than  $(u - g) = 1.0$  which may well be high- $z$  quasars. The resulting catalogue of  $\sim 1$  million photometrically identified quasars and their photometric redshifts from SDSS Data Release 6 (DR6) is described in Richards et al. (2009). Only point sources (type = 6) with  $i$ -band magnitudes between 14.5 and (de-reddened) 21.3 ( $\text{psfmag}_i > 14.5$  and  $\text{psfmag}_i - \text{extinction}_i < 21.3$ ; where  $\text{psfmag}$  are the point-spread-function magnitudes). They estimate the overall efficiency of the catalogue to be better than 72 per cent, with subsamples (e.g. X-ray-detected objects)

being as efficient as 97 per cent. At the faint limit of the catalogue some additional galaxy contamination is expected.

There are 1611 sources with SDSS high-quality photometric redshifts and no spectroscopic redshifts in ChaMP (i.e. those with  $\text{good} \geq 0.0$ , where  $\text{good}$  is the quality flag; 6 = most robust;  $-6$  = least robust; Richards et al., 2009). Among them there are 14 sources with  $z_{\text{phot}} > 3$  and one with  $z_{\text{phot}} > 4$ , above the adopted ChaMP flux limit. All of these sources are detected in both soft and hard band. The SDSS photo- $z$  code also gives a probability of an object being in a given redshift range. In this way, we have not only the most likely redshift but also the probability that the redshift is between some minimum and maximum value, which is crucial for dealing with catastrophic failures. The redshift probability distribution for each source is taken into account for the estimation of the number counts and comoving space density (see Sections 2.4 and 2.5). As for C-COSMOS selection of high- $z$  sources, we also included 13 sources having  $z_{\text{photo}} + 1\sigma_{z_{\text{photo}}} > 3$  and  $z_{\text{photo}} < 3$ . This adds another 10 objects to the main sample, all of them detected in both soft and hard bands.

### High- $z$ candidate selection and photometric redshift estimation

For the remaining 7759 without a spectroscopic or photometric SDSS redshift, I selected the high-redshift AGN candidates using their optical and/or their infrared colours. Most of these sources ( $\sim 70$  per cent), despite being included in SDSS DR6 catalogue, were rejected from Richards et al. (2009) selection criteria. The remaining sources come from later SDSS data releases.

Following the same morphological criteria as Richards et al. (2009), a candidate is required to be unresolved in images taken through the two redder filters (e.g.  $g$  and  $r$  for  $z \sim 3$  selection). This minimizes contamination from low- $z$  galaxies since even type-2 AGN at  $z > 3$  appear point like. However, I avoid using any faint flux cut in order to ensure that we do not miss faint high- $z$  candidates since non-detection can imply high- $z$  dropouts. I reject sources with flags indicating that their photometry may be problematic (e.g. blending of close pairs of objects, objects too close to the edge of the frame, objects affected by a cosmic ray hit). Overall, I reject 5079 non-point like sources or with problematic photometry. This number ( $\sim 65$  per cent) is in good agreement with the rejected number of sources by Richards et al. (2009) using the same criteria which explain the lack of a photometric redshift for these sources.

Photometric redshift criteria must strike a quantifiable balance between completeness and efficiency, i.e. a probability can be assigned both to the classification and the redshift. Using the SDSS, UKIDSS, and WISE<sup>2</sup> photometric data can help us to select quasar candidates more efficiently than using each survey individually (see Table 2.1). The photometric redshift reliability, defined by Wu et al. (2012) as the fraction of the sources with the difference

<sup>2</sup>We use the colours related to WISE  $W3$  and  $W4$  magnitudes only for sources lacking SDSS and/or UKIDSS detections because WISE uncertainties are substantially larger (Wu et al., 2004).

TABLE 2.1: Photometric redshift reliability defined by (Wu et al., 2012) and number of sources for ChaMP sources without spectroscopic or SDSS photometric redshifts.

Surveys <sup>a</sup>	Reliability (%)	$N_{\text{obj}}^b$	$N_{\text{obj-lim}}^c$
W		955	359
U		27	19
U+W	67.4	19	16
S	70.4	637	367
S+W	77.2	733	526
S+U	84.8	71	44
S+U+W	87.0	238	177
Total		2,680	1,508

<sup>a</sup>S=SDSS; W=WISE; U=UKIDSS

<sup>b</sup>Number of point-like objects in each combination of surveys.

<sup>c</sup>Number of point-like objects in each combination of surveys with  $S_{0.5-2 \text{ keV}} > 3 \times 10^{-15} \text{ erg s}^{-1} \text{ cm}^{-2}$ .

between the photometric and spectroscopic redshifts smaller than 0.2 is given in Table 2.1. The highest reliability can be reached only in the UKIDSS surveyed area, which is much smaller (4000 deg<sup>2</sup>) than the sky coverage of both SDSS and WISE surveys.

Richards et al. (2002) used a 3D multicolour space to select high-redshift QSO candidates in SDSS:  $griz$  ( $g - r, r - i, i - z$ ) for candidates with  $z > 3.0$ . Following the SDSS group, we search for high- $z$  candidates in three redshift intervals ( $z \simeq 3.0-3.5$ ,  $z \simeq 3.5-4.5$ ,  $z \simeq 4.5$ ). The details of the selection criteria are given in the Appendix 2.A. Our selection criteria require that the sources lie outside of a  $2\sigma$  region surrounding the stellar locus. We still expect the sample to be contaminated by stars and low- $z$  galaxies. For this reason, I use some additional criteria described by Richards et al. (2002) to exclude objects in colour regions containing predominantly white dwarfs, A stars and unresolved red-blue star pairs. During the colour selection process, no specific line is drawn between optically selected quasars (type-1 AGN) and type-2 AGN. Taking into account that both type-1 and type-2 AGNs are unresolved in optical images at  $z > 3$  and type-2 AGNs should lie outside the stellar locus due to their red optical colours, I expect that the above criteria efficiently select both high-redshift AGN populations. I found 53 SDSS-detected high- $z$  candidates.

To increase the reliability of the photometric estimation, I also combine the SDSS selection with the redder baselines from UKIDSS and WISE, where the contamination of the stellar locus and low-redshift galaxies is lower. I used the combination of UKIDSS and SDSS colours in the  $Y - K$  versus  $g - z$  colour-colour diagram suggested by Wu & Jia (2010) to efficiently separate quasars with redshift  $z < 4$  from stars. Similarly, Wu et al. (2012) suggested that  $z - W1$  and  $g - z$  colours could be used to separate stars from quasars. Based on these criteria, I have rejected 10 sources associated with stars based on both SDSS-UKIDSS and SDSS-WISE colour-colour diagrams. For sources detected only by UKIDSS, I used the  $i = 21.3$  upper limit and a  $Y - K$  versus  $i - Y$  colour-colour diagram to separate stars and

low- $z$  galaxies from high- $z$  candidates. I found four high- $z$  candidates. In the case of sources detected only by *WISE*, there is no efficient way detailed in the literature to separate high- $z$  quasars from stars.

Photometric redshifts have been estimated for the high- $z$  candidates by comparing the observed colours with theoretical colour-redshift relations derived from samples with known redshifts (Richards et al., 2002; Wu & Jia, 2010; Wu et al., 2012). A standard  $\chi^2$  minimization method is used to estimate the most probable photometric redshifts. Here, the  $\chi^2$  is defined as (see Wu et al., 2004)

$$\chi^2 = \sum_{ij} \frac{[(m_{i,cz} - m_{j,cz}) - (m_{i,ob} - m_{j,ob})]^2}{\sigma_{m_{i,ob}}^2 + \sigma_{m_{j,ob}}^2}, \quad (2.1)$$

where the sum is obtained for all four SDSS colours and/or WISE and/or UKIDSS colours,  $m_{i,cz} - m_{j,cz}$  is the colour in the colour-redshift relations,  $m_{i,ob} - m_{j,ob}$  is the observed colour of a quasar, and  $\sigma_{m_{i,ob}}$  and  $\sigma_{m_{j,ob}}$  are the uncertainties of observed magnitudes in two bands.

The uncertainty in the measurement was obtained by mapping the  $\Delta\chi^2$  error. Since the above studies are dominated by optically selected quasars, we would expect that the photometric redshifts uncertainties in type-1 AGNs are smaller. However, since the Lyman break enters the  $g$  band at  $z \sim 3.5$ , the  $g - r$  colours quickly redden with redshift for both populations. Alexandroff et al. (2013) found that  $g - r$  colours are indistinguishable at an 84 per cent confidence level between type-1 and type-2 quasars at  $z > 2$  suggesting that even in the case of type-2 AGNs the photometric redshifts are reliably estimated. Overall, I found eight sources with  $z > 3$  at greater than  $1\sigma$  significance, four sources with  $z > 3$  but lower than  $1\sigma$  significance, and two sources with  $z_{\text{phot}} + 1\sigma_{\text{phot}} > 3$ .

### The ChaMP high- $z$ sample

The total  $z > 3$  ChaMP sample includes 87 sources with  $z > 3$ . Among them there are 44 sources with secure spectroscopic redshift, 15 sources with SDSS  $z_{\text{phot}} > 3$  and 13 sources with SDSS  $z_{\text{phot}} + 1\sigma_{\text{phot}} > 3$  available from Richards et al. (2009), and 15 sources with estimated photometric redshifts based on optical/infrared colour-redshift relations (13 with  $z_{\text{phot}} > 3$  and 2 with  $z_{\text{phot}} + 1\sigma_{\text{phot}} > 3$ ).

## 2.3 The C-COSMOS & ChaMP $z > 3$ AGN Sample

In summary, I have assembled a sample of X-ray selected AGN at  $z > 3$  in the C-COSMOS and ChaMP on the basis of both spectroscopic and photometric redshifts. The total sample includes 209 sources with  $z > 3$ . Of these, 45 are selected to be at  $z > 3$  from their broad  $P(z)$ . There are also 15 C-COSMOS sources considered to be at  $z > 3$  on the basis of their optical non-detection these are included only in the derivation of the upper boundary of the

$\log N - \log S$  curve. The properties of the sample members are given in Table A (Appendix) and the detailed numbers are given in Fig. 2.2. Fig. 2.4 shows the optical and near-infrared ( $i$ ,  $K$ , and  $3.6 \mu\text{m}$ ) observed magnitude distributions for the total high- $z$  population and for sources with spectroscopic and photometric redshifts, separately. Sources selected as  $i$ -dropouts are also presented.

The hard (2-10 keV rest frame) X-ray luminosity versus redshift plane is shown in Fig. 2.5 together with the flux limit of the C-COSMOS and ChaMP surveys (dashed line) and the applied flux cut for ChaMP (dotted line). Luminosities were computed in every case by assuming an intrinsic  $\Gamma = 1.8$ .

The C-COSMOS & ChaMP high- $z$  sample is a factor of 4-5 larger than all the previous individual X-ray selected samples at  $z > 3$  (e.g. Brusa et al., 2009; Hiroi et al., 2012; Vito et al., 2013). Most importantly, this is the first time that a significant sample of 29 X-ray selected AGNs at  $z > 4$  is assembled. At these redshifts previous studies had a maximum of nine sources. The  $z > 3$  X-ray-selected AGN sample also covers more than a factor of 2 of soft (2-10 keV rest frame) X-ray luminosity, and includes a significant number of both broad-line and non-broad line AGNs.

To discuss the obscured AGN fraction requires each object in our sample to be classified as obscured or unobscured. There are two commonly adopted methods for classification: one is based on the optical emission line widths (“optical type”) or, if a spectrum is unavailable, by the type of template that best fits the optical-infrared SEDs of the sources. The other is based on the column densities,  $N_{\text{H}}$ , in the X-ray spectra (“X-ray type”) or, if an X-ray spectrum is unavailable, by the hardness ratio (HR; e.g. Hasinger et al., 2001). X-ray absorption should typically correlate with optical AGN type. In the unified scheme (e.g. Lawrence & Elvis, 1982; Antonucci, 1993; Urry & Padovani, 1995) as the narrow emission line AGNs are viewed through the dusty torus, and hence have higher absorption column densities than broad emission line AGNs. In fact, evidence has been mounting over the years that the optical- and X-ray-based classifications often give contrasting results (Lawrence & Elvis, 2010; Lanzuisi et al., 2013; Merloni et al., 2014).

### 2.3.1 Optical Types

The optical type of the sources is determined by the measured full width at half-maximum (FWHM) of the permitted emission line. Those objects with emission lines having FWHM  $> 1,000 \text{ km s}^{-1}$  (e.g. Stern & Laor, 2012) are classified as “optical broad-line” (BLAGN), and all others as “optical non-broad-line” (non-BLAGN), i.e., they show narrow emission lines or absorption lines only, following Civano et al. (2011, 2012).

In the C-COSMOS spectroscopic  $z > 3$  sample, 21 of 32 sources are classified as BLAGN. These are mainly associated with the brighter optical sources ( $i_{AB} \sim 22 - 23$ ) of the spectroscopic sample. At fainter optical magnitudes ( $i_{AB} > 23$ ), equal numbers of

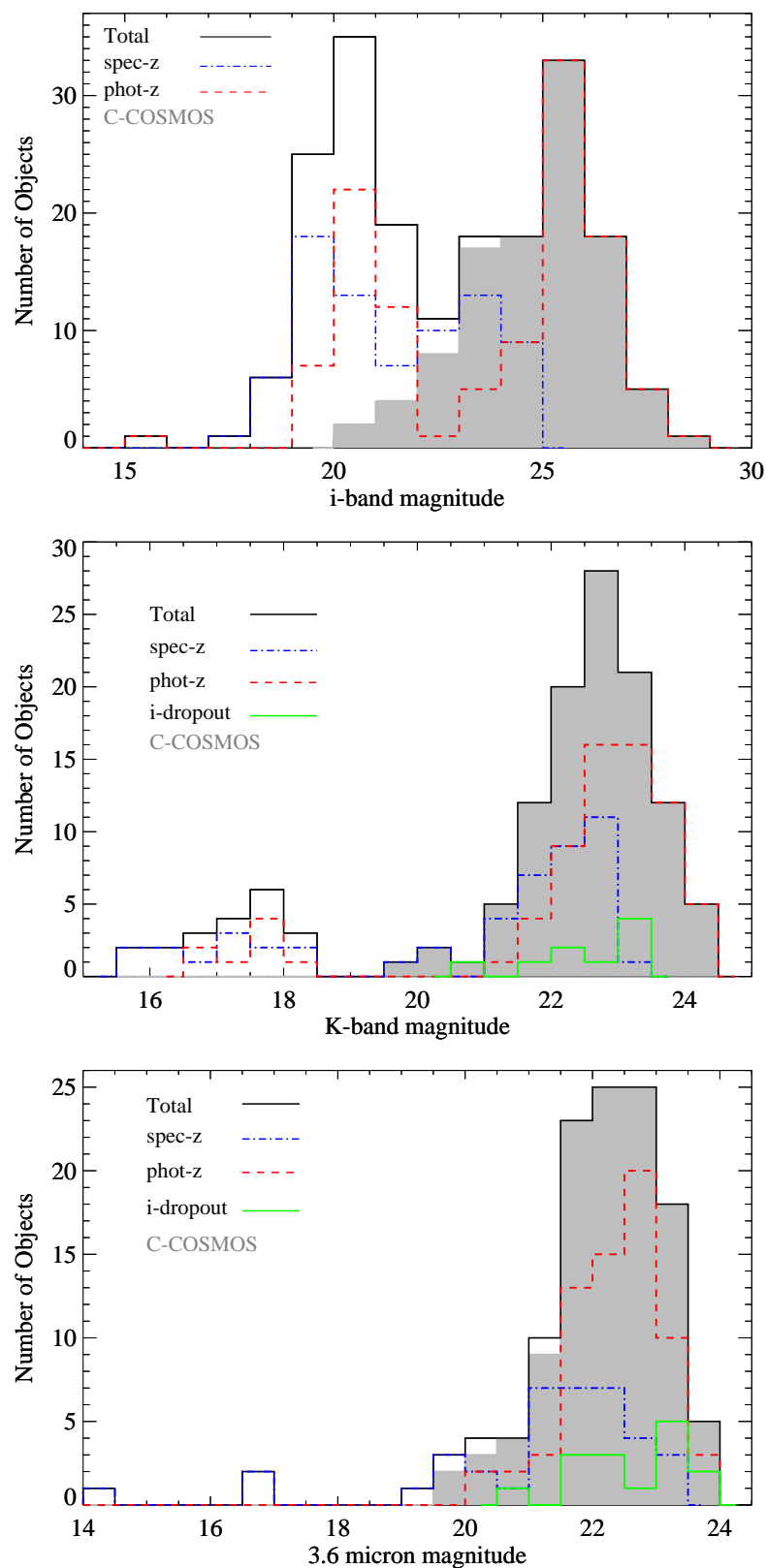


FIGURE 2.4: Observed AB magnitude distribution of all the  $i$ -band,  $K$ -band, and  $3.6 \mu\text{m}$  band (from top to bottom) high- $z$  objects. Black solid, blue dot-dashed, red dashed and green solid lines represent the total, spectroscopic, photometric redshift and  $i$ -dropout samples, respectively. The  $i$ -band dropouts are not included in the  $i$ -band histogram.

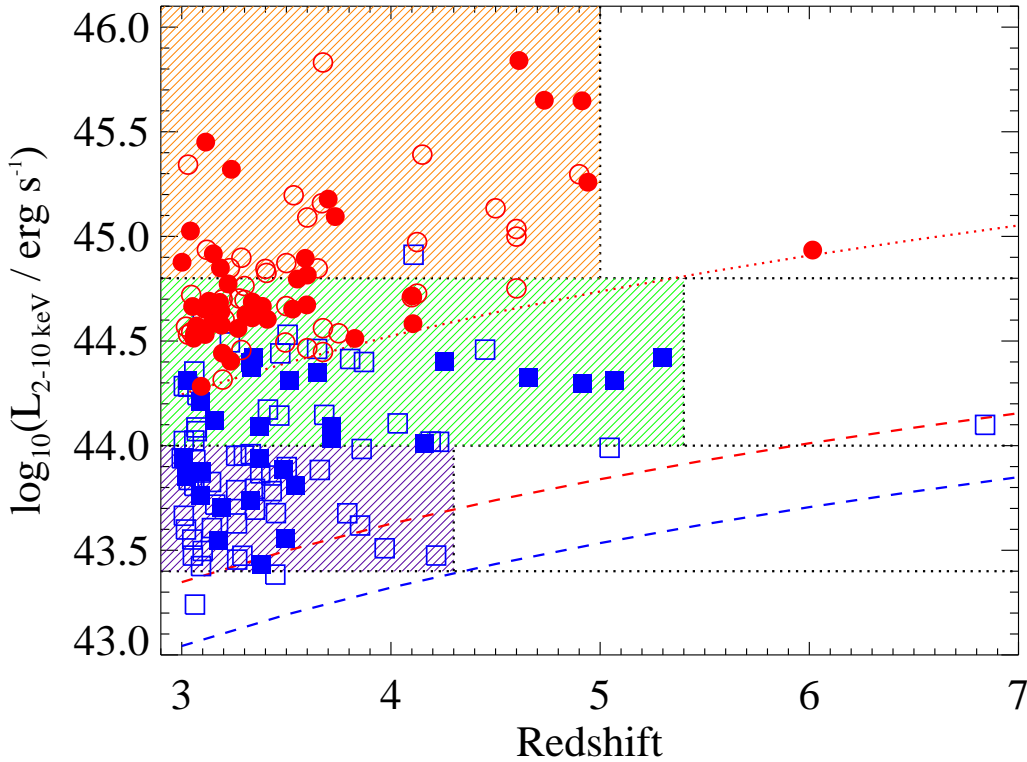


FIGURE 2.5: The hard X-ray luminosity (computed with  $\Gamma = 1.8$ ) redshift plane for the objects in our sample. Blue squares = C-COSMOS sample. Red circles = ChaMP sample. Filled = spectroscopic redshift. Open = photometric redshift. The dashed lines represent the 2-10 keV luminosity limit of the surveys computed from the 0.5-2 keV limiting flux. The dotted red line represents the completeness flux cut we have adopted at  $3 \times 10^{-15} \text{ erg cm}^{-2} \text{ s}^{-1}$ . The dotted black lines correspond to the flux limits we imposed for the computation of the space density and their associated areas, purple ( $43.4 < \log(L_X / \text{erg s}^{-1}) < 44.0$ ), green ( $44.0 < \log(L_X / \text{erg s}^{-1}) < 44.7$ ), orange ( $\log(L_X / \text{erg s}^{-1}) > 44.7$ ).

broad-line and non-broad-line AGNs are found. The classification for the 75 AGNs in C-COSMOS with photometric redshifts is obtained by the [Salvato et al. \(2011\)](#) photometric fitting method fitting, the SED via  $\chi^2$  minimization with code LEPHARE ([Arnouts & Ilbert, 2011](#))<sup>3</sup>. More details on the fitting can be found in [Salvato et al. \(2011\)](#). Briefly, two libraries of templates were used, depending on morphology, optical variability, and X-ray flux of the source. The first library (defined in [Salvato et al., 2009](#), table 2) consists of AGN templates, hybrid (host + AGN) templates, and a few normal galaxies and was used for all the point-like optical sources and for the extended sources with an X-ray flux brighter than  $8 \times 10^{-15} \text{ erg cm}^{-2} \text{ s}^{-1}$ . The second library (as defined in [Ilbert et al., 2009](#)) includes only normal galaxy templates and it was used for the remaining sources (i.e., extended and with X-ray flux  $< 8 \times 10^{-15} \text{ erg cm}^{-2} \text{ s}^{-1}$ ). The flowchart in fig. 6 of [Salvato et al. \(2011\)](#) summarizes the procedure. [Civano et al. \(2012\)](#), according to this fitting, divide the sources into

<sup>3</sup><http://www.cfht.hawaii.edu/~arnouts/LEPHARE/lephare.html>

obscured AGN, galaxies and unobscured AGN. About 40 per cent (28 sources) of the photometric sample is best fitted with an unobscured quasar template, and 47 sources with an obscured quasar template. For 29 AGN with spectroscopic identification, the photometric and spectroscopic types match. Given the mismatch rate of  $\sim 9$  per cent, I estimate that  $\sim 7$  out of the 75 AGNs could have been assigned the wrong SED classification.

In the ChaMP  $z > 3$  spectroscopic sample, as expected at these fluxes (e.g. [Brusa et al., 2009](#)), and due to the predominantly SDSS spectroscopic target selection, only 2/44 sources are non-BLAGN. The characterization of these sources based on their SED fittings has been obtained by [Trichas et al. \(2012\)](#). In order to be in agreement with the spectroscopic ChaMP sample, we followed the same SED fitting method for the characterization of the 43 sources without a spectroscopic classification. According to this fitting, 11 of 43 sources are best fitted with an obscured quasar template (non-BLAGN). More details on the fitting can be found in [Trichas et al. \(2012\)](#) and [Ruiz et al. \(2010\)](#). Briefly, a total of 16 templates has been used including QSO, Seyfert-2 galaxies, starburst galaxies, absorption line galaxies and composite templates that are known to harbor both an AGN and a starburst. The [Ruiz et al. \(2010\)](#) model has been adopted, which fits all SEDs using a  $\chi^2$  minimization technique within the fitting tool SHERPA ([Freeman et al., 2001](#)). The fitting allows for two additive components, one associated with the AGN emission and the other associated with the starburst emission. The fit with the lowest reduced  $\chi^2$  has been chosen as the best-fit model.

A general problem of relying on the optical type is that the classification may depend on the quality of the available optical spectra, since good signal-to-noise ratio is required to detect less-luminous broad-emission lines above the stellar continuum emission of host galaxies. Also, at  $z > 3$ , the  $H\alpha$  emission line moves into the infrared and so, until recently, was difficult to observe. Intermediate AGN types (1.8, 1.9; [Osterbrock & Koski, 1976](#)) rapidly lose their broad  $H\beta$  emission, and without  $H\alpha$  these may be misclassified as type-2. Nevertheless, such effects are not expected to be significant in our sample, as it consists predominantly of luminous AGNs for which contamination from the host galaxies is negligible.

### 2.3.2 X-ray Types

Most sources in our sample have a low number of detected counts (median  $\sim 25$  in the 0.5-8.0 keV full band). In this count regime, spectral fit results are not reliable, especially if more than one free parameter is fit; even if the fit converges the uncertainties on the parameters are large. For these reasons, we use the Bayesian Estimation of Hardness Ratios (BEHR) method ([Park et al., 2006](#)) to derive X-ray spectral type. Hardness count ratios (HR), defined as  $HR = (C_{HB} - C_{SB}) / (C_{HB} + C_{SB})$ , where  $C_{SB}$  and  $C_{HB}$  are the counts in the soft band and hard band, respectively.

BEHR is particularly powerful in the low-count Poisson regime, because it computes a

realistic uncertainty for the HR, regardless of whether the X-ray source is detected in both energy bands. Sources with unconstrained upper or lower limits due to non-detections (14 hard-only and 49 soft-only detections) have been computed by converting the  $3\sigma$  flux upper limit in the undetected band into counts.

To estimate the column density, curves of constant  $N_{\text{H}}$  as a function of redshift have been derived for two spectral slope values,  $\Gamma = 1.4$  and  $\Gamma = 1.8$ . The flatter spectral slope has been chosen to be consistent with the assumptions adopted in producing the original X-ray catalogs (Kim et al., 2007; Puccetti et al., 2009). The steeper value is more representative of the intrinsic value if the spectrum is not affected by obscuration (Nandra & Pounds, 1994). The relationship between HR and redshift of our C-COSMOS and ChaMP AGN samples is shown in Fig. 2.6. Curves of  $N_{\text{H}} = 10^{20}$ ,  $10^{22}$ ,  $5 \times 10^{22}$  and  $10^{23} \text{ cm}^{-2}$  are reported for  $\Gamma = 1.8$  (dashed lines) and  $\Gamma = 1.4$  (solid lines). We observe that C-COSMOS sample tend to be more obscured as expected due to the fainter X-ray sensitivity limit, than the ChaMP sample (Lawrence & Elvis, 1982; Ueda et al., 2003; Hasinger, 2008; Brusa et al., 2010; Burlon et al., 2011).

Though the two samples (C-COSMOS and ChaMP) of  $z > 3$  AGN show different trends regarding their obscuration, the large HR errors and the similarity in this redshift range of the curves with widely different  $N_{\text{H}}$  values for the same spectral slope, do not allow an accurate estimate of the column density for each source to be made. Using the CIAO<sup>4</sup> spectral analysis package, SHERPA<sup>5</sup>, I have simulated X-ray spectra for AGN populations at  $3 < z < 7$  in order to quantify the evolution of X-ray spectral slopes due to the  $k$ -correction of the observed AGN spectra toward high- $z$ . Based on these simulations, I find that the HR distribution for the ChaMP sample peaks at  $\Gamma \sim 1.8 - 2.0$  while the HR distribution for C-COSMOS sample peaks at  $\Gamma \sim 1.4 - 1.9$ . Hereafter, to better constrain the column density and for the purpose of comparison with previous studies, we fixed the photon index to  $\Gamma = 1.8$  and converted all source fluxes.

In this work, I adopt  $N_{\text{H}} = 10^{22} \text{ cm}^{-2}$  as the dividing criterion; AGNs with  $N_{\text{H}} < 10^{22} \text{ cm}^{-2}$  and  $> 10^{22} \text{ cm}^{-2}$  are classified as X-ray unobscured and obscured, respectively. This criterion is adopted by many authors, and is known to be generally in good agreement with the optical type (see e.g. Ueda et al., 2003; Hiroi et al., 2012).

### 2.3.3 X-ray/Optical flux ratio

The X-ray/Optical (X/O) flux ratio is a redshift dependent quantity for obscured AGN, given that the  $k$ -correction is negative in the optical band and positive for the X-rays (Comastri et al., 2003; Fiore et al., 2003; Brusa et al., 2010). As a result, obscured sources have higher X/O at high redshift. On the other hand, unobscured sources have similar  $k$ -corrections in the

<sup>4</sup><http://cxc.harvard.edu/ciao/>

<sup>5</sup><http://cxc.harvard.edu/sherpa/>

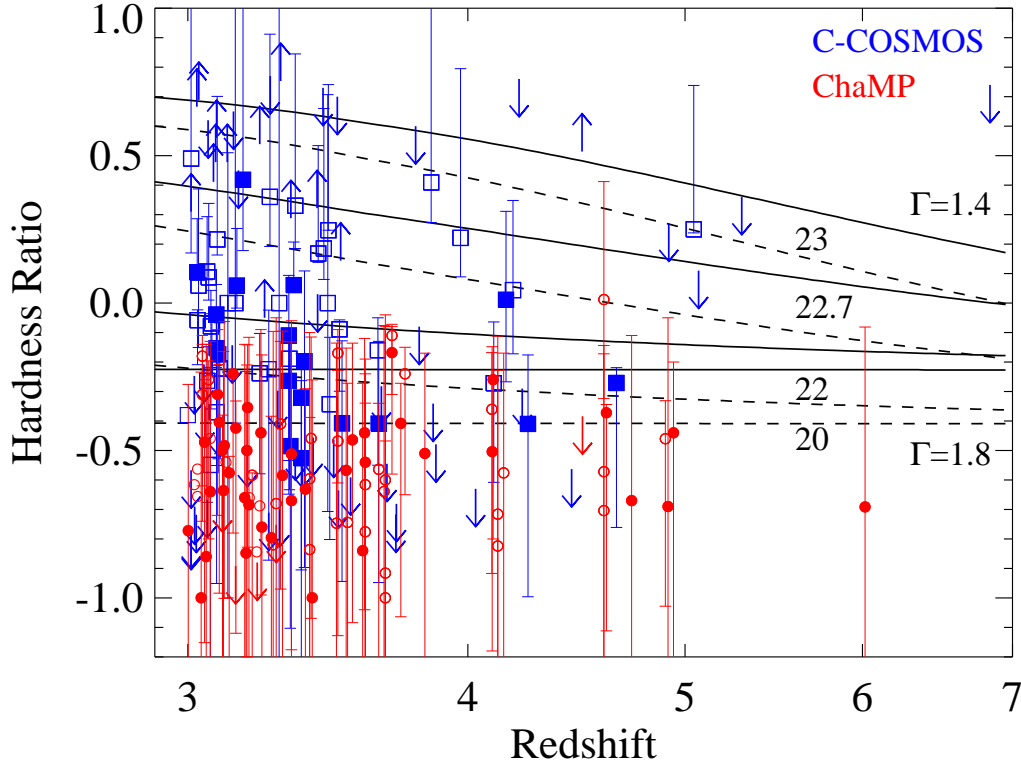


FIGURE 2.6: Hardness ratio versus redshift (in logarithmic scale). Blue squares = C-COSMOS sample. Red circles = ChaMP sample. Filled = spectroscopic redshift. Open = photometric redshift. Sources with no hard band or soft band detection are shown with arrows. Four curves of constant  $N_{\text{H}}$  ( $10^{20}$ ,  $10^{22}$ ,  $5 \times 10^{22}$  and  $10^{23}$   $\text{cm}^{-2}$ ) are reported for  $\Gamma = 1.8$  (dashed lines) and  $\Gamma = 1.4$  (solid lines).

two bands, and the distribution in X/O is not correlated with the redshift (Civano et al., 2012). Usually, the  $r$ - or  $i$ -band flux is used (e.g. Brandt & Hasinger, 2005) while a soft X-ray flux was originally used for this relation with the majority of luminous spectroscopically identified AGNs in the Einstein and ASCA surveys characterized by  $X/O = 0 \pm 1$  (e.g. Schmidt et al., 1998; Stocke et al., 1991; Lehmann et al., 2001). The same relation has been used also in the hard band, without really accounting for the X-ray band used or the change in spectral slope (e.g. Alexander et al., 2001; Fiore et al., 2003; Brusa et al., 2003; Civano et al., 2005; Laird et al., 2009; Xue et al., 2011).

Fig. 2.7 shows the distribution of X-ray soft (top) and hard (bottom) flux versus optical magnitude to illustrate the parameter space spanned by the broad-line and non-broad-line populations. The X/O ratio (Maccacaro et al., 1988) is defined as:

$$X/O = \log_{10}(f_X/f_{\text{opt}}) = \log_{10}(f_X) + C + m_{\text{opt}}/2.5 \quad (2.2)$$

where  $f_X$  is the X-ray flux in a given energy range,  $m_{\text{opt}}$ , is the magnitude at the chosen

optical wavelength, and  $C$  is a constant which depends on the specific filter used in the optical observations.

For both X-ray bands, the  $X/O = \pm 1$  locus (grey area) has been defined using as  $C(i) = 5.91$  (Civano et al., 2012), which was computed taking into account the width of the  $i$ -band filters in Subaru, CFHT (Canada-France-Hawaii Telescope), or for bright sources SDSS. In the hard band, the locus is plotted taking into account the band width and the spectral slope used to compute the X-ray fluxes ( $\Gamma = 1.8$ ). The majority of BLAGNs with a secure spectroscopic redshift, follow the trend of  $-1 < \log_{10}(f_X/f_i) < 1$ . However, given the variation in  $\alpha_{\text{OX}}$  with luminosity (e.g. Vignali et al., 2003; Young et al., 2010; Trichas et al., 2013), there can be some shift in the locations of QSOs with luminosity within the so-called BLAGN region. This shift is consistent with the X/O relation being originally calibrated on soft-X-ray-selected sources, bright in the optical and also in the X-rays. This might explain the mild shift between the ChaMP and C-COSMOS BLAGN.

Apart from the AGN population found in the BLAGN region, there is also a significant population that lie at  $\log(f_X/f_i) > 1$  suggesting obscured nuclei. The main characteristics of this sample are: 1) lack of spectroscopic redshifts (open symbols), 2) non-BLAGN optical classification (green symbols) and 3) low X-ray luminosities ( $10^{43} \text{ erg s}^{-1} < L_{2-10\text{keV}} < 10^{44} \text{ erg s}^{-1}$ ) with  $N_{\text{H}} > 10^{22} \text{ cm}^{-2}$  for  $\sim 65$  per cent of them, which is consistent with previous studies finding that mild obscuration is common at these luminosities (e.g. Silverman et al., 2010). Furthermore, nearly 75 per cent of all the sources with  $X/O > 1$  are obscured, thus confirming that selections based on high X/O ratio are efficient in finding samples of obscured AGN.

### 2.3.4 Comparison of optical and X-ray types

X-ray absorption is an alternative good indicator of AGN type. In order to compare our optical classification to the expected obscuration of BLAGNs and non-BLAGNs based on the unified scheme we have separated our total sample into broad-line and non-broad-line AGNs (as described in Section 2.3.1).

In the case of the BLAGN, the X-ray classification criterion ( $N_{\text{H}} = 10^{22} \text{ cm}^{-2}$ ) gives 28/124 X-ray obscured sources for  $\Gamma = 1.8$ . Half of these sources have a spectroscopic redshift and all but 3 come from C-COSMOS sample. If we also take into account the HR errors, then for the lower HR limits, 11 BLAGN are classified as X-ray obscured sources and 41 are classified X-ray obscured sources for the upper HR limits. In the non-BLAGN subset, the above criterion gives 49/71 X-ray obscured sources (detected in both soft and hard bands) for  $\Gamma = 1.8$ . The 27 soft band sources in non-BLAGN sample with no detection in the hard band (reported as downward arrows in Fig. 2.6) have very high upper limits on the HR, due to the conservative flux upper limit computed by Puccetti et al. (2009), but most of them do not thereby satisfy the  $N_{\text{H}} > 10^{22} \text{ cm}^{-2}$  criterion. These numbers are summarized

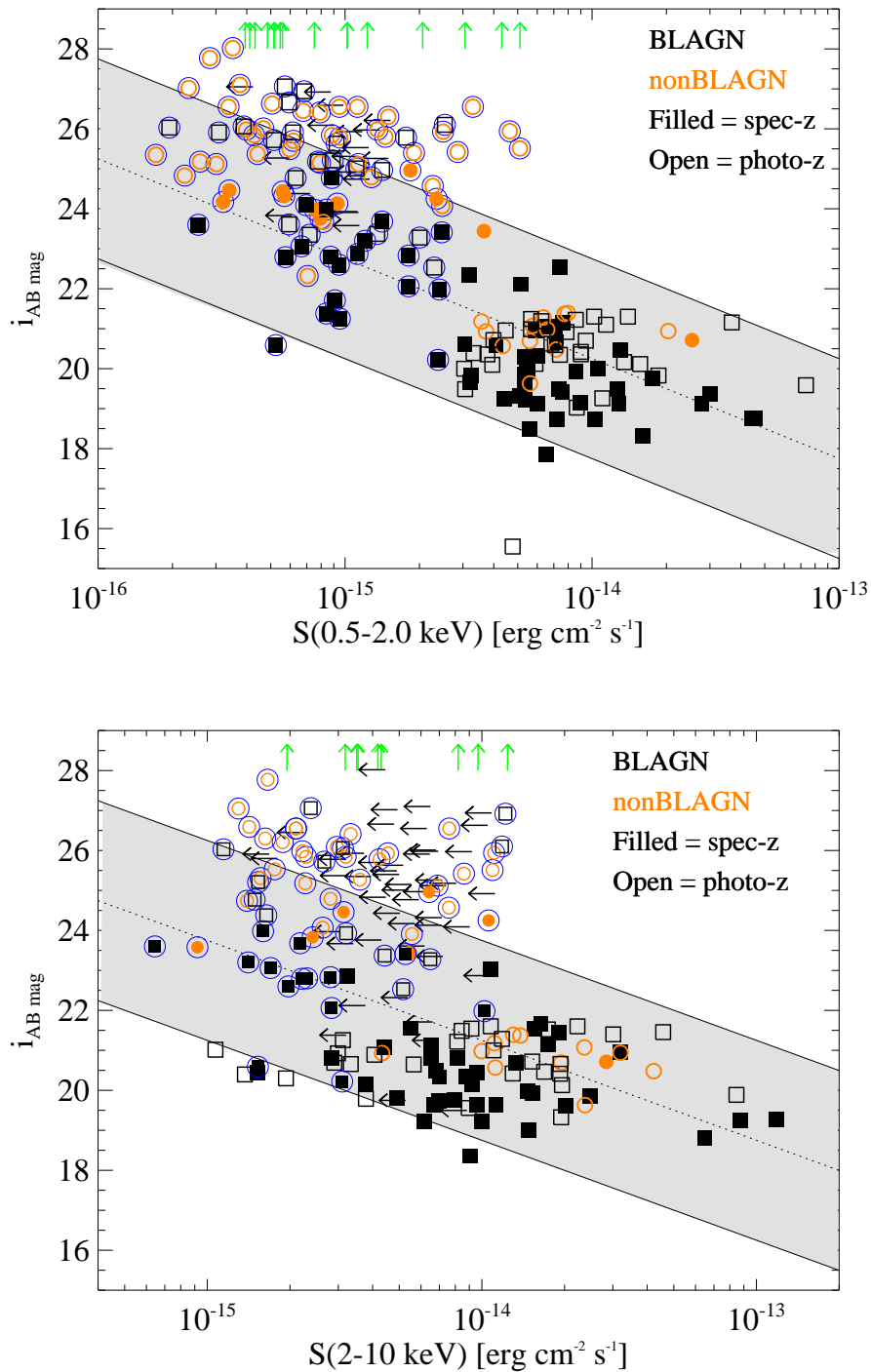


FIGURE 2.7: X-ray flux (soft-top, hard-bottom) vs. the  $i$ -band magnitude for all the X-ray sources with an  $i$ -band counterpart. The grey shaded region represents the locus of AGNs along the correlation  $X/O = 0 \pm 1$ . Sources with secure spectroscopic redshifts are represented by filled symbols and sources with a photometric redshift by open symbols. Orange circles and black squares represent non-BLAGN and BLAGN, respectively. Green upper limits represent  $i$ -band dropouts and black left pointing arrows represent soft and hard X-ray flux upper limits for undetected sources in each band. The C-COSMOS sample is represented by the open big blue circles.

TABLE 2.2: Comparison of optical and X-ray types. The upper and lower limits have been estimated taking into account only the error ranges in HR.

Number of sources	Unobscured	Obscured
	$N_{\text{H}} < 10^{22} \text{ cm}^{-2}$	$N_{\text{H}} \geq 10^{22} \text{ cm}^{-2}$
BLAGN	$96^{+16}_{-14}$	$28^{+14}_{-16}$
non-BLAGN	$22^{+13}_{-9}$	$49^{+9}_{-13}$

in Table 2.2.

For the total sample, we find agreement between the optical and X-ray classification for  $\sim 74$  per cent:  $\sim 77$  per cent for the BLAGN and  $\sim 69$  per cent for the non-BLAGN. These rates are consistent with recent studies (e.g. Lanzuisi et al., 2013; Merloni et al., 2014). Possible explanation can be a misclassification of faint type-1 with strong optical/IR contamination from host galaxy light.

To improve the statistics and gain information on the average properties of the two subclasses, I compared their mean HR values as a function of redshift (Fig. 2.8). Despite the  $\sim 30$  per cent misclassification for the individual sources, the mean properties of the BLAGN and non-BLAGN seem to agree with the  $N_{\text{H}} \sim 10^{22} \text{ cm}^{-2}$  division. These results do not change even only sources with spectroscopic redshifts are used. The upper and lower limits detected only in the soft or the hard band were used to compute the upper and lower boundary of the shaded area. I discuss the results in Section 2.5.

## 2.4 The logN-logS of the $z > 3$ AGN

I derived the soft band number counts of the  $z > 3$  and  $z > 4$  samples by folding the observed flux distribution through the sky coverage area versus flux curve of the C-COSMOS survey (Puccetti et al., 2009) and the ChaMP's 323 fields (Green et al., 2009). The number counts are corrected for ChaMP incompleteness in the spectroscopic/photometric coverage as a function of X-ray flux (i.e. Fig. 2.3).

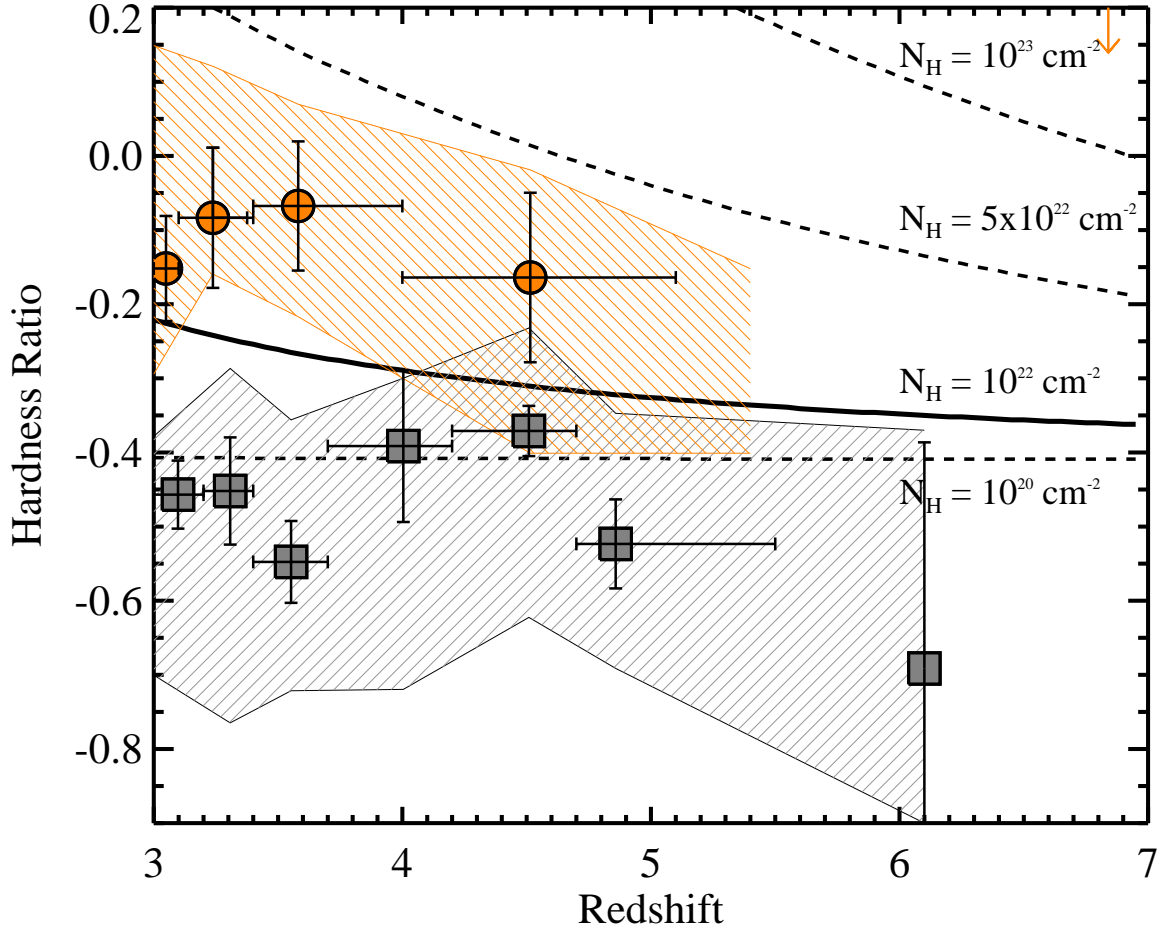


FIGURE 2.8: The mean hardness ratio as a function of redshift for BLAGN (black squares) and non-BLAGN (orange circles)  $z > 3$  AGN subsamples. The error bars represent the 68 per cent dispersion. Only sources with both soft and hard band detections are taken into account for the estimation of the mean HR in each bin. Undetected sources in one of these bands are included only for estimation of the upper and lower limits (dashed areas). The  $z_{\text{phot}} = 6.88$  source with an upper limit  $\text{HR}_{\text{up}} = 0.74$  has been shifted down to  $\text{HR} = 0.2$  in order to be included in the figure.

To minimize the errors associated with the most uncertain part of the sensitivity curve, I truncate the C-COSMOS sample at the flux corresponding to 10 per cent of the total area (blue dashed line in Fig. 2.1). All the sources with a  $0.5 - 2$  keV flux above  $3 \times 10^{-16}$  erg  $\text{cm}^{-2} \text{s}^{-1}$  have been considered (73 objects out of the 81 soft band detected). The flux limit applied to the sample is consistent with the signal-to-noise ratio thresholds chosen by Puccetti et al. (2009), on the basis of extensive simulations, to avoid the Eddington bias in the computation of the number counts of the entire C-COSMOS sample. Thus, by applying a flux limit cut, I also reduce the Eddington bias affecting our sample. For ChaMP this would be at  $S_{0.5-2\text{keV}} > 2 \times 10^{-15}$  erg  $\text{cm}^{-2} \text{s}^{-1}$ , below the flux limit already applied.

The binned  $\log N - \log S$  relations for two redshift ranges ( $z > 3$ ; orange points and  $z > 4$ ; blue points, with associated errors) are plotted in Fig. 2.9 (top panel). In integral

form, the cumulative source distribution is represented by

$$N(> S) = \sum_{i=1}^{N_S} \frac{1}{\Omega_i} \quad (2.3)$$

where  $N(> S)$  is the number of sources with a flux greater than  $S$  and  $\Omega_i$ , is the limiting sky coverage associated with the  $i$ th source. The associated error is the variance:

$$\sigma^2 = \sum_{i=1}^{N_S} \left(\frac{1}{\Omega_i}\right)^2 \quad (2.4)$$

The grey shaded area represents an estimate of the maximum and minimum number counts relation at  $z > 3$  obtained by considering three different effects:

- (1) the  $1\sigma$  uncertainty in the sky coverage area for each source using the sky coverage as a function of flux (see Fig. 2.1) and the  $1\sigma$  uncertainty in the flux;
- (2) the 14 sources from C-COSMOS with no-optical detection (seen in the soft band);
- (3) the sources with photometric redshift  $z_{\text{photo}} < 3$  but  $z_{\text{photo}} + \sigma_{z_{\text{photo}}} > 3$ .

To compute the upper boundary of the shaded area, we included all the sources in the main sample plus the sources with no optical detection at their flux+ $1\sigma$  error. For the lower boundary, we used the flux- $1\sigma$  error only for the sources with  $z_{\text{spec}} > 3$ . Under these assumptions, the lower limit corresponds to the (very unlikely) hypothesis that all the photometric redshifts are overestimated, while the upper limit corresponds to the assumption that non-detection in the optical band is a 100 per cent reliable proxy of high redshift in X-ray-selected samples.

I have compared the number counts of this work with previous X-ray surveys that span the range from deep, small area (CDF-S, at 464.5 arcmin<sup>2</sup> with a soft band flux limit of  $\sim 9.1 \times 10^{-18}$  erg cm<sup>-2</sup> s<sup>-1</sup>, Xue et al., 2011), to moderate area and moderate depth (C-COSMOS at 0.9 deg<sup>2</sup> with a 0.5-2 keV flux limit of  $\sim 1.9^{-16}$  erg cm<sup>-2</sup> s<sup>-1</sup>, Elvis et al., 2009) and finally to moderate area and shallower depth (XMM-COSMOS, at 2 deg<sup>2</sup> and a soft band flux limit of  $\sim 1.7 \times 10^{-15}$  erg cm<sup>-2</sup> s<sup>-1</sup>, Cappelluti et al., 2009). The binned  $\log N - \log S$  relations are plotted in Fig. 2.9 (top panel), together with the XMM-COSMOS (Brusa et al., 2009, open circles), C-COSMOS (Civano et al., 2011, open squares) and 4 Ms CDF-S number counts (Vito et al., 2013, filled triangles).

Good agreement exists among the comparison surveys presented here. At  $z > 3$  and fainter X-ray fluxes ( $S_{0.5-2\text{keV}} < 2 \times 10^{-15}$  erg cm<sup>-2</sup> s<sup>-1</sup>) our points confirm the agreement with the model predictions, previously found by Brusa et al. (2009); Civano et al. (2011); Vito et al. (2013). At the same redshift range but brighter X-ray fluxes, where only the XMM-COSMOS sample has available points (Brusa et al., 2009) based on 4 sources, we

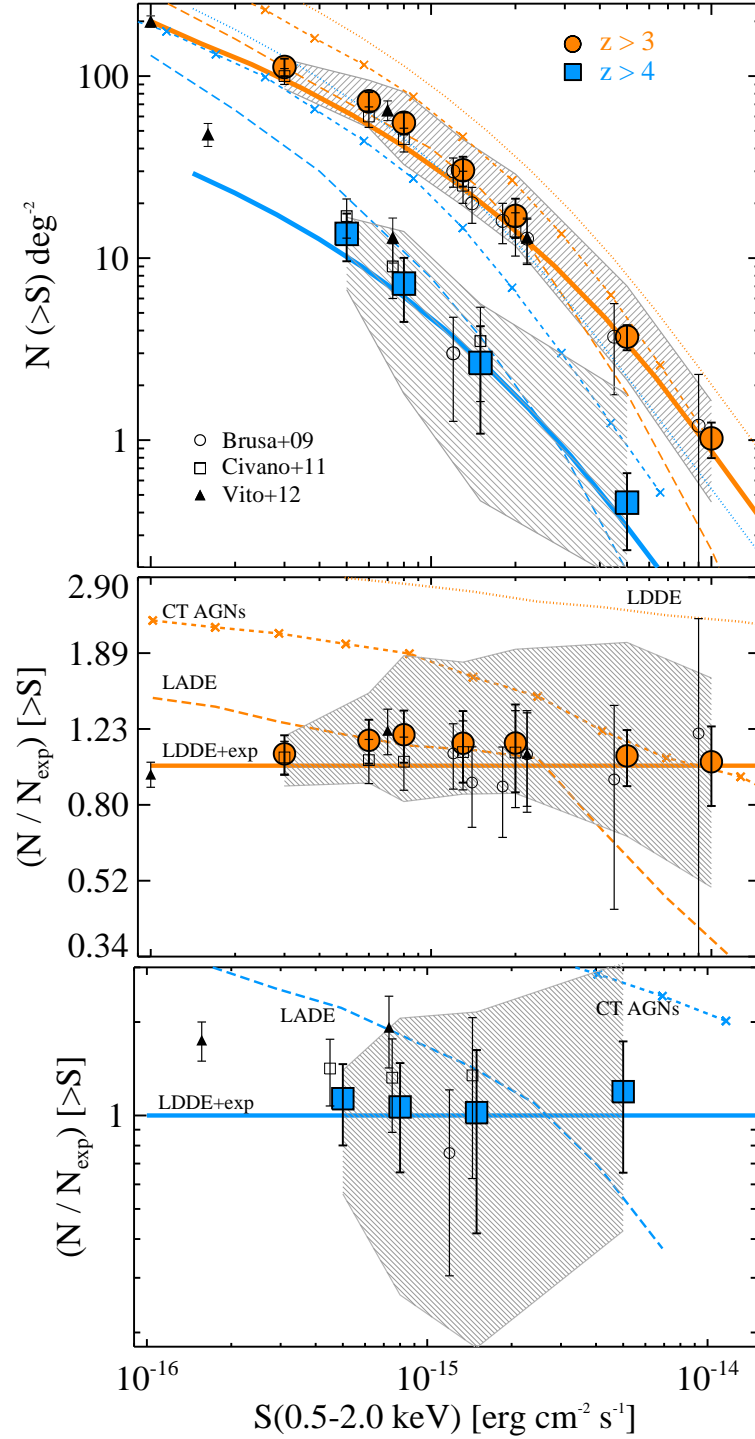


FIGURE 2.9: Top: The binned  $\log N - \log S$  relation of the  $z > 3$  (orange circles) and  $z > 4$  (blue squares) QSOs population. The grey shaded area represents the maximum and minimum number counts under the assumptions described in Section 2.4. The blue and orange curves correspond to the prediction based on the LDDE+exp (thick solid), LDDE (dotted), LADE (dashed) and CT AGNs (dash cross) models for each redshift range, respectively. The small open circles represents the number counts estimated by [Brusa et al. \(2009\)](#), the small open squares are from [Civano et al. \(2011\)](#) and small filled triangles from [Vito et al. \(2013\)](#). Middle: The ratio of the observed number counts for  $z > 3$  relative to the LDDE+exp model (thick solid line at the top panel). The thick solid line represents the LDDE+exp model  $N/N_{\text{exp}} = 1$ , the dotted line represents the LDDE, the dashed lines the LADE and the dash cross lines the CT AGNs model, all relative to the LDDE+exp model. Bottom: The ratio of the observed number counts for  $z > 4$  relative to the LDDE+exp model. Symbols are similar to the middle panel. The ratio of the LDDE relative to the LDDE+exp model is  $N/N_{\text{exp}} > 8.0$  and is not presented.

reduce the uncertainties by a factor of 4 using a sample of 66 sources with ( $S_{0.5-2\text{keV}} > 2 \times 10^{-15} \text{ erg cm}^{-2} \text{ s}^{-1}$ ). Notably, it is the first time that data points at the bright end at  $z > 4$  are included. At redshift  $z > 4$ , where the *XMM-COSMOS* sample had only 4 sources, the 4 Ms CDF-S 9 sources and the C-COSMOS 14 sources, the C-COSMOS & ChaMP sample has 27 sources (two to five times larger), making it possible to compare the slope of the counts with models. A comparison with the AGN number counts from three different phenomenological model predictions is also presented in Fig. 2.9 with the different types of curves (orange colour for  $z > 3$  and blue colour for  $z > 4$ ).

The thick solid lines correspond to the predictions of the XRB synthesis model of [Gilli et al. \(2007\)](#), based on the X-ray luminosity function observed at low redshift (e.g. [Hasinger et al., 2005](#)), parametrized with an LDDE and a high redshift exponential decline with the same functional form adopted by [Schmidt et al. \(1995\)](#) ( $\Phi(z) = \Phi(z_0) \times 10^{-0.43(z-z_0)}$  and  $z_0 = 2.7$ ) to fit the optical luminosity function between  $z \sim 2.5$  and 6 ([Fan et al., 2001](#)), corresponding to one  $e$ -folding per unit redshift (hereafter referred to as LDDE+exp).

The dotted curves correspond to the predictions of the LDDE model without the high- $z$  decline ([Gilli et al., 2007](#)), obtained extrapolating to high- $z$  the best-fit parameters of [Hasinger et al. \(2005\)](#).

The dashed line is the LADE model ([Aird et al., 2010](#)) which fits the hard X-ray luminosity function derived by ([Aird et al., 2010](#)) using the 2Ms Chandra Deep Fields and the AEGIS-X (200 ks) survey to probe the faint end ( $L_X < 10^{43} \text{ erg s}^{-1}$ ) and the high- $z$  ( $z \sim 3$ ) range.

The dash-crossed lines correspond to the [Treister et al. \(2009\)](#) X-ray background population synthesis predictions (CT AGNs).<sup>6</sup>

While at  $z > 3$  the two model predictions are very close, at  $z > 4$ , where the models have different slopes, the errors on the data of the previous studies do not allow a firm preference of one of the two models, highlighting the advantage of our sample with respect to previous surveys. In this work I find that the LDDE model without decline ([Gilli et al., 2007](#)) clearly overestimates the observed counts even in the most optimistic scenario (upper boundary) in both the  $z > 3$  and  $z > 4$  redshift ranges. The results for the  $z > 3$  sample (orange colour) are in good agreement with both LDDE+exp (thick solid line) and LADE (dashed line) model predictions but only up to flux  $\sim 2 \times 10^{-15} \text{ erg cm}^{-2} \text{ s}^{-1}$ , where the difference of the two models is  $< 20$  per cent. However, the main advantage of this sample becomes clear at brighter fluxes; the results strongly exclude the LADE model. This is in contrast to previous studies which could not distinguish between the two models due to their large uncertainties.

At  $z > 4$  (blue colour) the observations are in good agreement with LDDE+exp predictions. The LADE model can not be clearly excluded if we take into account the upper

<sup>6</sup>Model predictions from the work of [Treister et al. \(2009\)](#) for a range of input values are publicly available at [http://agn.astroudec.cl/j\\_agn/main.html](http://agn.astroudec.cl/j_agn/main.html)

and lower boundaries. However, I can point out for the first time that there is no sign of the expected decline to higher fluxes. LDDE is fully ruled out at  $z > 4$ . While fainter samples would be also useful for a better description of the model, considering only the  $z > 4$  subsample by Vito et al. (2013) (4 Ms CDF-S, filled triangles), the data lie between the LDDE+exp and LADE models prediction. Vito et al. (2013) have included the presence of 3 sources at  $5 < z < 7.7$ , whose redshifts are determined on the basis of relatively uncertain photometric information. If these sources were placed at  $3 < z < 4$ , a good agreement would be obtained with the LDDE+exp model (see Vito et al., 2013, fig. 9). In this case, the Vito et al., 2013  $z > 4$  sample would be consisted only by two sources.

## 2.5 2-10 keV Comoving space density

To investigate the cosmological evolution of AGN at  $z > 3$  I calculate the comoving space density from our sample utilizing the  $1/V_{\max}$  method (Schmidt & Olsen, 1968). This method takes into account the fact that more luminous objects are detectable over a larger volume and is readily adapted to the case in which the survey area depends on flux.

The maximum available volume, over which each source can be detected, was computed by using the formula:

$$V_{\max} = \int_{z_{\min}}^{z_{\max}} \Omega(f(L_X, z, N_H)) \frac{dV}{dz} dz \quad (2.5)$$

where  $\Omega(f(L_X, z, N_H))$  is the sky coverage at the flux  $f(L_X, z)$  corresponding to a source with absorption column density  $N_H$  and observed luminosity  $L_X$ , and  $z_{\max}$  is the maximum redshift at which the source can be observed at the flux limit of the survey. If  $z_{\max} > z_{\text{up,bin}}$ , where  $z_{\text{up,bin}}$  is the maximum redshift of the redshift bin, then the  $z_{\max}$  is the upper boundary of the redshift bin used for computing  $V_{\max}$ . In the case of the ChaMP sample,  $z_{\max}$  is estimated using both the X-ray and optical survey limits and is selected to be the minimum of the two estimates so the source can be observed at the flux limit of both surveys. I computed the space density using the luminosities derived with  $\Gamma = 1.8$ . The contribution of sources with photometric redshift to the space density is weighted for the fraction of their  $P(z)$  at  $z > 3$ .

After calculating the  $V_{\max}$  for each source, we sum the reciprocal values in each redshift bin:

$$\phi = \sum_{i=1}^{z_{\min} < z < z_{\max}} \left( \frac{1}{V_{\max,i}} \right) \quad (2.6)$$

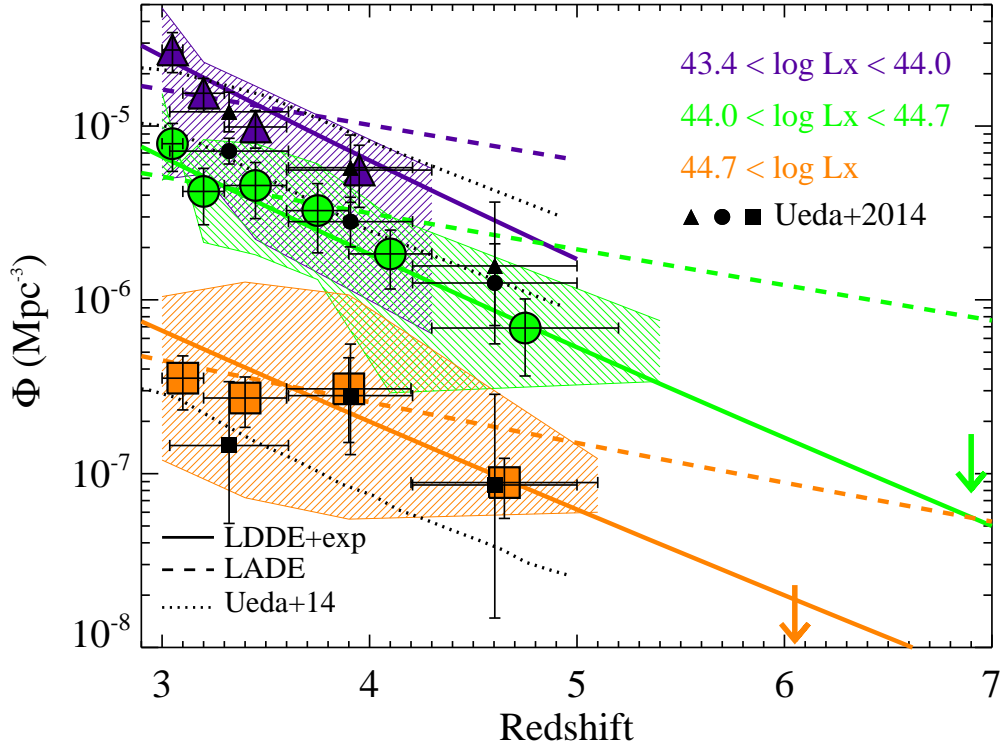


FIGURE 2.10: The comoving space density in 3 different 2-10 keV X-ray luminosity ranges. The solid lines corresponds to the X-ray selected AGN space density computed for the same luminosity limit from the [Gilli et al. \(2007\)](#) LDDE+exp model. The dashed curve corresponds to the space density derived from the LADE model of [Aird et al. \(2010\)](#). The colours respond to the shaded areas in Fig. 2.5 and the shaded area represents the maximum and minimum space density under the assumptions described in the text. When only one source is included in the bin it has been plotted as an upper limit (at  $3\sigma$ ). The small black symbols and dotted lines correspond to the comoving space density data points and model derived from [Ueda et al. \(2014\)](#) for similar X-ray luminosity ranges.

where  $\phi$  is the comoving space density in the range  $z = z_{\min} - z_{\max}$ , and  $i$  is the index of the sample AGN falling into the redshift bin. The  $1\sigma$  uncertainty is estimated as

$$\sigma\phi = \sqrt{\sum_{i=1}^{z_{\min} < z < z_{\max}} \left(\frac{1}{V_{\max,i}}\right)^2}. \quad (2.7)$$

Including soft, hard and full band detected sources allows us to compute a space density which takes into account both unobscured sources, which emit more at softer energies, and obscured sources, which emit more at harder energies, without having to introduce any further correction or assumption.

The resulting comoving space densities are shown in Fig. 2.10. To reduce the effects of incompleteness and to have a complete sample over a given redshift range, I divided the sample into three luminosity intervals (see Fig. 2.5, shaded areas):

- (1) At low luminosities (purple shading), I computed the space density in three redshift bins ( $z = 3 - 4.3$ ) at  $43.3 < \log(L_X/\text{erg s}^{-1}) \leq 44.0$ ;
- (2) At intermediate luminosities (green shading), I computed the space density in 3 redshift bins ( $z = 3 - 5.4$ ) at  $44.0 < \log(L_X/\text{erg s}^{-1}) \leq 44.7$
- (3) At high luminosities (orange shading), I computed the space density in 5 redshift bins ( $z = 3 - 5.0$ ) at  $\log(L_X/\text{erg s}^{-1}) > 44.7$ .

I also estimated space density upper and lower boundaries by taking into account the X-ray flux errors. If a source has been excluded from the main sample because its flux is lower than the flux limit applied, the same source could be included in the upper boundary sample if its flux+ $1\sigma$  error exceeds the flux limit. Likewise, if a source has been included in the main sample because its flux is higher than the flux limit applied, the same source could be excluded by the lower boundary sample if its flux- $1\sigma$  error is lower than the flux limit. The shaded areas include the above uncertainties affecting the computation of the space density, i.e. the flux errors and thus errors on the maximum volume associated to each source.

As explained in Section 2.2.1, the 15 sources with no optical band detection from C-COSMOS survey have not been included in the space density boundaries. However, the space density was computed assuming that all the 15 sources were at the redshift corresponding to the first bin, then to the second bin and so on. The space density values computed in this case, in the first three bins, are within the shaded areas.

The space density in the three luminosity ranges is compared with the predictions, at the same luminosity threshold, from the same three models discussed in Section 2.4. The LDDE+exp model (Gilli et al., 2007) used for the  $\log N - \log S$  (solid lines), including in the model all the sources up to a column density of  $10^{25} \text{cm}^{-2}$ . I also compare with the LADE model (Aird et al., 2010, dashed line). The LDDE model is fully ruled so it is not included in the following comparisons. In agreement with the results obtained from the number counts, the LDDE+exp model provides an excellent representation of the observed data, although the LADE model cannot be rejected taking into account the upper and lower boundaries. I confirm that the shape of the space density evolution of X-ray selected luminous AGN is consistent with that derived from optical quasar surveys within current uncertainties.

The results from the Ueda et al. (2014) for AGNs with the same X-ray luminosity ranges are also plotted for comparison (small black symbols). As can be seen, our results are consistent with those of Ueda et al. (2014) within the statistical errors, indicating a significant decline in the AGN space density from  $z = 3$  to higher redshifts. To take into account the observed decline in their LDDE model (Fig. 2.10, black dotted lines), Ueda et al. (2014) introduced another (luminosity-dependent) cutoff redshift above which the model declines. Their model indicates an ‘up-sizing’ evolution instead of the global ‘downsizing’ evolution, where

more luminous AGN have their number density peak at higher redshifts compared with less luminous ones. In the cases of lower and intermediate X-ray luminosities the Ueda et al. (2014) LDDE model slightly overestimates our results but it is within the upper boundaries. In the case of the higher X-ray luminosities, where our data significantly reduce the uncertainties of the Ueda et al. (2014) sample, their model underestimates our result while our data may indicate a flattening up to redshift  $z \sim 4$ .

### 2.5.1 Type-1 vs Type-2 AGN

Comparing the high- $z$  evolution of optical- and X-ray-selected AGN samples, the same declining profile has been revealed. Considering that X-ray-selected samples provide reduced obscuration bias in comparison with optically selected AGN, this similarity suggests no significant cosmological evolution of the obscured AGN fraction at least at higher redshifts. Supporting these results, previous studies have concluded that the obscured AGN fraction increases with redshift  $z = 1$  to  $z = 2$  (Ballantyne et al., 2006) but decreases at higher redshifts (Hasinger, 2008). To investigate further the cosmological evolution of type-1 and type-2 AGN and their fraction within the redshift range of  $z = 3 - 7$ , I calculate the comoving space density for the two sub-classes of AGNs in our sample following the same method as described in Section 2.5.

The co-moving space density is shown in Fig. 2.11. The upper and lower boundaries are estimated similarly to Section 2.5 taking into account the X-ray flux errors and the 15 C-COSMOS source with no optical band detection. Both optical (large symbols) and X-ray (small symbols) AGN classifications have been used and they seem to be in a good agreement. To estimate the upper and lower boundaries, we also take into account the  $\sim 29$  per cent of mismatches into the optical and the X-ray classification of AGN types, in order to estimate the upper and lower boundaries. Specifically, in the case of optically classified type-1 AGN, for the upper boundary I also include in each bin the sources classified as unobscured ( $N_{\text{H}} < 10^{22} \text{cm}^{-2}$ ) even if they are defined as type-2 AGN based on their optical classification. For the lower boundary, we exclude from each bin the type-1 AGN which have  $N_{\text{H}} > 10^{22} \text{cm}^{-2}$ . The same method is also applied for the type-2 AGN. So, the upper and lower boundaries include also the uncertainties due to the misclassification of sources.

The space density in the three luminosity ranges is compared with the predictions, at the same luminosity threshold, from the same LDDE+exp Gilli et al. (2007) model, including in the model all the sources with  $N_{\text{H}} \leq 10^{22} \text{cm}^{-2}$  for the case of type-1 AGN and all the sources with  $N_{\text{H}} = 10^{22} - 10^{24} \text{cm}^{-2}$  for the case of type-2 AGN. In agreement with the previous results, the LDDE+exp model provides an excellent representation of both type-1 and type-2 AGN. Since both type-1 and type-2 AGN follow the same decline profile it suggests that there is no significant cosmological evolution for their fraction above  $z > 3$ . The same results are obtained even if I follow the X-ray classification of the AGN sample

into obscured and unobscured sources (Fig. 2.11, small black symbols).

The LDDE+exp model for these three luminosity ranges and the  $N_{\text{H}} = 10^{22} \text{cm}^{-2}$  division predicts a fraction of objects classified as type-2 over the type-1 AGN sources of 0.63, 0.5 and 0.48 at low luminosities  $43.3 < \log(L_{\text{X}}/\text{erg s}^{-1}) \leq 44.0$ , intermediate luminosities  $44.0 < \log(L_{\text{X}}/\text{erg s}^{-1}) \leq 44.7$  and high luminosities  $\log(L_{\text{X}}/\text{erg s}^{-1}) > 44.7$  respectively. For the same luminosity bins, I have calculated the mean co-moving space density ratio for the two types  $\Phi_{\text{type2}}/\Phi_{\text{type1}} = 0.59 \pm 0.02, 0.48 \pm 0.04$  and  $0.31 \pm 0.18$  from low to high luminosities. These are in good agreement with the LDDE+exp model predictions.

Recently, [Hiroi et al. \(2012\)](#) estimated the X-ray type-2 AGN fraction, classified based on the  $N_{\text{H}} > 10^{22} \text{cm}^{-2}$  criterion, to be  $0.54_{-0.19}^{+0.17}$  at  $z = 3.0 - 5.0$  and in the luminosity range of  $\log(L_{\text{X}}/\text{erg s}^{-1}) = 44.0 - 45.0$  while for their optical selection of type-2 AGN they found a fraction of  $0.59 \pm 0.09$ . Their estimates are somewhat larger than our result of  $0.48 \pm 0.04$ , although they agree within the errors. This difference could be easily explained from the fact that their sample is significantly smaller (30 sources) than ours and contains only four sources with  $z > 4$  from which the two classified as type-2 AGN have only photometric redshifts.

## 2.6 Summary

I have presented the results of the largest X-ray selected sample of  $z > 3$  AGN to date, compiled from the C-COSMOS and ChaMP surveys. The large body of C-COSMOS and ChaMP data and their combination allowed us to devise a robust method to build a sizable sample of X-ray selected AGN and control the selection effects including both type-1 (unobscured) and type-2 (obscured) AGN, at  $z > 3$ . The sample consists of 209 detections in the soft and/or hard and/or full band. I find:

(1) The average HR of the type-1 and type-2 AGN samples is consistent with the  $N_{\text{H}} < 10^{22} \text{cm}^{-2}$  criterion for the classification of the X-ray unobscured AGN and the  $N_{\text{H}} > 10^{22} \text{cm}^{-2}$  criterion for the classification of the X-ray obscured AGN, respectively.

(2) For the individual sources there is a mis-match of  $\sim 26$  per cent between optical and X-ray classification. The contribution from starburst emission in the soft band, or misclassification of faint type-1 with strong optical/IR contamination from host galaxy light could possibly explain the differences between the two classifications.

(3) The number counts derived in this work (Fig. 2.9) are consistent with previous determinations from the literature, yet significantly reduce the uncertainties especially at bright fluxes and at high redshifts ( $z > 4$ ). The number counts of the combined C-COSMOS/ChaMP sources are consistent with the trend that the space density significantly declines at higher redshifts, similarly to *XMM-COSMOS* ([Brusa et al., 2009](#)) and C-COSMOS ([Civano et al., 2011](#)) results at similar fluxes at least within their errors and CDF-S ([Vito et al., 2013](#)) at fainter fluxes, and are better described by the LDDE+exp model ([Gilli et al., 2007](#)).

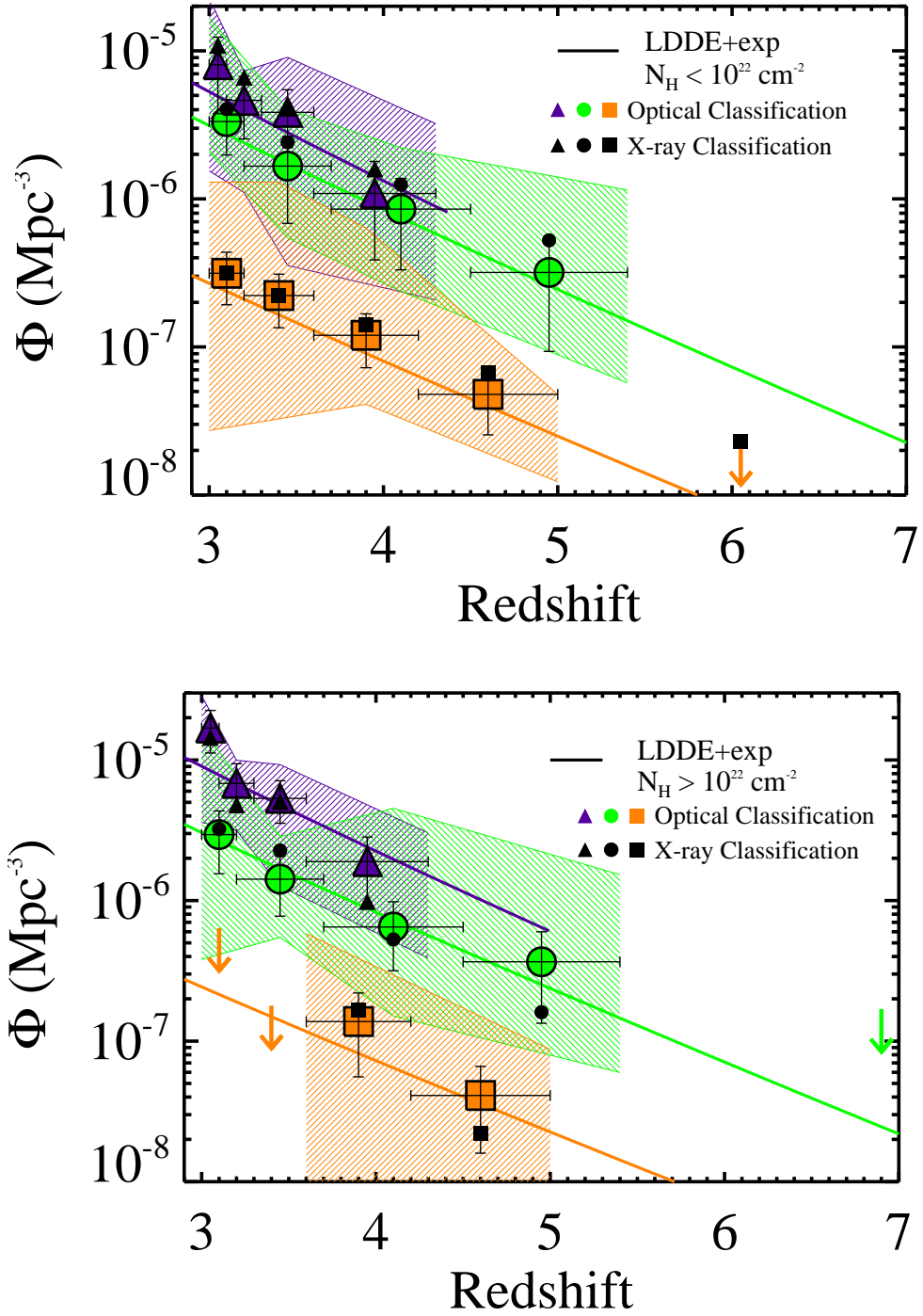


FIGURE 2.11: The comoving space density in 3 different 2-10 keV X-ray luminosity ranges for type-1 (top) and type-2 (bottom) AGN. The solid lines corresponds to the X-ray selected AGN space density computed for the same luminosity limit from the [Gilli et al. \(2007\)](#) model and for  $N_{\text{H}} \leq 10^{22} \text{ cm}^{-2}$  in the case of type-1 AGN and  $N_{\text{H}} > 10^{22} \text{ cm}^{-2}$  for type-2 AGN. The colours respond to the shaded areas in Fig. 2.5 and the shaded area represents the maximum and minimum space density under the assumptions described in Section 2.5. The small black symbols represent the comoving space density in the three different 2-10 keV X-ray luminosity ranges for sources classified as unobscured (top) and obscured (bottom) AGN based on the X-ray classification and the  $N_{\text{H}} = 10^{22} \text{ cm}^{-2}$  limit.

In contrast to the previous studies, and due mainly to the large sample and wide flux coverage, the results of this work exclude the [Aird et al. \(2010\)](#) LADE model, at the brighter fluxes. At fluxes  $2 \times 10^{-16} \leq (F_{0.5-2 \text{ keV}} / \text{erg cm}^{-2} \text{ s}^{-1}) \leq 2 \times 10^{-15}$  the predictions of this model are very similar to the [Gilli et al. \(2007\)](#) LDDE+exp model, but at fainter and brighter fluxes the two models deviate significantly. The [Vito et al. \(2013\)](#) results trace the [Gilli et al. \(2007\)](#) LDDE+exp model well at fainter fluxes, but only for  $z > 3$ , while my sample gives the same results at the brighter fluxes where (due to the low expected counts) a large sample is required.

(4) In agreement with the number counts, the space density is well described with the LDDE+exp model at all X-ray luminosity bins and redshifts, while the LADE model fails to fit the data. These results confirm the declining space density as observed in the optical wavelengths.

(5) Taking into account both optical and X-ray classifications, I derived the space density for type-1 and type-2 (obscured and unobscured) AGN separately. In both cases, the results are in agreement with the LDDE+exp model suggesting that the high-redshift evolution of obscured AGNs is similar to that of unobscured AGN. For each luminosity bin, I derived the type-2 AGN fraction among the total AGN sample to be  $0.59 \pm 0.02$ ,  $0.48 \pm 0.04$  and  $0.31 \pm 0.18$  at  $z > 3$  in the luminosity ranges of  $L_X = 10^{43.3-44.0}$ ,  $10^{44.0-44.7}$ ,  $10^{44.7-46.0} \text{ erg s}^{-1}$ .

The last result should have a significant impact on our understanding of the galaxy and black hole co-evolution. Either or both line-of-sight orientation or evolutionary phase (e.g. covering factor of high column obscuration) can affect the apparent obscuration (and therefore classification) of AGN. Given that orientation does not evolve preferentially towards us, this work allows us to say that the obscured and unobscured evolutionary phases do evolve similarly.

*Who knows, perhaps God is simply the search for God.*

[Saint Francis (1956)] - Nikos Kazantzakis

# 3

## *Herschel-ATLAS: Far-infrared properties of radio-loud and radio-quiet quasars*

This chapter is partly reproduced from the paper *Herschel-ATLAS: Far-infrared properties of radio-loud and radio-quiet quasars* by **E. Kalfountzou**, J. Stevens, M.J. Jarvis, M.J. Hardcastle, D.J.B. Smith, N. Bourne, L. Dunne, E. Ibar, S. Eales, R. J. Ivison, S. Maddox, M.W.L. Smith, E. Valiante, G. de Zotti, 2014, MNRAS, 442, 1181

### **Abstract**

I have constructed a sample of radio-loud and radio-quiet quasars from the Faint Images Radio Sky at Twenty-one centimetres (FIRST) and the Sloan Digital Sky Survey Data Release 7 (SDSS DR7), over the H-ATLAS Phase 1 Area ( $9^h$ ,  $12^h$  and  $14.5^h$ ). Using a stacking analysis I find a significant correlation between the FIR luminosity and 1.4-GHz luminosity for RLQs. Partial correlation analysis confirms the intrinsic correlation after removing the redshift contribution while for RQQs no partial correlation is found. Using a single-temperature grey-body model we find a general trend of lower dust temperatures in the case of RLQs comparing to RQQs. Also, RLQs are found to have almost constant mean values of dust mass along redshift and optical luminosity bins. In addition, I find that RLQs at lower optical luminosities tend to have on average higher FIR and 250- $\mu\text{m}$  luminosity with respect to RQQs with the same optical luminosities. Even if a two-temperature grey-body model is used to describe the FIR data, the FIR luminosity excess remains at lower optical luminosities. These results suggest that powerful radio jets are associated with star formation especially at lower accretion rates.

### 3.1 Unveiling the role of jets to the AGN/star-formation connection

In recent years it has been widely believed that AGN activity is an important phase in the evolution of every massive galaxy in the universe. Studying the optical spectra of powerful high-redshifts QSOs in the previous chapter, we found direct evidences of the AGN outflows impact to the host galaxy absorption line signatures. In the same sense, there are a number of pieces of evidence that support a global evolutionary connection between the star formation and AGN activity e.g.:

1. the differential redshift evolution of the AGN luminosity function, or “AGN downsizing” is also found for the star-forming galaxy population (e.g. [Hasinger et al., 2005](#); [Hopkins et al., 2006](#); [Aird et al., 2010](#)),
2. the redshift distribution of the most strongly star-forming galaxies traces that seen in the optical quasar population (e.g. [Chapman et al., 2005](#); [Wardlow et al., 2011](#)), and
3. the star formation rate density as a function of redshift is broadly similar with the black hole accretion rate density (e.g. [Boyle & Terlevich, 1998](#); [Merloni, 2004](#); [Aird et al., 2010](#)).

In the literature, there are several examples, particularly at  $z \approx 1$ , close to the peak of the AGN luminosity density in the Universe (e.g. [Barger et al., 2005](#); [Hasinger et al., 2005](#)), of “composite” objects where the AGN activity and star formation are associated (e.g. [Page et al., 2004](#); [Alexander et al., 2005](#)). However, the picture is still not clear, with investigations at different wavelengths producing many differences of opinion as to the amount of radiation that is absorbed and reprocessed by dust, how this is related to the host galaxy and whether the triggering mechanism behind the AGN activity is also responsible for massive star-formation activity. Moreover, it is also unclear how these processes depend on luminosity, radio-loudness and orientation.

As I have already described in more details in Chapter 1, a large number of theoretical models suggests that these possible correlations arise through feedback processes between the galaxy and its accreting BH. Such regulation has been shown to be important in large cosmological simulations (e.g. [Di Matteo et al., 2005](#); [Springel et al., 2005](#); [Croton et al., 2006](#)). In general, these can take two forms, AGN-winds (often referred to as quasar mode), which comprise wide-angle, sub-relativistic outflows and tend to be driven by the radiative output of the AGN, and jets (often referred to as radio mode), which are relativistic outflows with narrow opening angles that are launched directly from the accretion flow itself. In the case of quasar mode, the objects are accreting rapidly, at near their Eddington rate and their radiation can couple to the gas and dust in the interstellar medium, driving winds that may shut down

further accretion on to the BH or even drive material out of the galaxy, thereby quenching star formation (e.g. [Di Matteo et al., 2005](#)). Although there is no compelling evidence for AGN feedback quenching star formation, there is mounting evidence for quasar-driven outflows (e.g. [Maiolino et al., 2012](#)). However, recent surveys find little evidence that X-ray-luminous AGN quench star formation ([Harrison et al., 2012](#), cf. [Page et al., 2012](#)). Similarly, the radio mode and the role of RLAGN and their jets in the evolution of galaxies have been studied intensively suggesting that jets can have positive as well as negative feedback on SFRs with the observational consensus being mixed. Certainly, some studies advocate that radio jets effectively suppress or even quench star formation (e.g. [Best et al., 2005](#); [Croton et al., 2006](#); [Best & Heckman, 2012](#); [Chen et al., 2013](#); [Karouzos et al., 2014](#)) by warming-up and ionizing the ISM which leads to less efficient star formation, or through direct expulsion of the molecular gas from the galaxy, effectively removing the ingredient for stars to form (e.g. [Nesvadba et al., 2006, 2011](#)). On the other hand, positive feedback can enhance star formation which could be explained by shocks driven by the radio jets in the ISM that compress it and eventually lead to enhanced star-formation efficiency (e.g. [Silk & Nusser, 2010a](#); [Best & Heckman, 2012](#); [Gaibler et al., 2012](#); [Kalfountzou et al., 2012](#)).

It is therefore apparent, that although some form of feedback is needed to explain the observational results supporting co-evolution of central spheroids and their galaxies, much still remains unclear. Radio-loud and radio-quiet quasars provide ideal candidates for the study of star formation in powerful AGN under the presence of jets or otherwise. Indeed, optically selected RLQs are found to have enhanced star formation at lower luminosities using optical spectral feature as a diagnostic ([Kalfountzou et al., 2012](#)). The latter result raises the question of why such an effect is not seen at high radio power and/or AGN activity which could be explained under the assumption of a dominant mechanical feedback at low Eddington luminosities, in which case this would plausibly be the major source of positive feedback.

However, spectral diagnostics are not immune to AGN contamination and optical diagnostics, in particular, are susceptible to the effects of reddening. Indeed, the measurement of the star-formation activity in the host galaxy is difficult, mainly due to contamination by the AGN. Many studies have attempted to determine the star-formation activity in quasar host galaxies using optical colours (e.g. [Sánchez et al., 2004](#)) or spectroscopy (e.g. [Trichas et al., 2010](#); [Kalfountzou et al., 2011](#); [Trichas et al., 2012](#)) or X-ray selection (e.g. [Comastri et al., 2003](#); [Treister et al., 2011](#)). In addition, AGN emission can outshine both the UV and optical emission from young stars. By contrast, the FIR emission is shown to be dominated by emission from dust in the host galaxy, except in the most extreme cases (e.g. [Netzer et al., 2007](#); [Mullaney et al., 2011b](#)), and to be a proxy of its star formation activity that is largely uncontaminated by the AGN (e.g. [Haas et al., 2003](#); [Hatziminaoglou et al., 2010](#)).

### 3.1.1 Radio-loud and radio-quiet quasars

A property of quasars is the existence of radio-loud and radio-quiet populations (see Section 1.3.3 for definition). Typically, optically selected RLQs are only a small fraction,  $\sim 10$ -20 per cent, of all quasars (e.g. Ivezic et al., 2002 but see also Richards et al., 2006a with a small radio-loud fraction of 3 per cent), with this fraction possibly varying with both optical luminosity and redshift (Jiang et al., 2007). In contrast, X-ray selected samples show lower fractions of radio-loud AGN  $< 5$  per cent (e.g. Donley et al., 2007; La Franca et al., 2010). However, many low-power radio sources in these samples might be star formation-driven (e.g. Massardi et al., 2010). X-ray selections overall probe much higher (or complete) portions of the AGN populations than optical ones. This may affect the comparison of same subsamples (i.e., radio-loud) selected with different methods. RLQs usually reside in very massive galaxies and have typically a lower optical or X-ray output at given stellar mass (i.e. lower  $L/L_{\text{Edd}}$  at given  $L_{\text{Edd}}$ , Sikora et al., 2007) compared to radio-quiet quasars. This means that an  $L_{\text{X}}$ -limited sample will have a lower RLQs fraction, compared to a mass-limited sample. However, in the case of a strictly limited selection of X-ray-Type I AGN, then possibly the subsamples of radio-loud AGN might end up being more comparable to optical ones.

While a definitive physical explanation of this dichotomy remains elusive, a large number of models have been put forward to explain it. Both types of quasars are likely powered by similar physical mechanisms (e.g. Urry & Padovani, 1995; Shankar, 2010), but their radio loudness has been shown to be anti-correlated with accretion rate onto their central SMBHs (e.g. Fernandes et al., 2011). Additionally, it has been demonstrated that, relative to RQs, RLQs are likely to reside in more massive host galaxies (Kukula et al., 2001; Sikora et al., 2007). However, Dunlop et al. (2003) found that spheroidal hosts become more prevalent with increasing nuclear luminosity such that, for nuclear luminosities  $M_{\text{V}} < -23.5$ , the hosts of both radio-loud and radio-quiet AGN are virtually all massive ellipticals.

Along with the idea of different host galaxies it has been found that RLQs require more massive central BHs than RQs (e.g. Dunlop et al. 2003; McLure & Dunlop 2004; see also Shankar, 2010, who finds this to be redshift dependent) and it has also been suggested that RLQs host more rapidly spinning BHs holes than RQs (e.g. Blandford & Znajek 1977; Punsly & Coroniti 1990; Wilson & Colbert 1995; Sikora et al. 2007; Fernandes et al. 2011; but see also Garofalo et al., 2010). The low radio-loud fraction also suggests a change in jet occurrence rates among active super-massive black holes at low luminosities. This could be linked to changes in the Eddington fraction, evolutionary state of the black hole, or the host galaxy mass, evolutionary state, or environment. Recently, Falder et al. (2010) showed that radio-loud AGN appear to be found in denser environments than their radio-quiet counterparts at  $z \sim 1$ , in contrast with previous studies at lower redshifts (e.g. McLure & Dunlop,

2001). However the differences are not large and may be partly explained by an enhancement in the radio emission due to the confinement of the radio jet in a dense environment (e.g. [Barthel & Arnaud, 1996](#)).

If the radio-loudness is due to the physics of the central engine and how it is fuelled, and the environment plays a relatively minor role, the quasar properties may be connected with the star formation in their host galaxies (e.g. [Herbert et al., 2010](#); [Hardcastle et al., 2013](#)). On the one hand, AGN feedback could be stronger in the case of the RLQs due to their higher BH masses and therefore potentially stronger radiation field, reducing the star-formation rate compared to RQQs; on the other hand radio jets could increase the star-formation activity by compressing the intergalactic medium (e.g. [Croft et al., 2006](#); [Silk & Nusser, 2010b](#)).

### 3.1.2 This work

With the *Herschel* Space Observatory ([Pilbratt et al., 2010](#)) we are able to measure the FIR emission of AGN host galaxies and hence the cool-dust emission. *Herschel* offers an ideal way of measuring the instantaneous SFR of AGN (e.g. [Bonfield et al., 2011](#)). Until *Herschel*, hot dust emission has typically been determined from Spitzer data at near/mid-infrared wavelengths, but emission from the torus can also contribute at these bands, especially in the case of quasars. With *Herschel* we are able to determine the level of cool dust emission in AGN, providing a detailed picture of how the full SEDs of AGN change as a function of luminosity, radio-loudness and redshift. Under these circumstances, *Herschel* provides a good tool to study the star formation and AGN activity in a special type of AGN: quasars. We are also able to study the star formation in different types of quasars (e.g. RLQs vs RQQs) and thus to say how it might be affected by the presence of powerful radio jets.

The chapter is structured as follows. In Section 3.2 I discuss the selection of the sample and the observations I have used. In Section 3.4 I describe the statistical methods and the models I have used in order to estimate the FIR parameters (e.g. FIR luminosity, dust temperature, dust mass) of our sample. Here I also present the results of the comparison of the FIR parameters between the radio-loud and radio-quiet quasars. Finally, in Sections 3.5 and 3.6, I explore the general conclusions that can be drawn from our results.

## 3.2 Sample definition and measurements

### 3.2.1 The data

In this section I describe the data used throughout this chapter.

1. Radio source catalogues and images from the Faint Images of the Radio Sky at Twenty-one centimetres (FIRST; [Becker et al., 1995](#)) survey and NRAO NLA Sky Survey (NVSS; [Condon et al., 1998](#)). Both cover the entire H-ATLAS ([Eales et al., 2010](#))

Phase 1 area. To check the possibility of non-thermal contamination in the *Herschel* bands, I also cross matched our sample with the Giant Metrewave Radio Telescope (GMRT) catalogue of [Mauch et al. \(2013\)](#), who have imaged the majority of the Phase 1 area at 325 MHz, in order to estimate the radio spectral index for the radio-loud sample.

2. Point spread function (PSF) convolved, background subtracted images of the H-ATLAS Phase 1 fields at wavelengths of 100, 160, 250, 350 and 500  $\mu\text{m}$ , provided by the Photodetector Array Camera & Spectrometer (PACS; [Poglitsch et al., 2010](#)) and the Spectral and Photometric Imaging REceiver (SPIRE; [Griffin et al., 2010](#)) instruments on the *Herschel Space Observatory*. The Phase 1 area consists of three equatorial strips centred at  $9^h$ ,  $12^h$  and  $14.5^h$ . Each field is approximately  $12^\circ$  in RA by  $3^\circ$  in Dec ( $6^\circ$  by  $3^\circ$  for the  $12^h$  field). The construction of these maps is described in detail by [Pascale et al. \(2011\)](#) for SPIRE. From these maps, a catalogue of the FIR sources was generated ([Rigby et al., 2011](#))<sup>1</sup>, which includes any source detected at  $5\sigma$  or better at any SPIRE wavelength. PACS fluxes were derived using apertures placed on the maps ([Ibar et al., 2010](#)) at the locations of the 250  $\mu\text{m}$  positions. The  $5\sigma$  point source flux limits are 132, 121, 30.4, 36.9 and 40.8 mJy, with beam sizes ranging from 9 to 35 arcsec FWHM in the 100, 160, 250, 350 and 500  $\mu\text{m}$  bands, respectively.
3. Redshift and optical magnitudes from the Sloan Digital Sky Survey Data Release 7 (SDSS DR7) Quasar Catalogue ([Schneider et al., 2010](#)) which provides the most reliable classification and redshift of SDSS quasars with absolute  $i'$ -band magnitudes brighter than -22.

I constructed a sample of radio-detected quasars in the FIRST field with optical magnitudes and redshifts from SDSS DR7. A matching radius  $r \leq 5$  arcsec is used to identify the compact radio sources while a larger radius of 30 arcsec is used for extended sources ([Kalfountzou et al., 2012](#)). With this method we found 144 quasars with matching radius less than 5 arcsec and 3 extended quasars. In order to check that the radio maps from the FIRST survey do not miss a significant fraction of extended emission around the quasars, I also cross-correlate the optical positions with NVSS. I find no significant difference in the  $R_{1.4\text{GHz}}$  between FIRST and NVSS, with the distribution remaining statistically unchanged. This suggests that the radio emission from the quasars is generally fairly compact.

For the undetected quasars in FIRST I used a stacking analysis to estimate their flux densities following [White et al. \(2007\)](#), where they quantified the systematic effects associated with stacking FIRST images and examined the radio properties of quasars from the SDSS by median-stacking radio maps centered on optical position of these quasars. The stacked flux

---

<sup>1</sup>The cited paper is for the SV data release, but the same processing techniques were used to create the catalogue for the Phase 1 area.

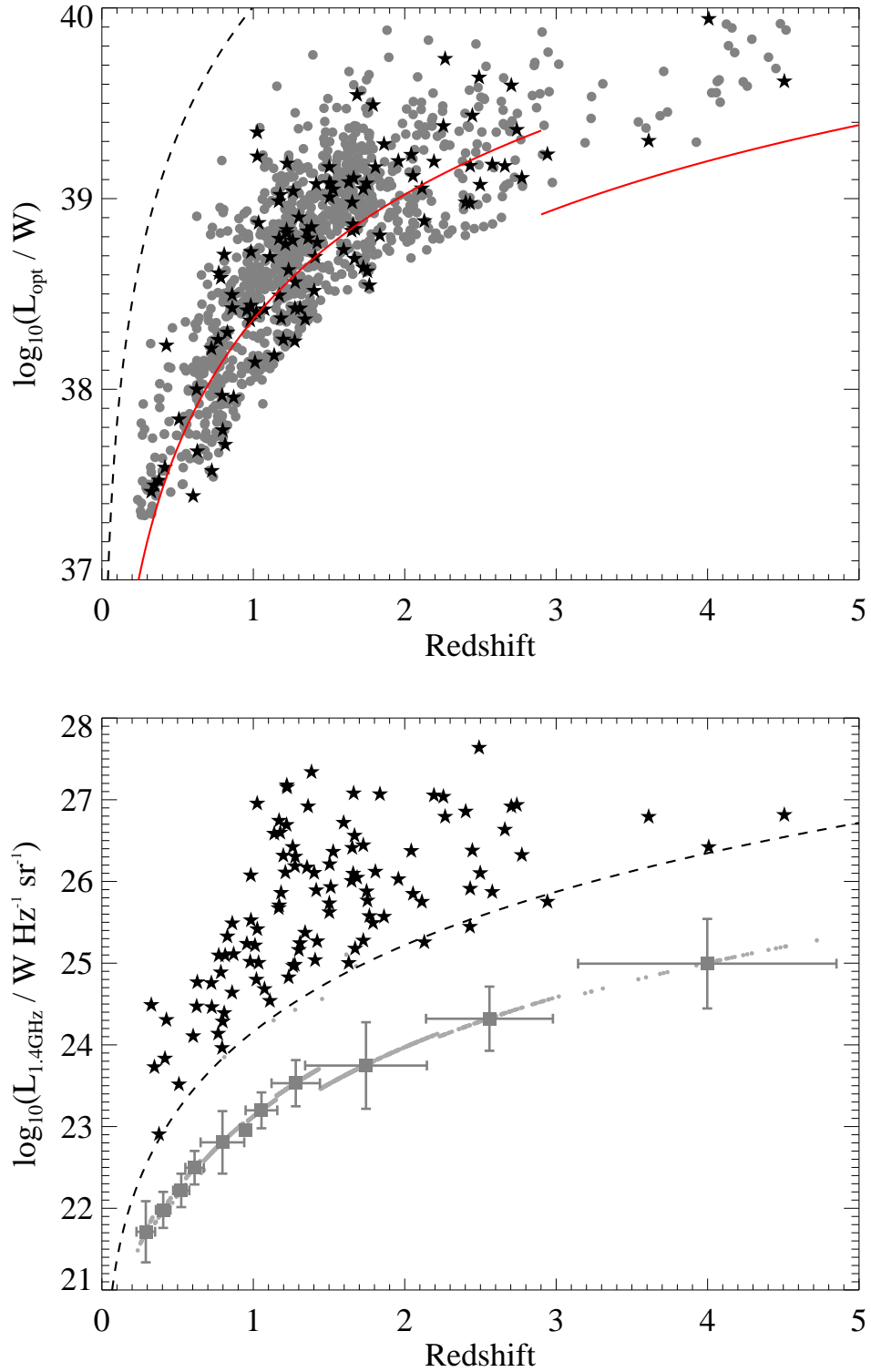


FIGURE 3.1: Left: Optical luminosity of the radio-loud (black stars) and radio-quiet (grey circles) samples as a function of redshift. The red lines show the corresponding  $M_i$  for  $i = 19.1$  ( $z < 2.9$ ) and  $i = 20.2$  ( $z > 2.9$ ), respectively, and the black dashed line shows the equivalent for  $i = 15$  (the bright limit for SDSS quasar targets; Shen et al., 2011a). Right: Radio luminosity as a function of redshift. The mean values and the errors for undetected quasars are represented by large grey circles. The dashed line corresponds to the nominal  $5\sigma$  flux cut-off of FIRST, i.e. 1.0 mJy.

densities sorted by redshift and  $i$ -magnitude for each bin are presented in Fig. 3.2 which shows that the majority of the undetected quasars fall far below the FIRST catalogue detection threshold, but in every bin a clear detection is achieved.

I separated the quasar sample into RLQs and RQQs based on the radio-loudness,  $R_i$ , parameter. The traditional radio-loud/quiet division is taken to be the radio-to-optical flux ratio of 10. In this work, following Ivezić et al. (2002), I compute the radio-to-optical flux ratio,  $R_i$ , using the radio flux density at 1.4 GHz and the  $i$ -band ( $\lambda_i = 7480 \text{ \AA}$ ) flux density from the SDSS.

A total of 1618 quasars (141 radio-loud and 1477 radio-quiet quasars) are found in the H-ATLAS Phase 1 field based on their optical positions. For this sample, we have investigated how many quasars are significantly detected in the H-ATLAS catalogue at the  $5\sigma$  level. Cross-matching with the H-ATLAS Phase 1 Catalogue applying a likelihood ratio technique (Smith et al., 2011) yielded 146 ( $\sim 9$  per cent) counterparts with a reliability  $R > 0.8$ . Among the 146 counterparts 9 are RLQs ( $\sim 7$  per cent of the radio-loud population). A similar percentage was found by Bonfield et al. (2011). Comparing the detected samples of radio-loud and radio-quiet quasars by applying a Kolmogorov-Smirnov (K-S) test gives a null hypothesis of  $p = 0.07$ ,  $p = 0.11$ ,  $p = 0.08$ ,  $p = 0.11$  and  $p = 0.14$  for 100, 160  $\mu\text{m}$  PACS and 250, 350 and 500  $\mu\text{m}$  SPIRE bands.

Since the radio-loud sample includes sources with high radio flux density we also investigated the possibility of synchrotron contamination, which is not associated with star formation, to the FIR flux densities. The method I am using to estimate the synchrotron contamination is described in Section 3.3. I have found that out of the 141 objects in our RLQs sample, 21 RLQs have significant non-thermal contamination in their FIR emission. These objects have been removed from our sample. I have also found that 27 sources are possible candidates for strong contamination using an upper limit for their radio spectral index. These sources have been also removed from the sample.

I then compare the distribution in  $z$  and  $L_{\text{opt}}$  of radio-loud and radio-quiet quasars and force the two subsamples to have the same  $L_{\text{opt}}$  and  $z$  distribution by randomly removing RLQs from our parent sample. Running a K-S test on these samples I find the distribution of the two populations in the optical luminosity - redshift plane is similar. A K-S test applied to the optical luminosity gives a result that corresponds to a probability,  $p = 0.69$  under the null hypothesis (i.e. they are statistically indistinguishable) while the K-S test to the redshift gives  $p = 0.75$ . A 2-d K-S test on the redshift and optical luminosity for both samples returns  $p = 0.58$ . I therefore assume the populations are matched in optical luminosity and  $z$ . This process provides a radio-optical catalogue of quasars with spectroscopic redshift up to  $z \sim 5$ . Fig. 3.1 shows the optical luminosity - redshift and the radio luminosity - redshift plots for the final sample of 93 RLQs and 1007 RQQs. I have randomly removed 470 radio-quiet quasars from our original sample in order to match the two populations into  $z$  and  $L_{\text{opt}}$ .

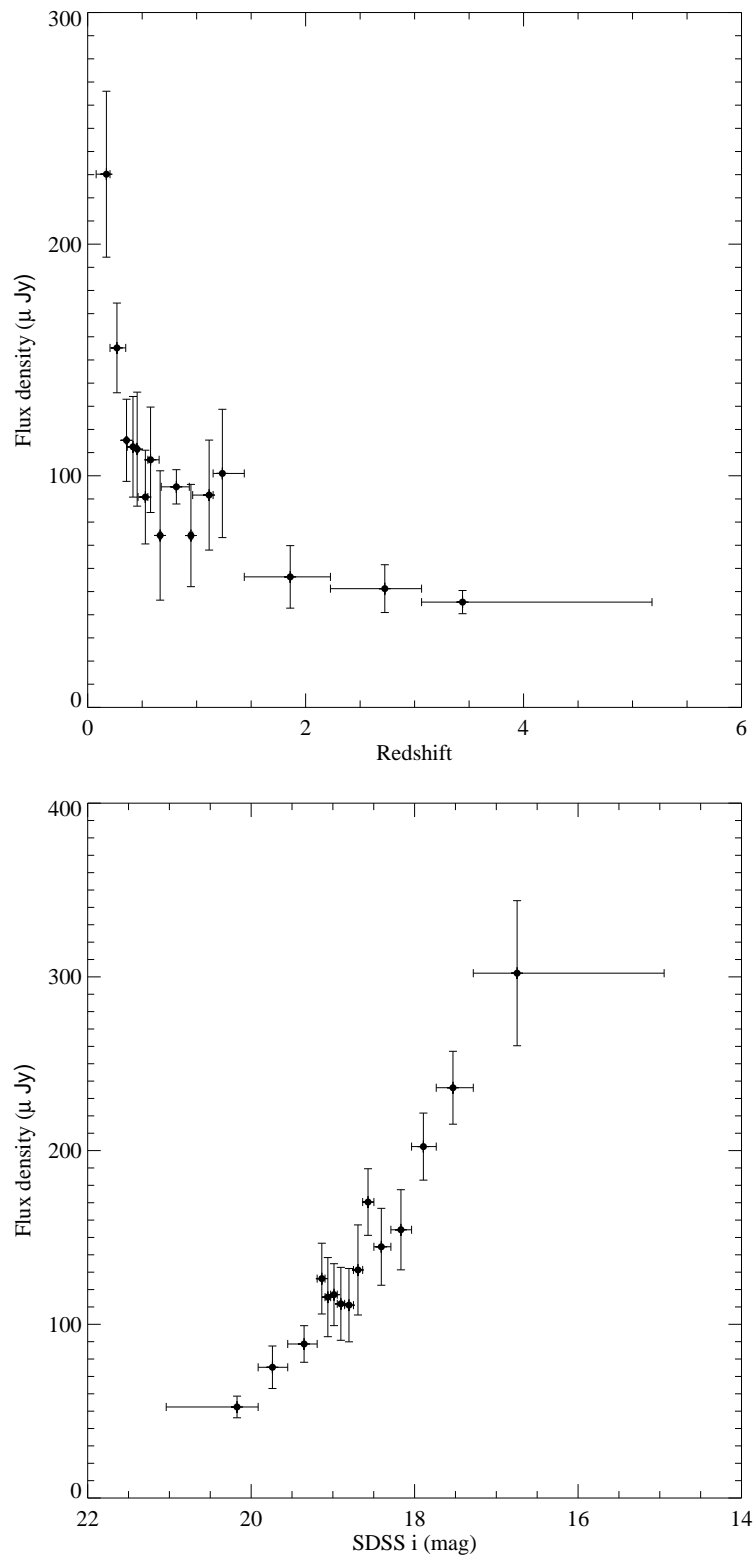


FIGURE 3.2: Left: The median radio flux density as a function of redshift. Right: The median radio flux density as a function of the SDSS  $i$ -magnitude. The  $1\sigma$  associated errors are presented. A bin size of about 100 quasars was used.

The optical luminosity was measured using the *i*-band magnitude since redder passbands measure flux from the part of the spectrum relatively insensitive to recent star formation and also suffer less dust extinction. Since the *i*-band luminosity itself is expected to correlate with the AGN luminosity and is less sensitive to recent star-formation activity we use the optical luminosity as an AGN tracer. The rest-frame 1.4-GHz radio luminosities of the quasars were calculated from the FIRST 1.4-GHz flux density and the spectroscopic redshift, assuming a power law of  $S_\nu \propto \nu^{-\alpha}$ . The spectral index was measured using the FIRST and GMRT data. For the sources undetected by GMRT either a spectral slope of  $\alpha = 0.71$  was used or the estimated spectral index using the nominal 5 mJy limit of the GMRT data (see Section 3.3).

### 3.2.2 *Herschel* flux measurements and stacked fluxes

Due to the limited sample of SPIRE-detected quasars, especially the RLQs, I directly measure the FIR flux densities from the PSF-convolved images for all three H-ATLAS fields rather than just use the  $5\sigma$  catalogues. For each of the quasars found inside the H-ATLAS Phase 1 field I derive the FIR flux densities in the two PACS and the three SPIRE bands directly from the background-subtracted, PSF-convolved H-ATLAS images. We take the flux density to be the value in the image at the pixel closest to the optical position of our targets. The errors are estimated from the centroid of the corresponding noise map including the confusion noise. In addition, the current H-ATLAS catalogue recommends including calibration errors of 10 per cent of the estimated flux for the PACS bands and 7 per cent for the SPIRE bands. The flux densities are background subtracted using a mean background value for each band. The mean background is estimated from 100 000 randomly selected pixels within the three H-ATLAS blank fields.

To establish whether sources in the bins were significantly detected, I compared the flux measurements with the background flux distribution from 100 000 randomly selected position in the fields, following [Hardcastle et al. \(2010\)](#). Using a K-S test, we can examine whether the flux densities are statistically distinguishable from those taken from randomly chosen positions, as a K-S test is not influenced by the non-Gaussian nature of the noise as a result of confusion. I found a distinguishable difference in all bands with K-S probability lower than  $10^{-5}$ . The mean background flux densities are  $0.06 \pm 0.01$ ,  $0.10 \pm 0.02$ ,  $1.12 \pm 0.03$ ,  $2.91 \pm 0.04$  and  $0.51 \pm 0.03$  mJy at 100, 160, 250, 350 and 500  $\mu\text{m}$ , respectively.

I have separated the samples in bins corresponding to redshift, radio luminosity and optical luminosity to investigate whether the FIR fluxes vary with those parameters. Within each bin I have estimated the weighted mean of the FIR background-subtracted flux densities in each *Herschel* band. The mean values for each band are shown in Table 3.1. The errors have been determined by bootstrapping. The bootstrapped errors are determined by randomly selecting galaxies from within each bin and determining the median for this subsample. The K-S test results for the two populations and the Mann-Whitney (M-W) test

TABLE 3.1: The radio-loud and radio-quiet quasars (RLQs and RQQs) FIR mean flux densities in the 100, 160, 250, 350 and 500  $\mu\text{m}$  bandpasses. The two populations have been separated into redshift, radio luminosity and optical luminosity bins. The number of objects within each stack is also given.

Class	$z$ -range	$N$ per bin	Mean flux density (mJy)				
			100 $\mu\text{m}$	160 $\mu\text{m}$	250 $\mu\text{m}$	350 $\mu\text{m}$	500 $\mu\text{m}$
RLQs	0.2 – 1.0	24	$7.9 \pm 1.9$	$7.6 \pm 1.7$	$18.5 \pm 2.2$	$26.9 \pm 4.4$	$20.1 \pm 3.4$
	1.0 – 1.5	30	$8.2 \pm 1.8$	$16.7 \pm 4.2$	$36.8 \pm 2.1$	$40.4.0 \pm 3.9$	$34.2 \pm 3.2$
	1.5 – 2.0	21	$4.1 \pm 1.4$	$7.1 \pm 1.3$	$17.3 \pm 2.3$	$23.0 \pm 2.2$	$18.5 \pm 2.7$
	2.0 – 5.0	18	$2.6 \pm 1.4$	$5.6 \pm 1.9$	$18.3 \pm 2.3$	$23.5 \pm 2.1$	$21.3 \pm 2.8$
RQQs	0.2 – 1.0	264	$7.3 \pm 0.5$	$9.9 \pm 0.7$	$21.2 \pm 1.0$	$20.0 \pm 0.7$	$12.3 \pm 0.6$
	1.0 – 1.5	355	$5.1 \pm 0.6$	$8.2 \pm 1.0$	$20.3 \pm 1.6$	$21.2 \pm 1.0$	$13.7 \pm 0.6$
	1.5 – 2.0	230	$3.9 \pm 0.4$	$9.5 \pm 0.5$	$18.7 \pm 0.8$	$21.2 \pm 0.7$	$14.7 \pm 0.7$
	2.0 – 5.0	158	$4.4 \pm 0.6$	$7.4 \pm 1.2$	$17.59 \pm 1.7$	$22.2 \pm 1.2$	$16.7 \pm 1.0$
Class	$\log_{10}(L_{1.4}/W \text{ Hz}^{-1})$	$N$ per bin	Mean flux density (mJy)				
			100 $\mu\text{m}$	160 $\mu\text{m}$	250 $\mu\text{m}$	350 $\mu\text{m}$	500 $\mu\text{m}$
RLQs	23.0 – 25.0	20	$9.7 \pm 1.7$	$9.2 \pm 2.5$	$19.9 \pm 3.3$	$27.4 \pm 3.1$	$20.1 \pm 2.7$
	25.0 – 26.0	35	$3.1 \pm 1.6$	$8.8 \pm 1.4$	$23.6 \pm 2.3$	$27.4 \pm 2.2$	$18.2 \pm 1.9$
	26.0 – 27.0	30	$6.8 \pm 1.3$	$12.8 \pm 3.6$	$26.4 \pm 5.3$	$33.5 \pm 6.1$	$30.9 \pm 8.3$
	27.0 – 28.5	8	$7.5 \pm 2.3$	$7.2 \pm 3.4$	$28.1 \pm 4.0$	$31.3 \pm 4.2$	$36.9 \pm 5.3$
RQQs	21.0 – 23.0	228	$7.4 \pm 0.6$	$9.7 \pm 0.7$	$20.9 \pm 1.1$	$19.4 \pm 0.7$	$11.8 \pm 0.6$
	23.0 – 23.5	249	$5.3 \pm 0.8$	$8.6 \pm 1.3$	$20.4 \pm 2.1$	$21.1 \pm 1.3$	$13.7 \pm 0.8$
	23.5 – 24.0	378	$4.3 \pm 0.3$	$8.9 \pm 0.4$	$18.8 \pm 0.7$	$21.3 \pm 0.6$	$14.5 \pm 0.5$
	24.0 – 25.5	152	$4.5 \pm 0.7$	$7.6 \pm 1.2$	$19.1 \pm 1.8$	$22.5 \pm 1.2$	$16.9 \pm 1.1$
Class	$\log_{10}(L_{\text{opt}}/W)$	$N$ per bin	Mean flux density (mJy)				
			100 $\mu\text{m}$	160 $\mu\text{m}$	250 $\mu\text{m}$	350 $\mu\text{m}$	500 $\mu\text{m}$
RLQs	37.3 – 38.5	31	$6.8 \pm 1.7$	$12.2 \pm 2.2$	$23.4 \pm 3.0$	$28.2 \pm 2.7$	$20.1 \pm 2.3$
	38.5 – 39.0	32	$7.2 \pm 1.5$	$9.9 \pm 3.7$	$19.5 \pm 2.1$	$25.5 \pm 1.8$	$18.0 \pm 1.8$
	39.0 – 40.3	30	$4.3 \pm 1.4$	$8.0 \pm 1.4$	$29.8 \pm 4.8$	$35.8 \pm 4.6$	$36.0 \pm 5.6$
RQQs	37.3 – 38.5	301	$5.9 \pm 0.5$	$9.0 \pm 0.6$	$19.1 \pm 0.9$	$19.6 \pm 0.6$	$12.6 \pm 0.6$
	38.5 – 39.0	400	$5.1 \pm 0.5$	$8.2 \pm 0.8$	$18.7 \pm 1.2$	$20.6 \pm 0.8$	$13.5 \pm 0.6$
	39.0 – 40.3	306	$5.0 \pm 0.4$	$9.5 \pm 0.7$	$21.7 \pm 1.1$	$22.9 \pm 0.8$	$16.1 \pm 0.7$

results are also presented in Table 3.2. I find that there is no statistical difference between the FIR flux densities of radio-loud and radio-quiet quasars as a whole. However, separating the two populations into redshift and optical luminosity bins I find different results. With this division, we can see that at lower redshifts and/or lower optical luminosities the mean 350  $\mu\text{m}$  and 500  $\mu\text{m}$  flux densities for the radio-loud objects are significantly higher than for the radio-quiet ones at greater than the  $3\sigma$  level.

### 3.2.3 Luminosity calculation

To convert between measured FIR flux density at *Herschel* wavelengths and total luminosity in the FIR band and to derive the dust temperature, I have to adopt a model for the FIR SED. I use a single temperature grey-body fitting function (Hildebrand, 1983) in which the thermal

TABLE 3.2: The K-S (left column) and M-W (right column) probabilities of RLQs flux densities being indistinguishable from RQQs in redshift and optical luminosity bins at 100, 160, 250, 350 and 500  $\mu\text{m}$ , respectively.

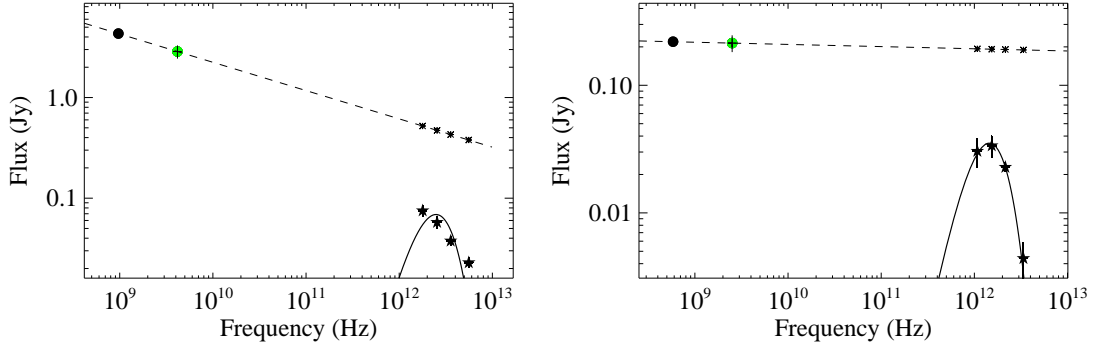
$z$ -range	K-S/M-W probability (%)				
	100 $\mu\text{m}$	160 $\mu\text{m}$	250 $\mu\text{m}$	350 $\mu\text{m}$	500 $\mu\text{m}$
0.0 – 1.0	41.0/22.3	10.5/6.7	82.2/15.0	0.9/4.2	0.1/0.3
1.0 – 1.5	44.8/38.8	67.0/39.4	54.6/31.7	3.5/4.8	3.6/4.9
1.5 – 2.0	88.9/30.8	56.0/35.2	96.4/29.2	57.5/36.4	39.9/7.6
2.0 – 4.0	80.5/39.4	14.4/4.1	18.7/3.3	64.6/15.8	67.9/26.7
$\log_{10}(L_{\text{opt}}/W)$	K-S/M-W probability (%)				
	100 $\mu\text{m}$	160 $\mu\text{m}$	250 $\mu\text{m}$	350 $\mu\text{m}$	500 $\mu\text{m}$
37.3 – 38.5	55.7/37.1	80.6/40.9	36.9/27.7	3.8/2.9	0.7/0.4
38.5 – 39.0	51.6/9.5	16.6/7.6	93.2/42.0	20.8/8.8	12.4/3.0
39.0 – 40.3	99.7/46.9	17.9/6.7	32.6/4.1	70.9/13.4	71.2/37.4

dust spectrum is approximated by:  $F_\nu = \Omega Q_\nu B_\nu(T)$ , where  $B_\nu$  is the Planck function,  $\Omega$  is the solid angle,  $Q_\nu = Q_0(\nu/\nu_0)^\beta$  is the dust emissivity (with  $1 \leq \beta \leq 2$ ) and  $T$  is the effective dust temperature. Since  $T$  and  $\beta$  are degenerate for sparsely sampled SEDs, following [Dye et al. \(2010\)](#) I have fixed the dust emissivity index to  $\beta = 2.0$  and varied the temperature over the range  $10 < T(\text{K}) < 60$ . The selection of the  $\beta$  parameter has been made based on the  $\chi^2$  value. Using a  $\beta = 2.0$  instead of e.g. 1.5, the best-fitting model returns lower  $\chi^2$  values for both of the populations. For each source we estimated the integrated FIR luminosity (8 – 1000  $\mu\text{m}$ ) using the grey-body fitting with the best fit temperature. The dust temperature was obtained from the best fit model derived from minimization of the  $\chi^2$  values. The uncertainty in the measurement was obtained by mapping the  $\Delta\chi^2$  error ellipse. In addition to the integrated FIR luminosity we calculate the monochromatic FIR-luminosity at 250  $\mu\text{m}$ , where the temperature-luminosity relation affects only the  $k$ -correction parameter, which is far less sensitive than the integrated FIR to the dust temperature (e.g. [Jarvis et al., 2010](#); [Hardcastle et al., 2013](#); [Virdee et al., 2013](#)).

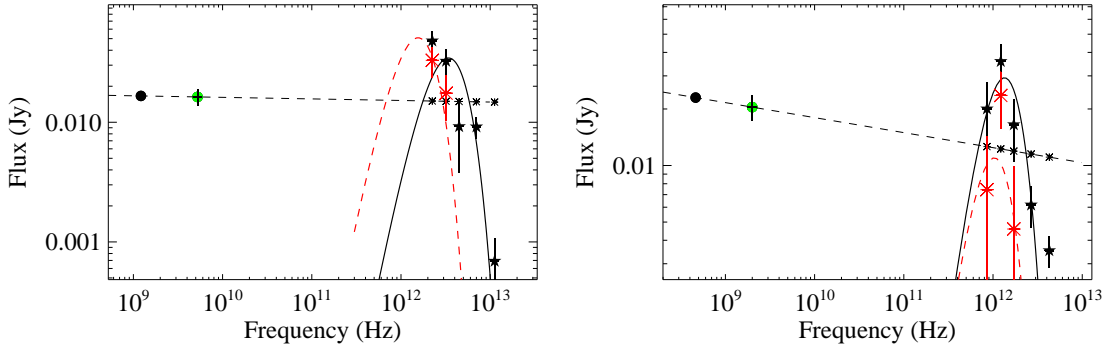
### 3.3 Synchrotron contamination

The FIR luminosity is used as a measure of the radiation from dust, which may be heated by star-formation and/or the central quasar nucleus. However, since the radio-loud sample includes high radio flux density sources, it is possible that the FIR flux densities we measure may be subject to contamination from synchrotron emission not associated with star formation. The spectra of powerful RLAGNs are in some cases entirely dominated by synchrotron emission from the jets at all wavelengths. Radio spectra have been compiled for each radio-loud source, with the aim of subtracting the radio contribution to the FIR emission.

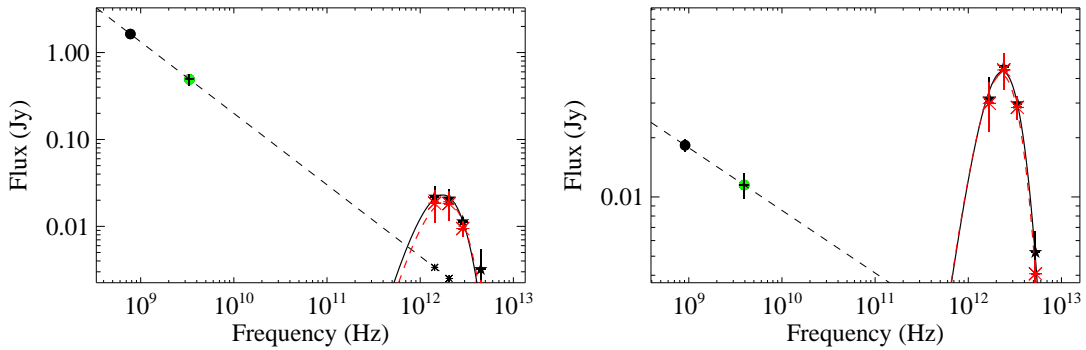
All of the RLQs in the sample have a detected counterpart in FIRST within a search radius



(a) Examples of the 9 sources where the extrapolation is massively overestimating the synchrotron contamination. The 9 sources with spectral energy distribution similar to these examples have been rejected from our sample.



(b) Examples of the 10 sources found having strong synchrotron contamination. The 10 sources with spectral energy distribution similar to these examples have been rejected from our sample.



(c) Examples of the 52 sources found having weak or no synchrotron contamination. The sources with spectral energy distribution similar to these examples have been included in our sample. Applying the correction to these sources has no impact on the derived temperatures and luminosities.

FIGURE 3.3: Spectral energy distribution at radio and FIR wavelengths for a selected sample of radio-loud quasars. *Filled black stars*: the FIR data, *Circles*: the radio data, green for FIRST and black for GMRT, *Black small stars*: synchrotron contamination at SPIRE and PACS bands, *Red asterisks*: the subtracted flux at SPIRE and PACS bands, *Black dashed line*: Linear fit to radio data, *Black solid line*: grey-body fit, *Red dashed line*: grey-body fit after synchrotron subtraction.

of 5 arcsec. In order to estimate their spectral index we also cross-matched our sample to the GMRT catalogue of [Mauch et al. \(2013\)](#), who have coverage of the H-ATLAS  $9^h$ ,  $12^h$  and  $14.5^h$  areas at 325 MHz, using a simple positional cross-matching with a maximum of 5 arcsec. Despite the incomplete sky coverage and variable sensitivity of the GMRT survey, a total of 71/141 sources are found to have 325 MHz counterparts. For the matched objects, we can measure their spectral index assuming a power law and then use their mean spectral index for the rest of the population.

In Fig. 3.3 I present a sample of the SEDs of the RLQs using the available radio and FIR fluxes. The data include the *Herschel* and the VLA (FIRST catalogue; [Becker et al., 1995](#)) observations presented in Section 3.2 and the 325 MHz radio fluxes taken from the GMRT catalogue. Using the extrapolation of the radio fluxes (dashed black line) I attempt to subtract the synchrotron contamination of the FIR fluxes. The subtracted FIR flux densities are fitted with the grey-body model once again (red dashed line) to produce a new estimation of the free parameters.

In the cases where the subtracted FIR fluxes do not fall close to the original FIR flux densities (within the errors) for more than two FIR bands, the parameters of the new grey-body fitting have changed significantly within the errors from the original ones. In these cases I have found that synchrotron emission strongly affects the FIR flux densities and the FIR luminosity and the sources are rejected from our sample. Specifically, we have divided our sample into 3 categories a) sources where the extrapolation of the radio fluxes massively overestimates the synchrotron contamination (Fig. 3.3a), b) sources where the synchrotron emission strongly affects the FIR flux densities (Fig. 3.3b) and sources where the synchrotron contamination is weak and the FIR flux densities are not affected at all (Fig. 3.3c).

From our sample of the 71 RLQs with both FIRST and GMRT radio detections I found 9 sources belong to the (a) category. The examples of two of these sources are presented in Fig. 3.3a. It is obvious that the straight-line extrapolation of the low-frequency radio emission massively overestimates the synchrotron contamination at the FIR bands; for these sources radio data at higher frequencies would be required in order to describe accurate radio spectra. Due to the lack of high-frequency radio data we had to reject these 10 sources from our sample in order to ensure that the synchrotron emission does not affect the star formation estimation in the radio-loud population. I should mention that only one of these sources has FIR detections at the  $3\sigma$  level.

In the second (b) category I have classified the 10 sources with strong synchrotron contamination. Examples of two of these sources are presented in Fig. 3.3b and they show that all the FIR flux densities appear to be seriously contaminated with non-thermal synchrotron. Although we expect the radio spectra to appear curve at higher frequencies and have less effect on the higher-frequency FIR bands (e.g. PACS bands) it seems that the  $500\text{-}\mu\text{m}$  and  $350\text{-}\mu\text{m}$  detections are likely to be seriously synchrotron contaminated. In order to classify a source as seriously contaminated we compare the results of the grey-body fitting using the

original FIR flux densities (black stars) and the FIR flux densities corrected for synchrotron contamination (red stars). As the examples show in Fig. 3.3b, the grey-body fitting after correction for synchrotron contamination (red dashed line) is significantly different from the original one (black solid line) implying that the parameters estimated using the original grey-body fitting are strongly affected by the synchrotron emission. These 10 sources have been rejected from our sample due to their probably serious contamination from non-thermal synchrotron emission.

In the third (c) category I have classified the remaining 52 sources out of the 71 with both FIRST and GMRT radio detections. The examples of two of these sources are presented in Fig. 3.3c. In this class are sources with weak (not significant) synchrotron contamination. As the examples show in Fig. 3.3c, the FIR flux densities after correction for synchrotron contamination (red stars) are within the  $1\sigma$  errors of the original FIR flux densities (black stars) and as a result the estimated parameters from the grey-body fittings (black solid line and red dashed line) using the corrected and the original FIR flux densities are within their errors. All 52 sources with similar SEDs to the examples in Fig. 3.3c are retained in our sample.

Overall, I have found 21 objects of the detected at 325 MHz sample where the synchrotron contamination strongly affects the estimates of the grey-body fitting, indicating that these objects have the potential for contamination by their synchrotron components. These sources are rejected from further study. For the rest of the sources which are detected at 325 MHz, I subtract the synchrotron contamination and fit a new grey-body model using the subtracted fluxes.

Among the rest 70/141 sources that are undetected in the GMRT data, there are 8 sources with available radio data in the literature which are used in order to estimate the spectral indexed (Griffith et al., 1995; Douglas et al., 1996; Cohen et al., 2007; Healey et al., 2007; Mason et al., 2009). One of them shows significant synchrotron contamination and has been removed from the sample. For the other 62 undetected in the GMRT data I conservatively used  $\alpha = -0.4$ , the minimum value observed in the GMRT-detected sources, to estimate the maximum possible synchrotron contamination. The main characteristic of the sample undetected by GMRT is the faint radio emission at 1.4 GHz, compared to the rest of the RLQs. The main bulk of these sources has  $S_{1.4\text{GHz}} < 10$  mJy while, the mean value of this sample is  $\langle S_{1.4\text{GHz}} \rangle = 5.79 \pm 0.81$  mJy. Due to their faint radio emission, we do not expect for most of them strong contamination. I found that 26 sources show possible synchrotron contamination and they have been removed from our sample. The final sample consists of 93 RLQs.

An alternative method of investigating the synchrotron contamination level is to study the level of core emission. A reasonable estimation of the level of compact emission can be derived from the comparison of the NVSS and FIRST fluxes, investigating whether the quasar radio fluxes are underestimated due to the FIRST survey resolving out extended flux.

The cross-match with the NVSS catalogue gave us a total of 90 matches within a 5 arcsec radius. Among these there are 58 sources with a GMRT detection. Comparing the NVSS - FIRST fluxes I found a fraction of  $7.0 \pm 1.7$  per cent excess in their NVSS fluxes. No significant differences were found even when we compared the NVSS - FIRST emission for the sub-samples that are detected and undetected with GMRT. Such a small fraction shows there is no evidence that either the FIRST fluxes or the estimated spectral indices of the sources are underestimated. On the other hand, the low level of extended emission shows that the radio sources are fairly compact and a flatter radio spectrum would be expected. However, a comparison of the spectral index with the NVSS shows no particular trend.

Overall, I have found that out of the 141 objects in the RLQ sample, 21 RLQs have significant non-thermal contamination in their FIR emission while an additional sample of 27 sources possible has strong contamination using an upper limit for their radio spectral index. These objects have been rejected from the sample. I emphasize that this is a conservative estimate, given that the steep-spectrum synchrotron component is likely to fall more quick than the fitted power-law at higher frequencies due to spectral aging of the electron population. Therefore, the fitting extrapolation is likely to provide an overestimate of the synchrotron contamination at FIR wavelengths in our sample, especially in the cases of power-law fitting. Radio data at higher frequencies would give us a clearer view of the possibility of a flat, core dominated spectrum in this frequency range, although our analysis does not support the presence of a flat spectrum at shorter wavelengths.

### 3.4 Far-infrared properties

In order to estimate the FIR properties of our samples based on the isothermal grey-body model, we use Levenberg-Marquardt  $\chi^2$  minimization to find the best-fitting temperature and normalization value for the grey-body model. The errors on the parameters were determined by mapping the  $\Delta\chi^2 = 2.3$  error ellipse, which corresponds to the  $1\sigma$  error for 2 parameters of freedom. For every source in our sample, I calculate the integrated FIR luminosity (8 – 1000  $\mu\text{m}$ ), the monochromatic luminosity at 250  $\mu\text{m}$  and the isothermal dust mass using the 250- $\mu\text{m}$  luminosity. The mass derived on the assumption of a single temperature for the dust, is given by:

$$M_{\text{dust}} = \frac{1}{1+z} \frac{S_{250} D_L^2}{\kappa B(\nu, T)} \quad (3.1)$$

where  $S_{250}$  is the 250  $\mu\text{m}$  observed flux,  $D_L$  is the luminosity distance,  $\kappa$  is the dust mass absorption coefficient, which [Dunne et al. \(2011\)](#) take to be  $0.89 \text{ m}^2 \text{ kg}^{-1}$  and  $B(\nu, T)$  is the Planck function.  $K$ -corrections have been applied <sup>2</sup>.

<sup>2</sup>The K-correction is given by:

$K = \left( \frac{\nu_{\text{obs}}}{\nu_{\text{obs}(1+z)}} \right)^{3+\beta} \frac{e^{(h\nu_{\text{obs}(1+z)}/kT_{\text{iso}})} - 1}{e^{(h\nu_{\text{obs}}/kT_{\text{iso}})} - 1}$ , where  $\nu_{\text{obs}}$  is the observe frequency at 250 $\mu\text{m}$ ,  $\nu_{\text{obs}(1+z)}$  is the rest-frame frequency and  $T_{\text{iso}}$  and  $\beta$  are the temperature and emissivity index.

### 3.4.1 Stacking

The majority of the sources are undetected at the  $5\sigma$  limit of the Phase 1 catalogue so, in order to calculate their properties I use two different stacking methods and I compare the results. The first method is based on a weighted stacking analysis which follows the method of [Hardcastle et al. \(2010\)](#). I determine the luminosity for each source from the background-subtracted flux density, even if negative, on the grounds that this is the maximum-likelihood estimator of the true luminosity, and take the weighted mean of the parameter I am interested in within each bin. I use the same redshift and optical luminosity bins across the radio-loud and radio-quiet samples in order to facilitate comparisons. The luminosity is weighted using the errors calculated from  $\Delta\chi^2 = 2.3$  and the errors on the stacked parameters are determined using the bootstrap method. The advantage of bootstrapping is that no assumption is made on the shape of the luminosity distribution. Tables [3.3](#) and [3.4](#) show the weighted mean values of the estimated parameter within each bin for both populations and the K-S/M-W test probabilities of the individual measurements comparing the radio-loud and radio-quiet quasars in the same bins.

Using the weighted stacking analysis might bias our measurement to the brightest and hottest objects. In order to ensure that the FIR parameters from the weighted stacking method are reliable, I calculate, as an alternative, the mean temperatures for objects using the Maximum Likelihood Temperature method (e.g. [Hardcastle et al., 2013](#)). As in the previous sections, I split the radio-loud and radio-quiet quasars into bins defined by their redshift, optical luminosity and radio luminosity. For each bin, I calculate the best fit temperature that gives the best  $\chi^2$  fit to the observed fluxes of every quasar in the bin. In order to do this, we cycle through temperatures between 5 - 60 K allowing each quasar to vary and have a free normalization. For each temperature step, I calculate the total  $\chi^2$ . This result is a distribution from which we determine the temperature with the lowest total  $\chi^2$ . Errors in this fitted temperature are estimated by finding the range that gives  $\Delta\chi^2 = 1$ . Using the best-fitting temperature and normalizations for all the galaxies, I estimate the FIR luminosity, the 250- $\mu\text{m}$  luminosity and the dust mass for each bin. The errors for each parameter are determined by bootstrapping. The results of this method are shown in Table [3.5](#). The advantages of this method are that all the sources in a given bin are used in the temperature estimation and the luminosities of the sources in bins are not automatically correlated. However, there are bins where the estimated mean temperature is significantly different from the individual temperature of each source, which could result in underestimation (or overestimation) of luminosities and dust masses.

In general terms, the two methods are in good agreement with some exceptions in the case of “sensitive” parameters related to temperature. Specifically, it seems that we get larger differences in bins where the objects span a greater range in temperature. In these cases, the

TABLE 3.3: Estimated weighted-mean FIR properties using a single-component grey-body fitting for RLQs and RQQs. The two populations have been separated into redshift, radio luminosity and optical luminosity bins.

Class	$z$ range	Weighted mean values			
		$\log_{10}(\text{LFIR}/L_{\odot})$	$T_{\text{iso}}$ (K)	$\log_{10}(M_{\text{dust}}/M_{\odot})$	$\log_{10}(L_{250}/W \text{ Hz}^{-1})$
RLQs	0.0 – 1.0	$11.11 \pm 0.07$	$18.42 \pm 1.30$	$7.79 \pm 0.08$	$25.80 \pm 0.08$
	1.0 – 1.5	$11.90 \pm 0.06$	$19.41 \pm 1.26$	$8.00 \pm 0.11$	$26.68 \pm 0.12$
	1.5 – 2.0	$12.17 \pm 0.06$	$25.79 \pm 1.49$	$8.06 \pm 0.09$	$27.07 \pm 0.10$
	2.0 – 4.0	$12.38 \pm 0.09$	$27.14 \pm 1.43$	$7.77 \pm 0.08$	$27.26 \pm 0.26$
RQQs	0.0 – 1.0	$11.23 \pm 0.17$	$22.48 \pm 0.35$	$7.91 \pm 0.02$	$25.96 \pm 0.04$
	1.0 – 1.5	$11.97 \pm 0.12$	$26.28 \pm 0.40$	$8.08 \pm 0.02$	$27.01 \pm 0.05$
	1.5 – 2.0	$12.22 \pm 0.11$	$26.35 \pm 0.36$	$8.15 \pm 0.02$	$27.28 \pm 0.03$
	2.0 – 4.0	$12.68 \pm 0.04$	$30.29 \pm 0.46$	$8.33 \pm 0.03$	$28.15 \pm 0.08$

Class	$\log_{10}(L_{1.4\text{GHz}}/W \text{ Hz}^{-1})$	Weighted mean values			
		$\log_{10}(\text{LFIR}/L_{\odot})$	$T_{\text{iso}}$ (K)	$\log_{10}(M_{\text{dust}}/M_{\odot})$	$\log_{10}(L_{250}/W \text{ Hz}^{-1})$
RLQs	23.0 – 25.0	$11.52 \pm 0.20$	$19.95 \pm 1.54$	$7.83 \pm 0.10$	$25.85 \pm 0.38$
	25.0 – 26.0	$11.95 \pm 0.06$	$24.25 \pm 1.01$	$7.94 \pm 0.05$	$26.70 \pm 0.14$
	26.0 – 27.0	$12.06 \pm 0.09$	$25.82 \pm 1.18$	$7.99 \pm 0.13$	$26.79 \pm 0.37$
	27.0 – 28.5	$12.33 \pm 0.19$	$27.18 \pm 1.17$	$8.10 \pm 0.09$	$27.08 \pm 0.23$
RQQs	21.0 – 23.0	$11.17 \pm 0.16$	$22.09 \pm 0.39$	$7.59 \pm 0.03$	$25.87 \pm 0.05$
	23.0 – 23.5	$11.89 \pm 0.17$	$25.91 \pm 0.45$	$8.05 \pm 0.03$	$26.86 \pm 0.09$
	23.5 – 24.0	$12.16 \pm 0.10$	$26.56 \pm 0.33$	$8.10 \pm 0.02$	$27.21 \pm 0.03$
	24.0 – 25.5	$12.74 \pm 0.04$	$31.91 \pm 0.51$	$8.38 \pm 0.03$	$28.21 \pm 0.09$

Class	$\log_{10}(L_{\text{opt}}/W)$	Weighted mean values			
		$\log_{10}(\text{LFIR}/L_{\odot})$	$T_{\text{iso}}$ (K)	$\log_{10}(M_{\text{dust}}/M_{\odot})$	$\log_{10}(L_{250}/W \text{ Hz}^{-1})$
RLQs	37.3 – 38.5	$11.74 \pm 0.08$	$18.89 \pm 1.29$	$7.90 \pm 0.02$	$26.57 \pm 0.25$
	38.5 – 39.0	$11.94 \pm 0.07$	$19.98 \pm 1.18$	$8.10 \pm 0.03$	$26.89 \pm 0.11$
	39.0 – 40.3	$12.32 \pm 0.10$	$27.05 \pm 1.06$	$8.15 \pm 0.02$	$27.31 \pm 0.26$
RQQs	37.3 – 38.5	$11.36 \pm 0.02$	$21.43 \pm 0.33$	$7.67 \pm 0.02$	$26.22 \pm 0.07$
	38.5 – 39.0	$12.00 \pm 0.08$	$25.94 \pm 0.33$	$8.01 \pm 0.03$	$27.04 \pm 0.05$
	39.0 – 40.3	$12.53 \pm 0.02$	$29.16 \pm 0.34$	$8.31 \pm 0.02$	$27.92 \pm 0.08$

TABLE 3.4: The K-S and M-W probabilities that FIR estimations using a single-component grey-body fitting for the RLQs in redshift, radio luminosity and optical luminosity bins are drawn from the same population as RQQs.

$z$ -range	K-S/M-W probability (%)			
	LFIR	$T_{\text{iso}}$	$M_{\text{dust}}$	$L_{250}$
0.0 – 1.0	11.9/9.5	25.0/29.8	93.3/29.8	21.8/38.7
1.0 – 1.5	95.7/39.5	60.6/24.8	25.8/26.2	38.2/33.1
1.5 – 2.0	15.0/4.2	74.4/22.4	79.1/17.6	11.9/8.1
2.0 – 4.0	27.7/6.7	6.0/1.0	7.6/1.1	21.2/4.8

$\log_{10}(L_{\text{opt}}/W)$	K-S/M-W probability (%)			
	LFIR	$T_{\text{iso}}$	$M_{\text{dust}}$	$L_{250}$
37.3 – 38.5	4.1/0.6	9.1/21.6	32.9/12.8	2.1/4.6
38.5 – 39.0	18.6/2.6	1.0/1.0	35.6/6.3	1.44/0.5
39.0 – 40.3	36.4/10.9	4.0/3.0	53.6/13.1	2.0/0.9

TABLE 3.5: Mean FIR parameters for each bin as they are estimated by the Maximum Likelihood (ML) stacking method. The best  $\chi^2$  for each bin is also presented.

Class	$z$ -range	ML mean values				$\chi^2$
		$\log_{10}(\text{LFIR}/L_{\odot})$	$T_{\text{iso}}$ (K)	$\log_{10}(M_{\text{dust}}/M_{\odot})$	$\log_{10}(L_{250}/W \text{ Hz}^{-1})$	
RLQs	0.0 – 1.0	$11.19 \pm 0.08$	$18.01^{+1.01}_{-0.72}$	$7.88 \pm 0.07$	$25.81 \pm 0.08$	1.11
	1.0 – 1.5	$11.81 \pm 0.07$	$21.72^{+1.61}_{-1.35}$	$8.26 \pm 0.09$	$26.70 \pm 0.08$	0.68
	1.5 – 2.0	$12.04 \pm 0.05$	$25.76^{+1.32}_{-1.13}$	$8.10 \pm 0.08$	$27.00 \pm 0.07$	0.56
	2.0 – 4.0	$12.42 \pm 0.08$	$27.22^{+1.54}_{-2.74}$	$7.97 \pm 0.08$	$27.19 \pm 0.08$	0.14
RQQs	0.0 – 1.0	$11.11 \pm 0.02$	$21.27^{+0.41}_{-0.38}$	$7.78 \pm 0.02$	$25.99 \pm 0.03$	0.69
	1.0 – 1.5	$11.86 \pm 0.03$	$24.19^{+0.53}_{-0.42}$	$8.09 \pm 0.03$	$26.88 \pm 0.03$	0.50
	1.5 – 2.0	$12.21 \pm 0.02$	$27.24^{+0.77}_{-0.43}$	$8.21 \pm 0.02$	$27.24 \pm 0.02$	0.46
	2.0 – 4.0	$12.56 \pm 0.17$	$30.26^{+1.20}_{-0.84}$	$8.27 \pm 0.04$	$27.88 \pm 0.04$	0.67
Class	$\log_{10}(L_{1.4\text{GHz}}/W \text{ Hz}^{-1})$	ML mean values				$\chi^2$
		$\log_{10}(\text{LFIR}/L_{\odot})$	$T_{\text{iso}}$ (K)	$\log_{10}(M_{\text{dust}}/M_{\odot})$	$\log_{10}(L_{250}/W \text{ Hz}^{-1})$	
RLQs	23.0 – 25.0	$11.19 \pm 0.13$	$17.79^{+2.75}_{-0.46}$	$7.81 \pm 0.12$	$25.77 \pm 0.16$	1.06
	25.0 – 26.0	$11.93 \pm 0.06$	$22.25^{+1.29}_{-1.50}$	$8.05 \pm 0.05$	$26.62 \pm 0.05$	0.60
	26.0 – 27.0	$12.09 \pm 0.07$	$25.03^{+1.98}_{-1.64}$	$8.10 \pm 0.10$	$26.91 \pm 0.07$	0.47
	27.0 – 28.5	$12.55 \pm 0.15$	$30.26^{+1.26}_{-3.16}$	$8.15 \pm 0.10$	$27.19 \pm 0.08$	0.23
RQQs	21.0 – 23.0	$11.03 \pm 0.03$	$19.75^{+0.43}_{-0.32}$	$7.79 \pm 0.02$	$25.84 \pm 0.03$	0.69
	23.0 – 23.5	$11.76 \pm 0.04$	$22.58^{+1.75}_{-0.42}$	$8.11 \pm 0.04$	$26.61 \pm 0.05$	0.50
	23.5 – 24.0	$12.16 \pm 0.01$	$27.55^{+0.58}_{-0.42}$	$8.17 \pm 0.02$	$27.19 \pm 0.02$	0.48
	24.0 – 25.5	$12.68 \pm 0.16$	$30.57^{+1.37}_{-0.73}$	$8.20 \pm 0.04$	$27.82 \pm 0.03$	0.70
Class	$\log_{10}(L_{\text{opt}}/W)$	ML mean values				$\chi^2$
		$\log_{10}(\text{LFIR}/L_{\odot})$	$T_{\text{iso}}$ (K)	$\log_{10}(M_{\text{dust}}/M_{\odot})$	$\log_{10}(L_{250}/W \text{ Hz}^{-1})$	
RLQs	37.3 – 38.5	$11.62 \pm 0.10$	$17.25^{+3.12}_{-1.20}$	$8.00 \pm 0.09$	$25.95 \pm 0.11$	1.96
	38.5 – 39.0	$11.93 \pm 0.06$	$21.25^{+1.28}_{-0.96}$	$8.18 \pm 0.06$	$26.50 \pm 0.05$	1.20
	39.0 – 40.3	$12.36 \pm 0.07$	$26.52^{+2.16}_{-1.21}$	$8.09 \pm 0.08$	$27.12 \pm 0.06$	1.56
RQQs	37.3 – 38.5	$11.22 \pm 0.03$	$19.22^{+1.25}_{-0.75}$	$7.84 \pm 0.02$	$25.81 \pm 0.03$	0.71
	38.5 – 39.0	$11.92 \pm 0.02$	$25.28^{+1.62}_{-0.35}$	$8.07 \pm 0.03$	$26.89 \pm 0.02$	0.44
	39.0 – 40.3	$12.36 \pm 0.02$	$28.06^{+1.83}_{-1.72}$	$8.20 \pm 0.02$	$27.33 \pm 0.03$	0.45

weighted mean method is dominated by the hotter objects returning higher luminosities. Despite the differences in temperature between the methods, we see that the monochromatic luminosities are broadly consistent in both methods implying that the temperature-luminosity correlation does not have a significant effect on the inferred monochromatic luminosities. In contrast, FIR luminosity and dust masses seem to be affected when hot objects are present. Despite the differences I get in some cases, both methods show that RLQs have systematically lower dust temperature than RQQs. Regarding their luminosities, and especially the 250- $\mu\text{m}$  luminosity which seems to be a safer choice as it is less affected by temperature, they tend to be comparable for most of the bins but not at lower optical luminosities (and/or redshifts) where an excess in the case of RLQs is found.

In order to study the FIR properties (e.g. FIR luminosity, dust temperature, dust mass) for the two populations as a function of redshift and optical luminosity I present in Fig. 3.4 the mean dust temperature as a function of the mean FIR luminosity. The two populations have been divided into redshift (top) and optical luminosity (bottom) bins which are represented by a rainbow colour-code with purple colour for lower and red colour for higher values. For each bin the weighted mean and the ML mean values are presented.

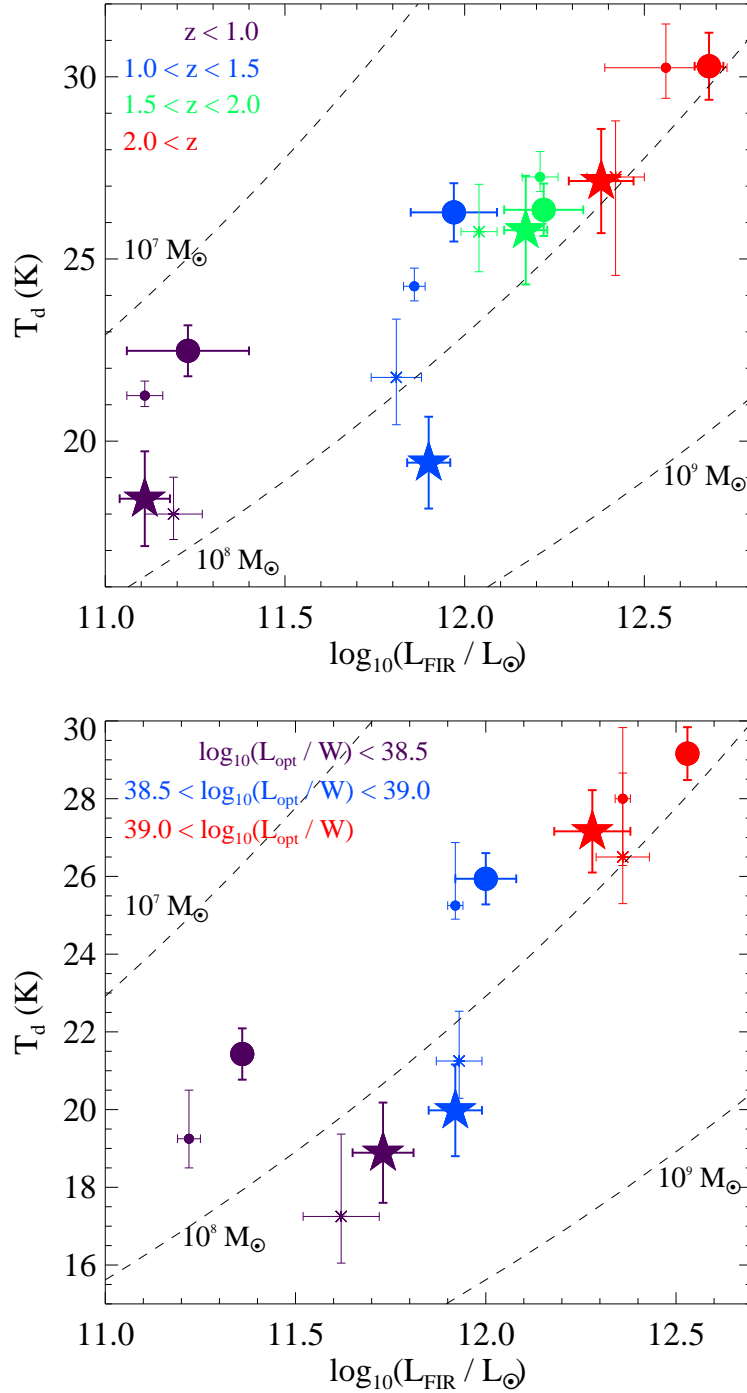


FIGURE 3.4: FIR luminosity versus dust temperature when the two populations are divided into redshift (top) and optical luminosity (bottom) bins. The rainbow colour-code represents the redshift/optical luminosity bin values, purple for lower and red for higher values respectively. The RLQs are represented by stars while the RQQs are shown as circles. The large symbols show the estimates based on the weighted mean method while the small symbols show the estimates based on the maximum likelihood stacking. The black lines correspond to the dust mass estimates based on the LFIR -  $T_{\text{dust}}$  relation ( $\text{LFIR} \propto \kappa_0 M_{\text{dust}} T_{\text{dust}}^{4+\beta}$ ), assuming  $\beta = 2.0$ , for dust masses of  $10^7$ ,  $10^8$  and  $10^9 M_{\odot}$ .

### 3.4.2 FIR luminosity

With respect to the redshift bins (see Fig. 3.4 top), the two populations have the same mean FIR luminosities within their errors for each bin. The largest difference between the mean FIR luminosities of the two populations is observed at the highest redshift bin ( $z > 2.0$ ; red colour) with RQQ having the higher FIR luminosity. However, this difference could be an effect of the calculation of the mean values as both methods do not return significant excess for the radio-quiet population (small versus large red symbols). To summarize, the mean FIR luminosities of the radio-loud and radio-quiet quasars show no significant differences when the two population are split into redshift bins. In contrast, when I divide the two populations into optical luminosity bins (see Fig. 3.4 bottom), there is a clear excess of FIR luminosity in lower-luminosity bins for the case of RLQs ( $\log_{10}(L_{\text{opt}}/W) < 38.5$ ; purple colour). The fact that both methods show the same significant excess indicates that the observed differences between the two populations are not a result of the calculation methods. At intermediate optical luminosities ( $38.5 < \log_{10}(L_{\text{opt}}/W) < 39.0$ ; blue colour) both of the populations have consistent mean FIR luminosity values. At the highest optical luminosity bin ( $\log_{10}(L_{\text{opt}}/W) > 39.0$ ; red colour) we have the same picture as at the highest redshift bin; a possible FIR luminosity excess for the RQQs which, however, is not supported by both of the methods.

### 3.4.3 Dust temperature and mass

The results reported in Fig. 3.4 and Tables 3.3, 3.5 show that there is a general trend that the RLQs have lower dust temperature than RQQs, at least at lower redshift and optical luminosity bins. This difference reaches  $\sim 5$  K in some bins. At higher redshift and optical luminosity bins both of the populations have the same mean dust temperatures within their errors.

The mean values of the estimated dust mass based on both calculation methods show that RLQs have almost a constant mean dust mass over the whole redshift and optical luminosity range. In the case of RQQs, the mean dust masses decrease at lower redshift/optical luminosity bins. Comparing the results for the two populations, it seems that RLQs have higher dust masses at lower luminosity bins while at higher luminosities both of the populations have similar mean values. Dust masses must be interpreted with care as they could be biased by the stacking analysis towards the brightest and hottest objects. The excess in dust mass, in the case of RLQs which are the class with the lower dust temperature, could be required in order to be detectable at a level that allows a temperature to be fitted.

### 3.4.4 250- $\mu\text{m}$ luminosity

In this section I present the stacked monochromatic luminosity at 250  $\mu\text{m}$  for both stacking methods and populations as a function of redshift, radio luminosity and optical luminosity (Fig. 3.5). The luminosities calculated using the weighted stack method are shown by solid error bars while the luminosities calculated via the Maximum Likelihood method are shown by the dashed error bars. Both methods show a good level of agreement within their  $1\sigma$  error. The cases with the larger disagreement are those where strong outliers are found within the bin (unusually hot or cold sources in comparison with the rest of the population). Based on these plots, we see that the Maximum Likelihood Temperature method is more sensitive to outliers. I therefore argue that the weighted stacking method is sufficiently accurate to calculate the stacked rest-frame monochromatic luminosity at 250  $\mu\text{m}$ . For clarity, I do not show the stacks generated by the Maximum Likelihood Temperature method in the subsequent sections, although consistency checks were performed throughout the analysis.

As we see in Fig. 3.5, 250- $\mu\text{m}$  luminosity is correlated with radio luminosity for both populations. However, the question is whether radio activity induces star formation, leading to FIR emission. Redshift will affect the correlation between the two luminosities so, as a first way to measure the strength of correlation between FIR luminosity and radio luminosity we use partial-correlation analysis (Akritas & Siebert, 1996), which allows us to determine the correlation between the two parameters while accounting for the effects of redshift. For this analysis, I avoid bias against FIR weak sources by adding undetected sources (‘censored’ sample) to the detected sample. For this reason, in order to measure the partial correlations I use the FORTRAN program CENS-TAU, available from the Penn State Center for Astrostatistics<sup>3</sup>, taking ‘censored’ data into account as upper limits using the methodology presented in Akritas & Siebert (1996).

The partial-correlation shows that radio luminosity is significantly correlated with 250- $\mu\text{m}$  luminosity in the case of RLQs with a partial-correlation of  $\tau = 0.17$ . The null hypothesis of zero partial correlation is rejected at the  $3\sigma$  level. In the case of RQQs I found that the correlation is not statistically significant with  $\tau = 0.06$  and a probability under the null hypothesis  $p = 0.11$ . The results are almost the same even when I compare the integrated FIR luminosity to the radio luminosity but even more significant for the case of RLQs with the null hypothesis of no correlation rejected at higher than the  $4\sigma$  level. Despite the results found for both the populations as a total, the different trends which I found for low ( $\log_{10}(L_{\text{opt}}/W) \leq 38.5$ ) and high ( $\log_{10}(L_{\text{opt}}/W) > 38.5$ ) optical luminosities lead us to investigate the correlations also for these sub-samples. In the case of RLQs, the significant correlation between radio luminosity and 250- $\mu\text{m}$  luminosity remains only for the low optical luminosity bin with  $\tau = 0.12$  ( $p < 0.001$ ; the probability of no correlation) while for the high

---

<sup>3</sup>Available at  
<http://www.astrostatistics.psu.edu/statcodes/censtau>.

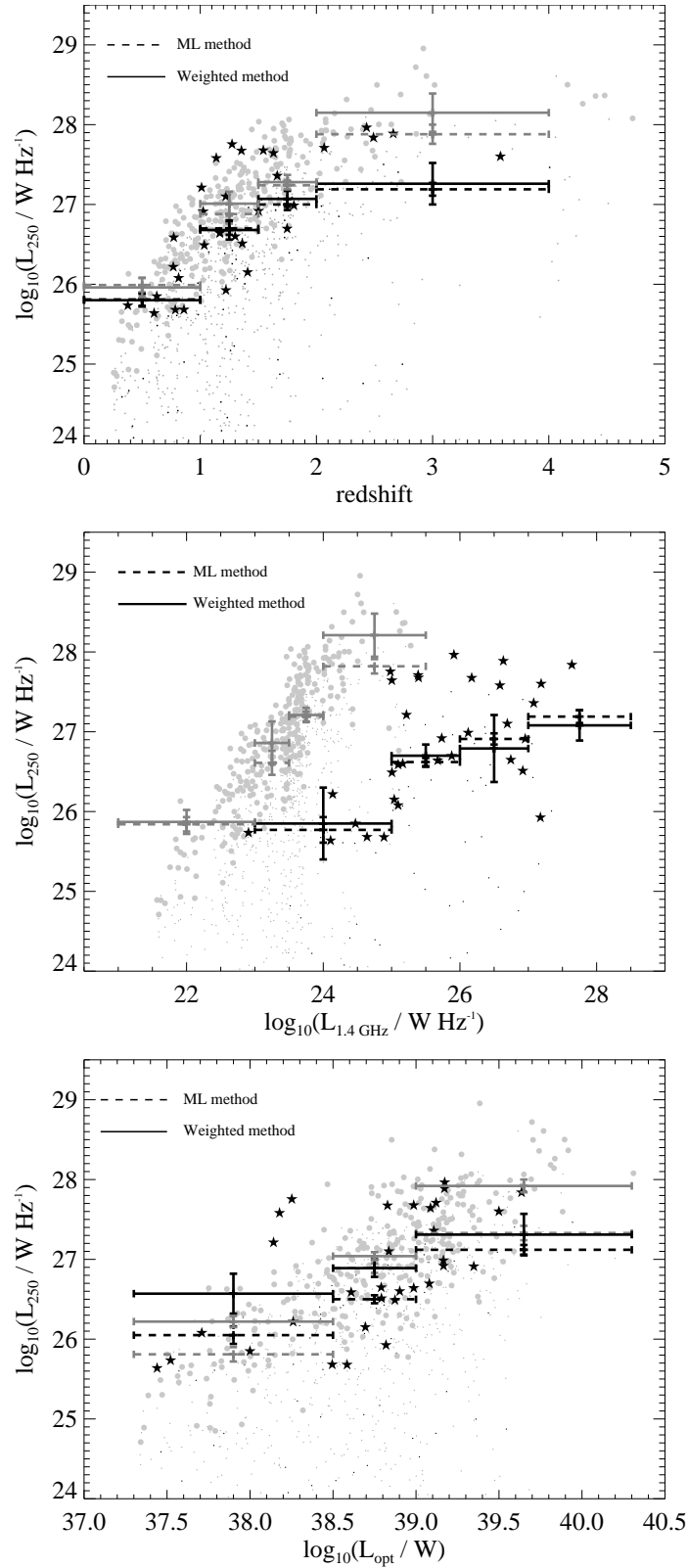


FIGURE 3.5: Correlation between infrared luminosity at  $250 \mu\text{m}$  and redshift (top), radio luminosity (middle) and optical luminosity (bottom). Individual measurements for radio-loud (black stars) and radio-quiet (grey circles) quasars detected at  $250 \mu\text{m}$  at the  $3\sigma$  level are also included. Dots represent the entire samples. Error bars with solid lines illustrate the stacked luminosities calculated using the weighted method. Luminosities calculated via the Maximum Likelihood method are dashed line error bars. The errors have the same colour as the population that they represent.

luminosity bin no significant correlation is found ( $\tau = 0.04$  and  $p \simeq 0.29$ ). In contrast, for RQQs no correlation is again found for either low ( $\tau = 0.02$  and  $p \simeq 0.26$ ) or high ( $\tau = 0.03$  and  $p \simeq 0.36$ ) optical luminosity bins. Similar trends are also obtained when I compare the FIR luminosity with the radio luminosity for the two populations at lower and higher optical luminosities. In terms of RQQs, all sources with  $\log_{10}(L_{250}/\text{W Hz}^{-1}) \geq 27.0$  are associated with optical luminosities above the threshold at which the dichotomy is found. At this level of 250- $\mu\text{m}$  luminosity it seems that all correlations with optical luminosity, radio luminosity and, possibly, also with redshift, tend to disappear. Regarding the correlation between  $L_{250}$  and radio luminosity, a significant number of RQQs with  $\log_{10}(L_{250}/\text{W Hz}^{-1}) \geq 27.0$  have radio-luminosity higher than  $10^{24} \text{ W Hz}^{-1}$ , a limit often used for the distinction between radio-loud and radio-quiet population.

### 3.4.5 Two-Temperature model

The estimation of the dust mass has been made based on the measured temperature of the grey-body model. Comparing our results with those of Dunne et al. (2011) for *Herschel*-detected  $z < 0.5$  galaxies, we see that the measured isothermal dust temperatures span the same range. Taking into account the fact that I use a  $\beta = 2.0$  emissivity index, the dust mass measurements should increase by 30 – 50 per cent from those of Dunne et al. (2011) with the same temperature. Indeed, for a mean temperature of 20 – 25 K the population of this work is found to have  $\sim 10^{8.0} M_{\odot}$ . One question is if the estimated isothermal dust mass can be biased low, as the dust exists at a range of temperatures in galaxies, while the mass I have estimated is that of the dust close to the source of heating (star-forming regions) which warm it enough to emit at FIR wavelengths. Another important question is whether the presence of a cold component could explain the differences I found for the two populations regarding their dust temperatures and dust masses.

To investigate this I use a model which requires two components of dust. The two required components consist of cold dust with  $T_c \sim 10 - 25 \text{ K}$  and warmer dust with  $T_w \sim 25 - 60 \text{ K}$ . The cold component is associated with the old stellar population and the warm one with the current star formation. The luminosity of the warm component is primarily the indicator of the star-formation rate. Previous studies preferred to use two fixed temperatures (a cold and a warm one) in order to fit the two-temperature model. However, the correct choice of the fixed temperatures would be difficult as our single-temperature results show that the two populations (radio-loud and radio-quiet quasars) may have different dust temperatures. In order to overcome this problem of the possible different temperatures between the two populations, I fit a two-temperature model for several different temperature pairs within  $\pm 5 \text{ K}$  of our initial chosen fixed temperatures,  $T_c = 15 \text{ K}$  and  $T_w = 35 \text{ K}$ .

Using each possible pair of cold and warm component temperatures I estimate the FIR luminosities and the dust mass for each component. For the two-component model the FIR

luminosity is:

$$\text{LFIR} = N_w \nu^\beta B_\nu \left( \frac{\nu}{1+z}, T_w \right) + N_c \nu^\beta B_\nu \left( \frac{\nu}{1+z}, T_c \right) \quad (3.2)$$

where  $N_w$  and  $N_c$  are the relative contribution due to the warm and cold dust components. The dust mass is computed from the sum of the masses in the two temperature components (Vlahakis et al., 2005):

$$M_d = \frac{L_{250}}{4\pi\kappa_{250}} \left[ \frac{N_w}{B_\nu \left( \frac{\nu}{1+z}, T_w \right)} + \frac{N_c}{B_\nu \left( \frac{\nu}{1+z}, T_c \right)} \right] \frac{1}{N_w + N_c} \quad (3.3)$$

where  $\kappa_{250} = 0.89 \text{ m}^2 \text{ kg}^{-1}$  is the dust mass absorption coefficient and  $B_\nu$  is the two-temperature modified Planck function.

In the cases where the objects are well described by a single temperature for the warm component that is significantly different from  $T_w = 35 \text{ K}$  the two-temperature model with fixed temperatures fit less well. However, I have found a good correlation between the FIR luminosities of the two fitting models. In contrast, the estimated dust masses show less good agreement with higher scatter. This suggests that, at least for this sample, the estimation of the FIR luminosity is not strongly affected by the fitting model, while the dust mass must be interpreted with a little more care. Comparing the contamination of the cold component to the total FIR and  $250 \mu\text{m}$  luminosities I found that in both populations the warm component dominated the overall luminosity at a higher level than 70 per cent. This result shows that any differences found should not be a result of a strong cold component in any of the two populations.

### 3.4.6 Star-formation rate

For the calculation of the SFR the FIR luminosity is required. As I discussed in Section 3.4.1, the FIR luminosity seems to be more sensitive to temperature dispersion compared to the  $250\text{-}\mu\text{m}$  luminosity. In this case, the SFR estimation could be strongly affected by the dust temperature. On the other hand, the rest-frame monochromatic luminosity at  $250 \mu\text{m}$  minimises the dispersion in our calculations and small differences are found, within their errors, between the two methods (weighted and maximum likelihood temperature). In addition, the FIR luminosity, as described using the two-temperature model, could be affected by a strong cold component. However, the results show that both FIR luminosity and  $L_{250}$  are dominated by the warm component. For these reasons the warm dust component is used as a tracer of the current star formation, whose mass and luminosity are primarily an indicator of the star-formation rate (Dunne et al., 2011; Smith et al., 2012b).

In order to investigate how strongly and in which cases the warm-component FIR luminosity is affected by the temperature, I compare the warm-component  $250\text{-}\mu\text{m}$  luminosity

to the warm-component FIR luminosity as they were estimated using the two-temperature model. For both of the populations I found the same linear correlation, within the errors, between the warm 250- $\mu\text{m}$  and integrated FIR luminosities. The linear regression between the warm 250- $\mu\text{m}$  luminosity and the warm FIR luminosity is found with the ordinary least squares (OLS) bisector (Isobe et al., 1990) fit being  $\text{LFIR}_{\text{RL}} \propto 10^{0.66 \pm 0.01} L_{250\text{RL}}$ ;  $\text{LFIR}_{\text{RQ}} \propto 10^{0.63 \pm 0.03} L_{250\text{RQ}}$  for radio-loud and radio-quiet quasars respectively. The same trends for both of the populations show that as long as we investigate only the differences of SFR between them, the selection of either the  $L_{250}$  or the integrated FIR luminosity as indicators of star formation would not affect our results or, at least, the effect should be the same for both populations.

The calculation of the SFR was performed using the equation by Kennicutt (1998):

$$\text{SFR}(M_{\odot} \text{ yr}^{-1}) = 4.5 \times 10^{-44} L_{\text{FIR}} \text{ (erg s}^{-1}\text{)}, \quad (3.4)$$

which assumes a Salpeter IMF in the mass range  $0.1 - 100 M_{\odot}$ , continuous starbursts of age  $10 - 100 \text{ Myr}$ , and requires the integrated IR luminosity over the range  $8 - 1000 \mu\text{m}$ .

Fig. 5.7 shows the weighted mean star-formation rates,  $\langle \text{SFR} \rangle$ , derived from the warm-component FIR luminosities, as a function of optical luminosity and redshift, for RLQs and RQQs. I split the samples into 4 redshift and 3 optical luminosity bins trying to keep the same number of objects within each bin for each population and determined the SFR as described in Section 3.4.5. The larger symbols represent the weighted mean SFR in each bin based on the  $T_c = 15 \text{ K}$  and  $T_w = 35 \text{ K}$  temperature fittings. Additionally, a dashed area is used to represent the mean values based on the different temperature pairs within  $\pm 5 \text{ K}$  of the original temperatures. Taking into account the errors of the original mean values, it seems that the selection of the temperatures would not strongly affect our results as in most of the cases the errors are larger than the estimated differences between the different temperature models. Comparing the  $\langle \text{SFR} \rangle$  for the two populations as a function of redshift, no difference is found. Both RLQs and RQQs seem to have the same  $\langle \text{SFR} \rangle$  within their errors in each bin. Even if we take into consideration any possible combination of different temperature pairs, we would not observe any particular differences. On the other hand, comparing the  $\langle \text{SFR} \rangle$  as a function of optical luminosity, a significant excess is found in the case of RLQs for  $\log_{10}(L_{\text{opt}}/W) \leq 38.5$ . This difference remains significant even if we assume that the two populations have different dust temperatures. For  $\log_{10}(L_{\text{opt}}/W) > 38.5$  both populations tend to have the same SFR within their errors. Another interesting point is the presence of a possible break at  $\log_{10}(L_{\text{opt}}/W) \sim 38.5$  in the case of RLQs while RQQs data points could be easily described by a linear function.

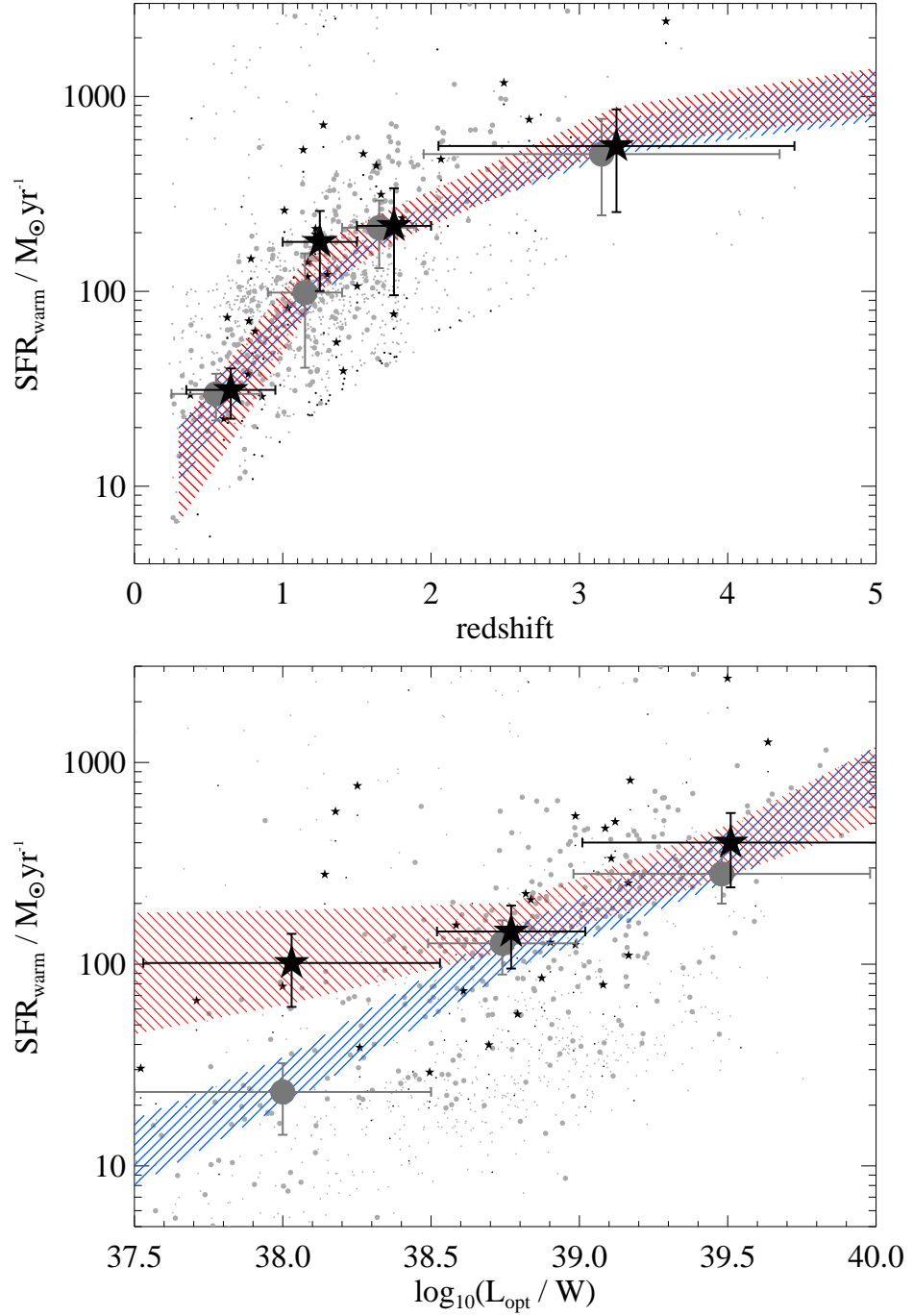


FIGURE 3.6: Weighted mean SFRs,  $\langle \text{SFR} \rangle$ , as a function of redshift (top) and optical luminosity (bottom). The dots represent the entire sample. Small black stars represent the RLQs detected at  $250 \mu\text{m}$  at the  $3\sigma$  level. Small grey circles represent the RQQs detected at  $250 \mu\text{m}$  at the  $> 3\sigma$  level. The same but larger symbols for each population represent the weighted mean values based on the  $T_c = 15 \text{ K}$ ,  $T_w = 35 \text{ K}$  two-temperature fitting model. The dashed regions (red for RLQs and blue for RQQs) show the range of the weighted mean values based on the  $\pm 5 \text{ K}$  two-temperature fitting model regarding to the initial ( $T_c = 15 \text{ K}$  and  $T_w = 35 \text{ K}$ ) choice of temperatures. In the top figure the large grey circles have been slightly left-shifted for clarity.

## 3.5 Discussion

The results of the previous sections show that RLQs tend to have different FIR properties from a matched sample in redshift and optical luminosity of RQQs. These differences lead to an excess of star-formation for the radio-loud population but are only significant in the case of low optical luminosity radio-loud and radio-quiet quasars.

Studying the FIR properties of an AGN population is usually a difficult task as possible contamination could affect the results. However, in chapter paper, I am mainly interested in studying the differences between the two populations instead of examining the exact properties for each one. In the case of this sample there are two main sources of contamination a) the warm dusty torus emission and b) the synchrotron emission of the powerful jets and lobes in the case of RLQs. In order to overcome these problems I followed two methods, one for each case. I try to remove the problem of the warm dusty torus emission by matching our populations in redshift and optical luminosity. In this way, although I expect that FIR emission is largely uncontaminated by the AGN (e.g. Haas et al., 2003; Hatziminaoglou et al., 2010), any possible contamination would be the same for both populations. Different evolutionary models for the two populations could be also a possibility for different AGN contamination in the case of more evolved AGN, in which the BH gets closer to its final mass. However, this could not affect our results as optical luminosity is a good tracer of the median accretion rate onto the central black hole and the Eddington ratio distribution is expected to be similar for the two populations at least at lower redshifts ( $z < 2.0$ ) and/or optical luminosity (e.g. Shankar, 2010) with both types of quasars being likely powered by similar physical mechanisms.

For the case of synchrotron contamination, I estimated an upper limit on the possible contamination at FIR bands. Based on these estimations, I either rejected contaminated objects from our sample or subtracted the synchrotron emission. Using these methods I consider that the results are unaffected by possible synchrotron contamination effects.

### 3.5.1 Star-formation excess

Although the initial formation mechanisms of SMBHs remain largely unknown, the notion of seed black holes that form primordially and grow into a distribution of BH masses has been around for four decades (e.g. Carr & Hawking, 1974; Silk & Rees, 1998). The mass distribution would necessarily be governed, at least partially, by the density of the surrounding gas; the most massive black holes would then form in regions of the highest gas density, and it will be in these sites where we observe high-redshift radio galaxies and RLQs. The highly relativistic, supersonic jets that power into the surrounding medium are able to trigger star formation along cocoons surrounding the jets (e.g. Bicknell et al., 2000; Fragile et al.,

2004). This model provides the means of orchestrating star formation over tens of kiloparsecs on light crossing timescales. This process has been invoked to explain the radio-optical alignment effect at high redshift (Rees, 1989). More recent, Drouart et al. (2014) suggested that radio galaxies have higher mean sSFR than typical star-forming galaxies with the same black hole mass at least at higher redshifts,  $z \leq 2.5$ .

Here I explore the link between radio AGN emission and star formation. Assuming that FIR luminosity is a good tracer of star formation, my results show a strong positive correlation between radio and FIR luminosity, independent of redshift, for RLQs (see Section 3.4.4). In contrast, no such correlation was found for RQQs. These results support the idea of a strong alignment between dust and jets from SMBHs. Powerful radio jets may increase the star-formation activity by compressing the intergalactic medium (e.g. Silk & Nusser, 2010b), resulting in the observed star-formation excess I found for the RLQs.

However, the results are not uniform over all the optical luminosity range of our sample. RLQs seem to have higher star-formation rates (and FIR luminosities) than RQQs only at lower optical luminosities. Specifically, I find that star-formation shows a possible break around to  $\log_{10}(L_{\text{opt}}/W) \approx 38.5$  in the case of RLQs. For lower optical luminosities, RLQs have higher star-formation than RQQs, while for higher optical luminosities both populations tend to have comparable  $\langle \text{SFR} \rangle$  within their errors. The same results were found no matter which method we used to estimate the FIR luminosity. This difference between the two populations could be an effect either of redshift or of AGN activity, as the optical luminosity is affected by both of these parameters. However, both populations seem to have the same FIR luminosity distribution over all redshifts within their errors. As the star-formation excess is not observed in the case of redshift distribution I deduce that the AGN activity is the main reason of this difference. Although I have found no strong evidence of star-formation suppression due to the radio activity at any redshift there are some hints like the decrease of the mean FIR flux densities at higher redshift in the case of RLQs (see Table 3.1). A possible suppression of the star-formation due to the radio-jet activity would be in agreement with a model of short-lived episodes of radio-loud states in the life of all AGN. These events are associated with the active nucleus and AGN feedback.

The physical mechanisms responsible for triggering the active AGN phase are still debated. Indeed, it is still poorly understood whether the AGN activity impacts star formation or vice versa. Negative AGN feedback, where the AGN emission is believed to be responsible for gas heating, is necessary in order to explain the strong suppression of star formation especially in the most massive galaxies (e.g. Croton et al., 2006; Hopkins et al., 2010). The feedback process becomes more complicated in the case of powerful radio sources where there are results that suggest a positive feedback due to the jets inducing star formation in the host galaxy (e.g. Elbaz et al., 2009). These two mechanisms could be the possible explanation for the star-formation difference between the two populations and the minimum observed in the case of RLQs.

I found that the  $\langle \text{SFR} \rangle$  as a function of optical luminosity shows a bi-modality for  $\log_{10}(L_{\text{opt}}/W) \leq 38.5$  with the RLQs covering the upper level. If this bi-modality could be explained by the presence or absence of powerful radio jets, what could explain the same level of star formation for both populations at  $\log_{10}(L_{\text{opt}}/W) > 38.5$ ? As we move to higher optical luminosities, the AGN luminosity increases as a result the direct effect of the radiation from the AGN on the host galaxy ISM. In this case, the feedback is predominantly negative, though occasional positive feedback may occur in the form of jet-induced star formation. As the jets cannot now play the critical role they did at lower luminosities both of the populations have the same star-formation trend. These results are in agreement with our previous work in radio-loud and radio-quiet quasars (Kalfountzou et al., 2012).

### 3.5.2 Host galaxy and dust properties

Based on diverse studies of several samples, it can be said that RLQs are associated with luminous elliptical galaxies while RQs are usually found in both elliptical and spiral hosts, depending on the optical luminosity threshold. Generally, it has been proposed that the nuclear luminosity is related to the morphology of the host, but AGN more luminous than a certain luminosity limit can only be hosted by massive spheroidals (e.g. McLure et al., 1999; Dunlop et al., 2003). Based on this assumption, our results for different dust temperature could have their origin in the different hosts of radio-loud and radio-quiet quasars.

In the case of the single-temperature model, I found that RLQs tend to have lower dust temperatures, at least for lower redshifts and/or lower optical luminosities. Low temperatures are associated with the old stellar population of elliptical galaxies. This fact is in agreement with the previously mentioned studies regarding the hosts of radio-loud and radio-quiet quasars. On the other hand, the low dust temperature could be associated with a strong cold component described by the two-temperature grey-body model. Dust temperatures of 10-15 K would imply dust masses of up to  $10^{10} M_{\odot}$ , quite unrealistic for the case of elliptical hosts and generally for quasar hosts where the expected range of dust mass is  $10^7 - 10^9 M_{\odot}$ . In this sample, despite the low temperatures just a few sources are found to have  $M_{\text{dust}} > 10^9 M_{\odot}$ , which is not unexpected as most of them have FIR fluxes even lower than the  $2\sigma$  detection limit. Moreover, based on the single-temperature model, I found that both the populations tend to have statistically indistinguishable dust masses.

An additional point which could play a significant role in the observed differences would be the gas supply in the host galaxies of RLQs and RQs. The gas content is the fundamental ingredient driving star formation in galaxies. Additionally, AGNs are preferentially hosted by gas rich galaxies (e.g. Silverman et al., 2009; Vito et al., 2014) which is not surprising since gas accretion onto SMBH is the process at the origin of nuclear activity. Given the dependency of both SFR and AGN on the gas content, the enhanced star formation in AGN galaxies appears to be primarily the result of a larger gas content, with respect to the bulk

of the galaxy population at similar stellar masses (e.g. [Rosario et al., 2012](#); [Santini et al., 2012](#)). Many semi-analytic models and direct observations suggest that the gas fractions in galaxies grow at lower stellar masses and, at fixed mass, increase at earlier cosmic epochs. In the local Universe, low mass galaxies are generally gas-rich and actively star-forming, while the highest mass galaxies are almost always gas-poor and have very little ongoing star formation. This is probably why optical AGN with the highest values of  $L/L_{Edd}$  tend to occur in galaxies with the smallest bulges and black holes ([Heckman et al., 2004](#)). Assuming Gaussian quasar Eddington ratio distributions at all epochs, then the optical luminosity which is used as an AGN activity tracer would map into BH mass and thus on galaxy mass. In this case, RLQs with lower optical luminosities should, on average, be associated with lower mass and gas-rich galaxies (see [Figure 3.4](#), bottom panel) for which the effects of a jet-driven star-formation rate may be more evident. On the other hand, the fact that no SFR difference is detected between the two populations at higher redshifts or at higher optical luminosities, when gas fractions should grow, could imply that both populations evolve in gas fractions at the same rate.

In order to explain these possible temperature differences I have to take into account that the integrated dust temperature depends also on the dust distribution throughout the galaxy. Previous studies (e.g. [Goudfrooij & de Jong, 1995](#); [Leeuw et al., 2004](#)) investigating the origin of dust in elliptical galaxies proposed the presence of various components. Similarly, I used a two-component model to describe the FIR properties of our sample, a warm dust component ( $T_w = 35$  K) and a cold one ( $T_c = 15$  K). [Goudfrooij & de Jong \(1995\)](#) proposed the presence of at least two sources of the observed interstellar matter (ISM) in elliptical galaxies, mass-losing giant stars within the galaxy and galaxy interactions. Minor mergers and/or accretion of material from nearby companions could possibly explain the presence of the warm and cold components. Such an assumption of an external origin for the ISM in the early-type galaxies leads to a strong link with the environment of quasars. [Falder et al. \(2010\)](#) showed that RLAGNs appear to be found in denser environments than their radio-quiet counterparts at  $z \sim 1$ . These environments represent ideal candidates for galaxy-galaxy interactions. In this case, the cold dust properties in RLQs could have an external origin.

## 3.6 Conclusions

In this chapter I have studied the FIR properties and the star-formation of matched samples of radio-loud and radio-quiet quasars. The main result of our study is that RLQs have higher SFRs than RQs at low optical luminosities. This result is in agreement with my previous work ([Kalfountzou et al., 2012](#)) where the [O II] emission was used as a tracer of the star-formation.

Additionally, I have found a strong correlation between jet activity and the star-formation,

controlling the effect of redshift, in the case of RLQs and especially at low optical luminosities and redshifts. This correlation supports the idea of the jet-induced star-formation.

The possible differences I found between the two populations regarding the dust mass and dust temperature could explain the differences in star-formation rate, but they also point the way forwards further investigation of the evolution of their host galaxies and their environment and their correlation with AGN activity.

*With silent strides Odysseus then shot back the bolt, passed lightly through the courtyard and sped down the street. Some saw him take the graveyard's zigzag mountain path, some saw him leap on rocks that edged the savage shore, some visionaries saw him in the dead of night swimming and talking secretly with the sea-demons, but only a small boy saw him in a lonely dream sit crouched and weeping by the dark sea's foaming edge*

[The Odyssey: A Modern Sequel (1938)] - Nikos Kazantzakis

# 4

## The star formation rate of $z \sim 1$ AGN

This chapter is reproduced from the paper: *The star formation rate of  $z \sim 1$  AGN* by **E. Kalfountzou**, J. Stevens, M. J. Jarvis, D. Wilner, M. J. Hardcastle, M. Elvis, M. Trichas et al. to be submitted for publication in MNRAS, 2015

### Abstract

Several studies support the existence of a link between AGN activity and the star formation in their host galaxy. In addition, radio jets have been argued to be an ideal mechanism for the direct interaction between the AGN and the host galaxy. However, a drawback of previous surveys is that they are fundamentally limited by the degeneracy between redshift and luminosity in flux-density limited samples. To overcome this limitation, I present FIR *Herschel* observations of 74 RLQs, 72 RQQs and 27 RGs, selected at a single cosmic epoch of  $0.9 < z < 1.1$  which span over two decades in optical luminosity. Submillimeter Array (SMA) observations at  $1300 \mu\text{m}$  for the RLQ sample were obtained to estimate the level of the synchrotron contamination of the FIR bands. By decoupling luminosity from evolutionary effects and using the FIR luminosity as a tracer of the SFR, I investigate how the SFR depends on AGN luminosity, radio-loudness and orientation. I find that: 1) the SFR shows a weak correlation with the bolometric luminosity for all AGN sub-samples, 2) the RLQs show a SFR excess of about  $300 M_{\odot} \text{ yr}^{-1}$  (a factor of 1.4) compared to the RQQ sample, matched in terms of black hole mass and bolometric luminosity, suggesting either positive radio-jet feedback or radio AGN triggering being linked to the star formation triggering and 3) RGs have lower SFRs by a factor of 2.5 than the RLQs sub-sample with the same BH mass and bolometric luminosity but not jet power. I suggest that there is some jet power threshold at which radio-jet feedback switches from enhancing star formation (by compressing gas) to suppressing it (by ejecting gas). I expect that this threshold depends on both galaxy mass and jet power.

## 4.1 Decoupling the evolution effects

Observationally, the fact that at high redshift AGN offer the only opportunity to directly investigate the evolution of the BH - galaxy relation has re-invigorated interest in studies of AGN host-galaxy evolution. However, a drawback of previous works is that they are fundamentally limited by the strong correlation between redshift and luminosity, i.e., only the most powerful sources are observed at high redshifts and, due to the much smaller volume probed, only the less luminous, more abundant populations are found at lower redshifts.

In Chapter 3, I investigated the FIR properties of a large RLQ and RQQs sample, over a wide range of optical, radio luminosity and redshift. My results of higher SFRs in RLQs than RQQs particularly at low optical luminosities supports the idea of the jet-induced star formation. Although it is apparent that some form of feedback is needed to explain these results, we have to keep in mind that many parameters could cause the observed differences. Specifically, evolution effects could be strong as low and high optical luminosity sources have significantly different redshift,  $z \approx 0.9$  and  $z \approx 2.5$ , respectively.

While fundamental questions about the relation between radio-loud and radio-quiet AGN, and how they affect the host galaxy, are in principle soluble with multiwavelength surveys, with already interesting results, most of them remain intractable until we have a comprehensive AGN sample in which influence of cosmological evolution have been decoupled from the effects of luminosity, radio-loudness and orientation. The sheer size of the SDSS QSO sample (Schneider et al., 2005) makes it possible to generate a homogeneous sample of quasars covering a large range in luminosity at a single epoch. The redshift range  $0.9 < z < 1.1$  is ideal for this study because this allows us to probe over two decades in optical luminosity. Importantly, this redshift is the minimum at which we have a large enough sample of high luminosity quasars with which to compare to the bright quasars found at higher redshifts.

The *Herschel Space Observatory* (Pilbratt et al., 2010), with its unprecedented FIR sensitivity and wavelength coverage, offers the only way of measuring the instantaneous SFR with the minimal AGN contamination (e.g. Netzer et al., 2007; Hatziminaoglou et al., 2010; Mullaney et al., 2011b). To do this, we obtained five-band *Herschel* photometry for a  $z \approx 1$  benchmark sample of 173 AGN using the *Photodetector Array Camera* (PACS) at 70 and 160  $\mu\text{m}$  and the *Spectral and Photometric Imaging Receiver* (SPIRE) at 250, 350 and 500  $\mu\text{m}$  on-board the *Herschel Space Observatory*. We have additionally obtained millimeter observations of the RLQs sub-sample using Submillimeter Array (SMA) radio interferometer at 1300  $\mu\text{m}$  to investigate the radio-jets synchrotron contamination to the FIR emission.

This chapter is structured as follows. In Section 4.2 I describe the sample selection, the *Herschel* and SMA observations carried out, and the steps used for measuring the flux densities in the observed bands. BH and host galaxy properties and analysis are presented in Section 4.3. In Sections 4.4-4.6 I present our results about the star formation dependence on

AGN luminosity, radio jets and orientation, respectively. In Section 4.7 I list and discuss the conclusions of this work.

## 4.2 Data

The data presented in this chapter consist of *Herschel*-PACS and SPIRE images of 173 AGN, along with millimeter images taken at  $1300\ \mu\text{m}$  with SMA for the RLQs. The sample is split into three sub-samples, all at the single cosmic epoch of  $0.9 < z < 1.1$ : 74 RLQs, 72 RQQs and 27 RGs. This redshift range is convenient because, as shown in Fig. 4.1, the SDSS survey allows us to probe over 5 magnitudes in quasar optical luminosity. This sample thus enables us to decouple luminosity generated effects from evolutionary ones, something which has plagued many other flux density limited studies in this area.

This redshift is the minimum at which we have a large enough sample of high luminosity quasars ( $M_i < -25.0$ ) which can be compared to the bright quasars found at higher redshifts. Observing both unobscured (type-1) AGN, in the form of quasars, and obscured (type-2) AGN, the RGs, allows us to test AGN unification schemes (e.g. Antonucci, 1993). Details of the selection of the quasars are presented by Falder et al. (2010) while the RG selection is described by Fernandes et al. (2015). A list of the main properties of the sample objects is given in Appendix B (Table A). In the next section I give a brief description of the sample criteria as they affect this chapter.

### 4.2.1 Sample selection

The quasars were selected by their optical colours in the SDSS Quasar Survey (Schneider et al., 2005). The sheer size of the SDSS Quasar Survey allowed us to select a large enough initial sample to define matched samples of RLQs and RQQs. The initial quasar sample was then cross referenced with the NRAO VLA Sky Survey (NVSS; Condon et al., 1998), the VLA FIRST survey (Becker et al., 1995) and the Westerbork Northern Sky Survey (WENSS; Rengelink et al., 1997) to pick out the RLQs and RQQs. Regarding the RLQs in the sample, the initial cross-match was done with the WENSS low-frequency survey (325 MHz). Therefore, the RLQs are selected based on optically thin extended emission, which means that the sample selection should be largely orientation independent. The RGs were selected from the low frequency, (178 or 151 MHz; orientation independent) radio samples 3CRR (Laing et al., 1983), 6CE (Eales, 1985), 7CRS (Willott et al., 1998) and TOOT surveys (Hill & Rawlings, 2003). For the 6C objects the redshifts are taken from Best et al. (1996), Rawlings et al. (2001) and Inskip et al. (2005), and for the 6C\* and TOOT objects from Jarvis et al. (2001b) and Vardoulaki et al. (2010), respectively. Combining these surveys, 27 RGs are found in the same  $0.9 < z < 1.1$  redshift range as our quasars. The smaller RGs sample thus arises from the limit of the known RG population at  $z \approx 1$  at the time the samples were defined.

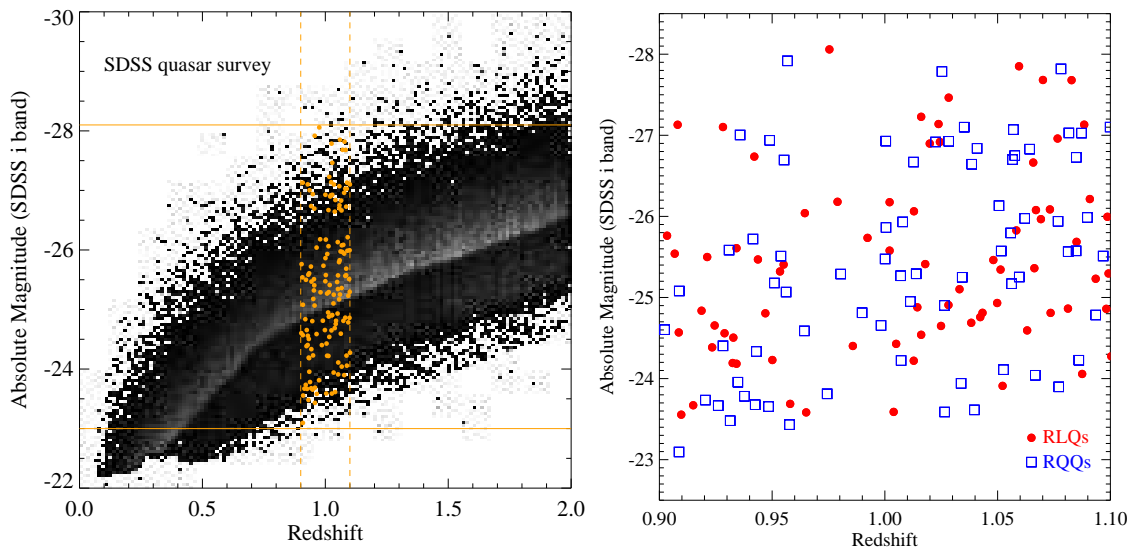


FIGURE 4.1: Left: Optical (SDSS  $i$ -band) absolute magnitude density map of the SDSS quasar sample as a function of redshift. The orange dots are the RLQs and RQQs included in the  $z \approx 1$  sample. Selecting the sample at  $z \approx 1$  ensures that we have the maximum coverage in luminosity while still probing enough volume to sample the bright end of the luminosity function, where most of the quasars at higher redshift lie. Optical absolute magnitude (SDSS  $i$ -band) plotted against redshift for the quasars of our sample. RLQs are shown with red circles and RQQs with open blue squares.

RLQs were chosen to have a low frequency WENSS (325 MHz) flux density of greater than 18 mJy, which is the  $5\sigma$  limit of the survey (see Fig. 4.2). This selection ensures that the vast majority of the RLQs included are characterized by steep radio spectrum, avoiding flat radio spectrum quasars and blazars. Additionally, the low frequency radio flux selection allows us to compare the RLQs to the RGs without a severe orientation bias. Falder et al. (2010) also presents a classification of the quasar population into radio-loud and radio-quiet based on the definition used by Ivezić et al. (2002). With the exception of 4 objects all of our RLQs have  $R_i > 1$  where  $R_i = \log_{10}(F_{\text{radio}}/F_i)$  and  $F_{\text{radio}}$  and  $F_i$  are flux densities measured at 1.4 GHz and in the  $i$ -band respectively, so that the RLQ class we use here maps well onto traditional radio-loud/quiet definitions.

The RQQs were defined as being undetected by the FIRST survey at the  $5\sigma$  level. FIRST was used for this definition because it provides a more sensitive flux density limit than WENSS. Falder et al. (2010) performed a stacking experiment to reveal the average value of the radio power at 1.4 GHz (e.g. White et al., 2007) for the RQQs in our sample. Using this technique they found an average flux density for the RQQs at 1.4 GHz of  $0.10 \pm 0.02$  mJy (i.e. a  $5\text{-}\sigma$  detection). We extrapolate this estimate to a 325 MHz flux density of  $0.30 \pm 0.06$  mJy assuming a spectral index of 0.7. At  $z = 1$  this corresponds to a 325 MHz luminosity,  $\log_{10}(L_{325\text{MHz}}/\text{W Hz}^{-1} \text{sr}^{-1}) = 23.82$ .

74 RLQs and 72 RQQs matched in  $i$ -band and spanning 5 optical magnitudes were chosen for *Herschel* follow-up observations. The distribution of optical magnitudes as a

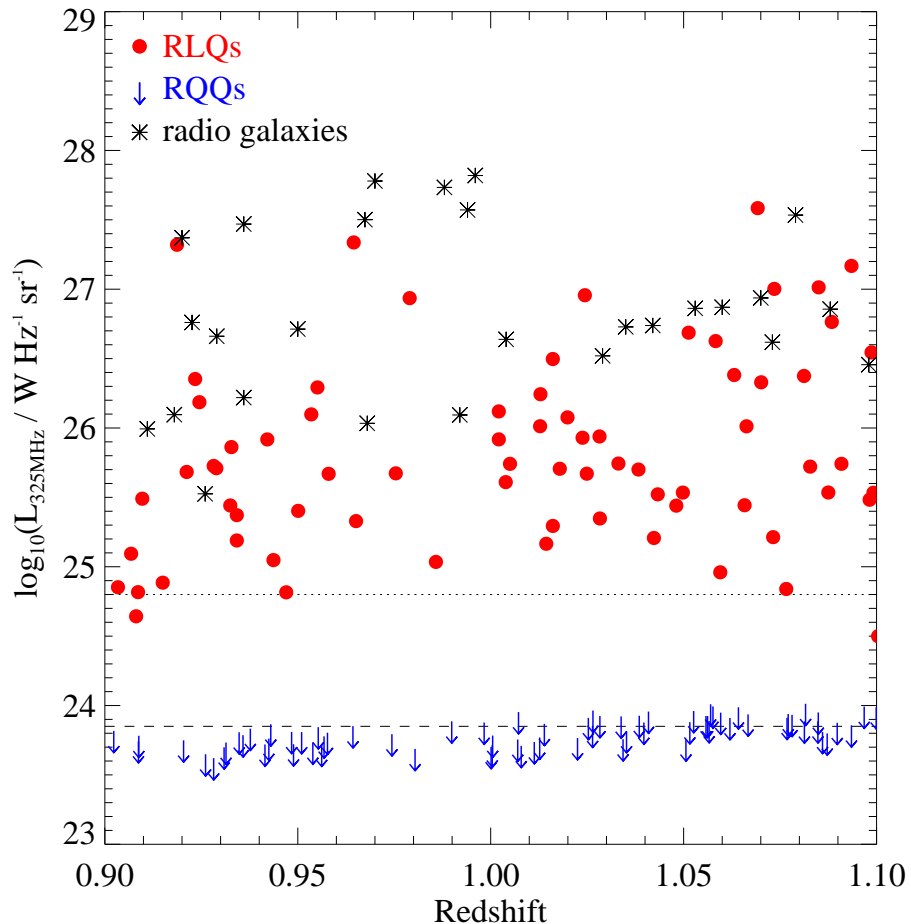


FIGURE 4.2: 325 MHz radio luminosity vs. redshift for our sample. RLQs are shown with red circles and RGs with black asterisks. For the RQQs,  $5\sigma$  upper limits (extrapolated to rest-frame 325 MHz) from the FIRST survey are shown as blue upper limits. The dashed line shows the average  $5\sigma$  limit of the WENSS survey, converted to a luminosity at  $z \approx 1$  by assuming  $\alpha = 0.7$ . The dotted line shows the average  $5\sigma$  limit of the FIRST survey, extrapolated to 325 MHz. The RQQs were selected to have a radio luminosity falling below this line. The assumed spectral indices for some conversions explains why some objects fall between the lines on this plot.

function of redshift of the selected sources is shown in Fig. 4.1. Fig. 4.2 shows the radio luminosity distribution within the selected redshift range for RLQs and RGs. It is clear that, on average, the RGs are more radio-luminous than the RLQs, albeit with a significant overlap. The results of this selection are further discussed in Section 4.6. For the RQQs I have placed an upper limit on their radio luminosity (see Fig. 4.2). In comparison to these limits, RLQs are at least one order of magnitude more radio-luminous than RQQs. The radio luminosity gap between the RLQs and RQQs (Fig. 4.2) is due to our selection rather than a real radio power dichotomy, because of the different WENSS and FIRST survey depths from which the RLQs are selected.

### 4.2.2 Herschel photometry

The data for this work were obtained as part of the *Herschel* project ‘A benchmark study of active galactic nuclei’ with 55.1 hours of observations allocated. SPIRE observations for 25 objects in our sample were obtained as part of other public *Herschel* projects (see Table A). The raw data for these objects were retrieved from the *Herschel* Science Archive (HSA), and the data reduction was performed as detailed below.

#### PACS

PACS (Poglitsch et al., 2010) photometric observations at 70  $\mu\text{m}$  (5 arcsec angular resolution) and 160  $\mu\text{m}$  (10 arcsec angular resolution) bands were carried out in the scan-map observational mode. A concatenated pair of small maps of 4 arcmin length, each at two different orientations was obtained for each source with a total integration time per source of 426-860 secs. The *Herschel Interactive Processing Environment* (HIPE, Ott, 2010, version 9.1.0) was used to perform the data reduction, following the standard procedures for deep field observations. The high-pass filtering method was applied to create the maps allowing us to minimize the point-source flux loss (Popesso et al., 2012). A preliminary map was created after combining the individually (for each scan orientation) processed scan maps. Using results from Popesso et al. (2012), I choose a masking strategy based on circular patches at prior positions. This method avoids significant flux losses due to the high-pass filter while leads to flux losses which are independent of the PACS flux densities (Popesso et al., 2012). The final data reduction and mosaicing were then performed using the mask generated in the previous step.

Due to the fact that none of the sources show extended FIR emission and almost  $\sim 50$  per cent of the total sample is not detected at  $>3\text{-}\sigma$  level I do not carry aperture extraction of the FIR fluxes in order to consider all sources equally, even the ones with non-detections, rather than using their  $3\sigma$  upper limits. Instead, I directly measure the FIR flux densities from the PSF-convolved images for both bands. I take the flux density to be the value in the image at the pixel closest to the optical position of our targets. I compared the direct flux density measurements to the aperture extraction for the FIR-detected sources and found an insignificant  $< 5$  per cent difference. The photometric uncertainties of each map were estimated from a set of 500 randomly selected positions (e.g. Lutz et al., 2011; Popesso et al., 2012). The only requirement was that the measured pixels should have a total integration time at least 0.75 times the integration time of that of the source of interest in order to exclude the noisy map edges (e.g. Leipski et al., 2013). The  $1\sigma$  photometric uncertainty of the map is taken to be the  $\sigma$  value of the fitted Gaussian to the flux densities measured in these 500 random positions.

## SPIRE

SPIRE (Griffin et al., 2010) photometric observations at 250 (18.2 arcsec angular resolution), 350 (24.9 arcsec angular resolution) and 500  $\mu\text{m}$  (36.3 arcsec angular resolution) were carried out in small scan-map observational mode. The total time per source was 487 secs. Similarly to the PACS data, I used the HIPE standard pipeline to reduce SPIRE data. The FIR flux densities in each band were directly measured from the PSF-convolved images at the pixel closest to the optical position of our targets.

As demonstrated from deep extragalactic observations (e.g. Nguyen et al., 2010), SPIRE maps are dominated by confusion noise at the level of 6-7 mJy beam<sup>-1</sup>. The method I have adopted in order to determine the photometric uncertainties in the SPIRE maps is fully described by Elbaz et al. (2011) and Pascale et al. (2011). I have measured the noise level at the position of each source on the residual map produced by removing all individually-detected sources above the detection threshold, and then is convolved with the PSF (Elbaz et al., 2011). On this convolved residual I determined the dispersion of pixel values in a box around each target, whose size is 8 times the PSF full width at half maximum (the PSF FWHM for the SPIRE passbands is: 18.2 arcsec, 24.9 arcsec, and 36.3 arcsec at 250, 350, and 500  $\mu\text{m}$ , respectively) (e.g. Elbaz et al., 2011; Leipski et al., 2013). The box size was chosen as a compromise between appropriate sampling of the surroundings of the target source and avoiding the noisy areas at the edges of the map.

### 4.2.3 SMA photometry

#### Synchrotron Contamination

Radio-loud quasars are known to have strong non-thermal beamed core components which could possibly enhance the emission all the way through to the thermal-infrared and possible the optical waveband (e.g. Blandford & Rees, 1974). However, non-thermal components such as lobes and hot spots could also contaminate FIR emission, despite the fact that their flux falls toward higher frequencies. Archibald et al. (2001) proposed that high-frequency radio observations are needed to measure the contribution from non-thermal emission to the FIR waveband of radio sources (e.g. a straight-line extrapolation or a parabolic fit which reflects a degree of the steepening). We expect that the RLQ sample should be dominated by steep-radio-spectrum sources as they are selected on their optically thin lobe emission by using low frequency WENSS (325 MHz) observation. However, given the lack of high-frequency radio observations, the best estimate of the synchrotron contamination assumes a spectral index based on the available radio data (WENSS and FIRST or NVSS). This could be a conservative estimate, given that the steep-spectrum synchrotron component is likely to fall more quickly than the fitted power law, or be a highly uncertain extrapolation to the SPIRE bands. RGs are expected to have fainter flat-spectrum core components as a result of

their larger angle to the direction of the observer.

### The SMA sample

Given that in this work I am interested in studying the heating mechanism of the warm/cool dust sampled through the FIR, we have to be aware of how possible non-thermal, synchrotron emission could bias our star-formation rate estimate. For a RLQ to be considered as a candidate for synchrotron contamination at the SPIRE bands, the power-law extrapolation of the total (steep-spectrum-dominated) radio lobe/hot-spot flux must fall close to (within the  $3\sigma$  error) or above the  $500 \mu\text{m}$  flux density (*Herschel*-SPIRE). I emphasize that this is a conservative estimate, given that the steep-spectrum synchrotron component is likely to fall quicker than the fitted power law at higher frequencies. Indeed, other authors (e.g. Archibald et al., 2001; Jarvis et al., 2001b; Shi et al., 2005; Cleary et al., 2007) fit a parabola, or multiple power-law fits, to the steep-spectrum components in order to take this high-frequency steepening into consideration.

However, the power-law extrapolation does not take into account the potential contribution from a flatter spectrum core/jet component. Using the 1.4 GHz radio observations or the additional data at higher frequencies from the literature as a reference point, and assuming the core spectral shape to be flat, I deem non-thermal contamination to be possible for those objects for which the highest available radio frequency flux falls close to (within the  $3\sigma$  error) or above the  $500 \mu\text{m}$  flux density. Note again that this is fairly conservative criterion in the sense that the shape of flat-spectrum radio core components may not remain flat up to FIR bands as I have assumed. High-frequency SMA observations at  $1300 \mu\text{m}$  for the RLQ sample allow us to measure the possible contribution of the non-thermal components to the FIR emission accurately, and minimise the high uncertainties (1-2 orders of magnitudes) caused due to the use of different types of extrapolations (steep-spectrum or flat-spectrum components).

I initially used the existing radio data to assess the potential for synchrotron contamination. For each RLQ we have used an upper (flat-spectrum-dominated; red dashed line) and a lower limit (steep-spectrum-dominated; black dashed line; Fig. 4.3). I have found that 24 RLQs have potential contamination only when I assume a flat-spectrum core/jet component (Fig. 4.3; left), and 20 RLQs have potential contamination to their thermal FIR emission from either a steep-spectrum or a flat-spectrum component (Fig. 4.3; right). For each of these sources, using the  $500 \mu\text{m}$  flux density as a reference and assuming the spectral shape to be flat, I have estimated the minimum flux density at  $1300 \mu\text{m}$  in order to have a significant level of non-thermal contamination (Fig. 4.3; upper limit). For the vast majority of the sources this level is at  $\sim 7 - 10 \text{ mJy}$ .

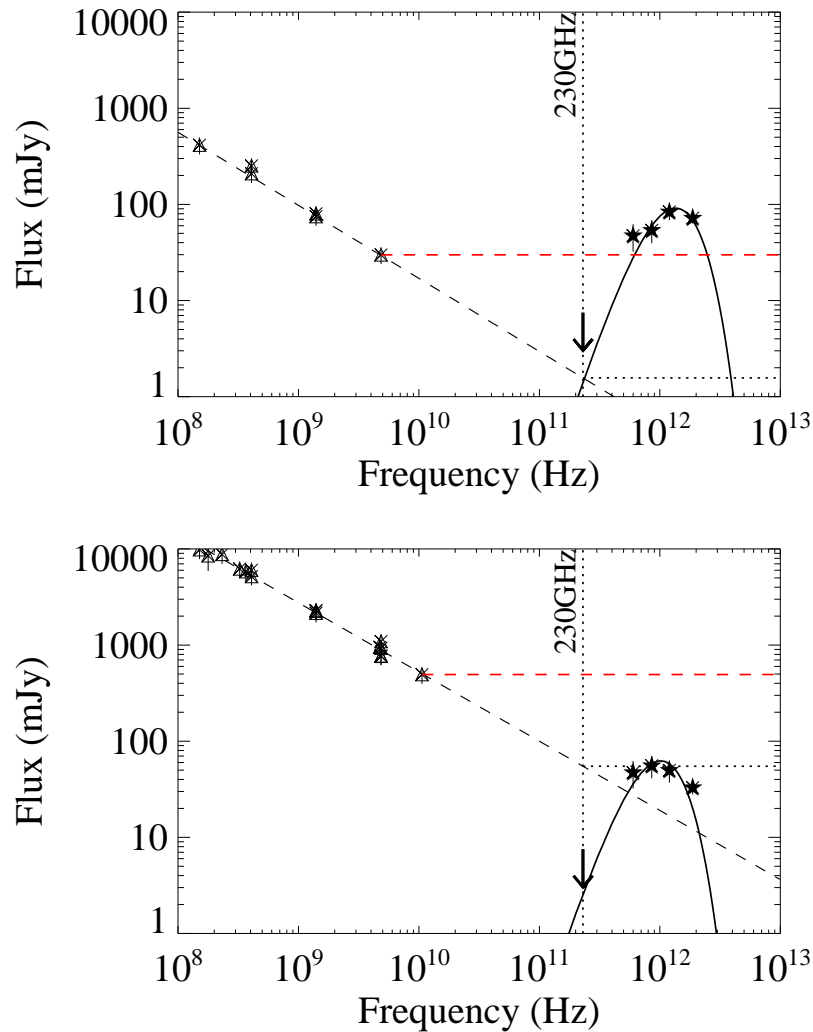


FIGURE 4.3: Spectral energy distribution at radio and FIR wavelengths for a representative sample of the 44 RLQs. Filled black stars: the FIR data (*Herschel*-SPIRE), Triangles: the radio data (FIRST, NVSS, WENSS and literature), Arrow: the maximum required flux at  $1300\ \mu\text{m}$  in order to not have a significant synchrotron contamination in the FIR bands. Error bars illustrate the  $3\sigma$  errors. Black dashed line: Linear fit to radio data; red dashed line: flat radio spectrum; black solid line: grey-body fit; black dotted horizontal line: flat radio spectrum extrapolation at  $1300\ \mu\text{m}$ .

### The SMA observations

I used the SMA (Ho et al., 2004) to observe the 44 RLQ candidates at wavelengths near  $1300\ \mu\text{m}$  (frequencies near 230 GHz) to assess the contribution from synchrotron emission to fluxes measured in the FIR bands. The SMA observations were performed in the 2014-2015 summer and winter semesters, typically in snapshots with 20 minutes on source bracketed by 2 minutes on nearby calibrators to determine complex gains. Many of the observations were executed in available short timeslots before or after other scheduled programmes and shared receiver tunings, correlator setups, as well as flux and passband calibrators. The total bandwidth available was 8 GHz, derived from two sidebands spanning  $\pm(4 - 8)$  GHz from the local oscillator (LO) frequency. For each source, flux densities were measured by fitting

a point source model to the visibilities using the task `uvfit` in the Miriad software package. Each source was also imaged in order to confirm the visibility fit results. Table A lists the dates of observation, the characteristic atmospheric opacity during the observations, and the fitted flux densities. Variations in sensitivity are due to both weather conditions and the number of array antennas operating at the time of the observations. Overall, 15 sources were detected at the  $> 4\sigma$  level (a conservative threshold for these snapshot observations). The absolute flux scale has an estimated systematic uncertainty of  $\sim 20$  per cent.

Using the SMA observations I have classified the 44 sources identified as having possible synchrotron contamination into two categories. In the first category, I have identified 14 sources with significant synchrotron contamination. All of these sources have been rejected from the sample and from further analysis. The vast majority of them (10) were detected at  $> 4\sigma$  with the SMA with some extreme cases reaching even  $S_{1300\mu\text{m}} \approx 200$  mJy. Some representative examples of the SEDs from this group are presented in Fig. A.1. In this category the SMA data exceed the linear extrapolation from the lower-frequency radio data for 8 sources (three are upper limits), for three sources they follow the linear prediction, while for the last three sources they indicate the need of a steeper radio component at the higher frequencies. However, even in the last two cases, the contamination to the FIR band is significant and therefore these sources have also been excluded from this work.

In the second category I have classified 30 sources without significant synchrotron contamination. For four cases there is a clear SMA detection at  $> 4\sigma$  while all the other observations indicate an upper limit. For this group of sources, the SMA data exceed the linear extrapolation in seven cases (all of them are upper limits) while in 18 cases they indicate the need of a steeper radio component at the higher frequencies. Examples of the SEDs from this group are also presented in Fig. A.1.

Overall, I have rejected 17 RLQs from our sample, 14 based on their SMA observations, while three additional sources were classified as flat-spectrum RLQs or Blazars based on literature radio observations ([HB89] 0906+015, SDSS J133749.63+550102.2, SDSS J161603.76+463225.2) have been rejected. As I describe in Section 4.3.2, there are no particular trends for the sources excluded from our sample and they do not affect the sample matching between RLQs and RQQs.

From these results, it is clear that high-frequency radio observations for similar studies are crucial as the linear extrapolation from lower frequencies seems to work only for a small fraction of our sources ( $\sim 20$  per cent). Although most of the cases indicate that the steep-spectrum synchrotron component is likely to fall quicker at higher frequencies, I find that in  $\sim 30$  per cent (almost half of them are upper limits) a high-frequency core radio component is required to describe the radio spectrum. This would also agree with recent findings (e.g. Whittam et al., 2013, 2015). I note that almost half of these SMA observations are upper limits. Radio core variability might be responsible for some of these strong high-frequency components (e.g. Barvainis et al., 2005).

### 4.3 The black hole and host galaxy properties

In this section I describe how the key parameters for the analysis of this work are derived, namely BH and stellar masses, Eddington ratios, bolometric luminosities and FIR luminosities. I further explore the importance of AGN contamination in the form of hot dust around the putative torus at FIR wavelengths comparing their FIR colours against normal galaxies. I finally study the correlation between the radio and FIR emission, examining at the same time whether some of the radio emission could be the result of star formation, rather than AGN activity.

#### 4.3.1 Stellar mass and black hole mass

Early studies (e.g. [Kormendy & Richstone, 1995](#); [Magorrian et al., 1998](#)) suggest a correlation between galaxy bulge and its BH mass. The ratio of the so-called  $M_{\text{BH}}-M_{\text{bulge}}$  relation ([Magorrian et al., 1998](#)) was estimated to be approximately 0.6 per cent. In the same context, more recent studies using nearby galaxy samples (e.g. [Häring & Rix, 2004](#)) find that the median BH mass is  $0.14 \pm 0.04$  per cent of the bulge mass.

For the quasars in this sample, the BH masses are computed using the virial estimator and the MgII line at 2800 Å using SDSS spectroscopy, a technique described by [McLure & Jarvis \(2002\)](#), and based on work of [McLure & Dunlop \(2004\)](#). As the  $H\beta$  line moves out of the optical window, we have to rely on the MgII lines for AGNs at  $z > 0.7$  (e.g. [Wang et al., 2009](#)). BH masses for the quasars are given in Table A. We can use the BH mass of the quasars in the sample, along with the  $M_{\text{BH}}-M_{\text{bulge}}$  relation to estimate the stellar mass of the galaxy. Despite the convenience of calibrating and using these virial estimators, one must keep in mind that the estimates of these lines are uncertain, potentially by as much as 0.4 dex (e.g. [Shen et al., 2011b](#)), due to the systematics involved in the calibration and usage (e.g. [Jarvis & McLure, 2002, 2006](#); [Marconi et al., 2008](#); [Kelly et al., 2009](#)). I assume that there is no significant evolution of the  $M_{\text{BH}}-M_{\text{bulge}}$  relation at  $z \approx 1$  from the local relation and thus use  $M_{\text{BH}} \sim 0.0014M_{\text{bulge}}$ . Indeed, studies on  $z \leq 1$  RLAGN BH-bulge mass relation found that the estimated ratio lies within the uncertainties of that found in the local Universe (e.g. [McLure et al., 2006](#)). Although evolution in the  $M_{\text{BH}}-M_{\text{bulge}}$  relation of about 0.2 dex at  $z \approx 1$  has been claimed in some papers (e.g. [Merloni et al., 2010](#)), that would not significantly add to the uncertainties and would not affect the results of this work, as all of the AGN are selected in a very small redshift range.

For the RGs of the sample, because the broad-line region is obscured, I do not have BH mass estimates as I did for the quasars. For this reason, I use the stellar mass of the galaxy,  $M_{\text{gal}}$ , determined by the SED fitting of [Fernandes et al. \(2015\)](#) for the same radio galaxy sample as used in this work. [Fernandes et al. \(2015\)](#) used the same BH-bulge mass relation ([Häring & Rix, 2004](#)) in order to calculate the BH mass of the radio galaxy sample. Implied

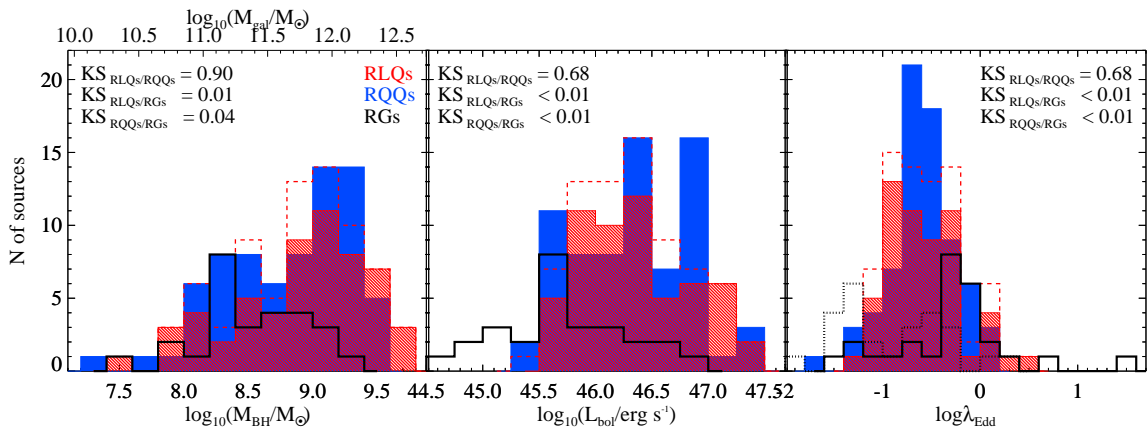


FIGURE 4.4: Distributions of BH mass,  $M_{\text{BH}}$ , bolometric luminosity,  $L_{\text{bol}}$  and Eddington ratio,  $\lambda_{\text{Edd}}$ , for RLQs (red filled), RQQs (blue filled) and radio galaxies (black line). The total RLQs population, including the sources with significant synchrotron contamination is also presented with dashed red lines. In the last panel, the Eddington ratio distribution obtained with both methods of calculating for radio galaxies is presented (dotted black line considering only the accretion energy and solid black line including also the jet mechanical energy). Note the significant increase of the total accretion energy.

$M_{\text{BH}}$  are given in Table A. The radio galaxies of the sample have BH masses in the range  $10^{7.5} - 10^{9.4} M_{\odot}$  (corresponding to  $M_{\text{gal}} = 10^{10.3} - 10^{12.0} M_{\odot}$ ) while the quasars have  $10^{7.2} - 10^{9.7} M_{\odot}$  (corresponding to  $M_{\text{gal}} = 10^{10.1} - 10^{12.4} M_{\odot}$ ). These are consistent with the range of values found in the literature for similar objects (e.g. McLure & Dunlop, 2004; McLure et al., 2006; Seymour et al., 2007; Salviander et al., 2007).

To test whether the BH and stellar mass distributions differ between the three populations we conducted a Kolmogorov-Smirnov (K-S) test for each pair. The test suggested that the BH masses for the RLQs and RQQs samples are not significantly different. The K-S test gives a result that corresponds to a probability,  $p = 0.90$  under the null hypothesis (i.e. they are statistically indistinguishable). The mean BH masses are  $\langle \log_{10}(M_{\text{BH}}/M_{\odot}) \rangle = 8.87 \pm 0.06$  for the RLQs and  $\langle \log_{10}(M_{\text{BH}}/M_{\odot}) \rangle = 8.81 \pm 0.06$  for the RQQs so the means of the two samples are consistent and well within  $1-\sigma$  of each other. I stress that this result does not contradict previous works which suggest that RLQs have more massive BH than RQQs (e.g. McLure & Jarvis, 2002) but rather, it indicates that our samples were initially matched in absolute optical magnitude and colours.

In contrast, the RG sample could not be selected to match the quasar sample in absolute optical magnitude. The RGs have nominally lower mean BH masses  $\langle \log_{10}(M_{\text{BH}}/M_{\odot}) \rangle = 8.53 \pm 0.08$ , the K-S test to the quasar sample returns 0.01 probability under the null hypothesis, a marginally significant result. Selection effects might also contribute to the observed differences (e.g. RGs are selected from radio surveys without a pre-requisite to be optically bright). I further discuss these effects in Section 4.6. The distribution of BH masses is shown for all samples in Fig. 4.4.

### 4.3.2 Accretion rate

In order to make an estimate of the AGN power for the radio galaxies an estimate of the bolometric radiative power of an AGN,  $L_{\text{bol}}$ , is required. For the radio galaxy sample, I adopted the values of  $L_{\text{bol}}$  calculated by [Fernandes et al. \(2015\)](#) from the rest-frame  $12\mu\text{m}$  luminosity, using a bolometric correction of 8.5 (e.g. [Richards et al., 2006b](#)),  $L_{\text{bol}} = 8.5\lambda L_{12\mu\text{m}}$ . The bolometric luminosity for the quasar sample has been computed from the  $3000\text{ \AA}$  luminosity ( $L_{3000}$ ) using the SDSS spectral fits and a bolometric correction of 5.15 from the composite SED in [Richards et al. \(2006b\)](#),  $L_{\text{bol}} = 5.15\lambda L_{3000}$ .

The bolometric luminosity is proportional to the accretion rate of the BH,  $\dot{M}$ , and to the fraction of accreted mass that is radiated, i.e. the radiative efficiency,  $\epsilon$ , through the expression:

$$L_{\text{bol}} = \epsilon \dot{M} c^2. \quad (4.1)$$

Assuming that  $\epsilon$  takes the fiducial value of 0.1 (e.g. [Marconi et al., 2004](#); [Shankar et al., 2004](#); [Martínez-Sansigre & Taylor, 2009](#)), I determine the accretion rate of our sources using their estimated bolometric luminosity.

With both the BH mass and the accretion rate, I can estimate the Eddington ratio of the sources in the sample. The Eddington luminosity,  $L_{\text{Edd}}$ , corresponds to a maximum accretion rate which a black hole can reach, without preventing further accretion onto it. This energy is a function of the mass of the system and is given by  $L_{\text{Edd}} = 1.3 \times 10^{31} \left(\frac{M_{\text{BH}}}{M_{\odot}}\right) \text{ W}$ . The Eddington ratio,  $\lambda$  is therefore simply,

$$\lambda \equiv \frac{L_{\text{bol}}}{L_{\text{Edd}}}. \quad (4.2)$$

Although for SMBHs accreting at a high fraction the Eddington ratio can be defined as in equation 4.2, for radio galaxies, especially those with SMBHs accreting at very low rates (e.g. low-excitation galaxies; LEGs), the contribution of the jet mechanical energy in the output of the accretion energy should be considered for the definition of the Eddington ratio. In this case, the total energy from the black hole accretion should equal the sum of the radiative luminosity and the jet mechanical luminosity (e.g. [Hardcastle et al., 2007](#); [Best & Heckman, 2012](#)). Including the contribution of the jet power,  $Q_{\text{jet}}$ , the Eddington ratio is given by

$$\lambda_{\text{rad+mec}} = \frac{L_{\text{bol}} + Q_{\text{jet}}}{L_{\text{Edd}}}, \quad (4.3)$$

where  $\lambda_{\text{rad+mec}}$  is the Eddington ratio accounting for both the radiative energy and the jet mechanical energy. I estimate the jet power using the relation

$$Q_{\text{jet}} \simeq 3 \times 10^{38} f^{3/2} (L_{151\text{MHz}}/10^{28})^{6/7} \text{ W} \quad (4.4)$$

([Willott et al., 1999](#)), where  $1 \leq f \leq 20$  represents the combination of several uncertainty

terms when estimating  $Q_{\text{jet}}$  from  $L_{151\text{MHz}}$ . Following [Fernandes et al. \(2015\)](#), I chose  $f = 10$  as this is the expectation value of a flat prior in natural space. I note that the  $Q_{\text{jet}}$  contributes significantly to the total power only in the radio galaxies of the sample, which is derived from the  $L_{12\mu\text{m}}$ , and not in the RLQs ( $< 10$  per cent). The use of any derived radio-luminosity – jet-power relation should be treated with caution, especially for the derivation of the kinematic luminosity function, as they may depend sensitively on selection effects (e.g. [Shabala & Godfrey, 2013](#)).

The distribution of bolometric luminosity and Eddington ratio are shown for all samples in Fig. 4.4. The solid black line is for  $\lambda = (L_{\text{bol}} + Q_{\text{jet}})/L_{\text{Edd}}$  and the dotted line for  $\lambda = L_{\text{bol}}/L_{\text{Edd}}$ . The Eddington ratio for radio galaxies is significantly higher in the first case, where  $\lambda = (L_{\text{bol}} + Q_{\text{jet}})/L_{\text{Edd}}$ , and this trend is dominated by high-excitation galaxies (HEGs; see [Fernandes et al., 2015](#); Fig. 7). The red shaded histograms in Fig. 4.4 represent the RLQ sample after excluding the synchrotron contaminated sources. The total RLQ population is also overplotted (red dashed lines) to stress that no selection biases are introduced in our sample after removing synchrotron contaminated RLQs. No particular trends are observed in any of the distributions between the RLQs and the RQQs as a result of the original matching in absolute optical magnitude and colours.

### 4.3.3 FIR emission in RLQs, RQQs and RGs

For each of the quasars in the sample I derive the FIR flux densities in the two PACS and the three SPIRE bands directly from the PSF-convolved images measuring the value at the image pixel closest to the optical position of our targets. The errors are estimated as described in Sections 4.2.2 and 4.2.2. I find that about 33 per cent (43/149) of the QSOs and 8 per cent (2/27) of the RGs in the sample have robust PACS and SPIRE detections. These detection rates are translated to ULIRG-like star formation luminosities suggesting SFRs of hundreds of solar masses per year.

I have separated the RLQ and RQQ samples in bolometric luminosity, BH mass and Eddington ratio bins to examine whether the fluxes vary. Within each bin I have estimated the mean of the FIR flux densities in each *Herschel* band. The estimation for each band and bin are shown in Fig. 4.5. Errors have been estimated by applying the bootstrap technique using randomly selected galaxies from within each bin. The advantage of bootstrapping is that no assumption is made on the shape of the flux distribution. Radio galaxies have significantly lower mean flux densities compared to RLQs and RQQs with a K-S test probability of  $p < 0.05$ . The only exception is the  $500 \mu\text{m}$  band which might indicate contribution for synchrotron contamination, or confusion bias, or a combination of them in the case of RGs. Regarding the total quasar sample, the mean flux density appears to increase at high  $M_{\text{BH}}$ ,  $L_{\text{Bol}}$  and  $\lambda_{\text{Edd}}$ . Comparing the RLQs to the RQQs we see that at low  $M_{\text{BH}}$ ,  $L_{\text{Bol}}$  and  $\lambda_{\text{Edd}}$  RLQs have higher flux densities in all SPIRE bands and all bins, these differences seem to

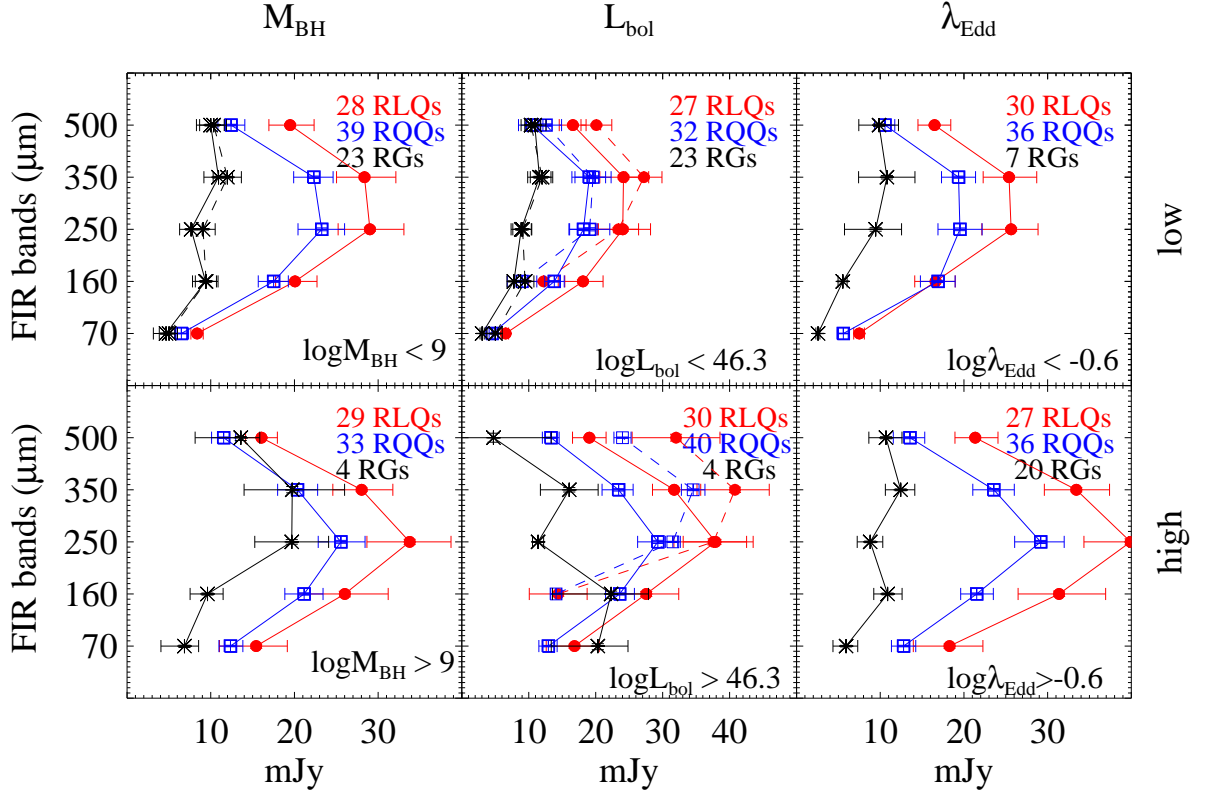


FIGURE 4.5: The PACS and SPIRE mean flux densities for RLQs (red filled circles), RQQs (blue filled squares) and RGs (black stars) as a function of BH mass (left panel), bolometric luminosity (middle panel) and Eddington ratio (right panel). For low BH mass and bolometric luminosity bins I also present the mean flux density of the total RG population (dashed black line) in order to indicate the contribution of the only four sources found at high bins. I compare the measurements to Chapter 3 RLQs (red open circles) and RQQs (blue open squares) with similar bolometric luminosities but different redshift in the middle panels. Table 3.1 of Chapter 3 provides the mean flux densities over their total RLQ sample. Here, for comparison reasons, I present their mean flux densities after removing the RLQs with potential synchrotron contamination.

become more significant at the high  $M_{\text{BH}}$ ,  $L_{\text{Bol}}$  and  $\lambda_{\text{Edd}}$ . As no obvious differences are found for the RLQs and RQQs between bolometric luminosity, BH mass and Eddington ratio bins, I give in Table 4.1 the mean flux estimations from each band and population only for high and low bolometric luminosity bins.

How do these results fit with the results in Chapter 3? For comparison, I have overplotted in Fig. 4.5 the mean flux densities from Table 3.1 (dashed lines) for low and high optical luminosity RLQs (red circles) and RQQs (blue squares). I should note that there are two main differences between these two works. Although in Chapter 3 low bolometric luminosity sample the mean redshift is  $z \approx 0.9$  and I do not expect the evolution effects to significantly change the mean properties, almost all the quasars with high bolometric luminosities have  $z > 1.0$  up to  $z \approx 3$ . Due to these difference, in order to make possible the comparison, the Table 3.1 mean fluxes have been converted to the  $z \approx 1$  rest-frame. Additionally, due to the much larger sample of RQQs in Chapter 3 ( $> 10$  times larger than

TABLE 4.1: The RLQs, RQQs and RGs FIR mean flux densities in the 70, 160, 250, 350 and 500  $\mu\text{m}$  bandpasses. The AGN populations have been separated into bolometric luminosity bins. The number of objects within each stack is also given.

Class	$\log L_{\text{bol}}$ ( $\text{erg s}^{-1}$ )	$N$ per bin	Mean flux density (mJy)				
			70 $\mu\text{m}$	160 $\mu\text{m}$	250 $\mu\text{m}$	350 $\mu\text{m}$	500 $\mu\text{m}$
RLQs	$< 46.3$	27	$6.55^{+0.44}_{-0.57}$	$18.10^{+3.00}_{-2.72}$	$24.04^{+4.15}_{-3.86}$	$24.15^{+3.76}_{-3.53}$	$16.59^{+1.97}_{-2.04}$
	$\geq 46.3$	30	$16.83^{+3.68}_{-4.22}$	$27.55^{+4.85}_{-4.85}$	$37.89^{+4.65}_{-4.82}$	$31.72^{+3.41}_{-3.24}$	$19.05^{+2.50}_{-2.51}$
RQQs	$< 46.3$	32	$4.53^{+0.31}_{-0.45}$	$13.83^{+1.48}_{-1.43}$	$18.17^{+2.06}_{-2.17}$	$19.04^{+2.44}_{-2.60}$	$10.48^{+1.64}_{-2.01}$
	$\geq 46.3$	40	$12.93^{+1.31}_{-1.42}$	$23.58^{+2.20}_{-2.11}$	$29.28^{+2.96}_{-3.02}$	$23.42^{+2.17}_{-2.47}$	$13.33^{+1.21}_{-1.30}$
RGs	$< 46.3$	23	$3.04^{+0.31}_{-0.32}$	$7.78^{+0.98}_{-1.04}$	$8.88^{+1.50}_{-1.52}$	$11.60^{+1.72}_{-1.76}$	$10.90^{+1.67}_{-1.49}$
	$\geq 46.3$	4	$20.32^{+4.50}_{-6.96}$	$22.30^{+5.58}_{-8.75}$	$11.39^{+0.83}_{-0.83}$	$16.05^{+4.31}_{-4.31}$	$4.73^{+8.63}_{-8.63}$

this work) the uncertainties of this sub-class are expected to be higher in this work. Fig. 4.5 suggests that at low bolometric luminosities, both results are in excellent agreement, at least for the SPIRE bands. The disagreement between PACS flux densities used in Chapter 3 is not unexpected since H-ATLAS PACS observations are about 5 times less sensitive than our observations (Ibar et al., 2010). Despite the similar trends, the differences between the RLQ and RQQ populations were more significant in Chapter 3 due to the smaller uncertainties for the RQQs. On the other hand, for the high bolometric luminosity bin, both H-ATLAS/SDSS RLQs and RQQs show significantly higher flux densities than the sample in this chapter, especially at 350  $\mu\text{m}$ , with a characteristic shift of the the mean peak to the 350  $\mu\text{m}$  band, with a characteristic shift of the the mean peak to the 350  $\mu\text{m}$  band, indicating colder dust temperatures. These differences provide evidences about the evolution of the FIR emission between  $z \approx 2.0$  and  $z \approx 1.0$  high bolometric luminosity quasars. That would be expected if QSOs' host galaxies are evolving with cosmic time in the same way to the general galaxy population (e.g. Madau & Dickinson, 2014).

#### 4.3.4 The FIR colours of RLQs, RQQs and RGs

I now investigate the FIR colours of our sample of AGN. A straightforward approach towards exploring the effect of AGN light on FIR emission is to compare the FIR colours of AGNs against a control sample consisting of galaxies not hosting AGNs. AGN radiation field can heat the dust resulting to systematically warmer temperatures and causing the SED to flatten out at long IR wavelengths which, in turn, leads to bluer FIR colour in galaxies with a significant AGN contamination in the FIR.

In Fig. 4.6, I compare the FIR colours of the detected AGN sub-sample and the stacked values of the total sub-samples (large symbols) to the FIR colours of  $10^6$  randomly generated black-body spectra models at a single dust temperature  $T_d$ , modified by a frequency-dependent emissivity function  $\epsilon_\nu \propto \nu^\beta$ . In generating these models, I follow the method

of [Amblard et al. \(2010\)](#) considering uniform ranges of dust temperature from 10 to 60 K, emissivity parameter  $0 < \beta < 2$  and redshift range similar to our sample ( $0.9 < z < 1.1$ ). In order to consider for flux uncertainties in the colour-colour diagram, we have broadened the SED tracks by adding an extra Gaussian standard deviation of 10 per cent to the model fluxes. Thus, the choice of emissivity parameter would make just a minor difference.

As shown in Fig. 4.6 (top), I find that in the SPIRE-only colour diagram the colours of the sources are well within the limits defined by the models we have considered. This is the case for all AGN sub-classes of the sample and also for the individually SPIRE-detected AGN and the mean values. I find no significant dependence of SPIRE colours on any of the AGN associated parameters (e.g. BH mass, bolometric luminosity, Eddington ratio) for each of the AGN sub-classes, so I only present the mean colour-colour values for the total RLQ, RQQs and RG populations. This result along with the similarity between the AGN SPIRE colours and the model, indicates that SPIRE bands are not significantly affected by emission from the torus (or hot dust surrounding the AGN). Although both quasars' and radio galaxies' mean colours lie inside the model tracks, the mean colour of the RGs is shifted from the bulk of the model galaxies and the quasars, indicating that it is possible that RGs are associated with redder colours, and therefore cooler dust, or or be affected by synchrotron contamination.

Similarly, Fig. 4.6 (middle) shows that the 160  $\mu\text{m}$  band does not suffer from torus emission contamination, as the quasars' and RGs'  $S_{160}/S_{250}$  colours are similar to that of the models. I find that a few individually detected points lie outside the model set of tracks; however, these outlier points are possibly caused by the fractionally larger flux errors of the PACS band. By and large, most AGNs can safely be assumed to be dominated by cool dust emission in the SPIRE and 160  $\mu\text{m}$  FIR bands. As in the top panel, the mean  $S_{250}/S_{350}$  for the RGs indicates colder dust temperatures. Again, I find no significant dependence of  $S_{160}/S_{250}$  on any of the AGN associated parameters.

In contrast, when I examine the PACS 70  $\mu\text{m}$  colour, I find that most of the individually FIR detected AGN and the stacked mean colours lie outside the same set of tracks as used for the SPIRE-only colour diagram, suggesting that the PACS 70  $\mu\text{m}$  band may be significantly contaminated by AGN emission. In the Fig. 4.6 (bottom) the  $S_{160}/S_{70} - S_{250}/S_{160}$  colour-colour diagram for SPIRE 250  $\mu\text{m}$  and PACS bands of the sample are shown. Although the fractionally larger PACS flux errors could explain some of these outliers, it is possible that some of these sources require a second, warmer dust component (e.g. [Dunne & Eales, 2001](#)) or a more complex SED model than a simple isothermal SED model. For the low and high bolometric luminosity sub-samples there is a clear separation, despite the large error bars, in the  $S_{160}/S_{70}$  colours. This difference seems to arise from the AGN contamination at 70  $\mu\text{m}$  ( $\sim 35 \mu\text{m}$  at the rest-frame). Indeed, at the redshifts of this sample, the PACS 70  $\mu\text{m}$  contains the longer wavelengths of the torus emission (e.g. [Mullaney et al., 2010](#); [Xue et al., 2010](#)). If this is the case, then the strong correlation between the 70- $\mu\text{m}$  emission and AGN emission (e.g. X-ray luminosity) found for powerful AGN (e.g. [Mullaney et al., 2012b](#); [Harrison et al.,](#)

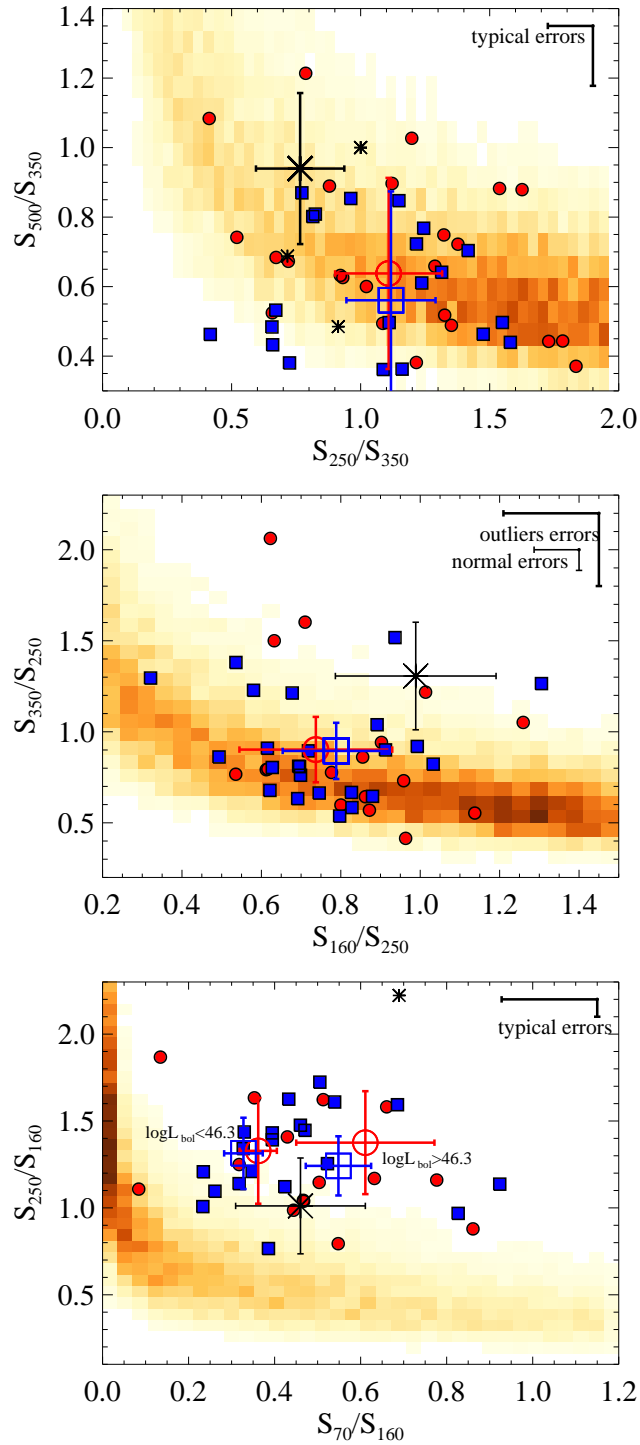


FIGURE 4.6: SPIRE and PACS colour-colour diagrams of the AGN in our sample. Small symbols indicate the FIR detected AGN (RLQs = red circle, RQQs = blue squares, RGs = black stars). Detected sources have been selected by imposing a  $3\sigma$  cut in each band but 70 and  $500\ \mu\text{m}$  where we use a  $2\sigma$  cut due to the low detection rates. Their typical  $1\sigma$  errors are also presented in each panel. Stacked measurements for all AGN classes are shown as large symbols with their  $1\sigma$  errors. The background density map indicates the colour-colour spaces of our  $10^6$  randomly generated model SEDs. The darker colours of the density map correspond to denser regions. In the bottom panel, the mean values correspond to the low and high bolometric bins as indicated.

2012) could be explained by the heavy torus contamination. For this reason, the 70  $\mu\text{m}$  emission is not used for the FIR luminosity calculation (see Section 4.3.5). On the other hand, the  $S_{250}/S_{160}$  ratio seems to be unaffected by the AGN emission indicating that 160- $\mu\text{m}$  emission is largely generated by cold dust, heated by star formation.

### 4.3.5 SED fitting

As discussed in the previous section, I expect that the rest-frame FIR emission (160-500  $\mu\text{m}$ ) is mainly generated by cold dust heated by star formation in the AGN host galaxy. Therefore, I interpret the FIR emission as being powered by star formation (e.g. Rowan-Robinson, 1995; Schweitzer et al., 2006; Netzer et al., 2007), and I represent it with a black-body modified by frequency-dependent emissivity component (Hildebrand, 1983), given by

$$S_\nu \propto B_\nu(T)\nu^\beta, \quad (4.5)$$

where  $B_\nu$  is the Planck function,  $T$  is the effective dust temperature and  $\beta$  is the dust emissivity index. Since  $T$  and  $\beta$  are degenerate for sparsely sampled SEDs, I reduced the numbers of free parameters by fixing the dust emissivity. Using a  $1.4 < \beta < 2.2$  range (see e.g. Dye et al., 2010; Hardcastle et al., 2010; Smith et al., 2013) I find that the best-fitting model returns lower  $\chi^2$  values for a fixed  $\beta = 1.6$  dust emissivity for all AGN populations in the sample. The selection of  $\beta = 1.6$  is consistent with the work of Dye et al. (2010). The remaining two free parameters are the cold dust temperature, which I have varied over the range  $10 < T(\text{K}) < 60$  and the flux normalization of the modified black-body component.

For each source I estimated the integrated FIR luminosity (8–1000  $\mu\text{m}$ ) using a modified black-body fitting with the best fit temperature. The dust temperature was obtained from the best fit model derived from minimization of the  $\chi^2$  values. The uncertainty in the measurement was obtained by mapping the  $\Delta\chi^2$  error ellipse, allowing the individual photometric measurements to vary within their  $1\sigma$  ranges of uncertainty. In addition to the integrated FIR luminosity I calculate the mass of the FIR emitting dust component using

$$M_{\text{dust}} = \frac{1}{1+z} \frac{S_{250} D_L^2}{\kappa B(\nu, T)} \quad (4.6)$$

where  $S_{250}$  is the 250  $\mu\text{m}$  observed flux,  $D_L$  is the luminosity distance,  $\kappa$  is the dust mass absorption coefficient, which Dunne et al. (2011) take to be  $0.89 \text{ m}^2 \text{ kg}^{-1}$  and  $B(\nu, T)$  is the Planck function.

In the case of RGs and RLQs, I also extend the modified black-body model to the radio bands with either a power-law slope  $S_\nu \propto \nu^{-\alpha}$ , with  $\alpha$  estimated from 325 MHz and 1.4 GHz radio observations or, a broken power-law for the RLQs with available SMA observations at 1300  $\mu\text{m}$ . In the second case, the broken point is fixed at the 1.4 GHz. Examples of the SED fits are presented in Fig. A.1. As the majority of the sources are undetected at the  $3\sigma$  limit

in all *Herschel* bands, in addition to probing the properties of the individually FIR-detected objects, I carry out a weighted stacking analysis on the FIR luminosities for the total sample which follows the method of [Hardcastle et al. \(2010\)](#). For convenience, I refer to the former objects as FIR-detected, and to the latter as non-detected. I determine the luminosity for each source from the *Herschel* flux densities (excluding 70  $\mu\text{m}$ ), even if negative, on the grounds that this is the maximum-likelihood estimator of the true luminosity, and take the weighted mean of the parameter we are interested in within each bin. I use the same bins across the AGN sub-classes in order to facilitate comparisons. The luminosity is weighted using the errors calculated from  $\Delta\chi^2 = 2.3$  and the errors on the stacked parameters are determined using the bootstrap method. The advantage of bootstrapping is that no assumption is made on the shape of the luminosity distribution. In Chapter 3 I also presented, as an alternative, the mean temperature estimation using the Maximum Likelihood Temperature method (e.g. [Hardcastle et al., 2013](#)). I found small but insignificant differences between the two methods, so for convenience I present here only the results of the weighted mean method.

Fig. 4.7 shows the FIR luminosity and dust temperature ( $T_d$ ) plane divided into dust mass ( $M_d$ ) regions based on the  $L_{\text{FIR}} \propto M_d T_d^{4+\beta}$ , assuming  $\beta = 1.6$ , for the FIR-detected AGN of the sample (similar cuts to Fig. 4.6 top) and the weighted mean values for the total sample and for each sub-class. The sources have been additionally divided into bolometric luminosity bins as specified in Table 3.1. Both types of quasar show high FIR luminosity with most of the detected sources and the weighted mean values having  $L_{\text{FIR}} > 10^{12} L_\odot$ , characterizing them as ultra-luminous infrared galaxies (ULIRGs). The weighted mean FIR luminosity of the RGs is significantly lower, even compared to the low bolometric luminosity quasars. Similar differences are also found for low BH mass and Eddington ratio bins. Comparing the FIR luminosity of the RLQs and RQQs it is notable that RLQs have higher mean FIR luminosity than RQQs in both bolometric luminosity bins at  $> 1\sigma$  level with a significance of  $p = 0.014$ . Similar trends are also found for BH masses and Eddington ratio.

As already indicated from the colour-colour plots, RGs show lower dust temperatures than both RLQs and RQQs (by about 5K) at a significance level of  $p = 0.036$  and  $p < 0.001$ , respectively, under a K-S test. For all AGN subclasses and bins, the weighted mean values follow the  $10^8 M_\odot$  dust mass curve, with the exception of high bolometric luminosity RQQs which have slightly lower weighted mean dust mass (and lower dust temperature). Most of the FIR detected RLQs lie between the  $10^{8-9} M_\odot$  dust mass curves. This mass range is comparable to that obtained for submillimetre galaxies (e.g. [Santini et al., 2010](#)) at similar redshifts to our sample.

### 4.3.6 FIR-radio correlation

In this section I determine whether the radio emission could be the result of star formation, rather than AGN activity, by comparing the observed radio flux with that predicted from the

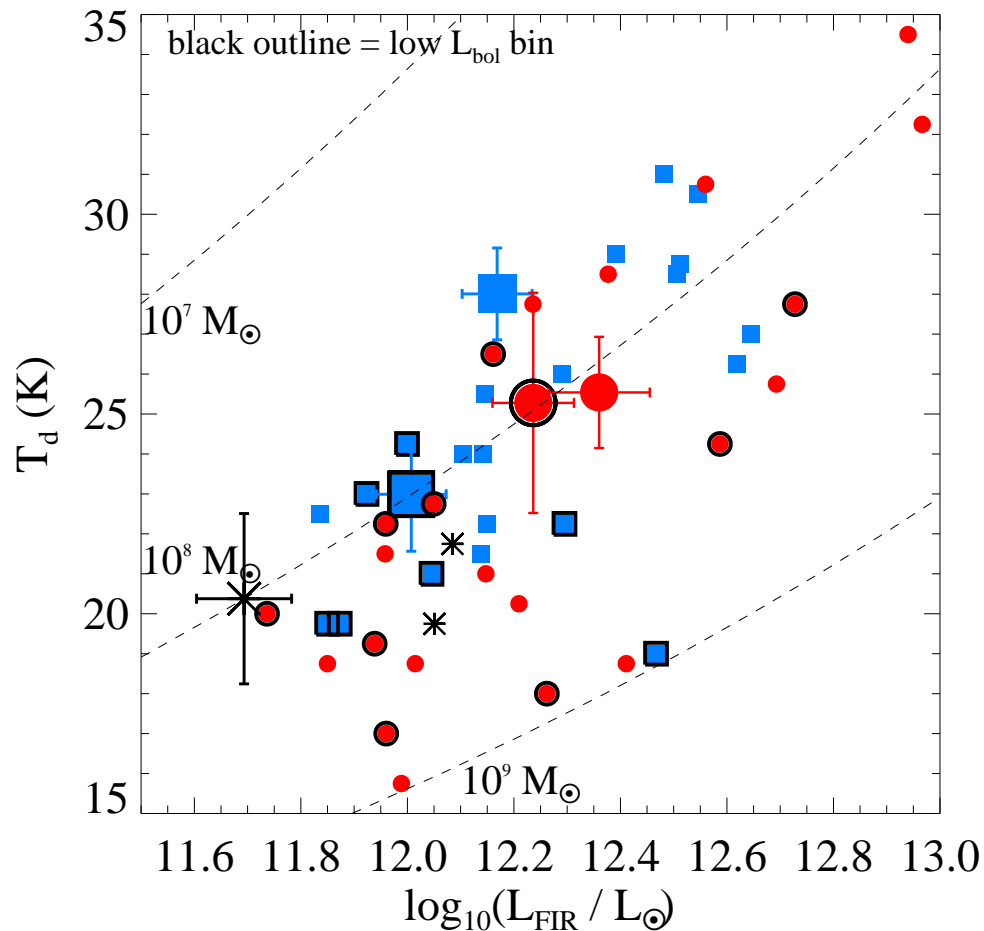


FIGURE 4.7: FIR luminosity versus dust temperature for individually FIR detected AGN and weighted mean values when the RLQs and RQQs are divided into bolometric luminosity bins. For RGs, I present the mean values for the total population as all the sources but 4 belong to the low bolometric luminosity bin. Black outline indicates the sources and the mean values for the low bolometric luminosity bin. Colours and symbols are similar to Fig. 4.6. The black lines correspond to the dust mass estimates based on the  $L_{\text{FIR}} - T_{\text{d}}$  relation  $L_{\text{FIR}} \propto M_{\text{d}} T_{\text{d}}^{4+\beta}$ , assuming  $\beta = 1.6$ , for dust masses of  $10^7$ ,  $10^8$  and  $10^9 M_{\odot}$ .

FIR/radio correlation. As the high detection rates and the mean FIR flux densities in the RLQ sample indicate, almost 50 per cent of the population is expected to have high star formation activity. High star formation activity, at the level of  $L_{\text{FIR}} > 10^{11} L_{\odot}$ , could result in radio emission up to  $10^{24} \text{ W Hz}^{-1}$  at 1.4 GHz, which is the detection level of the RLQs in this sample. I additionally investigate whether radio excess (i.e. radio emission associated with radio jets) correlates with star formation as one would expect assuming a jet-induced star formation (positive feedback) model.

I calculate the ratio between the IR and radio emission ( $q$ ) using the definition given by Helou et al. (1985)

$$q = \log[f_{\text{FIR}} / (3.75 \times 10^{12} \text{ Hz})] - \log[S_{\nu}(1.4 \text{ GHz})] \quad (4.7)$$

where  $f_{\text{FIR}}$  is in units of  $\text{W m}^{-2}$ , determined from the *Herschel* photometry and  $S_\nu(1.4 \text{ GHz})$  is rest-frame 1.4 GHz radio flux density in units of  $\text{W m}^{-2} \text{ Hz}^{-1}$ . I extrapolate the above relation to 325 MHz using the power-law slope  $S_\nu \propto \nu^{-\alpha}$ , with  $\alpha = 0.7$ , typical for star-forming galaxies (e.g. Ibar et al., 2009, 2010; Condon et al., 2013).

In Fig. 4.8 I show the FIR and the radio 325 MHz luminosities for all of the RQQs (blue upper limits), RLQs (red circles and upper limits for FIR-undetected sources) and RGs (black point stars and upper limits for FIR-undetected sources) in the sample. The diagonal lines represent the mean  $q = 2.2$  value typically obtained for star-forming/starburst galaxies (e.g. Helou et al., 1985) and also typical radio-quiet AGN (e.g. Padovani et al., 2011; Sargent et al., 2010) and the mean  $q = -0.38$  for a sample of radio-loud AGN from Evans et al. (2005). For the separation between ‘radio-normal’ and radio-excess sources I have picked the mean  $q = 1.2$  value that perfectly separates the RLQs and RQQs in our sample. I note that this is a conservative value compared to previous works (e.g.  $q = 1.68$ ; Del Moro et al., 2013,  $q_{\text{max}} = 1.5$ ; Hardcastle et al., 2010,  $q_{\text{max}} = 1.1$ ; Jarvis et al., 2010) indicating that above this limit we are predominantly detecting genuine radio-loud AGN.

The average upper limit  $q$  for the RQQs lies near to the ‘radio-normal’ diagonal line, taking into account that the radio luminosities shown are the  $5\sigma$  limits. All but one of the RGs in our sample is found above the RLAGN  $q = -0.38$  diagonal line (orange dotted line) while about 70 percent of the RLQs lie in a region between those occupied by radio-galaxies and RQQs. This is consistent with the selection of the RG and RLQ samples. It is clear that the level of radio emission from star formation is insignificant for both RLQs and RGs. All radio-sources are found above the  $q = -0.38$  diagonal line suggesting that the radio emission associated with star formation may contribute by a maximum of 10 per cent for the least radio-luminous RLQs.

For each region, I have estimated the weighted mean FIR luminosity, represented by the large stars; orange for the sources in the RLAGN region, purple for the sources in the radio-excess region and black for the radio normal region. As expected based on Fig. 4.7 the objects in the radio-excess region, which consists only of RLQs, show a higher FIR luminosity. In contrast, the mean FIR luminosity at the RLAGN region is lower than that in both the ‘radio-normal’ and radio-excess regions. Although the RLQs in this region are associated with higher FIR luminosities compared to the RGs, and have about a 50 per cent detection rate, their individually measured FIR luminosities do not exceed the mean FIR luminosity of the radio excess region. Weighted mean values of the total radio population, including both RGs and RLQs, show an anti-correlation between FIR and radio luminosity. Sources with higher radio luminosity show weaker star formation. We can investigate the apparent anti-correlation further considering the individual sources, although the numerous upper limits might affect the establishment of such a correlation. In order to consider also the sources with FIR upper limits, I use Kendall’s Tau statistical test. For this, the IRAF statistics package, which implements the Astronomical Survival Analysis programs

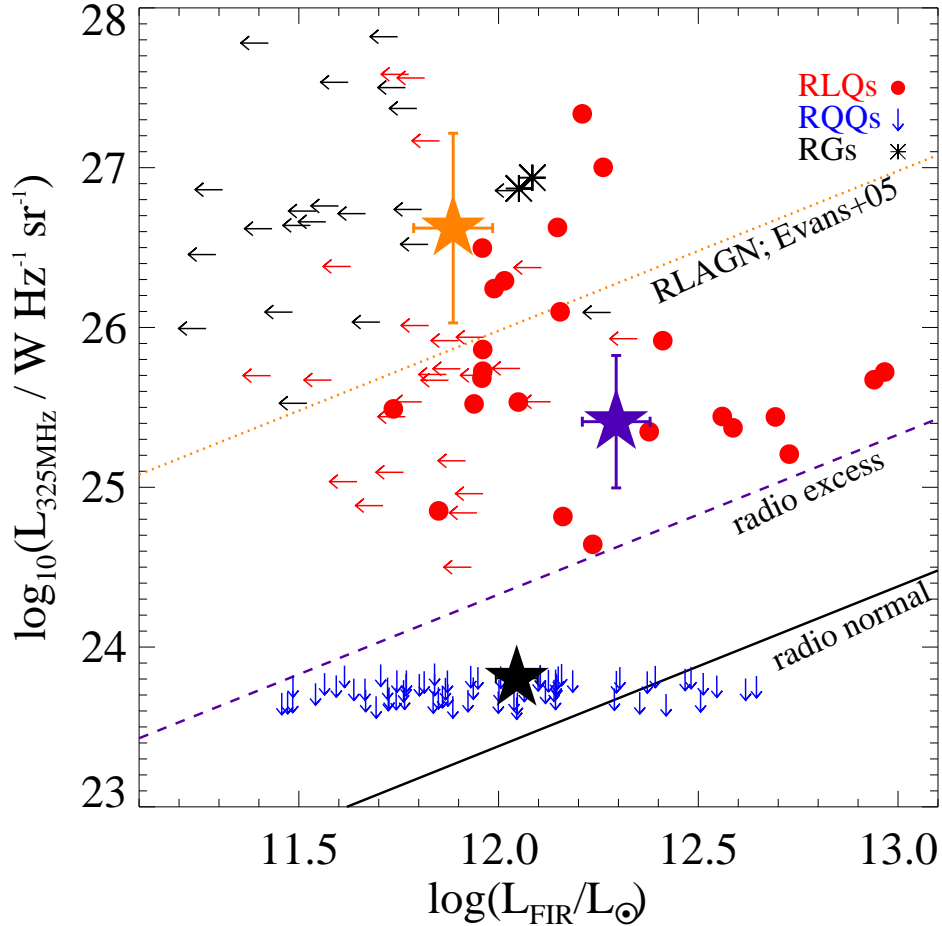


FIGURE 4.8: FIR luminosity ( $L_{\text{FIR}}$ ) vs. radio 350 MHz luminosity ( $L_{325\text{MHz}}$ ); the orange dotted line correspond to  $q = -0.38$  (average for a sample of radio-loud AGN from [Evans et al., 2005](#)); the black solid line correspond to  $q = 2.2$  (average for ‘radio-normal’ sources) and the purple dashed line correspond to  $q = 1.68$ , our selection limit for radio-excess sources. The large stars are the mean values of all sources in each region. Colours are associated to the lines. For individually FIR detected sources, colours and symbols are similar to Fig. 4.6. FIR undetected sources are presented as upper limits.

(see [Feigelson & Nelson, 1985](#); [Lavalley et al., 1992](#)), was used. This test examines the null hypothesis that no correlation is present between the two variables being tested. For the total radio sample the generalized Kendall’s correlation coefficient is  $\tau = -0.13$  with a null hypothesis probability of  $p = 0.12$ , implying no significant correlation.

The fact that high radio luminosity RGs and RLQs (see orange star; Fig. 4.8), are associated with lower FIR luminosity (M-W test;  $p \approx 0.015$ ) compared to lower radio luminosity RLQs (purple star; Fig. 4.8) may indicate two possible physical scenarios. In the first scenario, we can assume that there is a radio-jet power limit above which radio jets suppress the star formation in the host galaxy. That would be consistent with the negative radio-jet feedback scenario (e.g. [Croton et al., 2006](#)). In contrast, lower power radio-jets might enhance the star formation (positive feedback) and that would explain the FIR excess between RQQs and RLQs with intermediate radio luminosity, the ones found in the radio-excess region.

However, we should expect that these processes are controlled by the gas availability (i.e. galaxy mass). Indeed, RLQs with the similar radio luminosities to the RGs have higher FIR luminosities as they are hosted by galaxies with larger masses, assuming that the Maggiorian relation holds. Although this interpretation could explain the observed anti-correlation, the effects of the radio jets cannot be so straightforwardly understood unless we control for galaxy mass. I discuss this scenario further in Section 4.6. Another important parameter is the environment of these sources, which can lead to a second possible scenario. Taking into consideration that the RGs have been selected from radio surveys whereas the RLQs are optically selected, we might have picked the two populations in either different evolutionary stages or different environments (see the discussion in Section 4.6). This fact could drive the apparent anti-correlation when we consider both RGs and RLQs.

## 4.4 The star formation dependence on AGN activity

Using measurements of FIR luminosity, I will now study the relationship between FIR emission and SMBH accretion. In Fig. 4.9, FIR luminosity is plotted against bolometric luminosity  $L_{\text{bol}}$ . The plotted points indicate both individual (small symbols) and weighted mean FIR luminosities. The plotted  $L_{\text{bol}}$  is the median value for the objects in each bin with their associated  $1\sigma$  error bars. Different colours are used to represent the different AGN classes. A crucial point of our results is that about 30 per cent of our QSOs are FIR-detected, indicating high FIR luminosities at the level of  $L_{\text{FIR}} \gtrsim 10^{12} L_{\odot}$ . The high FIR emission suggests that starburst activity in 30 per cent of our QSOs has not been quenched yet. These results argue for a scenario in which powerful quasars, on average, have not suppressed the star formation in the host galaxy (see e.g. Harrison et al., 2012; Mullaney et al., 2012b but also e.g. Page et al., 2012). The massive host galaxies and black holes of these sources might have been formed over a series of coeval episodes of strong star formation and BH activity.

To search for possible trends between bolometric and FIR luminosity I performed a correlation analysis on each of the sub-samples. In order to take account of the sources with FIR upper limits, I use Kendall's Tau statistical test as described in Section 4.3.6. This test examines the null hypothesis that no correlation is present between the two variables being tested. The correlation analysis returns  $\tau = 0.34$  ( $p = 0.02$ ),  $\tau = 0.28$  ( $p = 0.02$ ) and  $\tau = 0.15$  ( $p = 0.32$ ) for RLQs, RQQs and RGs, respectively, suggesting a moderately significant correlation over more than 2 orders of magnitude in  $L_{\text{bol}}$  for both RLQs and RQQs. For RGs a no significant correlation is observed over  $\lesssim 2$  orders of magnitude.

A correlation between AGN luminosity and host galaxy star formation rate has been reported by several studies of high redshift AGNs and QSOs (e.g. Lutz et al., 2008; Shao et al., 2010; Rosario et al., 2012; Rovilos et al., 2012). Netzer et al. (2007) found for luminous PG QSOs that this relationship has a slope of  $\alpha \approx 0.8$  (see black dotted line in Fig. 4.9). Consistent slopes have also been suggested by other authors for mm-bright QSOs at  $z \sim 2$

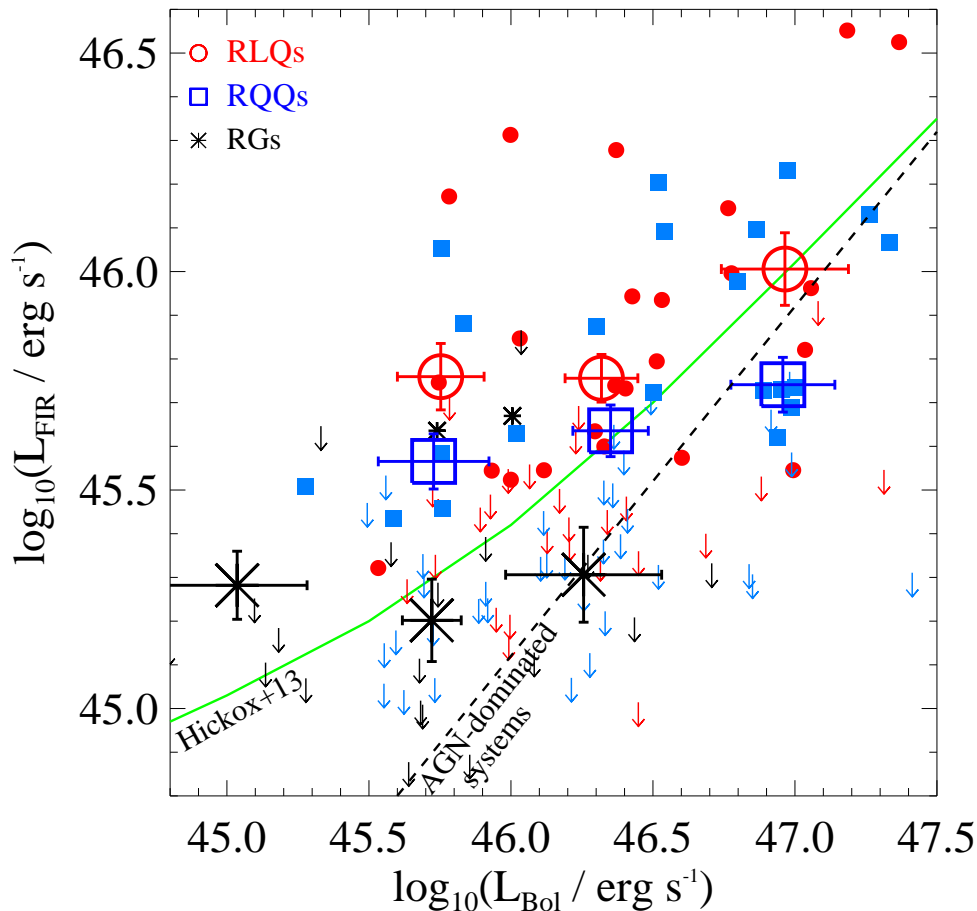


FIGURE 4.9: FIR luminosity ( $L_{\text{FIR}}$ ) vs. bolometric luminosity ( $L_{\text{bol}}$ ) for each AGN class in 3  $L_{\text{bol}}$  bins. For RLQs and RQQs each bin contains about 18 and 23 sources, respectively, while for RGs about 9 sources. The large symbols (red circles, blue squares and black stars) are the mean values of each bin for RLQs, RQQs and RGs, respectively. No significant differences are found when the median values are used. For individual sources, colours and symbols are similar to Fig. 4.6. FIR undetected sources are presented as upper limits. The dashed black line is the correlation line shown by AGN-dominated systems in [Netzer \(2009\)](#). The solid green line show the predictions of the [Hickox et al. \(2014\)](#) fiducial model on BH variability and star formation-AGN connection.

(e.g. [Lutz et al., 2008](#)) and X-ray AGN (e.g. [Rosario et al., 2012](#)) at least for high AGN luminosities. We note that [Rosario et al. \(2012\)](#) suggested a flatter or even zero slope at low AGN luminosities ( $L_{\text{AGN}} < 10^{44} \text{ erg s}^{-1}$ ). As these works have selected their AGN samples without any use of radio information, we expect that they are dominated by radio-quiet AGN. Radio-loud AGN are expected to make up to 10 per cent of uniformly selected AGN samples, so they should not significantly affect the estimation of these works.

The RQQs of this sample are very similar to that of [Netzer et al. \(2007\)](#), with a good overlap on AGN luminosity up to  $L_{\text{AGN}} \sim 10^{46.5} \text{ erg s}^{-1}$ , while our sample extends to about an order of magnitude higher in AGN luminosity. The correlation between the FIR and AGN luminosity based on the [Netzer et al. \(2007\)](#) QSO sample is presented in Fig. 4.9. One important difference is the redshift range of the two samples, with the QSOs of [Netzer et al.](#)

(2007) having  $z < 0.3$ . Notwithstanding this difference, the selection of our sample in a narrow redshift range decouples the evolution effect and makes it perfect for comparison to either lower or higher redshift samples. One can immediately notice from Fig. 4.9 that the  $L_{\text{AGN}}-L_{\text{FIR}}$  correlation is much weaker and flatter than the one proposed by Netzer et al. (2007). The correlation slope for the RQQs of this work is found to be  $\alpha \approx 0.26 \pm 0.06$ . Specifically, the lower  $L_{\text{AGN}}$  sources in our sample show a weighted mean  $L_{\text{FIR}}$  of one order of magnitude higher than that implied by the correlation of Netzer et al. (2007) while at higher  $L_{\text{AGN}}$  they are in better agreement. Such an increase of the FIR luminosity at a fixed AGN luminosity bin with redshift has been suggested by other authors (Rosario et al., 2012; about 0.7 dex from  $z \sim 0.3$  to  $z \sim 1$  AGN) and it would explain the FIR luminosity difference between our and that of Netzer et al. (2007) in fixed  $L_{\text{AGN}}$  bins. On the other hand, QSO selection at lower redshifts (e.g.  $z < 0.3$ ) where the star formation density in the universe is very low, might be affected by Malmquist bias. A similar trend for shallower slope ( $\alpha = 0.58 \pm 0.18$ ) at similar  $L_{\text{AGN}}$  and redshift but for X-ray AGN was suggested by Rosario et al. (2012) although the quality of the fit is rather poor. Even in this case, our data suggest a much lower slope ( $\alpha \approx 0.26 \pm 0.06$ ) for the RQQs. Note that even if I include the RLQs the estimated slope can reach a maximum of  $\sim 0.32$ .

We know that AGNs are variable over a large dynamic range in luminosity. Luminous, high-redshift quasars typically yield lifetimes for luminous accretion of  $\sim 10^6 - 10^7$  years (e.g. Hopkins et al., 2005; Gonçalves et al., 2008; Shankar, 2010). On the other hand, star formation on scales of the entire galaxy has a dynamical time of around  $10^8$  yr. In addition, as FIR emission arises mostly from dust that can be heated by both young and old stars, it can average over timescales of tens to hundreds of Myr, especially in galaxies with star formation at a relatively steady rate over their lifetime. Thus, the weak observed correlation between star formation and BH accretion might be attributed to the timescale difference between the AGN accretion efficiency and star formation variability (e.g. Mullaney et al., 2012b; Chen et al., 2013; Hickox et al., 2014).

From a theoretical point of view, Hickox et al. (2014) suggested a simple model in which accretion and star formation are perfectly connected, but this connection is ‘hidden’ by short-timescale AGN variability over a large dynamic range (see Fig. 4.9 green solid line). Despite the fact that the model goes through our data points for the individual QSOs, the mean measurements lie systematically off the expected trend. Although the model of Hickox et al. (2014) describes well the lack of a strong correlation between  $L_{\text{FIR}}$  and  $L_{\text{AGN}}$  for moderate-luminosity AGN and the shift to higher  $L_{\text{FIR}}$  with redshift as suggested by observational results, it suggests a strong correlation between  $L_{\text{FIR}}$  and  $L_{\text{AGN}}$  at high luminosities, in contrast to my results. However, the apparent disagreement could arise from limitations in the simplistic AGN variability model (for a discussion see Hickox et al., 2014) or from the fact that our sample contains exclusively powerful QSOs with high accretion rates. An alternative model, suggested by Aird et al. (2013), assumes that the probability of a galaxy hosting

an AGN is determined by a universal specific accretion rate distribution that is independent of host stellar mass or star formation properties. This model would be consistent with the observed weak AGN/star-formation correlation of this work even in the most luminous QSOs.

In Fig. 4.10 I present the average FIR luminosity of each AGN population, as a function of  $M_{\text{gal}}$ . I have to note that the galaxy masses are not actual stellar mass measurements for our QSOs but they have been estimated based on the black hole measurements assuming a Magorrian relation. This fact may introduce high uncertainties. As expected under the assumption of a hidden AGN ‘main sequence’ due to the different timescales between star formation and QSOs phase, we find no correlation for any AGN sub-class between FIR luminosity and stellar mass, in contrast to the result of Mullaney et al. (2012b). The most luminous AGN, like the ones in our sample, are generally missed from small field surveys. However, at redshift  $0.9 < z < 1.1$  they make up to 10 per cent (e.g. Aird et al., 2010) of the total AGN population ( $L_X > 10^{42} \text{ erg s}^{-1}$ ). Despite their large FIR excess, an order of magnitude in FIR luminosity, their rarity means that they might not significantly change the results found by Mullaney et al. (2012b).

Comparing the average SFRs of this sample to the observed relationship between SFR and stellar mass of normal star forming galaxies, which is known as the ‘main sequence’ (e.g. Elbaz et al., 2007, 2011; Schreiber et al., 2015; Johnston et al., 2015) I can examine whether QSOs have SFRs that are consistent with being selected from the overall star forming galaxy population. To make this comparison I use the Schreiber et al. (2015) definition of the ‘main sequence’ at  $z \sim 1$  (see Eq. 9 of Schreiber et al., 2015). They found evidence for a flattening of the main sequence at high masses ( $\log_{10}(M_{\text{gal}}/M_{\odot}) > 10.5$ ), similar to the one observed for the sources in our sample. Note that they use stellar masses up to  $\log_{10}(M_{\text{gal}}/M_{\odot}) \approx 11.5$  to extract their model. Although the mean FIR luminosity of the RGs (large point stars) is consistent with that of star forming galaxies of the same redshift and mass, the weighted mean FIR luminosity for QSOs is systematically higher than the higher end of the FIR luminosity region covered by ‘main sequence’ galaxies. Santini et al. (2012) have also reported that, on average, X-ray AGN hosts show somewhat enhanced star-formation activity respect to a control sample of inactive galaxies, although they found them to be consistent with star forming galaxies. While different interpretations are possible, our findings are consistent with a scenario whereby periods of enhanced AGN activity and star-forming bursts are induced by major mergers (e.g. De Breuck et al., 2005; Elbaz et al., 2011; Sargent et al., 2013).

## 4.5 The dependence of star formation on radio jets

In this section I will discuss the effect of the presence of radio jets in a QSO on star formation activity. As is already clear from the previous section (see Fig. 4.9), RLQs are associated with higher FIR luminosity than RQQs. This excess is almost constant and independent of

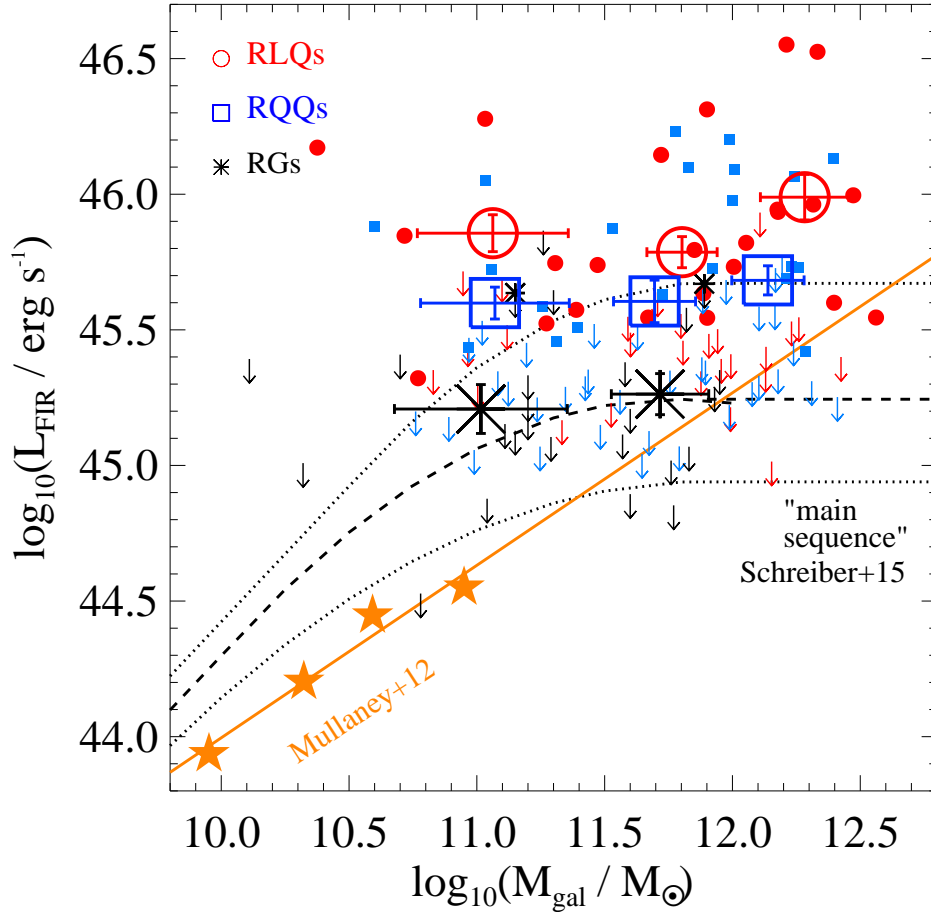


FIGURE 4.10: FIR luminosity ( $L_{\text{FIR}}$ ) vs. galaxy mass ( $M_{\text{gal}}$ ) for each AGN class in 3  $L_{\text{bol}}$  bins. Colours and symbols are similar to Fig. 4.9. The large symbols (red circles, blue squares and black stars) are the mean values of each bin for RLQs, RQQs and RGs, respectively. Similar results are obtained even when the median values are used for each bin. The solid orange line and orange stars correspond to the average FIR luminosity and stellar mass for Mullaney et al. (2012b)  $z \sim 1$  sample of star-forming galaxies. The black dashed line with the associated scatter (dotted black lines) corresponds to the expected  $L_{\text{FIR}} - M_{\text{gal}}$  relation for  $z \sim 1$  as defined by Schreiber et al. (2015).

AGN properties. Fig. 4.11 shows the SFR excess, defined as the SFR difference between RLQs and RQQs, for the individual sources in each  $L_{\text{bol}}$  bin, taking into account the total population (orange filled area) or only the FIR detected QSOs (purple shaded area). Apart from the highest bolometric bin, where only a few sources are found, the SFR excess is almost constant with  $\Delta\text{SFR} \approx 315 M_{\odot}/\text{yr}$  for the total sample and  $\Delta\text{SFR} \approx 380 M_{\odot}/\text{yr}$  for the FIR-detected QSOs. This excess corresponds to about a factor of two. A similar increase in SFR due to the onset of radio-jets has been suggested also by simulations of massive gas-rich high-redshift galaxies (Silk & Nusser, 2010a; Gaibler et al., 2012).

SFR-enhancing phases in RLQs can be caused by the large enhancing amount of thermal energy generated by the jet as it forces its way through the interstellar medium (ISM). Jet create cocoons of turbulent gas surrounding the jet leading to a much more efficient clumping of molecular hydrogen and thus accelerated star formation (e.g. van Breugel et al.,

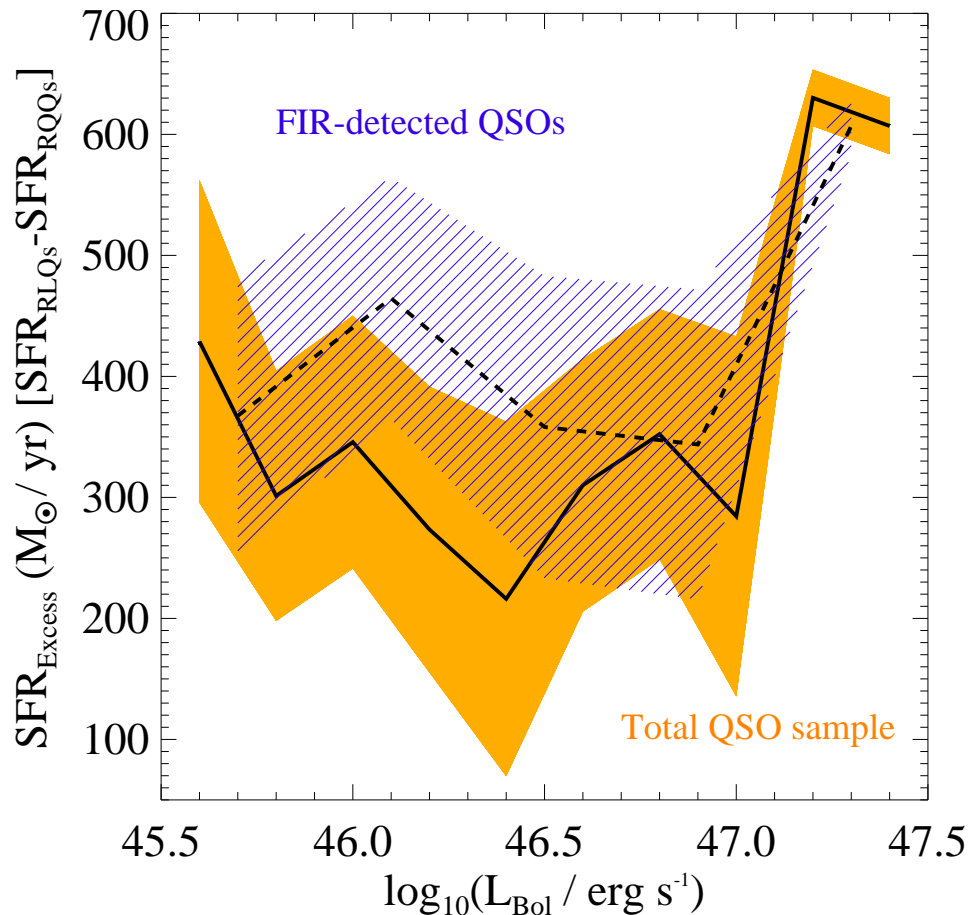


FIGURE 4.11: SFR excess between RLQs and RQQs as a function of bolometric luminosity for the total QSO sample (orange) and the FIR detected QSO sample (blue). The solid and dashed lines represent the mean SFR excess and the coloured areas the  $1\sigma$  error for the total QSO sample and the FIR detected QSO sample, respectively.

2004; Gaibler et al., 2012; Wagner et al., 2012; Ishibashi & Fabian, 2012). Simulations have shown that, although powerful jets would interact with clouds in a limited volume, the resulting pressure can impact the galactic disk also at larger radii at the early stage and eventually all of the galaxy once the bow shock has moved beyond the galaxy’s radial extent (see Gaibler et al., 2012). Although direct interaction of the jet beam with clouds can be limited to a small volume, the resulting pressure may affect a fair fraction of the galactic disc at the early stage and eventually all of the galaxy once the bow shock has moved beyond the galaxy’s radial extent (see Gaibler et al., 2012). Thermal or kinetic AGN feedback is often thought to heat and expel most residual gas from the galaxy (e.g. Springel et al., 2005; Croton et al., 2006; Bower et al., 2008; Dubois et al., 2012), reducing the SFR. On the contrary, our results suggest an entirely opposite effect, indicating the formation of an additional population of stars, compared to the RQQs. The need for additional enhancement of star formation has been recently suggested by Khochfar & Silk (2011) for high-redshift galaxies ( $z > 5$ ) who introduced stochastic boosts in star formation in order to reproduce

the observations. Such enhancement could indeed be triggered by jet activity in gas-rich galaxies; however, there are very few radio galaxies at  $z > 5$  (e.g. [Jarvis & Rawlings, 2000](#); [Jarvis et al., 2001a](#); [Wall et al., 2005](#); [Rigby et al., 2011, 2015](#)). Therefore, it is important to understand at which epochs and under which conditions radio jets can efficiently boost the host galaxy star formation. Near future synergies between optical spectroscopy (WHT Enhanced Area Velocity Explorer, WEAVE; [Dalton et al., 2012](#)) and radio continuum (e.g. Low Frequency Array, LOFAR; [van Haarlem et al., 2013](#)) surveys will provide much greater sample sizes for radio AGN allowing more stringent constraints on the evolution of the radio population, out to greater redshifts (e.g. WEAVE-LOFAR; [Smith, 2015](#)).

In the previous chapter I compared the SFR between RLQs and RQQs over a wide redshift range, up to  $z \sim 3$  with a couple of QSOs at even higher redshifts and I found an excess of  $\leq 100 M_{\odot}/\text{yr}$  for RLQs with low bolometric luminosity and no difference at high bolometric luminosities. This excess corresponds to more than a factor of 2, but to much lower SFRs than the ones found here. We note that the vast majority of low bolometric QSOs in Chapter 3 sample have  $z < 1.0$  while the high bolometric luminosity QSOs are found in much higher redshift. The differences between these two studies give some evidence regarding the evolution of the jet-induced star-formation efficiency. As, in this chapter, I do not find any effect of bolometric luminosity on SFR excess, I assume that the results of Chapter 3 are associated with redshift evolution. In this case it would be possible that radio jets positive feedback efficiency evolves with redshift, peaking at  $z \approx 1.0$  where we find the maximum SFR excess. However, both RLQs and RQQs may have more star formation at higher redshifts due to the same process as in normal galaxies (e.g. [Madau & Dickinson, 2014](#)). Therefore, the ratio of SFR from radio jets to the normal SFR might be smaller and harder to be detected at higher redshifts. The scenario of positive feedback having a peak at  $z \approx 1.0$  is similar to the radio-AGN space density evolution from the local Universe to  $\sim 1.0$  (with a radio luminosity dependence; [Rigby et al., 2011](#)) and the amount by which the cosmic SFR density has increased over the same interval (e.g. [Best et al., 2014](#); [Madau & Dickinson, 2014](#)). Indeed, a consistent picture emerges whereby the availability of a cold gas supply regulates both the radiative-mode AGN and star formation activity (e.g. [Hardcastle et al., 2007](#); [Heckman & Best, 2014](#)).

While this work is consistent with positive feedback, we should be aware of selection effects and the conditions under which radio jets would enhance the star-formation. For example, our sample consists of very massive QSOs with high SFR even in the case of RQQs. The high SFRs would suggest that these QSOs might have gone through recent, major gas-rich merger events indicating high gas supplies. Especially for RLQs, minor or major merger events might be more common as they are often associated with high density environments (e.g. [Venemans et al., 2007](#); [Falder et al., 2010](#); [Kuiper et al., 2011](#)). Under these assumptions, radio jet feedback might depend on gas availability associated with the environment and cold gas supplies.

## 4.6 Star formation in RGS and RLQs

It has been suspected from submillimetre studies that the hosts of powerful radio-loud AGN undergo episodes of vigorous star formation which increase with redshift (e.g. Archibald et al., 2001). Using *Herschel* data, Seymour et al. (2011) found a mean SFR range of 80 to 600  $M_{\odot} \text{ yr}^{-1}$  for  $1.2 < z < 3.0$  radio selected AGN. In the same context, Drouart et al. (2014) estimated SFRs of a few hundred to a few thousand solar masses per year for  $1 < z < 5$  radio galaxies. Recently, Podigachoski et al. (2015), comparing the SFR of 3C radio-loud AGN and radio quasars at  $z > 1$ , found similar SFRs for the two classes and at the same levels with the previous works. The idea that the hosts of high- $z$  radio-loud AGN can form stars at high rates is consistent with the jet-induced star formation model.

In this work, while I find that RLQs are associated with vigorous star formation activity, the RGS of this sample have significantly lower SFRs of about a factor of 2.5 for the same BH masses with only two FIR detected sources. Priddey et al. (2003a) found quite similar differences (about a factor  $\sim 2$ ) using submillimetre observations of  $1.5 < z < 3$  RQQs and RGS drawn from SCUBA surveys (Archibald et al., 2001). On the other hand, Isaak et al. (2002) suggested that these differences are far less marked at  $z > 4$ .

The FIR-radio luminosity plane is presented in Fig. 4.8. The RGS in our sample are associated with higher radio luminosities than RLQs (see Fig. 4.2; almost all RGS have  $\log_{10}(L_{325\text{MHz}}/\text{W Hz}^{-1} \text{ sr}^{-1}) > 26.0$ ). Assuming that both RGS and RLQs emanate from the same parent population, I find that the FIR luminosities of the most radio luminous sources in Fig. 4.8 (see RLAGN region) are significantly lower (M-W test  $p \approx 0.015$ ) than the radio sources with lower radio luminosities. However, no significant evidences found regarding an anti-correlation between FIR and radio luminosity.

A possible interpretation of this result would be that star formation enhancement efficiency depends on the radio power, with powerful radio jets associated with negative feedback reducing the star formation in the host galaxy. In fact, radio jet pressure can be sufficiently large to expel significant quantities of gas from the galaxies (Nesvadba et al., 2006), thereby quenching the star formation (Croton et al., 2006). However, this interpretation should also depend on galaxy mass. Indeed, the fraction of radio-loud AGN is a strong function of both stellar mass and redshift (e.g. Jiang et al., 2007; Donoso et al., 2009) suggesting that radio jets feedback predominantly occur in massive halos. Thus, we might expect that its influence will have a most clear signature in massive galaxies. Observational studies on this issue return controversial results (e.g. Nesvadba et al., 2010; Papadopoulos et al., 2010) with positive feedback being directly observed in a few local (e.g. Croft et al., 2006), intermediate (e.g. Inskip et al., 2008) and high redshift sources (e.g. Dey et al., 1997; Bicknell et al., 2000). The observed differences could be explained by the fact that gas masses and velocity dispersions vary strongly with redshift but also amongst radio galaxies at the same redshift regime. In Fig. 4.8 I compare the SFR between RLQs and RGS with similar radio power (see

RLAGN region) and it is clear that RLQs have higher FIR luminosity than RGs. That can be explained as a consequence of the RLQs in the RLAGN region apparently having higher galaxy masses than the RGs (e.g. see Fig. 4.4 where RLQs are associated with higher black hole masses). This conclusion arises from the assumption that the Magorrian relation holds both ways around.

The RG selection from radio surveys favours objects with the highest values of radio luminosity (i.e. jet power) explaining why the RGs in our sample are more radio luminous than the RLQs. On the other hand, the RLQ selection from both optical and radio surveys favours objects with both high jet power and bolometric luminosity (e.g. accretion rate). However, in all likelihood the quasars are probably biased towards bigger black holes due to the optical selection, as we are selecting on BH properties rather than host galaxy properties.

In order to explain the observed differences regarding the SFR in the two populations taking into account both the galaxy mass and jet power, I suggest a ‘toy model’ in which there is some jet power threshold at which radio-jet feedback switches from enhancing star formation (by compressing gas) to suppressing it (by ejecting gas). Then that threshold will be dependent on both galaxy mass and jet power. In this model, the SFR enhancement (i.e. the level of SFR excess compared to a control sample of radio-quiet AGN with the same bolometric luminosity and galaxy mass) starts from zero for AGN without radio jets, has a mass-dependent peak as jet power increases, and then decreases gradually for higher jet power. The first step in order to investigate how our observations fit in this ‘toy model’ was to use the RQQs as a control sample. I have separated the RQQs into 4 bolometric luminosity bins, with about the same number of sources ( $\sim 18$ ), and for each bin I have estimated the weighted mean sSFR.

From low to high bolometric luminosity bins I found  $1.472 \pm 0.554$ ,  $0.314 \pm 0.103$ ,  $0.388 \pm 0.089$  and  $0.180 \pm 0.039 \text{ Gyr}^{-1}$ . Then, the sSFR of each RLQ and RG in our sample was normalised by the weighted mean sSFR from the RQQ control sample, depending on the bolometric luminosity of each source, in order to estimate the sSFR enhancement fraction associated with the radio jets. I prefer the use of sSFR instead of the SFR in order to control the galaxy mass dependence as described in the ‘toy model’. I have excluded 6 RGs from this analysis with bolometric luminosities lower than the lower RQQ bolometric luminosity bin ( $L_{\text{Bol}} < 10^{45.3} \text{ erg s}^{-1}$ , see Fig. 4.4 middle panel). I note that 5 of these 6 RGs have been classified as LERGs by [Fernandes et al. \(2015\)](#).

In Fig. 4.12, I present the fraction of sSFR enhancement due to the radio jets as a function of jet power. As described above, I expect a mass-dependent peak therefore I normalize the jet power to the Eddington luminosity (i.e. black hole or galaxy mass) in order to control for this dependence. Higher-mass galaxies will be able to hold on to their gas better for a given jet power, so there will be some mass-dependent threshold in jet power beyond which jets tend to have an increasingly suppressing effect on star formation. It seems that our observations follow the suggested ‘toy model’ with sources at the low and intermediate

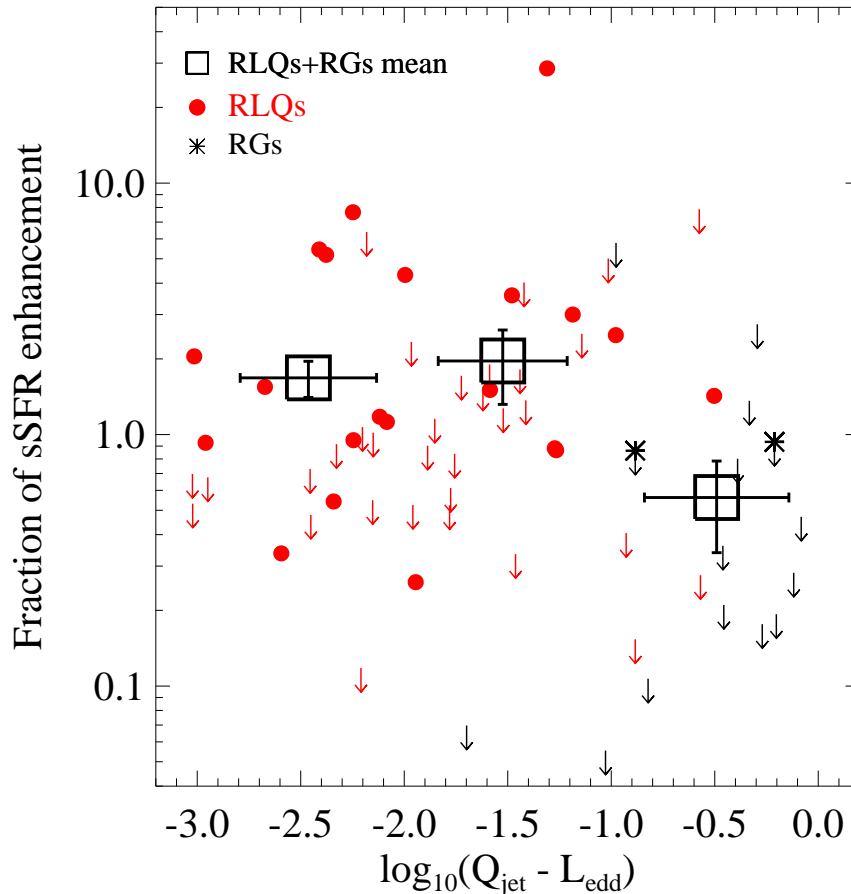


FIGURE 4.12: Fraction of sSFR enhancement for RLQs and RGS as a function of  $Q_{\text{jet}}/L_{\text{Edd}}$  (jet power over Eddington luminosity). The large black squares are the weighted mean values for the three  $Q_{\text{jet}}/L_{\text{Edd}}$  bins taking into account both RLQs and RGS in each bin. For individual sources, colours and symbols are similar to Fig. 4.6. FIR undetected sources are presented as upper limits.

jet power found at the peak of the star-formation enhancement, while at the highest jet power the radio sources have passed the jet power threshold at which radio-jet feedback switches from enhancing star formation to suppressing it. Indeed, the estimated mean sSFR enhancement fraction is  $< 1$  suggesting that powerful jets for a given galaxy mass suppress the star formation in the host galaxy compared to a radio-quiet source. Larger RG samples, covering a wide range of galaxy masses and radio luminosities, would provide us with additional observational constraints for our model.

Although the suggested model seems to explain the observations, we have to keep in mind that the star formation in the host galaxies of these RLQ and RG systems might be controlled by many additional parameters, like the environment and merger activity, which we expect to be quite common especially for the quasars in our sample (e.g. [Santini et al., 2010](#); [Kartaltepe et al., 2012](#); [Ramos Almeida et al., 2012](#)). For instance, [Stevens et al. \(2003\)](#) presented submillimetre imaging of seven high-redshift RGS, several of which appear to contain extended dust emission ( $\sim 30 - 150$  kpc), co-spatial in some cases with similarly extended

UV emission (e.g. Hatch et al., 2008). This suggests that the brightest submillimetre companions trace to the high-redshift RGs may trace a large-scale structure which would contain the densest cross-sections of gas. In this case the very brightest radio sources in our sample, dominated by RGs due to the method of the selection, might be physically associated with over-dense regions. In this case, the high jet power sources of our sample might have formed their stars at earlier epochs and we now observe them at a passive evolutionary stage.

## 4.7 Conclusions

I have presented *Herschel* photometry of RLQs, RQQs and RGs selected at a single epoch,  $z \approx 1$ . Combining the *Herschel* observations with SMA observations I performed a full radio-FIR SED analysis to investigate the non-thermal contamination to the FIR bands. SDSS data for the QSOs and mid-IR data for the RGs in our sample were used to estimate the AGN luminosity of each source. The FIR observations were used to estimate the SFR for the individually FIR detected sources and the stacked SFR for a variety of AGN and radio properties. I summarize the results below:

1. About 33 per cent (43/149) of the QSOs and 8 per cent (2/27) of the RGs have robust PACS and SPIRE detections. These detection rates are translated to ULIRG-like star formation luminosities suggesting SFRs of hundreds of solar masses per year.
2. SMA 1300  $\mu\text{m}$  observations lead us to reject 17 RLQs in which the 500  $\mu\text{m}$  flux may suffer significant synchrotron contamination.
3. I find that about 40 per cent (22/57) of RLQs have robust FIR detections and 30 per cent (21/72) of RQQs. The SFRs of the FIR detected QSOs are higher than a simulated mass-matched, non-AGN galaxy sample supporting the scenario of a merger induced star formation activity. Additionally, the high SFRs and detection rates suggest that there is no clear evidence that the star formation has been quenched in the hosts of these powerful QSOs compared to the non-AGN galaxies. Although radio-jets can enhance the SFR in the RLQs compared to the RQQs, they are not the likely cause of the star formation as RQQ systems as still found with significantly high star formation activity.
4. The FIR luminosity does not show a strong correlation with the AGN luminosity or the stellar mass for any of the three sub-samples in contrast to what is expected for AGN-dominated systems. The lack of dependence on AGN luminosity might suggest that neither the QSO continuum is the cause of star formation activity in any of the AGN systems we studied in this work. A multi-wavelength SED for the measurement of the bolometric luminosity would improve the uncertainties arise from the  $L_{12\mu\text{m}}$  and

$L_{3000}$  use for the  $L_{\text{bol}}$  calculation and their associated bolometric corrections, in order to confirm our results.

5. The RLQs are found to have a SFR excess of about  $300 M_{\odot} \text{ yr}^{-1}$  (a factor of 2.5) over RQQs of the same bolometric luminosity, similar to the one suggested from simulations in gas-rich radio-loud AGN (Gaibler et al., 2012).
6. Merger induced star formation activity is a possible mechanism leading to the SFRs obtained for RQQs while radio-jet triggered star formation seems to be the likely cause for the SFR excess in RLQs compare to the AGN luminosity matched RQQ sample. It is expected that RGs' low detection rates are associated with the radio selection of the sample, suggesting the existence of a jet power threshold below which the radio jets enhance the star formation and above which they suppress the star formation in the host galaxy by ejecting gas.

Future observations with instruments with better sensitivity/resolution, such as ALMA, and Integral Field Spectroscopy (IFS) will likely help us pinpoint the exact location of the ongoing star formation in these AGN and determine how radio jets can regulate the gas in the host galaxy. Photometric observations from X-ray to radio bands for the total QSO sample will be used to construct a comprehensive library of spectral energy distributions. In doing so, we will decouple luminosity effects from evolutionary effects and so determine the amount of radiation that is absorbed and reprocessed by the torus, and how this depends on the presence, or absence, of a radio jet. The SED library will represent a fundamental resource to reconcile the conflicting results on AGN obscuration at different wavelengths, determine robust star formation rates for AGN host galaxies, and for future investigations of the accretion history of massive black holes.

*Time is most short and space most narrow between these two pyres, the rhythm of this life is most sluggish, and I have no time, nor a place to dance in. I cannot wait. Then all at once the rhythm of the earth becomes a vertigo, time disappears, the moment whirls, becomes eternity, and every point in space insect or star or idea turns into dance.*

[The Saviors of God (1923)] - Nikos Kazantzakis

# 5

## HerMES: Far-Infrared properties of narrow emission line galaxies

This chapter is partly reproduced from the paper: *HerMES: Far-Infrared properties of narrow emission line galaxies* by **E. Kalfountzou**, M. Trichas, D. Rigopoulou, A. Ruiz, J. Bock, D. Farrah, A. Feltre, E. A. González Solares, E. Hatziminaoglou, L. Marchetti, S. Oliver, N. Seymour, M. Vaccari, to be submitted for publication in MNRAS, 2015

### Abstract

In this chapter, I explored the FIR nature of a large ( $\sim 600$  sources)  $24\mu\text{m}$ -selected spectroscopic sample of galaxies in the Lockman Hole, for which *Herschel* Multi-tiered Extragalactic Survey (HerMES) FIR data are available. The sample were classified into type-1 active galactic nucleus (AGN), type-2 AGN and non-AGN sources based on emission line diagnostics. I compiled extensive photometry from ultraviolet to FIR wavelengths to derive detailed SEDs for the extragalactic sources of the sample. A variety of templates were fitted to determine bolometric luminosities, and constrain the AGN and starburst components where both are present. The spectroscopic classification was compared with the SEDs, and good agreement between the two methods was observed. Within our sample we identified 452 sources having a HerMES counterpart (close to the confusion limit at  $250\mu\text{m}$ ) and 20 per cent of this population was detected at a level of  $5\sigma$  or greater at  $250\mu\text{m}$ . The number of  $5\sigma$  detected sources shows a sharp drop above  $z \sim 1.0$ . The  $250\mu\text{m}$  emission shows no correlation with the fractional contribution of AGN and/or starburst components (as estimated by the SED fitting). However, the results indicate that at high infrared luminosities, a strong AGN component is required (i.e. AGN luminosity) for the total SED fitting suggesting that powerful AGN are associated with strong star-formation events. In agreement with previous studies, the type-2 AGN displays on

average higher SFR than type-1 AGN.

## 5.1 Introduction

The ‘unification model’ of AGN ascribes obscuration of AGNs to different lines of sight through a dusty ‘torus’ surrounding the SMBH (e.g. [Urry & Padovani, 1995](#); [Antonucci, 1993](#)). This model predicts no difference in host galaxy properties between obscured and unobscured AGNs. To date, it is still a matter of debate whether the obscuration in luminous quasars can be explained solely by the orientation-based unification model or if it is also enhanced due to dust on larger scales throughout the host galaxy. Indeed, the results presented in [Chapter 4](#) suggest that radio galaxies have different host galaxy properties RLQs suggesting that the unified model of AGN cannot exclusively explain the observed differences.

As I have analytically presented in [Chapter 1](#), several studies have shown results supporting a scenario departing from the unification model, such as the enhanced SF activity (e.g. [Canalizo & Stockton, 2001](#); [Page et al., 2004](#); [Hiner et al., 2009](#)) and the more disturbed structure (e.g. [Lacy et al., 2007](#)) of the host galaxies of dust-obscured quasars when compared to unobscured quasars. [Hatziminaoglou et al. \(2010\)](#) found that type-2 AGN detected at  $250\ \mu\text{m}$  show on average a higher SFR than type-1 AGN. That being said, a larger sample is required in order to establish whether this trend indicates stronger star formation activity. More recently, [Chen et al. \(2015\)](#) measured the star formation properties of mid-IR-selected, optically unobscured and obscured quasars. They found that obscured quasars have roughly twice the FIR detection fractions, fluxes and star formation rate luminosities than a matched sample of unobscured quasars.

Based on the above, it is apparent that a detailed study of the AGN and the star formation connection is needed to reach a full understanding of galaxy formation and evolution. To understand the star formation process, it is essential to investigate the optical/infrared SEDs. Also, optical spectroscopy and emission lines provide valuable insight for such a study. The SED modeling (e.g. [Trichas et al., 2012](#)) and the Baldwin - Phillips - Terlevich (BPT) diagrams ([Baldwin et al., 1981](#)) can provide more information about the type of the dominating energy source in order to distinguish between different type of AGN and star-forming galaxies.

With the advent of *Herschel Space Observatory* ([Pilbratt et al., 2010](#)), it is possible to investigate the FIR properties of different types of galaxies and link their observed differences to the various viewing angle. Based on the dusty torus unified scheme (e.g. [Urry & Padovani, 1995](#)), broad and narrow emission line AGN are intrinsically identical sources - dust around the accretion disk exclusively covers certain lines of sight, leaving the broad emission lines and the optical and ultraviolet continuum undetectable. However, in the case of a galaxy rich in gas and dust, the dust distributed within the host galaxy can also cause obscuration (e.g. [Lawrence & Elvis, 1982](#); [Fabian, 1999](#)). The FIR emission, almost uncontaminated by the

AGN, gives us also the opportunity to study the star formation activity into different types of AGN.

The work presented here intends to compare the FIR and optical properties of a large sample of  $24\ \mu\text{m}$  selected galaxies spectroscopically observed by the 6.5m Multiple Mirror Telescope (MMT). The FIR results are based on the *Herschel* Multi-tiered Extragalactic Survey (HerMES; [Oliver et al., 2012](#)) data taken as part of the Herschel Science Demonstration Phase ([Oliver et al., 2010](#)). The chapter is organized as follows; Section 5.2 describes the observations, the optical spectroscopy, and the multi-wavelength data. In Section 5.3 I summarize the template fitting method used to model SEDs. Section 5.4 discusses emission-line diagnostics and their combination with SEDs and FIR data. In Section 5.5 I present the FIR emission for the different classes of sources in our sample. Finally, Section 5.6 summarizes the results.

## 5.2 Sample & Observations

### 5.2.1 The $24\ \mu\text{m}$ flux-limited sample

The sample used in this paper comes from a  $24\ \mu\text{m}$  flux-limited sample in the  $\sim 22\ \text{deg}^2$  Lockman Hole - Spitzer Wide-area InfraRed Extragalactic Survey (SWIRE; [Lonsdale et al., 2003](#)). The SDSS imaging also covers the Lockman Hole - SWIRE (LHS) region to  $r = 22.2$  at 95 per cent detection repeatability, but can go as deep as  $r = 23$ . A  $24\ \mu\text{m}$  flux limit of  $S_{24\ \mu\text{m}} > 0.4\text{mJy}$  ( $\approx 8\sigma$ ) was firstly applied. The completeness at this limit for SWIRE-MIPS catalogue is  $\sim 90$  per cent ([Shupe et al., 2008](#)). The sample was then matched to the SDSS DR7 catalogue. Adopting a matching radius of 2.5 arcsec it is found that 87 per cent of the  $24\ \mu\text{m}$  sources satisfy  $r < 22.5$ . This  $r$  limit allows follow-up optical spectroscopic observations with the MMT. More details about the  $24\ \mu\text{m}$  sample and the optical observations can be found in [Dai et al. \(2014\)](#).

The spectroscopic data of this study were carried out in 2009 (PI: Huang) using the Hectospec spectrograph ([Fabricant et al., 2005](#)) on the 6.5m MMT with a total area coverage of  $\sim 12\ \text{deg}^2$  (50 per cent of LHS field). Hectospec is a 300 fiber spectrograph which covers a 1 deg diameter field of view at the f/5 focus of the telescope. Each fiber aperture is 1.5 arcsec in diameter while the spectral coverage is 3500–9000Å with a spectral resolution of 1.21Å.

In brief, fiber configurations for five different fields were generated, targeting sources from the parent sample of 3000 targets. The  $\sim 600$  spectroscopic targets were selected from the MIPS and  $r$ -band flux limited catalog described above. We required that the Hectospec place fibers on 4-7 spectrophotometric F-type stars selected from SDSS, and 30 fibers were placed on blank-sky locations to measure the sky brightness. The remaining fibers (typically

>250) were placed on sources from the parent sample. The observations were executed during July of 2004 using an exposure time of 45 minutes split into three 15 minute exposures. Seeing was typically subarcsecond. The optical spectroscopic completeness  $S_{24\mu m} > 0.4\text{mJy}$  objects is  $\sim 30$  per cent.

The MMT Hectospec data were reduced using the HSRED pipeline (Cool et al., 2008, <http://mmt.org/rcool/hsred/index.html>), which is based on the SDSS pipeline. HSRED extracts one dimensional (1d) spectra, subtracts the sky and then flux-calibrates the spectra. The flux-calibration is done using spectra of 6-10 SDSS selected F-type stars that are observed simultaneously with the main galaxy and quasar sample. The flux calibration correction is obtained combining the extinction-corrected SDSS photometry of these stars with Kurucz (1993) model fits (Cool et al., 2008). The redshifts measured by HSRED also use code adapted from SDSS and use the same templates as SDSS. All spectra were visually inspected for validation. The confidence level of these redshifts is typically  $> 95$  per cent.

The original LHS sample was cross-matched with the HerMES catalogues as described in Section 5.2.3. The spectroscopic (sub-)sample used throughout this paper consists of a total of 567 spectroscopically confirmed,  $24\ \mu\text{m}$  selected sources in the Lockman-SWIRE (LS) field.

## 5.2.2 Optical Spectral Modeling: The Emission Lines

The focus of this work is to investigate the optical and FIR properties of our sample. In the case of narrow-line emission galaxies, the optical classification is based on the BPT diagrams (Baldwin et al., 1981). In order to place the sample galaxies on the BPT diagrams, we have to estimate the strength of a number of emission lines such as  $\text{H}\alpha$ ,  $\text{H}\beta$ ,  $[\text{OIII}]\lambda 5007$ ,  $[\text{NII}]\lambda 6584$ . Apart from the necessary emission lines for the BPT diagrams, we have also taken measurements for the most common emission lines in each spectrum.

In order to perform the optical spectral fitting, I developed a code in IDL (Interactive Data Language) which makes use of the IDL - based MPFITEXPR algorithm<sup>1</sup> developed by Markwardt (2009) to perform the Levenberg-Marquardt least-squares fit. The same code was also used for the Kalfountzou et al. (2012) work. The algorithm is used to obtain the best-fit parameters - the central wavelength, the width of the Gaussian ( $\sigma = \text{FWHM}/2.35$ ), and the integrated flux for each emission line. The first step is to fit the continuum part of the spectrum. Due to the differing nature of the sources, fitting all the sources by a single power law proved to be challenging. For this reason, we estimated the local power-law of each emission line from space surrounding it that was free of other emission/absorption lines.

The emission lines were predominantly fitted with one Gaussian. However, the strong emission lines (e.g.  $\text{Ly}\alpha$ ,  $\text{MgII}$ ,  $\text{H}\beta$ ,  $\text{H}\alpha$ ), were fitted with the additional combined profile of two or three Gaussian components, to which no physical meaning is imbued, but they fit

<sup>1</sup><http://www.purl.com/net/mpfit>

the observed line as well. In these cases, the best fit was determined from a minimization of the  $\chi^2$ . As a first stage, the FWHM and peak amplitude of the Gaussians were determined based on the expected wavelength position of the emission line, as it was calculated from redshift. Then the position of the line is free and modelled together with the FWHM and peak amplitude. Finally, the above parameter was used to refit the Gaussians. The errors on the fit results were derived from the formal errors on the  $\chi^2$  minimization. Fig. 5.1 shows various examples of the emission line fittings.

Based on these measurements our sample consists of 385 narrow emission line (NL) galaxies ( $\text{FWHM} \leq 1000 \text{ km/s}$ ) and 182 broad emission line (BL) galaxies ( $> 1000 \text{ km/s}$ ). Out of the 385 NL galaxies, 166 have all four BPT emission lines available. As we describe later, the spectroscopic classification is in good agreement with the SED fitting results.

### 5.2.3 FIR Sample selection

The Spectral and Imaging Receiver (SPIRE; Griffin et al., 2010) observations of the Lockman-SWIRE (LS) field were carried out in October 2009 by the *Herschel Space Observatory* (Pilbratt et al., 2010) as part of the HerMES program (Oliver et al., 2012). Maps and source catalogues at wavelengths of 250, 350 and 500  $\mu\text{m}$  were constructed (Smith et al., 2012a). Source extraction was performed via the method described by (Roseboom et al., 2010, 2012, hereafter XID catalogue) which uses a 24  $\mu\text{m}$  sources as priors, provides more accurate flux densities, and recovers a larger fraction of faint SPIRE sources, as close as possible to the confusion limit, than a more values of 5.8, 6.3 and 6.8  $\text{mJy beam}^{-1}$  at 250, 350 and 500  $\mu\text{m}$ , straightforward source extraction/catalogue cross-identification approach. Confusion noise respectively, are reported in Nguyen et al. (2010). The 24  $\mu\text{m}$  positions were matched against IRAC positions using a 3.0 arcsec search radius, and UV/Optical/NIR positions were then matched against IRAC positions using a 1.5 arcsec search radius.

We found that  $\sim 80$  per cent of our sources (457 sources) have a *Herschel* counterpart in the 24  $\mu\text{m}$  prior source catalogues (XID). It is worth noting that 140 of these objects, almost 30 per cent, have a 250  $\mu\text{m}$  detection at the  $5\sigma$  level or better. The number of sources detected at a signal-to-noise ratio greater than 3 ( $S_{250\mu\text{m}} > 18 \text{ mJy}$ ) is almost double (256 sources) reaching the  $\sim 55$  per cent of the total population.

Fig. 5.2 (top) shows the redshift distribution of the 457 extragalactic sources which have been divided into broad emission line ( $N = 149$ ; black solid line) and narrow emission line objects ( $N = 308$ ; black dashed histogram). Also presented is the redshift distribution of the 140 sources with  $> 5\sigma$  detections at 250  $\mu\text{m}$  (red filled histogram). The  $> 5\sigma$  250  $\mu\text{m}$  detected sources span over  $0.11 < z \leq 3.48$  with only 4 sources having  $z > 1.0$ . The highest redshift source with a 250  $\mu\text{m}$   $5\sigma$  detection is found at  $z = 3.48$ . We found that  $\sim 80$  per cent (62) of the sources with  $> 5\sigma$  detections at 250  $\mu\text{m}$  are narrow emission line objects while 19 sources have broad emission lines. Even at the  $3\sigma$  detection limit the percentage

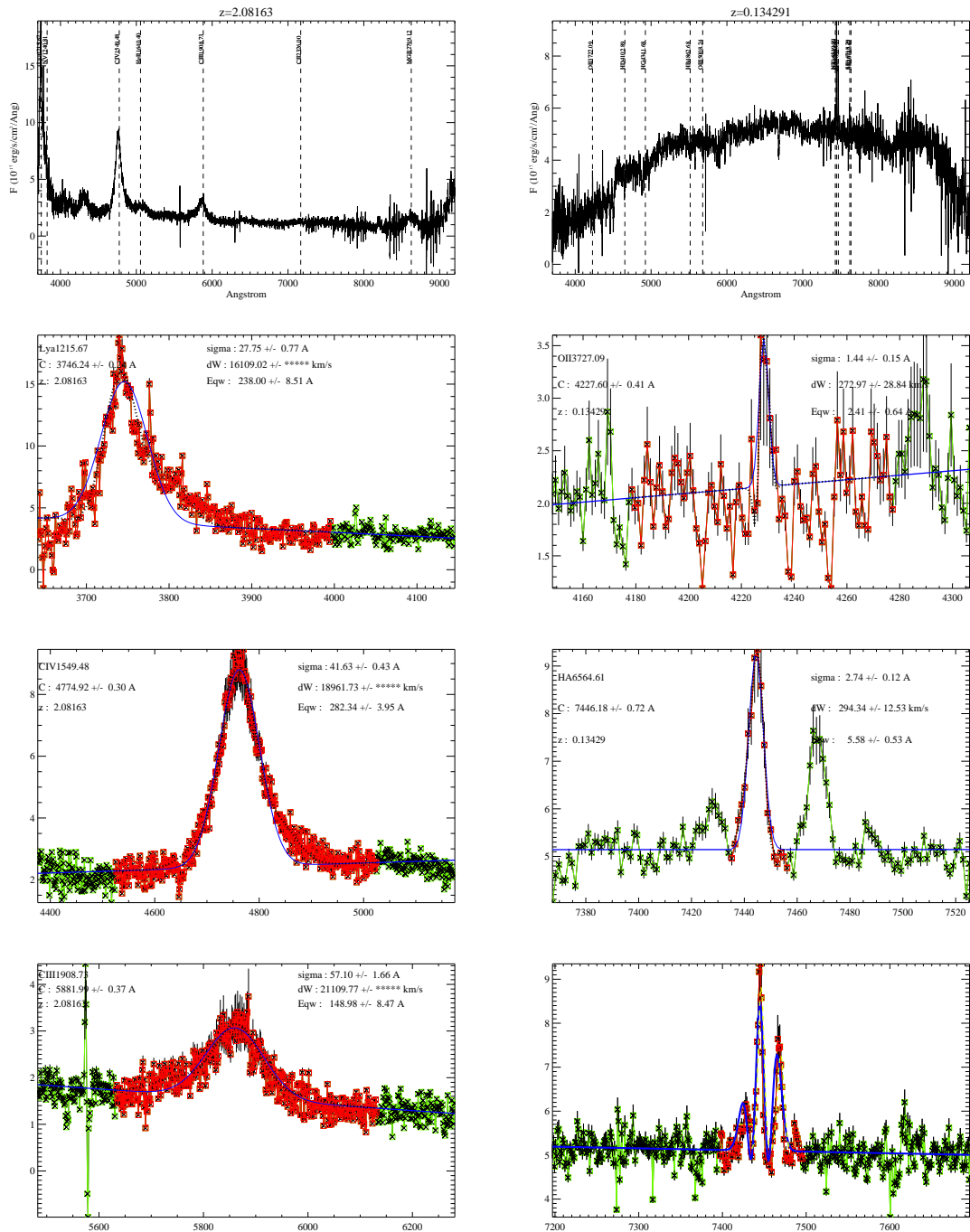


FIGURE 5.1: A sample of rest frame spectra drawn from our sample with their strongest emission lines. The first row shows the spectra of two objects with their detected emission lines. The rest of the figures show the single Gaussian fitting and the continuum level (blue line) in different type of emission lines (broad lines, narrow lines, blended lines). The multiple-Gaussian fitting is also presented (black bot line). With red is represented the part of the spectrum which is used for the fitting.

of detected narrow emission line and broad emission line sources remains the same. Only 4 sources ( $\sim 10$  per cent) of the  $z > 1.0$  sample had  $> 5\sigma$  detections at  $250 \mu\text{m}$ , while 7 sources ( $\sim 30$  per cent) had  $> 3\sigma$  detections.

Fig. 5.2 (bottom) shows the distribution of the  $24 \mu\text{m}$  luminosity as a function of redshift for type-1 (broad emission line) sources and type-2 AGN. The classification of the narrow emission line sample into type-2 AGN is based on BPT diagrams and SEDs; this is described in Sections 5.3 and 5.4. In order to ensure that the two AGN subsets have similar evolution and AGN properties, and that any following comparison is not affected by redshift and different AGN contribution, we compare the distribution in  $z$  and  $L_{24}$  of type-1 and type-2 AGN. The observed  $24 \mu\text{m}$  radiation is expected to be dominated by AGN light reprocessed by dust in the circumnuclear region of the AGN. Thus, the  $L_{24}$  should be a tracer of the intrinsic AGN emission. It is obvious that at lower redshifts ( $z < 0.18$ ), the AGN population is massively dominated by type-2 sources while at higher redshifts ( $z > 0.18$ ) only type-1 AGN are found. For these reasons, the redshift range for this comparison was chosen to be  $0.18 < z < 1.1$ . Furthermore, the two subsamples were forced to have the same  $L_{24}$  at the selected redshift range by randomly removing type-2 AGN from our parent sample. In this procedure, 11 type-2 AGN were randomly removed. The Kolmogorov-Smirnov (KS) test results are  $d = 0.12$ ,  $p = 0.50$  in the case of redshift and  $d = 0.12$ ,  $p = 0.54$  in the case of  $L_{24}$  where small values of probability ( $p$ ) imply that the null hypothesis that the samples are drawn from the same parent population can be rejected. On this way, we have matched the type-1 and type-2 AGN subsamples into redshift and AGN equivalent power ( $24 \mu\text{m}$  luminosity).

### 5.3 Spectral Energy Distributions

To characterize the SEDs of extragalactic objects, estimate bolometric luminosities and investigate for the presence of starburst and/or AGN activity in our sample, we combined *Herschel*/SPIRE data with the Spitzer Data Fusion<sup>2</sup>, which compiles *Galaxy Evolution Explorer Deep Imaging* (GALEX DIS GR6 Plus 7; Morrissey et al., 2007), Sloan Digital Sky Survey Data Release 10 (SDSS-DR10; Ahn et al., 2014), Isaac Newton Telescope Wide Field Camera (INT-WFS; González-Solares et al., 2011), Two Micron All Sky Survey (2MASS; Skrutskie et al., 2006), UKIRT Infrared Deep Sky Deep Extragalactic Survey Data Release 10 (UKIDSS DXS DR10; Lawrence et al., 2007), Spitzer-SWIRE data for a Spitzer/IRAC-selected sample covering our field. The  $24 \mu\text{m}$  positions, which were used for *Herschel*/SPIRE flux measurements, were matched against IRAC positions using a  $3.0 \text{ arcsec}$  search radius, and UV/Optical/NIR positions were then matched against IRAC positions using a  $1.5 \text{ arcsec}$  search radius.

<sup>2</sup><http://www.mattiavaccari.net/df>

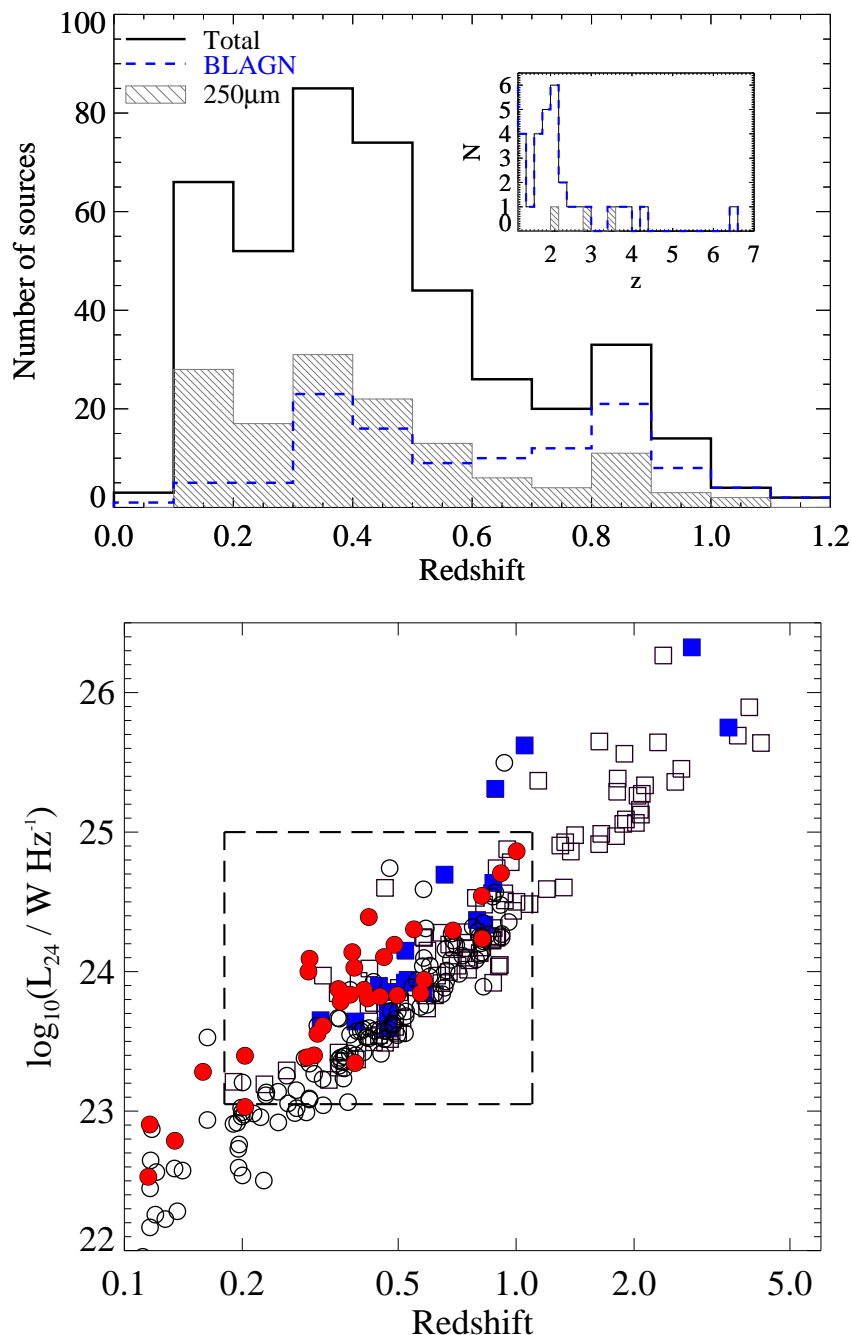


FIGURE 5.2: Top: Redshift distribution of all 567 spectroscopically identified extragalactic sources. The black line histogram represents the total sample, the grey filled histogram represents the sources detected at  $250\mu\text{m}$  at the  $5\sigma$  level and the blue dashed-line histogram the broad emission line sources. Bottom:  $24\mu\text{m}$  luminosity versus logarithmic redshift for type-2 AGN (circles) and type-1 AGN (squares). Detections ( $5\sigma$  level) at  $250\mu\text{m}$  are over-plotted as red circles for the type-2 AGN and blue squares for the type-1 AGN. The dashed box defines the parameter space in which the samples are matched in both  $24\mu\text{m}$  luminosity and redshift.

Of the 452 sources with a *Herschel*-SPIRE counterpart,  $\sim 73$  per cent have full UV-to-FIR coverage while  $\sim 13$  per cent have a  $> 5\sigma$  detection level at the *Herschel*-SPIRE bands,  $\sim 17$  per cent have full optical-to-FIR coverage, while the remaining  $\sim 10$  per cent is detected in a combination of bands.

The fitting procedure is a two-step process analogous to that applied in the SWIRE photometric redshift catalogue (Rowan-Robinson et al., 2008), but implemented with python, Sherpa (Freeman et al., 2001) and Astropy using the model described in Ruiz et al. (2010) and Trichas et al. (2012). In both steps we used a  $\chi^2$  minimization technique. In a first pass the optical/NIR region of the SED (wavelengths shortward of  $3.2 \mu\text{m}$ ) is fitted using a set of nine templates, including the extinction component  $A_V$  as a free parameter (using the Calzetti et al., 2000 extinction law). The set of optical templates includes galaxy templates (E, Sab, Sbc, Scd, Sd and starburst) and three QSO whose main difference is the presence/lack of  $\text{Ly}\alpha$  and CIV emission, as well as the amount of flux longward of  $1 \mu\text{m}$  (see Rowan-Robinson et al., 2008 for a complete description of these templates).

In the second pass, the IR region is fitted with a combination of four templates. The best-fit template found for the optical part is also included (with the normalization fixed) in order to take into account the stellar contribution. We employed the set of IR templates from Rowan-Robinson et al. (2008). It includes a cirrus template (IR emission from a quiescent galaxy), an AGN dust torus and two SB templates (M82 and Arp 220). Our IR model is a combination of three components: cirrus + SB + AGN. We tested this model with each SB template, and selected as best-fit the one with the lowest  $\chi^2$ . Finally, the optical and IR best-fit models were added to obtain a complete model of the SED covering the entire wavelength range.

The above can be combined to derive the total (bolometric) luminosity, the AGN fractional contribution and the IR luminosity due to star-formation:

$$\begin{aligned} L_{SED;tot} &= L_{SED;opt} + L_{SED;IR} \\ \text{AGN}_{cont} &= L_{AGN;MIR}/L_{SED;MIR} \\ L_{SF} &= L_{M82} + L_{Arp220} + L_{cirrus} \end{aligned} \quad (5.1)$$

Several physical components contribute to the emission that comprises the broadband SED of these objects, including stellar emission and star-formation heated dust from the host galaxy, emission from the AGN torus, and nuclear emission from the accretion disk. In particular, the IR emission is a result of both the AGN (primarily in the near and mid-IR) and the host galaxy (FIR being dominated by dust heated by massive young stars). As a result, the SED fitting of such objects presents a complicated task and often requires multi-component fits (e.g. Hatziminaoglou et al., 2008, 2009, 2010; Barthel et al., 2012; Feltre et al., 2013). The

optical to near-IR emission is mostly dominated by either a strong old stellar component, or an optical AGN, while the mid-IR to FIR emission is mostly dominated by either a torus or a star-formation component. Although emission from either component extends within the other half of the SED, these processes are physically distinct and can be studied quasi-separately. As a result we are able to effectively separate the AGN and the galaxy component contributions for each object.

The mid-IR colors have been extensively used for the AGN selection against star-forming galaxies (e.g. [Stern et al., 2005](#)). Additionally, the need of an AGN dust torus template to describe the photometric observations of each source can distinguish between type-1 and type-2 AGN. Therefore, we use the fractional contribution of each component at the  $4.5\mu\text{m}$  to separate the sources into AGN or starburst dominated.

Of the 126 broad emission line objects with a *Herschel* counterpart, 105 ( $\sim 85$  per cent) are classified as AGN-dominated systems, with half of them also requiring starburst contribution. All of them have been fitted with one of the QSO optical templates. AGN-dominated systems are defined as those whose SED fit gives an AGN component bolometric luminosity fractional contribution higher than 50 per cent. The remaining 21 broad line objects have an AGN contribution between 1 per cent and 50 per cent and are classified as AGN-composite. Although the lower limit for AGN-composite systems of 1 per cent appears low, for very luminous objects even 1 per cent contribution to the bolometric luminosity results to considerable AGN luminosity.

Out of the 331 narrow emission line objects with a *Herschel* counterpart, 42 are fitted with one of the optical non-AGN templates (i.e. elliptical, spiral, SB), 176 are fitted with the IR AGN template, while 46 sources do not require any AGN contribution for their SED fits. There are 57 sources for which both an optical and IR AGN template is used for their SED fit. We classify as type-2 AGN the 166 sources that are fitted with the IR AGN template and the AGN contribution dominates to the mid-IR emission. These results indicate an excellent agreement between the SED fitting AGN/SB contamination and optical spectroscopic classification in the case of broad and narrow emission line objects. [Fig. 5.3](#) shows examples of SED best-fitting and their best-fit models.

[Fig. 5.4](#) shows the average fractional contribution of AGN and/or starburst components (as was estimated by the SED best-fitting) to the  $250\mu\text{m}$  flux density of the objects with  $5\sigma$  detections. We have estimated the average  $250\mu\text{m}$  flux and AGN/SB contribution into five  $\log_{10}(F_{250})$  bins with the same number of objects. The objects with intermediate AGN and starburst components (composite objects) are those with the lower average  $250\mu\text{m}$  emission. The SB contribution appears to peak at intermediate  $250\mu\text{m}$  fluxes while at higher fluxes the AGN contribution slightly increases. However, taking into account the errors at the average estimations no correlation is obvious between the AGN/SB contribution and the  $250\mu\text{m}$  flux density. The lack of correlation is in contrast to the findings of [Page et al. \(2012\)](#) where more powerful AGN are not associated with  $250\mu\text{m}$  emission. These differences could be a

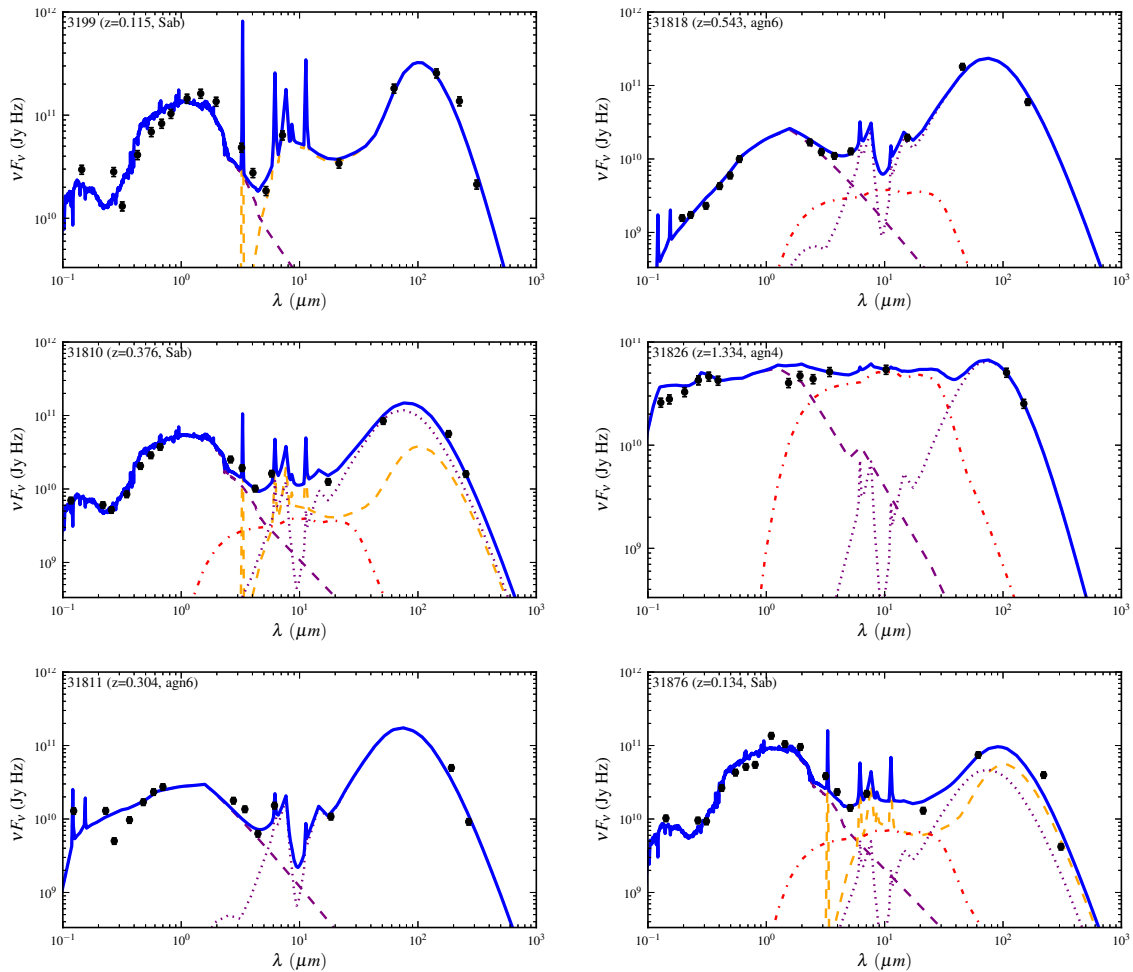


FIGURE 5.3: Examples of best-fit SEDs. The different components used in the fit are shown: optical component (dashed purple), cirrus template (dashed orange), starburst component (dotted green), and AGN dusty torus component (dot-dashed red). The total SED is shown with the solid blue line. The error bars are associated with 10% errors.

result of the different sample selection (mid-IR selected AGN in our work) and the different redshift ranges between the two works since [Page et al. \(2012\)](#) used an AGN sample with  $1 < z < 3$ .

## 5.4 Emission Line Diagnostic Diagrams

Emission lines in galaxy spectra can be produced by a variety of mechanisms. The spectra classification of emission line objects at low redshift is now routinely done with high quality calibrations. Using a set of four strong emission lines ( $[\text{OIII}]\lambda 5007$ ,  $\text{NII}\lambda 6584$ ,  $\text{H}\alpha$ , and  $\text{H}\beta$ ), [Baldwin et al. \(1981\)](#) distinguished star-forming galaxies, Seyfert - 2 galaxies, Low Ionization Nuclear Emission Region (LINER), and composite galaxies with both star-forming regions and an AGN.

The emission line measurements of 121 narrow emission line galaxies were used with a

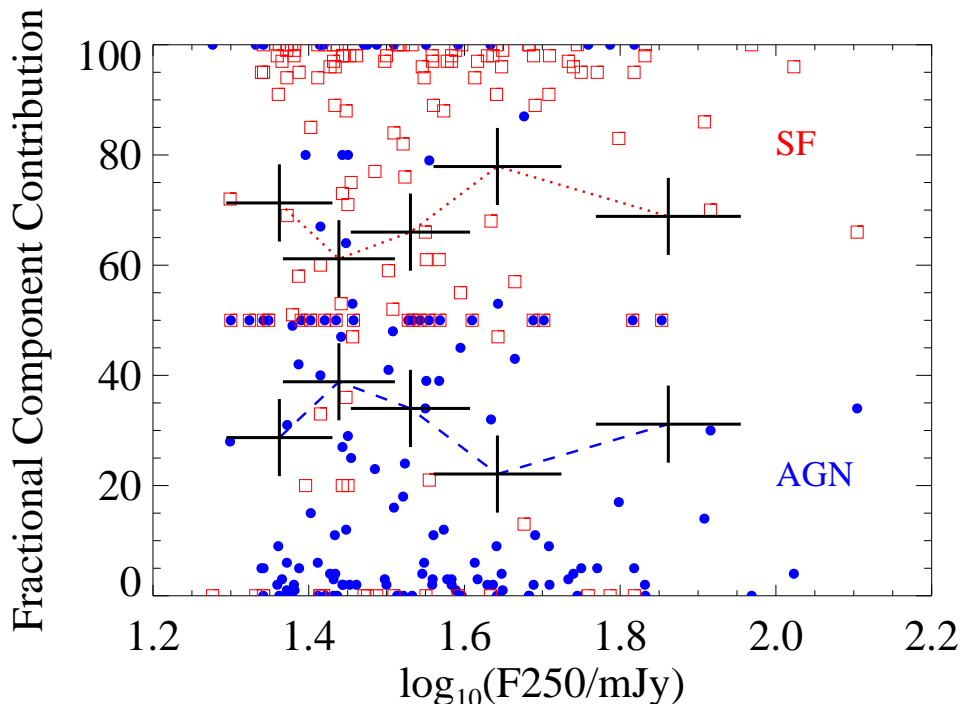


FIGURE 5.4: Fractional contribution of AGN (blue dots) and starburst components (red squares) to the total bolometric emission as a function of  $250 \mu\text{m}$  emission. Points represent the fractional AGN and/or starburst contributions for all objects with  $5\sigma$  detection at  $250 \mu\text{m}$ . Dotted red line represents the average value of starburst fractional contribution per  $\log_{10}(\text{F}250/\mu\text{m})$  bin. Dashed blue line represents the average value of AGN fractional contribution per  $\log_{10}(\text{F}250/\mu\text{m})$  bin. The  $1\sigma$  error bars are also plotted for each bin.

redshift range of  $0.1 < z < 0.4$  since the  $\text{NII}\lambda 6584$  and  $\text{H}\alpha$  emission lines used in the BPT diagram are redshifted beyond the optical band at  $z > 0.4$  (Fig. 5.5). We selected emission-line galaxies with the following criterion: the signal-to-noise ratio in the equivalent width of the emission lines used in the BPT diagrams must be greater than 3 and their FWHM must be lower than  $1000 \text{ km s}^{-1}$ . Even so, the limit of  $\text{S/N} > 3$  could bias our results against AGN population. The AGN-to-SF number ratio depends on the adopted cut-off for the emission-line detection significance. This could result in a low ratio because many AGN are very weak-lined LINERs (Heckman et al., 2004), an effect which increases in the case of noise spectra. For this reason, we extended our sample to also take into account objects with at least two out to four significant detected emission lines.

Recently, Juneau et al. (2014) suggested that the use of detection limits to the emission line ratios (rather than to the individual lines) would lead to more complete samples because the BPT diagram deals with line ratios. The emission line ratios are required to have  $\text{S/N} > 2.12 (= 3/\sqrt{2})$ , where the lower limit is equivalent to each line being detected at exactly  $3\sigma$ . Furthermore, this cut includes the combination of a poorly-detected line ( $< 3\sigma$ ) with a strongly-detected line, provided that the overall ratio is constrained to greater than  $\text{S/N} =$

2.12. The additional 34 sources selected based on their emission line ratios are presented in Fig. 5.5 with open symbols.

### 5.4.1 Adding SED information on the BPT diagrams

In this section I attempt to add an extra dimension to the BPT diagrams, based on SED fits, to investigate how the location of a sample galaxy may change on the BPT diagram when the SED classification is taken into account (see Section 5.3). Based on the  $[\text{NII}]\lambda 6582/\text{H}\alpha$  versus  $[\text{OIII}]\lambda 5007/\text{H}\beta$  BPT diagnostic diagram (see Fig. 5.5), we found 10 (13) Seyferts, 94 (106) star-forming galaxies, 47 (63) composites and 15 (18) LINERs. The numbers in the parenthesis represent the total number of sources based on both selection criteria (emission line limits and emission line ratio limits; filled and open circles in Fig. 5.5-top), while the original numbers consist only for the selected sources based on the emission line limits (filled circles). Based on these numbers, the percentage of sources which lie onto the extreme star-forming region (dashed black line; Kewley et al., 2001) is  $\sim 57$  per cent. If the sources from the pure star-forming regions (solid black line; Kauffmann et al., 2003) are added, the percentage increase to approximately 85 per cent. This detection rate is in agreement with the  $250\ \mu\text{m}$  detections (which arises from cold dust in the star-forming regions) for the 93 per cent of our BPT diagram sample. These rates are unaffected by the BPT selection criteria I have used.

In the same figure, I used a colour diagnostic based on the AGN contribution of the objects as it arises from SED fits. Galaxies with AGN contribution ( $\text{AGN}_{\text{con}}$ ) higher than 75 per cent occupy the AGN/LINER region while these with AGN contribution lower than 25 per cent are found in the star-forming region. Objects with intermediate AGN contribution mainly cover the pure star-forming/composite region. Specifically, 40 per cent of the objects with  $\text{AGN}_{\text{con}} > 75$  per cent are found in the AGN region. If we also add the sources into the LINER region, the rate rises to 70 per cent. There are only 3 outliers which are located in the extreme star-forming region. For these objects, both SED fitting and emission line measurements seem to be quite significant. Regarding the objects with  $\text{AGN}_{\text{con}} < 25$  per cent, the SED classification of the vast majority ( $\sim 94$  per cent) is in agreement with the BPT classification, which also takes into account the sources in the pure star-forming region. Five of the outliers are classified as LINERs and the only one that is classified as an AGN based on the BPT diagrams could fall into the composite region due to their emission line uncertainties. Fig. 5.5 (bottom) shows the perpendicular distance above and below the maximum starburst line against the AGN contribution to the SED fitting. I find a strong Pearson correlation of  $r = 0.6$  and  $p = 0.02$ .

Relative to the more traditional approach, if I include the sources selected based on their emission line ratio rather than the individual line detection limits (Fig. 5.5; open symbols),

we increase the sample by  $\sim 23$  per cent (38 additional sources). This includes more numerous, massive, metal-rich star-forming galaxies, as well as LINERs and passive galaxies, all of which tend to have comparatively faint [OIII] $\lambda$ 5007 lines. That being said, even if the less traditional approach is used (Juneau et al., 2014), the objects that are added in the BPT (open circles) are once more well classified by SED fitting, so the overall classification’s ‘success rate’ does not change.

The high ‘success rate’ between photometric (SEDs) and spectroscopic (BPT diagrams) classification provides a useful result. While spectroscopic classification is usually more secure, it can only be used objects with good quality available spectra and redshift range up to  $z \sim 0.4$ , which reduces our sample to less than the 1/3. The good agreement of the SEDs and the BPT diagrams permits us to use, whenever necessary, the SED classification.

## 5.5 Far-Infrared properties

### 5.5.1 250 $\mu$ m emission in type-1 & 2 AGN

One of the major aims of the present study is to investigate the origin of the FIR emission in the different types AGN. In this section, I use the classification of our sources based on the BPT diagram and their spectroscopic features where they are available, while when unavailable I use the SED classification.

In Fig. 5.6, I present the 250  $\mu$ m flux distribution for the matched in redshift ( $z < 1.1$ ) and  $L_{24}$  type-1 and type-2 AGN with a *Herschel* counterpart (as described in Section 5.2.3). While both populations display similar distribution at lower 250- $\mu$ m fluxes ( $< 18$ mJy associated to  $< 3\sigma$  detection level), type-2 AGN distribution is skewed towards higher values. Specifically, the K-S test for the total distribution returns  $d = 0.24$ ,  $p = 0.005$  showing that the 250- $\mu$ m flux density distributions are different at the  $> 95$  per cent level, while the mean 250  $\mu$ m flux densities are  $24.12 \pm 1.74$  mJy (type-2 AGN) and  $18.76 \pm 1.56$  mJy (type-1 AGN).

### 5.5.2 Star-formation rate

Based on the results stated above, it seems important to study the occurrence of star formation in the different types of AGN. The calculation of the SFR was performed using the equation by Kennicutt (1998) (see eq. 3.4).

Although the actual fraction is still under debate, it is known that the AGN can significantly contribute to both the mid-IR and, to a lesser degree, to the FIR luminosity of a source. For this reason it is crucial to distinguish between the star-formation and the AGN components in the SEDs. Therefore, in order to calculate the SFR for these sources, I derive the infrared luminosities of the sources as the integral over the 8 - 1000  $\mu$ m range of the M82,

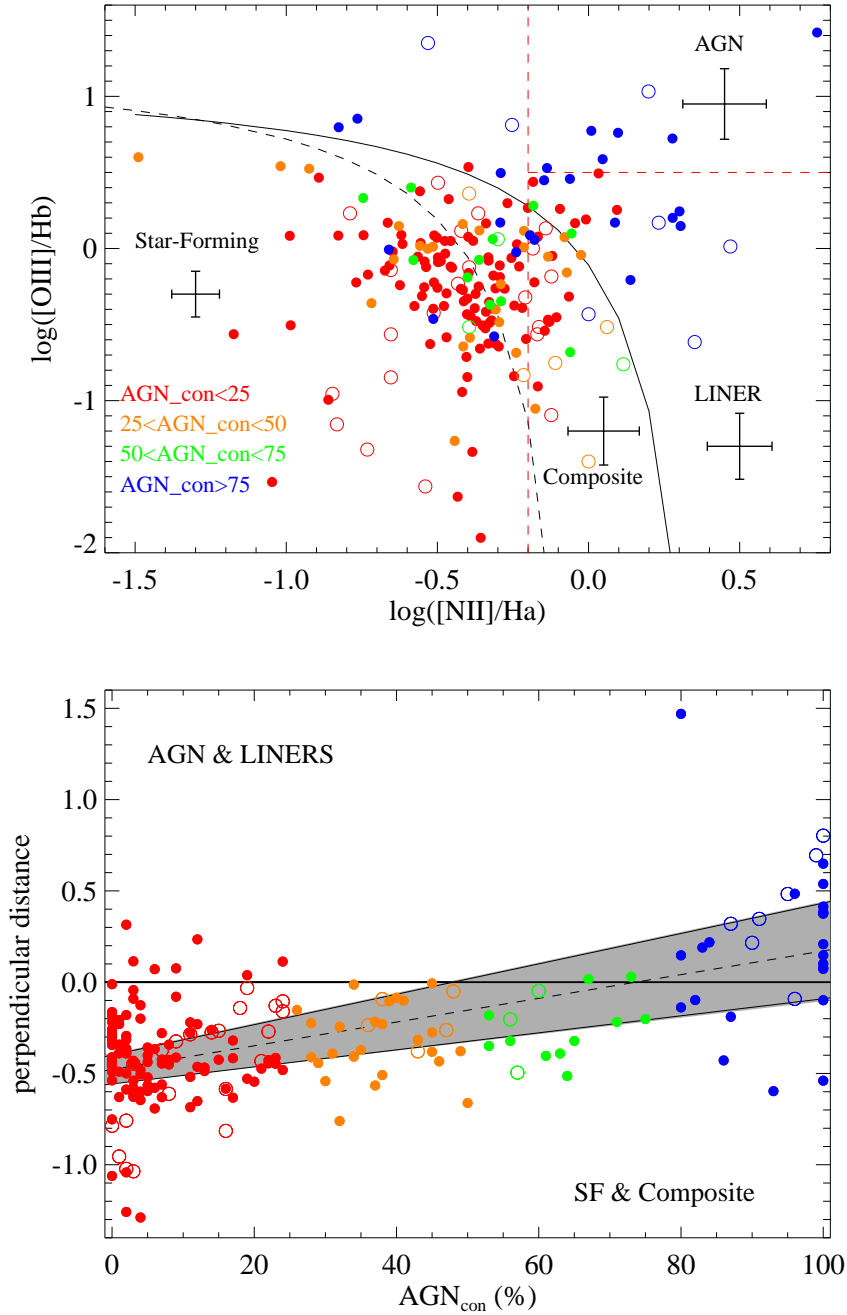


FIGURE 5.5: Top: The  $[\text{NII}]\lambda 6582/\text{H}\alpha$  versus  $[\text{OIII}]\lambda 5007/\text{H}\beta$  diagnostic emission line diagram for the 121 narrow emission line sources with available lines. The black dashed line represents the extreme star-forming line (Kewley et al., 2001) while the black solid line is the pure star-forming line (Kauffmann et al., 2003). The red-dashed lines are the Seyfert/LINER lines (Ho et al., 1997). The colour code is based on the AGN contribution of the objects as it arises from their SEDs. The open circles represent the selected sample based on the emission line ratio limits suggested by Juneau et al. 2014. We indicate an average error bar for each class. Bottom: The perpendicular distance above (positive values) and below the maximum starburst line (black thick line) in the BPT diagram against the AGN contribution. The dashed line represents the linear best fit for all the sources, with the associated errors (shaded area).

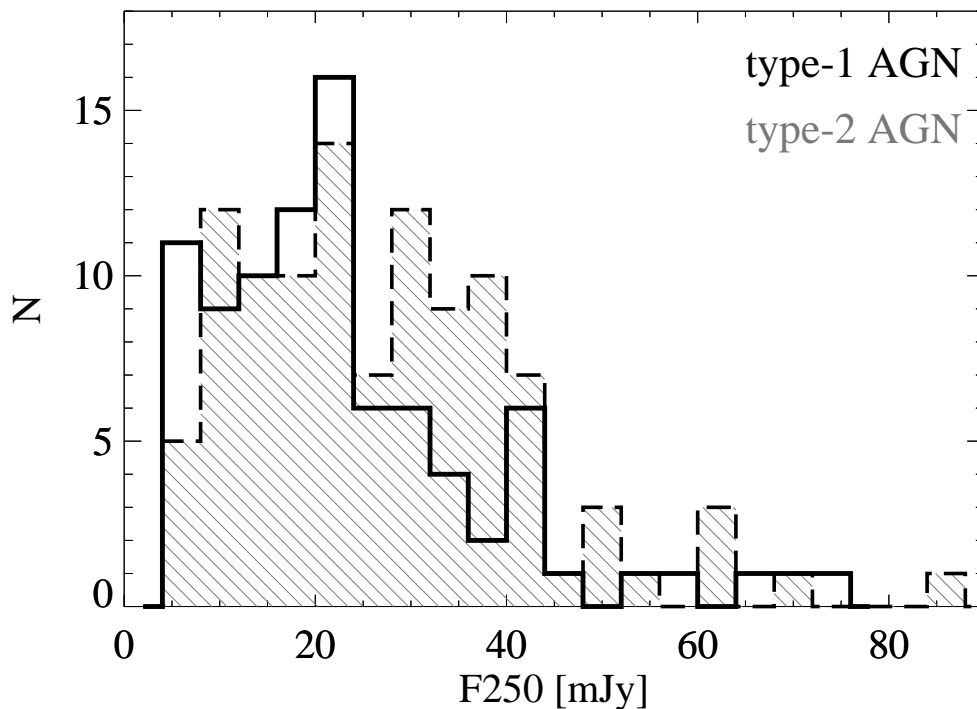


FIGURE 5.6: 250- $\mu\text{m}$  flux density distribution for type-1 and type-2 AGN. The filled histogram represents type-2 AGN and the black solid-line histogram the type-1 AGNs.

Arp220 and cirrus templates used for the SED fit of each source. As described in Section 5.3, in addition to these starburst templates, an AGN torus and a galaxy template were used. The AGN torus luminosity is not considered in the calculation of the SFR.

The observed SEDs were derived for all sources regardless their FIR detection level. Due to the large sample of sources which are not detected at a significant level ( $> 5\sigma$ ) by *Herschel*, I used two methods to investigate the SFR trends. In the first case, a weight mean technique for the total population of sources was used to estimate their SFR. The SEDs  $\chi^2$  fitting value is used as a weight for each source. With this method, the less significant detected sources are also taken into consideration but their effect to the mean values will be smaller due to their larger errors. This ensures that the results are not biased towards the brighter FIR objects. As previously mentioned, in most of the cases of spectroscopically confirmed AGN, a significant contamination of a starburst component is required to reproduce the observed SPIRE data points. Despite the low significance of some of the 350  $\mu\text{m}$  and 500  $\mu\text{m}$  data points (specifically in sources with detections below the  $3\sigma$  level), the starburst template fitting returns low  $\chi^2$  values. This indicated that they do not have a strong effect on the fit due to their large photometric errors. In the second case, I used only the detected sample at  $> 5\sigma$  level where the estimates of SFR are more robust.

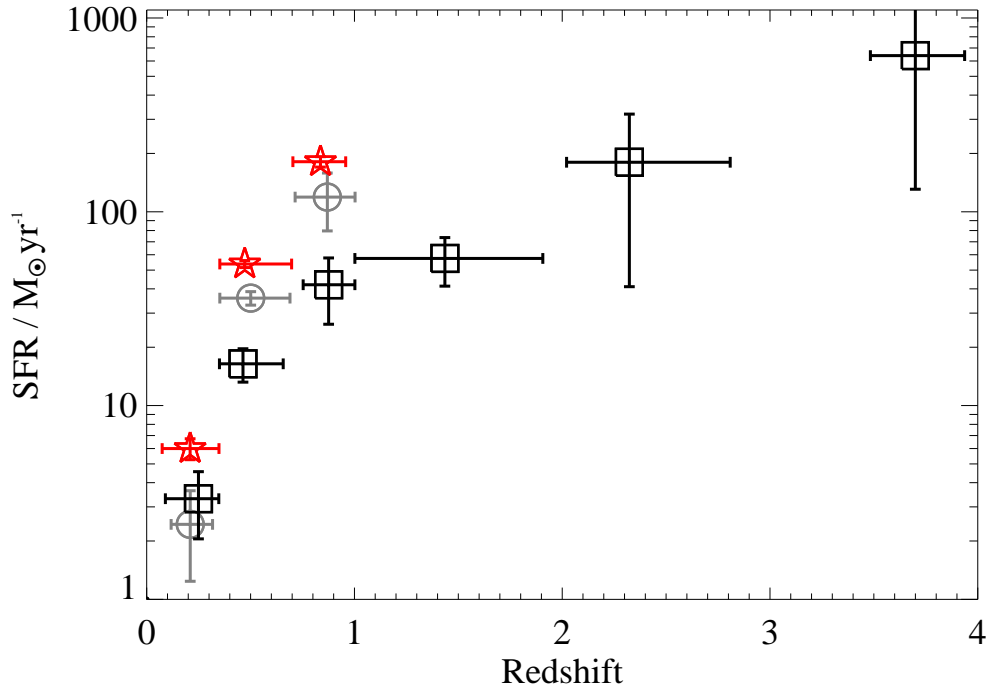


FIGURE 5.7: Weighted mean SFRs as a function of redshift. Non-AGN galaxies are shown with red stars, type-1 AGN with black squares and type-2 AGN with grey circles. The error bars represent the  $1\sigma$  errors.

Fig. 5.7 shows the weighted mean SFR versus redshift for type-1, type-2 AGN and non-AGN sources. The luminosity is weighted using the errors calculated from  $\Delta\chi^2$  and the errors on the stacked parameters are determined using the bootstrap method. The bootstrapped errors are determined by randomly selecting galaxies from within each bin and determine the median for this subsample. These averages are independent of the SPIRE 250  $\mu\text{m}$  detections because they are obtained from a stack of all sources with a SPIRE counterpart within a given redshift range. For redshift  $z < 1.1$ , we use a bin size of  $\Delta z = 0.35$  while for  $z > 1.1$  where only type-1 AGN are found the bin size is  $\Delta z = 1.0$ . We use the same redshift bins across the type-1 and type-2 AGN in order to facilitate comparisons. Comparing the mean SFR for type-1 and type-2 AGN at  $z < 1.1$  we observe that type-2 AGN tend to have higher SFR than type-1 AGN within their  $1\sigma$  errors. A similar case of excess of star-formation when comparing type-2 AGN to type-1 AGN is also found by [Hatziminaoglou et al. \(2010\)](#) for a smaller sample of objects and more recently by [Chen et al. \(2015\)](#) for mid-IR selected and classified type-1 and type-2 AGN at  $0.7 < z < 1.8$  with only 32 ( $\sim 9$  per cent) of the type-2 AGN having *spec-z* measurements.

Fig. 5.8 shows the SFR distribution of the 250  $\mu\text{m}$  detected at  $> 3\sigma$  and  $> 5\sigma$  (filled histograms) level type-1 and type-2 AGN alone. The redshift distribution of the two populations should not affect these results as both are matched on the  $L_{24}$  vs  $z$  parameter space

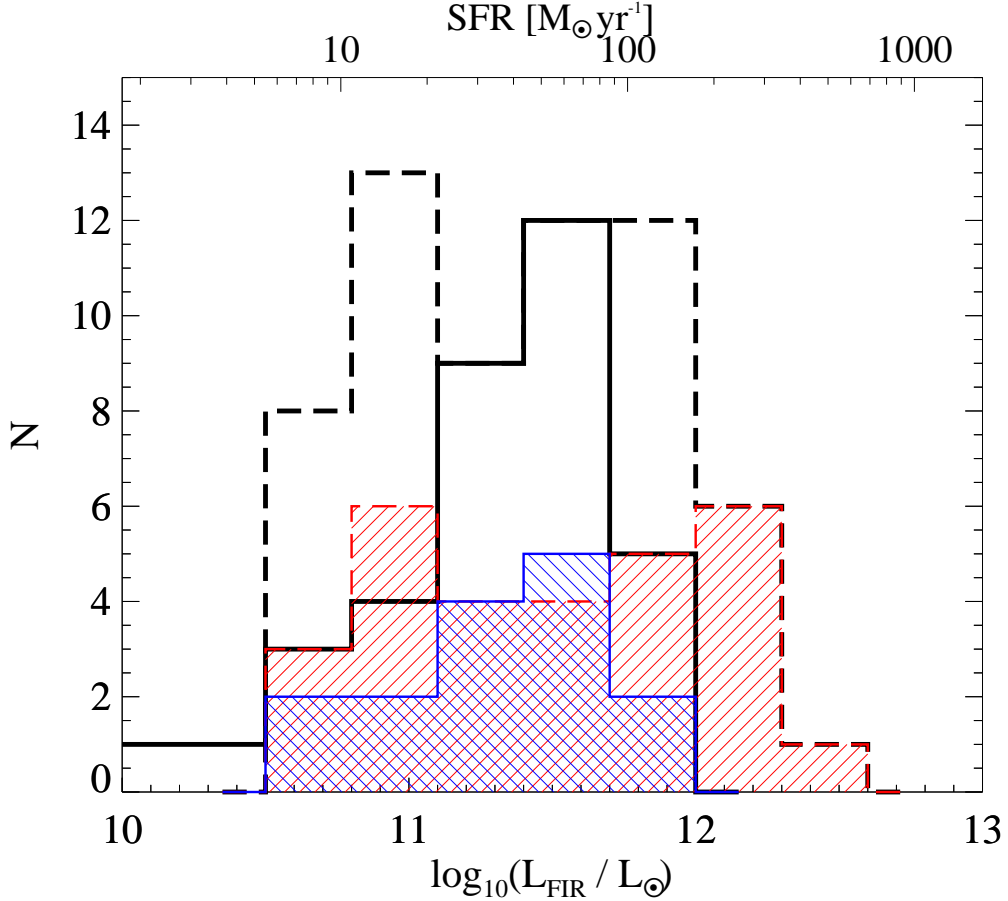


FIGURE 5.8: Histograms showing the FIR luminosity (and SFR) distribution for the type-1 (black solid line) and type-2 (black dashed line) AGN with  $3\sigma$  detections at  $250\mu\text{m}$ . The red and blue filled histograms represent the type-1 and type-2 AGN with  $5\sigma$  detections at  $250\mu\text{m}$ , respectively.

with  $z < 1.1$ . While the distributions of the two populations show no significant difference with a K-S test probability of  $p = 0.23$  and  $p = 0.08$  for  $3\sigma$  and  $5\sigma$  detection levels respectively, type-2 AGN are associated with higher SFR while no type-1 AGN was found with  $L_{\text{FIR}} > 10^{12} L_{\odot}$ . In addition, type-2 AGN tend to have on average higher SFR with  $\langle \text{SFR} \rangle = 114.8 \pm 22.4 M_{\odot}/\text{yr}$  at  $> 5\sigma$  detection level while, for type-1 AGN it is found to be  $\langle \text{SFR} \rangle = 49.6 \pm 9.6 M_{\odot}/\text{yr}$ . In the case of  $3\sigma$  detection level, the difference between the two populations is smaller with  $\langle \text{SFR} \rangle = 80.4 \pm 12.1 M_{\odot}/\text{yr}$  and  $\langle \text{SFR} \rangle = 49.2 \pm 6.2 M_{\odot}/\text{yr}$  for type-2 and type-1 AGN, respectively. The above results indicate that while both samples show similar SFR at lower  $250 \mu\text{m}$  ( $< 30 \text{ mJy}$ ) emission, type-2 AGN skew towards higher SFRs implying a wider range of FIR emission and SFR.

### 5.5.3 AGN contribution and FIR luminosity

Using the SED fitting results, it is evident that AGN luminosity fractional contribution behaves as a function of FIR luminosity. The results are shown in Fig. 5.9 (top) where the average fractional contribution of AGN and/or starburst components to the FIR luminosity

are presented. The galaxies have been divided into 5 bins with mean  $\log_{10}(L_{\text{FIR}}/L_{\odot}) = 10.58, 11.16, 11.51, 11.79$  and  $12.32$  so that each bin contains the same number of galaxies. Based on the average values, the AGN contribution increases with the  $L_{\text{FIR}}$ . However, the narrow emission line and broad emission line objects with high AGN fractional contribution in our sample tend to lie at higher redshift objects. As a result, the FIR emission could be biased by the different redshift distribution between the starburst and AGN populations. For this reason in Fig. 5.9 (bottom) I present the average fractional contribution of AGN and/or starburst components to the FIR luminosity normalized by the bolometric luminosity. This value gives the fraction of the  $L_{\text{FIR}}$  in the bolometric luminosity. When comparing the two figures, it is apparent that objects with significant contribution from both AGN and SB components tend to have higher FIR emission.

## 5.6 Conclusions

Spectroscopic analysis and multi-wavelength photometry have been combined with HerMES FIR observations in the Lockman Hole field to study the FIR properties of different type of AGN and non-AGN sources. The spectroscopic observations have been obtained using the Hectospec spectrograph on the Multiple Mirror Telescope. The spectroscopic classification of the sources into AGN and non-AGN have been confirmed by the SED fitting where excellent agreement was found. The SED fitting returns the fractions of AGN, starburst and galaxy contributions. The results show that most of the AGN sources require a significant starburst contribution to describe the SPIRE data points, yet no significant correlation is found between the AGN contamination and the  $250 \mu\text{m}$  emission.

Comparison of the FIR properties of the type-1 & 2 matched AGN samples shows that the type-2s have higher  $250 \mu\text{m}$  emission and higher star-formation rate than the type-1s. This result is in agreement with previous studies where type-2 AGN found to have on average higher SFR than type-1s (e.g. Hatziminaoglou et al., 2010; Chen et al., 2015) or being associated with stronger starburst components in order to describe their SED fitting (e.g. Trichas et al., 2010; Kalfountzou et al., 2011). Since FIR emission mainly arises from cool dust which is heated by star formation, the differences between the two types of AGN should be linked to an excess of star formation in type-2 AGN. This excess raising the possibility that type-2 AGN are observed during a different epoch compared to type-1 AGN when star-formation activity is enhanced which could be linked to the growth phase of the galaxy spheroid. Similar scenarios have been discussed in the literature (e.g. Page et al., 2004; Stevens et al., 2005; Hopkins et al., 2006; Coppin et al., 2008) suggesting an undergoing transition between a hidden growth phase and an unobscured AGN phase.

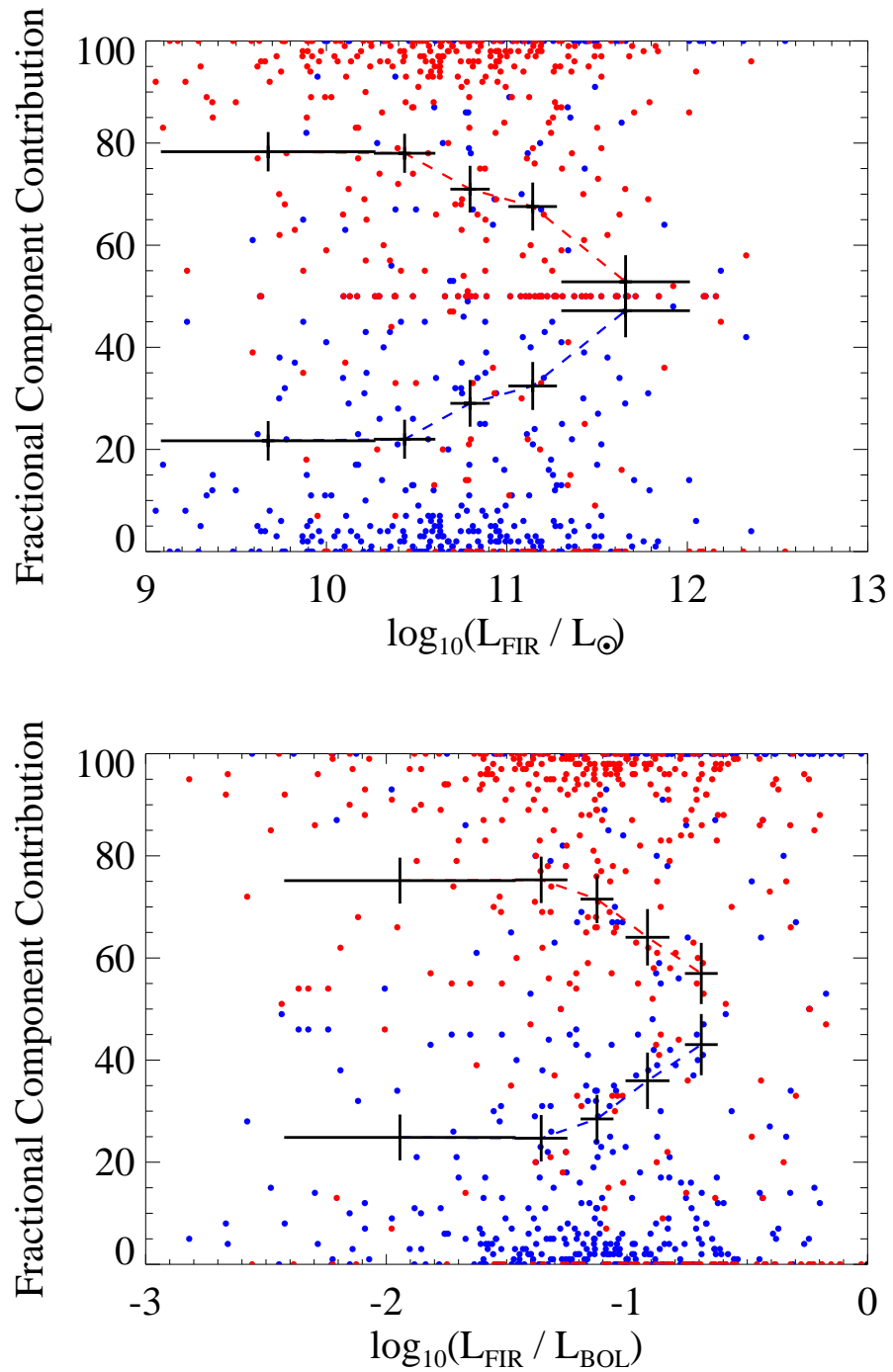


FIGURE 5.9: Fractional contribution of AGN (blue dots) and starburst components (red dots) to FIR luminosity (top) and normalized  $L_{\text{FIR}}$  by the bolometric luminosity (bottom). Points represent the fractional AGN and/or starburst contributions for all objects available estimation of their  $L_{\text{FIR}}$  based on the SED fitting. Solid red line represents the average value of starburst fractional contribution per  $\log_{10}(L_{\text{FIR}}/L_{\odot})$  (top) and  $\log_{10}(L_{\text{FIR}}/L_{\text{bol}})$  (bottom). Dashed blue line represents the average value of AGN fractional contribution. Error bars are also plotted for each bin.

*All those who actually live the mysteries of life  
haven't the time to write, and all those who have the  
time don't live them! D'you see?*

[Zorba the Greek (1946)] - Nikos Kazantzakis

# 6

## Conclusions and Future prospects

In this thesis I have highlighted how cosmic X-ray, optical and FIR surveys of distant AGNs have provided key insight into the demographics, physics and the connection of growing SMBHs to their host galaxies. Due to X-ray facilities such as *Chandra* (but also XMM-Newton and NuStar) we now have a dramatically improved picture of how SMBHs grew through cosmic time, their accretion and obscuration physics, and the connection between SMBHs, their host galaxies and the larger scale environment. On the other hand, wide field optical surveys (e.g. SDSS) have provided as with large samples of powerful but rare QSO population which are usually missed from the small field X-ray surveys. *Herschel* FIR observations have provided a unique tool for the study of the FIR emission in the host galaxies of powerful AGN with the minimal AGN contamination up to date.

In Chapter 2 *Chandra* space telescope X-ray data are utilised to create the largest high-redshift ( $z > 3$ ) X-ray-selected AGN sample. For this purpose, I have combined the *Chandra* Cosmological Evolution Survey and *Chandra* Multi-wavelength Project surveys, doubling previous samples. The sample comprises 209 X-ray-detected AGNs, over a wide range of rest-frame 2-10 keV luminosities  $\log(L_X/\text{erg s}^{-1}) = 43.3 - 46.0$  and column densities  $N_H = 10^{20} - 10^{23} \text{cm}^{-2}$ . Utilizing the  $1/V_{max}$  method, I confirm that the comoving space density of all luminosity ranges of AGNs strongly declines with redshift above  $z > 3$  and up to  $z \sim 7$ . Due to the large size and the wide X-ray luminosity range of this sample, I was able, for first time, to distinguish between competing evolution models (e.g. LDDE, LADE, CT AGNs) and suggest that observations appear to favor the LDDE model (e.g. [Gilli et al., 2007](#)) indicating a luminosity dependence of AGN evolution. The measured comoving space

density of type-1 and type-2 AGNs shows a constant ratio between the two types at  $z > 3$ . Our results for both AGN types at these redshifts are consistent with expectations of the LDDE model.

In Chapter 3 FIR *Herschel* data from the H-ATLAS Phase 1 Area survey are used to look at SDSS RLQs and RQQs host galaxy properties. The main result of this work is that RLQs at lower AGN luminosities tend to have on average higher FIR and 250- $\mu\text{m}$  luminosity with respect to RQQs matched in AGN luminosities and redshift. These results suggest that powerful radio jets are associated with star formation especially at lower accretion rates and are in agreement with my previous work on RLQs and RQQs using optical emission lines to trace the SFR in the host galaxies of these quasars (Kalfountzou et al., 2014a).

However, a drawback of this work is that the sample was fundamentally limited by the degeneracy between redshift and luminosity in flux-density limited samples. To overcome this limitation, in Chapter 4 I extend the previous work using a quasar sample at a single cosmic epoch  $0.9 < z < 1.1$  in order to decompose the evolution effects from the AGN/star-formation study. I present FIR *Herschel* observations of 74 RLQs, 72 RQQs and 27 RGs, which span over two decades in optical luminosity and I investigate how the SFR depends on AGN luminosity, radio-loudness and orientation. I find that: 1) the SFR shows a weak correlation with the bolometric luminosity for all AGN sub-samples, 2) the RLQs show a SFR excess of about  $300 M_{\odot} \text{ yr}^{-1}$  compared to the RQQ sample, matched in terms of black hole mass and bolometric luminosity, suggesting either positive radio-jet feedback, in agreement with our previous work or radio AGN triggering being linked to the star formation triggering and 3) the RGs have lower SFRs than the RLQs sub-sample with the same black hole mass and bolometric luminosity by a factor of 2.5. The main conclusion of this chapter is that there is some threshold at which radio-jet feedback switches from enhancing star-formation (by compressing gas) to suppressing it (by ejecting gas). Such a results seems to dependent on both galaxy mass and jet-power. Then we expect more massive galaxies to have more star-formation for a given jet-power because their star-formation is more enhanced by the jet.

In Chapter 5, I explore the FIR emission associated with the star-formation in the host galaxies of BLAGNs and NLAGNs. For with work I use a large 24  $\mu\text{m}$  flux-limited spectroscopic sample ( $\sim 600$  sources) selected in the Lockman Hole. The SFRs are studied using the FIR data from Herschel Multi-tiered Extragalactic Survey (HerMES) in the selected field. I used the optical spectra and emission line diagnostics to classify the sources into BLAGNs, NLAGNs and non-AGNs. Our predictions have been compared with our Spectral Energy Distribution template fitting methods and mid/FIR selection methods where an excellent agreement between the spectroscopic and the photometric methods was found. The main conclusions of this chapter are that at high infrared luminosities, a strong AGN component is required (i.e. AGN luminosity) for the total SED fitting suggesting that powerful AGN are associated with strong star-formation events. Also, in agreement with previous studies, the

type-2 AGN are found to display, on average, higher SFRs than BLAGNs.

However, many fundamental questions about AGN and their host galaxy evolution remain unanswered. In the next sections, I focus on some of the key remaining questions which arise from my results and discuss how current and future projects can be used to address them over the next years.

## 6.1 The AGN/host galaxy interplay at the early Universe

Our results in Chapter 4 and previous work (e.g. Rosario et al., 2012) suggests an evolution of the AGN/star-formation connection with redshift. This evolution refers not only to the increase of the SFR from the local Universe to  $z \sim 2.5$  but also to a change of the slope of the correlation. However, fast AGN variability very likely plays a role in shaping this correlation (Hickox et al., 2014), but different mechanisms deserve further scrutiny.

Given the different conditions between the local, distant ( $z = 1 - 3$ ) and early Universe ( $z > 3$ ), an important question is how does this evolve with cosmic time? To-date the AGN/star-formation constraints at  $z > 3$  are relatively poor (particularly at  $z > 4$ ) as they mainly focus on either target observations or optically selected samples which are strongly affected by obscuration biases. Our high-redshift AGN sample presented in Chapter 2 is the best constrained  $z > 3$  X-ray selected AGN sample to-date to provide the first detailed knowledge of the role AGN/star-formation connection when the Universe was  $< 1.2$  Gyr old. It includes 209  $z > 3$ , 0.5-2 keV selected AGN (122 C-COSMOS & 87 ChaMP), 4 times larger than the previous X-ray selected samples at  $z > 3$  (e.g. Brusa et al., 2009; Vito et al., 2013). Most importantly, this is the first time that a significant sample of 29 X-ray AGNs at  $z > 4$  has been assembled ( $< 9$  sources in previous works). The sample covers  $\sim 3$  orders of  $L_{2-10 \text{ keV}}$  and includes a significant number of both unobscured ( $N = 118$ ;  $N_{\text{H}} < 10^{22} \text{ cm}^{-2}$ ) and obscured ( $N = 77$ ) AGN up to  $\sim 1.5 \times 10^{24} \text{ cm}^{-2}$ . In this context, the large body of our sample allows to study the submillimetre emission in a sizable sample of X-ray AGN and associate it with the AGN obscuration.

The aim is to extend this work with follow-up submillimetre observations with SCUBA-2 (and/or ALMA) of this complete X-ray selected AGN sample and push the constraints at high- $z$  providing the first detailed knowledge of the role of AGN in the first galaxies. All the data necessary to perform this study from X-ray to radio, except from the requested SCUBA-2 submillimetre data for ChaMP, are already available. The submillimetre observations are crucial for the success of this project since no information about the cold dust properties of the ChaMP sample (e.g. *Herschel* data) are available. COSMOS SCUBA-2 submillimetre data are already available. *Chandra* X-ray observations and optical spectroscopy along with SDSS ugriz, WISE, UKIDSS, *Spitzer*, *Herschel* (only for COSMOS) photometry are also available. Radio data will also be used to define the origin of the submillimetre emission.

The submillimetre observations of the high-redshift X-ray AGN sample will be used in

conjunction with the available data to address the following issues:

**The AGN/star-formation connection:** The most efficient way for the identification of a connection between the star-formation and accretion rate is to isolate the characteristic emission bands of both processes, namely the hard X-ray emission from AGN and the submm emission from cold dust. Previous studies have shown hints of a correlation, which is more prominent in AGNs with higher luminosities and redshifts (e.g. [Lutz et al., 2010](#); [Rosario et al., 2012](#)). QSO-mode models predict that there is a residual level ( $\sim 20$  per cent) of star-formation while the AGN is at its peak. Recently, the lack of detections at FIR wavelengths of the brightest X-ray AGN was reported, interpreting the suppression of star-formation in their hosts ([Page et al., 2012](#)). While consistent with the QSO feedback, the nature of the suppression of the obscured star-formation is still very open, especially at high- $z$ . ChaMP is able to find these rare QSOs with ongoing star-formation while, using the total sample I will compare the submillimetre emission in the moderate- and high- $L_X$ . Although submillimetre detections would be direct evidence of triggered star-formation in these powerful systems, the absence of enhanced star-formation events will also provide useful information suggesting a possible suppression of star-formation or a time-lag between the peak of the star-formation and the black hole accretion.

**The AGN/star-formation evolution:** Many studies have tried to establish the fiduciary properties of cold dust emission from optical quasars over a wide range in redshift (e.g.  $z < 1$ : [Isaak et al., 2002](#);  $z = 2$ : [Priddey et al., 2003b](#);  $z > 4$ : [Priddey et al., 2003c](#)). Although they suggest that a significant fraction of optically-bright quasars are also FIR bright, they found no significant difference between the  $z = 2$  and  $z > 4$ . However, we expect that optical selection might suffer from obscuration biases and also misses the moderate- $L_X$  AGN. [Mullaney et al. \(2012a\)](#) confirmed that the SFR of AGN hosts increases by a factor of  $\sim 43$  from  $z < 0.1$  to  $z = 2 - 3$  for AGN with the same range of  $L_X$  (see also [Rosario et al., 2012](#)). The wide range in  $L_X$  makes our sample ideal for comparison with AGN at different redshifts, since it can be matched with nearly any lower- $z$  sample.

**AGN obscuration:** It is still a matter of debate whether AGN obscuration can be explained solely by the orientation-based unification model or if it is also enhanced due to dust on larger scales throughout the host galaxy. The results presented in Chapter 5 along with several studies at moderate redshifts support a scenario departing from the unification model (e.g. [Stevens et al., 2005](#); [Chen et al., 2015](#)) suggesting that obscured AGN appear to show high submillimetre fluxes (e.g. [Coppin et al., 2008](#)). Submillimetre observations will provide the component of SEDs at longer wavelength, the only way to test whether objects with absorbed X-ray spectra show a submillimetre excess.

**Clustering in  $z > 3$  AGN fields:** SCUBA-2 is the only submillimetre bolometer, which provides a large enough field of view (CV DAISY mode) around the target source to study the submillimetre galaxy (SMGs) density in the environments of high- $z$  AGN. Several groups have searched for proto-clusters forming around high- $z$  radio galaxies (e.g. [Stevens et al.,](#)

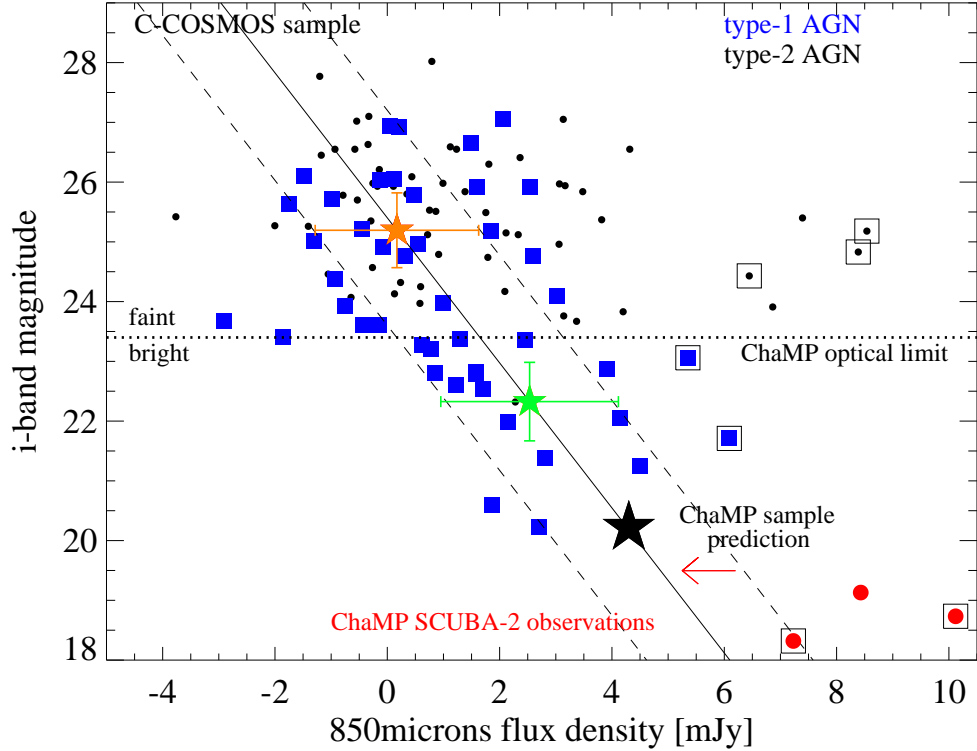


FIGURE 6.1:  $i$ -band magnitude vs.  $850\mu\text{m}$  flux density for C-COSMOS sample. The dotted line represents the optical limit of ChaMP sample ( $i_{AB} = 23.4$ ), the solid line the C-COSMOS results extrapolation and the dashed lines the  $1\sigma$  errors. Black symbols: type-2 AGN, blue squares: type-1 AGN, black squares:  $850\mu\text{m}$  detected AGN at the  $> 3$ -sigma level, orange star: mean estimation for the faint sample with  $1\sigma$  associated errors, green star: mean estimation for the bright sample with  $1\sigma$  associated errors, red circles: ChaMP targets observed by SCUBA-2.

2003; Venemans et al., 2007) and QSOs (e.g. Stevens et al., 2004, 2010; Priddey et al., 2008). Most of these studies have concentrated on extreme objects, those with the highest luminosities and redshift, and all have found overdensities of star-forming galaxies in the fields of the AGN. Using SCUBA-2 observations, I will extend these works at even higher- $z$  to investigate the environments of moderate- and high- $L_X$ , obscured and unobscured X-ray AGN. Following Stevens et al. (2010), I will compare the results for the AGN fields to these from submm blank-field surveys (e.g. Coppin et al., 2006).

### 6.1.1 Predictions and first results

In order to propose for submillimetre observations of the ChaMP sample, I have used the available SCUBA-2 observations in the COSMOS field from SCUBA2 Cosmology Legacy Survey (S2CLS; Geach, private communication). As I have presented in Chapter 2 (see Fig. 2.4), C-COSMOS sample is fainter than ChaMP by a factor of 2. Measuring the  $850\mu\text{m}$  flux densities directly from the SCUBA-2 PSF-convolved image, I get a statistical detection of the whole sample at the  $>5$ -sigma level, with an average flux of  $0.90 \pm 0.012$  mJy. For

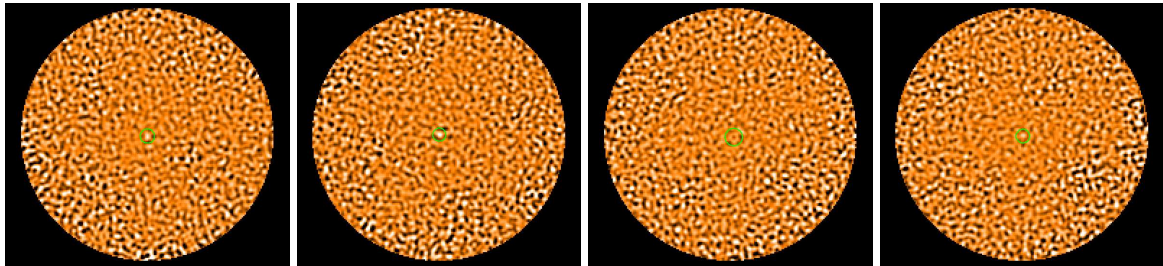


FIGURE 6.2: 850  $\mu\text{m}$  image for the four targets observed by SCUBA-2 during Semester 15A as part of our m15ai106 proposal for the summer bright targets of ChaMP  $z > 3$  sample. From left to right: SDSS 130147-000644, SDSS 131252+422818, SDSS 152046+525923, SDSS 171304+612249 QSOs with 18.32, 17.73, 19.50 and 19.13  $i$ -band magnitude, respectively. Their X-ray positions are marked by open green circles. The measured flux densities are  $7.23 \pm 2.35$ ,  $10.12 \pm 2.82$ ,  $3\sigma < 6.2$  and  $8.43 \pm 3.87$  mJy, respectively.

comparison reasons, I split C-COSMOS into optically bright and faint sources using as a limit the fainter  $i$ -band magnitude in ChaMP sample ( $i_{AB} = 23.4$ ). As the ChaMP sample is dominated by type-1 AGN (85/87), I use the type-1 AGN sources in C-COSMOS (blue squares; Figure 6.1) to estimate the mean 850  $\mu\text{m}$  fluxes. Comparing the  $i$ -band magnitude to the 850  $\mu\text{m}$  flux densities for C-COSMOS type-1 AGN, I find a strong correlation. Extrapolating these results to the total ChaMP sample (Fig. 6.1; solid line), I expect an average flux of 4.5 mJy at the  $>5$ -sigma level (Figure 6.1; large black star). In comparison, [Isaak et al. \(2002\)](#) for a similar sample of 38 SDSS QSOs <sup>1</sup> ( $z > 4$ ) found an average flux of  $5.0 \pm 1.0$  mJy including 8 sources detected at the  $> 3\sigma$  level ( $S_{850} > 10$  mJy).

The first SCUBA-2 observations from the successful SCUBA-2 proposal (ID:m15ai106, PI:Kalfountzou) for the bright summer sources during Semester 15A are presented in Fig. 6.2 and are in perfect agreement with our predictions. Their estimated fluxes are found within the range of our prediction (see Fig. 6.1) with three of them having  $S_{850} > 7$  mJy while for the fourth we can only estimate an upper limit. Observations of the total sample will help us to reveal whether AGN activity is correlated to the submillimetre emission.

## 6.2 The evolution from binary QSOs to QSOs

My results, especial in Chapter 4, suggest that QSOs are associated with powerful star-forming events. Simulations which include AGN feedback and postulate that AGN form during galaxy mergers (e.g. [Hopkins et al., 2007](#)) have received much attention because of their success in reproducing a range of observed properties of both AGN and galaxies. In this scenario, galaxy interactions trigger the AGN and also produce nuclear starbursts that both feed and obscure the central engine for much of its active lifetime. AGN-driven outflows eventually develop, which at later stages become strong enough to rapidly quench the star-formation, allowing the AGN to shine unobscured for a short period ( $\sim 10^8$  yr), leaving

<sup>1</sup>The ChaMP sample includes 44 SDSS QSOs associated with the optically brighter sources.

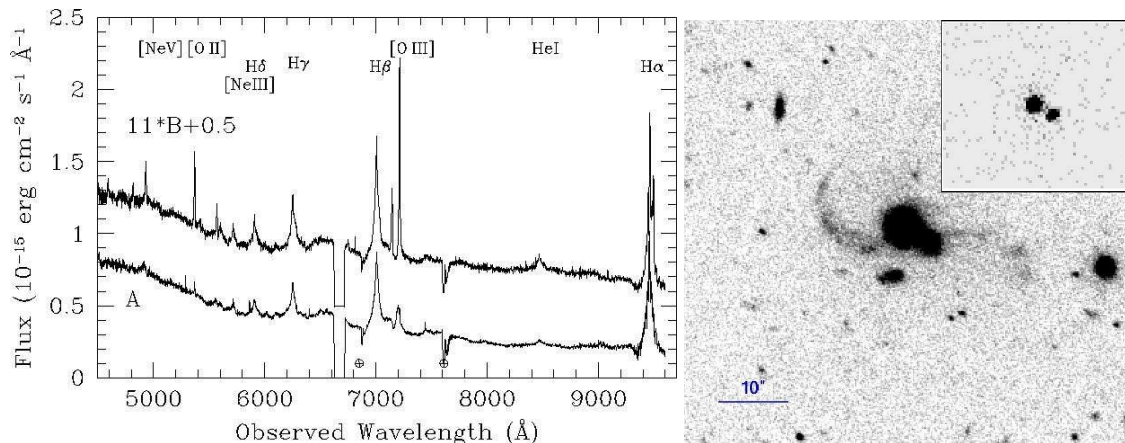


FIGURE 6.3: Optical images and spectra and X-ray images of the two components of SDSSJ1254+0846. Redshift, continuum and broad-line shapes are remarkably similar. X-rays reveal the two bright QSO nuclei while the optical images clearly shows the tidal arms of a host galaxy merger. Figures from [Green et al. \(2010\)](#).

behind a red, passive remnant.

A clear prediction of these facts suggests not only that binary SMBHs should be commonplace, but also that merging galaxies with binary quasars should be common. However, examples of binary quasars are rather isolated in the literature. Most major mergers may have occurred at high- $z$  (e.g. [Silverman et al., 2005](#)). Active mergers may be heavily obscured and as a result detectable only as ULIRGs [Cui et al. \(2001\)](#) or, the lifetime of the interacting phase may be extremely short [Mortlock et al. \(1999\)](#). A handful of new close (sub-kpc) binary AGN have been found recently (e.g. [Liu & Shapiro, 2010](#)), however these intriguing lower-luminosity objects are not homogeneously selected. It takes sensitive, wide-area searches to find binary quasars. In the wake of wide, deep SDSS photometry, the number of known binary quasars has mushroomed, thanks to the statistical surveys of [Hennawi et al. \(2006\)](#) and [Myers et al. \(2008\)](#). In particular, the latter survey targets quasars separated by  $<40\text{kpc}$  over  $0.4 < z < 2.5$ , from which the first, luminous, spatially resolved binary QSO in a disturbed host galaxy merger showing obvious tidal tails was observed ([Green et al., 2010](#); Fig. 6.3).

A major problem is explaining the observed excess of binary quasars with separations  $<200\text{ kpc}$ . It has been proposed that this excess is evidence for nuclear triggering in galaxies during dissipative mergers (e.g. [Myers et al., 2007](#)). According to [Hopkins et al. \(2007\)](#), the excess measured clustering ([Myers et al., 2007, 2008](#)), represents compelling evidence for the merger-driven origin of QSOs. However, they also suggested that attaching all QSOs to moderately rich dark matter environments in which mergers are likely to occur is sufficient to explain the observed excess of quasars with small ( $<200\text{ kpc}$ ) separations. That is, they just happen to be neighbors where the observed  $\Delta z$  could represent  $\sim\text{Mpc}$  separations rather than dynamical velocities and their properties should be statistically indistinguishable from those of single QSOs. As a result, the discovery of binary QSOs whose hosts are clearly

interacting with evidence of enhanced star-formation, presents rare opportunities to study the merging/triggering mechanisms. Submillimetre photometry can help us test these ideas by revealing the presence of triggered ongoing star-formation. The aim is to obtain submillimetre observations of a complete sample of spectroscopically confirmed binary QSOS from SDSS and compare its submillimetre properties to the nearly ideal comparison sample of single QSOS observed by HerMES (Hatziminaoglou et al., 2010).

The suggested sample is drawn from the complete sample of binary quasars discussed in Myers et al. (2008) and Green et al. (2011), restricted to velocity differences  $-500 < \Delta V < 500 \text{ km s}^{-1}$  and proper separations  $R_P < 200 \text{ kpc}$ , resulting in a total of 28 pairs. The separation criterion selects hosts likely to be interacting on their first or second pass while the velocity criterion removes most chance projections but still allows for hosts in a variety of environments from isolated pairs to massive clusters. Binary quasars were selected as having  $g < 20.85$  and either the UVX and/or low-redshift quasar Bayesian classification of Richards et al. (2009). These cuts ensure a high efficiency of quasar pairs in the targets and a reasonably homogeneous sample from  $0.4 < z < 2.4$ . Pairs of quasar candidates were then followed up spectroscopically and with X-rays confirming their binary QSO nature. The parent sample thus reflects typical SDSS optical QSO selection and as a result is therefore directly comparable to the sample of 156 SDSS spectroscopically identified Type-1 AGN Hatziminaoglou et al. (2010), observed by *Herschel* as part of the shallow HerMES-Lockman Science Demonstration Phase field. For all 28 pairs in our sample we have available deep  $u, g, r, i, z$  photometry and spectroscopy, archival SDDS and 2MASS photometry plus X-rays either from ChaMP or *Chandra* archival. With this project I will try to address the following issues:

**Test the merger hypothesis:** Submillimetre detections will provide the first direct evidence for the presence of cool dust in these systems, a tracer of ongoing star-formation. Star-formation rates can be estimated by combining broad-band SEDs and available spectroscopy using the methods described in Buat et al. (2010) and Rowan-Robinson et al. (2010). These rates will then be compared with the rates estimated in the Hatziminaoglou et al. (2010) sample of single QSOS. A substantial difference in the SFR among our targets and single quasars would be direct evidence of triggered star-formation. The absence of enhanced star-formation events will suggest that the link between AGN and galaxy formation is more complex than current merger models assume and might be evidence for a time-lag between the peak of the star-formation and the black hole accretion. In addition, the SFR and mass of the cool dust present in these systems will provide a better constraint on the properties of the host galaxies used for the merger simulations we present in Fig. 6.4, enabling us to check whether these systems are consistent with a merger-triggered scenario for QSO formation.

**The starburst-AGN connection:** It has been suggested that obscuration in AGN may often not be from star forming regions in the host galaxy (e.g. Fabian et al., 1998). Indeed, many observations point to a starburst-AGN connection, which can be most easily understood if

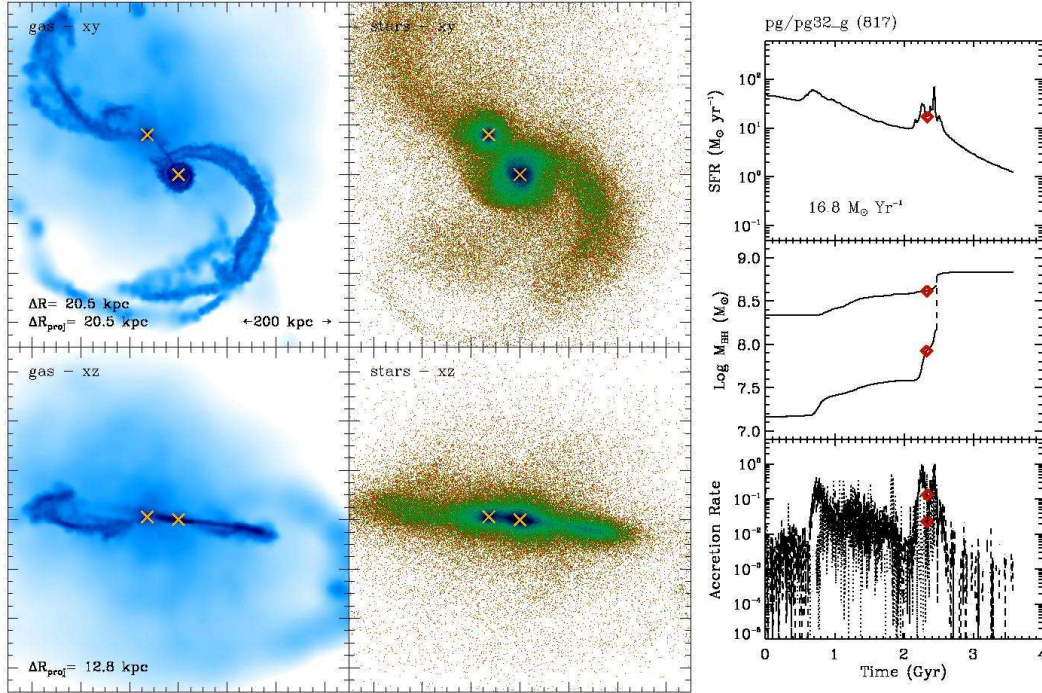


FIGURE 6.4: Numerical simulation of a merger like SDSSJ1254+0846, a pair typical of the sources in our sample (Green et al., 2010). Left, middle and right panels show the gas distribution, the stars in the xy and xz planes and the model star-formation rates, nuclear black hole masses and accretion rates for the two components respectively. Red diamonds mark the nuclear separation, position and extent of tidal features, black hole masses and accretion rates at 2.3 Gyr, similar to those of SDSSJ1254+0846.

both forms of activity have a common origin, such as in a merger. A major problem in assessing the level of star-formation in AGN is the difficulty in decomposing the star-forming from the AGN emission, especially in the case of dust enshrouded systems. Combining X-ray data with longer submillimetre wavelengths can provide a handle on this issue. The X-rays provide the most efficient way of identifying active BHs, least biased by obscuration, while the submillimetre band is considered a clean star-formation diagnostic. Galaxies undergoing a burst of star formation should show an excess in the long wavelength data, from which the star formation rate can be estimated (e.g. Rowan-Robinson et al., 2010). I can examine the starburst-AGN connection by seeing if the SFRs in the binary sources are typically enhanced with respect to single QSOs. I can also perform a qualitative test of the starburst obscuration hypothesis comparing the SFR with obscuration measures from the X-ray, or from optical SED/NIR SED fitting.

**Spectral Energy Distributions:** From the X-ray to submillimetre broad-band SEDs and  $L_{\text{Bol}}$ , I will be able to calculate the probability that the merger scenario is viable, i.e., that these quasars show evidence for triggered, high  $L/L_{\text{Edd}}$  accretion. I will also correlate the SEDs and  $L_{\text{Bol}}$  with binary characteristics like  $R_P$  and  $\Delta V$  and test whether smaller separations and/or lower velocities result in luminous, high column systems. The broad emission lines from the spectra, can help us estimate  $M_{\text{BH}}$  (e.g. Vestergaard & Peterson, 2006). From

the SEDs and  $M_{\text{BH}}$ , I can measure the Eddington ratio (Warner et al., 2004), to constrain whether these quasars are in especially high mass accretion phases (analog to spectroscopic binary stars; White et al., 1983).

### 6.3 What is the role of radio-jets in the hosts of X-ray AGN?

I will pursue and expand my results on optically selected QSOs presented in Chapters 3 and 4 studying the effects of radio feedback on the host galaxies of RLAGN in order to address key science questions about:

1. the impact of radio-jets to the AGN/star-formation connection,
2. the star-formation in the host galaxies of radio-loud/quiet AGN,
3. the dependence on obscuration and
4. the dependence on the quasar feedback and/or AGN activity.

Existing observations with *Chandra* and *Herschel* in conjunction with a large program of radio (e.g., JVLA) observations will significantly further our understanding of these issues. Combining the *Chandra* and *Herschel* Multitiered Extragalactic Survey (HerMES) surveys I will have obtained the largest ever X-ray/far-IR AGN database ( $\sim 10\,500$ ). I will take advantage of the large number of sources to identify rare populations like RLAGN ( $\sim 5 - 10$  per cent; e.g., Hao et al., 2014). The current X-ray/far-IR database will be extended including the ‘COSMOS Legacy’ survey (PI: Civano), which is expected to increase the number of RLAGN by  $\sim 25$  per cent. Dedicated follow-up observations will be part of my research in order to study the morphology of the host galaxies and the effects of radio feedback to the host galaxy’s gas.

In the results presented in this thesis, I have demonstrated that radio-jets enhance star-formation in optically (broad emission lines) selected QSOs. However, optically selected RLQs cover only a fraction of the RLAGN population excluding low luminosity and obscured AGN. The next step in understanding the process and the sequence in which radio-jets affect star-formation requires extension of the optically selected samples to X-ray selected AGN. Large X-ray surveys are appropriate since they include both the rare high-luminosity quasars and the more typical-low luminosity AGN.

X-rays can pierce through large amounts of dust and gas ( $N_{\text{H}} < 10^{24} \text{ cm}^{-2}$ ). Also, normal star-formation processes rarely exceed  $L_{\text{X}} > 10^{44} \text{ erg s}^{-1}$  (e.g. Brandt & Hasinger, 2005), whereas AGN luminosities extend to  $\sim 10^{46} \text{ erg s}^{-1}$ , making X-ray selection an efficient high contrast way for locating both obscured and unobscured AGN at all redshifts. *Chandra* can give a fundamental contribution to this topic identifying thousands of AGN, locating efficiently both obscured and unobscured sources. On the other hand, FIR observations are

uniquely sensitive to star-formation. Combining X-ray with FIR wavelengths provide a handle on the issue of star-formation properties of AGN hosts. Although some progress has been made by exploiting the submillimetre from the ground (e.g. Page et al., 2001) and the long wavelength channels of *Spitzer*/MIPS (e.g. Kalfountzou et al., 2011), it is *Herschel* and its capability to make large sensitive surveys in the FIR, which offers a clean diagnostic even in the most powerful AGN (e.g. Hatziminaoglou et al., 2010).

*Chandra*/HerMES fields are covered by wide-angle (e.g., NVSS, FIRST) and deep radio surveys (e.g., JVLA COSMOS) which will be used to identify the RLAGN (Fig. 6.5 top). Observations at higher frequencies (e.g., SMA, JCMT, IRAM) will give a full picture of the radio spectra and the synchrotron contamination to the FIR bands.

With this project I will address the key questions by using *Chandra* along with FIR data from HerMES and radio data to construct the largest library of X-ray RLAGN and a comparison RQAGN sample both covering  $\sim 3$  dex in  $L_X$ . Fig. 6.5 (bottom) shows how the  $L_X - z$  distribution for the *Chandra*/Hermes fields spans the plane relatively uniformly up to  $z \sim 3$  and  $L_X \sim 10^{45}$  erg s $^{-1}$ . The total catalogue contains  $\sim 10500$  AGN (Gilli et al., 2007 model) with  $> 3000$  FIR detected AGN at  $> 3\sigma$ . Deep radio observations increase the fraction of radio detected AGN with  $> 500$  RLAGN expected to be found.

**The SFR in RLAGN:** I will estimate the RLAGN fraction associated with FIR detected AGN and compare their SFR to the RQAGN. Stacking of X-ray sources at FIR wavelengths will also be carried out to estimate their mean SFR and explore, with the largest sample possible, the role of jets. For each population, the SFR will be compared with various AGN parameters obtained by X-ray observations and optical data. This sample will provide the statistics over a wide range of AGN and radio luminosities in order to address the key question of the radio-jets impact to the AGN/star-formation connection and whether star-formation is different in the RLAGN and RQAGN hosts.

**Decoupling the evolution effect:** Although the *Chandra*/HerMES fields provide the largest X-ray/FIR sample, this selection is limited by the strong  $L_X - z$  correlation. I will use the advantage of the large sample and the approach described in Chapter 4 to decouple luminosity effects from evolutionary effects and investigate the radio feedback in low/high luminosity AGN. I will generate a homogeneous sample of AGN covering a large range in  $L_X$  at a single epoch (shaded boxes in Fig. 6.5 bottom). A key aspect of this study is the construction of matched RLAGN and RQAGN in order to compare the effects of the presence or not of radio-jets. The size of the *Chandra*/HerMES catalog allows me to compile a sample of RLAGN (40-60 sources/bin) selected in the same way as the RQAGN, i.e. optical colors, stellar masses.

The selected epochs are associated with the peak of AGN and star-formation density ( $1 < z < 3$ ; e.g., Hasinger et al., 2005) and the ‘feedback’ energetic output of radio-AGN ( $z \sim 0.5$ ; e.g., Best et al., 2005). With this sample I will associate AGN luminosity and

each cosmic epoch with the radio-jet impact to the host galaxies and test my previous results where positive radio-jet feedback is only found in RLQs with low optical luminosity (Kalfountzou et al., 2012, 2014b). The redshift  $0.9 < z < 1.1$  sample is expected to play the most important role for this research and the follow-up observations (see Chapter 4). Specifically, this allows us to probe over three decades of X-ray luminosity. Importantly, this redshift is the minimum at which we have a large enough sample of high luminosity quasars with which to compare to the bright quasars found at higher redshifts. Moreover, I ensure that the AGN within this sample have the optimum redshifts for follow-up CO surveys with ALMA and IRAM. The  $0.4 < z < 0.6$  sample will be used for HST observations.

Almost >90 per cent of the *Chandra*/HerMES AGN are identified using spectroscopic or photometric redshift. Despite the high optical/IR completeness level, a detailed study requires secure redshift estimations for sources covering the whole  $L_X$  range over each redshift bin. For this purpose, dedicated spectroscopic follow-up observations will be proposed at the selected redshifts. In addition, IFU observations (e.g. GEMINI, VIMOS, SINFONI) will provide a key insight into the coupling between the jet and the gas.

I will particularly focus on ALMA follow-up observations, in order to understand how radio feedback affects the molecular gas properties and how this mechanism regulates cooling and in turn governs star formation and the power output of the AGN. ALMA high-resolution imaging of CO will allow us to probe the dynamics of the cool gas and will significantly further our understanding the effects of jets to the AGN/star-formation connection. HST archival and new observations will be used to study the host galaxy morphology of selected RLAGN at  $z \sim 0.5$  as a function of SFR and  $L_X$ . In this way, I will test if and how the radio activity is associated with the galaxy morphology of RLAGN.

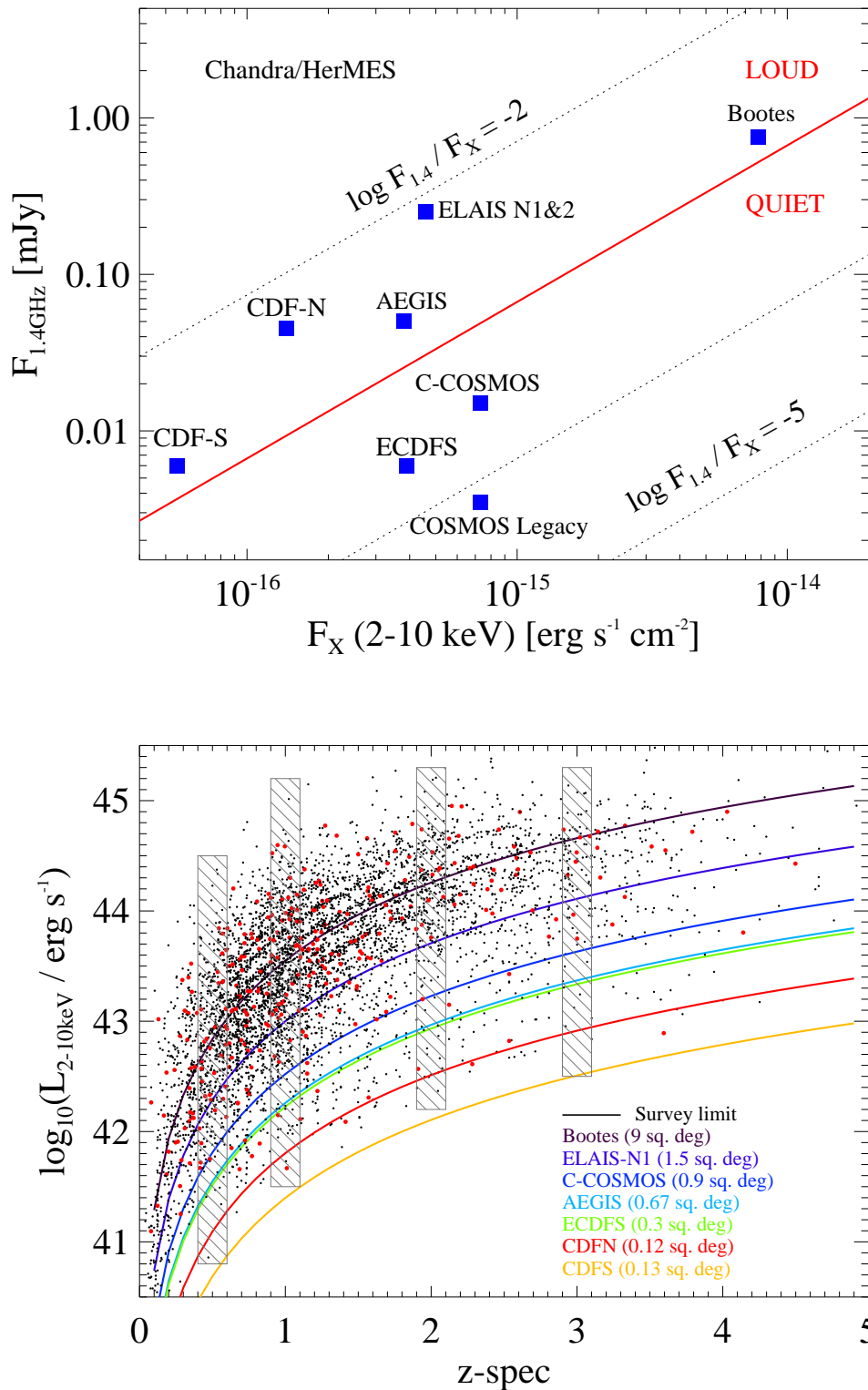


FIGURE 6.5: Top: Lower ( $5\sigma$ ) radio flux 1.4 GHz limits vs. X-ray 2-10 keV flux limits for each *Chandra/HerMES* field. Dashed lines show the loci with radio-loudness ratios as shown by the labels. Bottom: X-ray luminosity vs. redshift for the AGN spectroscopic sample. RLAGN are represented by red color.

# A

## Appendix

### Appendix A

QSO candidates at redshift  $\simeq 3.0 - 3.5$  satisfied the following cuts:

$$\begin{aligned} \sigma_r &< 0.13 && \text{AND} \\ u &> 20.6 && \text{AND} \\ u - g &> 1.5 && \text{AND} \\ g - r &< 1.2 && \text{AND} \\ r - i &< 0.3 && \text{AND} \\ i - z &> N && \text{AND} \\ g - r &< 0.44(u - g) - 0.76. \end{aligned} \tag{A.1}$$

For the redshift range  $\simeq 3.5 - 4.5$  this selection becomes

$$\begin{aligned} \text{A)} \quad \sigma_r &< 0.2 \\ \text{B)} \quad u - g &> 1.5 \quad \text{OR} \quad u > 20.6 \\ \text{C)} \quad g - r &> 0.7 \\ \text{D)} \quad g - r &> 2.8 \quad \text{OR} \quad r - i < 0.44(g - r) - 0.558 \\ \text{E)} \quad i - z &< 0.25 \quad \text{AND} \quad i - z > -1.0, \end{aligned} \tag{A.2}$$

---

in the combination A AND B AND C AND D AND E. For the redshifts above  $\simeq 4.5$  we use

$$\begin{aligned} u &> 21.5 && \text{AND} \\ g &> 21.0 && \text{AND} \\ r - i &> 0.6 && \text{AND} \\ i - z &> N && \text{AND} \\ i - z &< 0.52(r - i) - 0.762. && \end{aligned} \tag{A.3}$$

TABLE A.1: Properties of the  $z > 3$  AGN sample (Chapter 2).

Survey <sup>1</sup>	R.A. (deg)	Dec. (deg)	$z_{\text{spec}}$	$z_{\text{phot}}$	$z_{\text{phot}}$ <sup>2</sup> lower	$z_{\text{phot}}$ <sup>3</sup> upper	Optical Type <sup>8</sup>	X-ray Type <sup>9</sup>	$S_{\text{soft}}$ <sup>4</sup>	$\log L_X$ <sup>5</sup>	HR <sup>6</sup>	HR low <sup>10</sup>	HR up <sup>11</sup>	$N_{\text{H}}$ <sup>7</sup>
1	1.682	-0.200	3.109	...	...	...	1	1	0.071	44.65	-0.50	-0.77	-0.12	0.1
1	5.826	-1.048	...	4.5	4.3	4.7	1	1	0.094	45.13	...	...	-0.38	< 1.0
1	18.192	-1.2188	3.592	3.545	3.35	4.37	1	1	0.090	44.90	-0.84	-0.98	-0.57	< 0.1
1	29.814	0.4529	...	3.675	3.51	4.05	1	1	0.039	44.56	-0.92	...	-0.84	< 0.1
1	29.886	0.482	...	4.6	4.3	4.9	2	1	0.037	44.75	-0.70	...	-0.53	< 0.1
1	32.680	-0.3051	4.733	4.565	4.05	4.98	1	1	0.277	45.65	-0.67	-0.85	-0.56	< 0.1
1	38.906	-0.722	...	4.15	3.72	4.58	2	1	0.203	45.39	-0.58	-0.76	-0.41	< 0.1
1	116.862	27.6253	3.152	2.905	2.58	3.25	1	1	0.072	44.67	-0.42	-0.70	-0.09	0.1
1	119.194	41.1201	3.734	3.135	2.88	4.29	1	1	0.130	45.09	-0.41	-0.66	-0.14	0.1
1	119.218	45.044	3.185	...	...	...	1	1	0.105	44.85	-0.85	-0.98	-0.62	< 0.1
1	120.287	36.1514	...	3.675	3.59	4.06	1	1	0.156	45.16	-0.64	-0.69	-0.56	< 0.1
1	125.411	12.2922	3.112	...	...	...	1	1	0.053	44.53	-0.64	-0.76	-0.47	< 0.1
1	125.412	12.2917	3.114	2.995	2.78	3.23	1	1	0.443	45.45	-0.48	-0.51	-0.42	< 0.1
1	127.837	19.151	...	4.6	4.2	5.0	2	1	0.065	44.99	-0.57	-0.73	-0.42	< 0.1
1	130.260	13.2202	...	2.945	2.76	3.29	1	1	0.078	44.66	-0.54	-0.66	-0.44	< 0.1
1	132.169	44.959	3.093	...	...	...	1	1	0.030	44.28	-0.31	-0.41	-0.22	4.0

<sup>1</sup>1=ChaMP; 2=C-COSMOS

<sup>2</sup>Photometric redshift lower limit

<sup>3</sup>Photometric redshift upper limit

<sup>4</sup>The 0.5-2 keV flux in units of  $10^{-13} \text{erg cm}^{-2} \text{s}^{-1}$  converted to  $\Gamma = 1.8$ . For sources undetected in soft band a negative symbol is given and the flux estimated by the hard or full band detection.

<sup>5</sup>The 2-10 keV luminosity in units of  $\text{erg s}^{-1}$ .

<sup>6</sup>Hardness ratio defined as  $\text{HR} = (\text{H} + \text{S})/(\text{H} - \text{S})$ , S: 0.5-2.0 keV count rate and H: 2.0-10 keV count rate.

<sup>7</sup>The absorption column density in units of  $10^{22} \text{cm}^{-2}$

<sup>8</sup>1: optical type-1 AGNs, and 2: optical type-2 AGNs

<sup>9</sup>1: unobscured AGNs, and 2: obscured AGNs; based on  $N_{\text{H}} = 10^{22} \text{cm}^{-2}$  limit.

<sup>10</sup>Hardness ratio lower limit

<sup>11</sup>Hardness ratio upper limit

1	133.446	57.987	....	4.1	3.4	4.8	2	1	0.043	44.70	-0.36	-0.55	-0.19	4.0
1	134.413	9.0255	3.130	3.065	2.76	3.39	1	1	0.076	44.69	-0.57	-0.89	-0.05	0.1
1	137.686	17.7420	4.098	4.105	3.35	4.47	1	1	0.044	44.71	-0.50	-0.67	-0.35	0.1
1	137.786	54.298	3.234	...	...	...	2	1	0.036	44.40	-0.44	-0.55	-0.35	0.1
1	138.042	5.7952	3.246	3.345	3.09	3.63	1	1	0.065	44.64	-0.50	-0.70	-0.29	0.1
1	139.086	29.522	3.098	...	...	...	1	1	0.054	44.53	-0.40	-0.57	-0.19	0.1
1	141.052	31.2774	...	2.795	2.21	3.03	1	1	0.367	45.34	-0.65	-0.79	-0.48	< 0.1
1	143.364	55.4032	...	3.045	2.78	3.33	1	1	0.086	44.72	-0.31	-0.43	-0.20	4.0
1	149.425	33.251	3.001	...	...	...	1	1	0.128	44.87	-0.77	-0.93	-0.49	< 0.1
1	149.594	7.7968	3.220	3.145	2.8	3.47	1	1	0.086	44.77	...	...	-0.88	< 0.1
1	150.700	32.7668	...	3.405	3.11	4.37	1	1	0.085	44.82	-0.45	-0.61	-0.34	0.1
1	155.452	13.1647	3.055	2.905	2.55	3.26	1	1	0.075	44.66	-0.47	-0.67	-0.21	0.1
1	156.595	47.3187	4.941	4.895	4.77	5.1	1	1	0.102	45.25	-0.44	-0.90	-0.24	0.1
1	162.590	58.625	...	3.65	3.47	3.83	2	1	0.077	44.84	-0.56	-0.82	-0.22	0.1
1	162.938	57.468	3.409	...	...	...	1	1	0.051	44.60	-0.99	N	-0.73	< 0.1
1	163.275	57.5735	...	2.755	2.52	3.1	1	1	0.045	44.44	-0.75	-0.87	-0.59	< 0.1
1	168.550	40.5661	3.597	3.495	3.09	4.35	1	1	0.053	44.67	-0.44	-0.6	-0.32	0.1
1	168.733	40.6372	4.913	1.305	0.9	1.52	2	1	0.253	45.64	-0.69	-0.73	-0.64	< 0.1
1	169.480	48.0722	...	2.905	2.54	3.23	1	1	0.101	44.84	-0.68	-0.77	-0.57	< 0.1
1	169.607	7.7262	...	3.75	3.45	4.05	1	2	0.035	44.53	-0.24	-0.41	-0.09	13.0
1	170.087	43.4292	3.552	3.665	2.92	4.12	1	1	0.073	44.79	-0.46	-0.61	-0.32	0.1
1	170.541	24.2938	3.336	3.045	2.73	3.39	1	1	0.054	44.61	-0.51	-0.66	-0.38	0.1
1	171.748	56.772	...	3.6	3.5	3.7	1	1	0.033	44.46	-0.77	-0.96	-0.53	< 0.1
1	175.151	66.221	3.337	...	...	...	1	1	0.065	44.68	-0.67	-0.74	-0.61	< 0.1
1	178.881	-1.770	3.202	3.495	3.16	4.21	1	1	0.055	44.57	-0.35	-0.47	-0.21	2.0
1	182.037	0.129	...	3.5	2.4	4.6	2	2	0.056	44.66	-0.17	-0.44	0.08	17.0
1	183.273	2.8584	...	3.145	2.76	3.83	1	1	0.165	45.11	-0.64	-0.71	-0.53	< 0.1
1	183.366	2.960	...	3.5	2.4	4.6	1	1	0.090	44.87	-0.46	-0.65	-0.24	0.1
1	188.125	47.6153	3.041	3.205	2.88	3.83	1	1	0.175	45.02	-0.99	-0.99	-0.76	< 0.1
1	190.459	9.6307	...	3.045	2.66	3.37	2	2	0.057	44.54	-0.18	-0.44	0.04	13.0
1	192.551	33.855	3.6	...	...	...	1	1	0.074	44.81	-0.54	-0.83	-0.35	0.1
1	192.929	0.1240	...	2.905	2.69	3.23	1	1	0.220	45.38	-0.5	-0.68	-0.27	0.1

1	195.008	1.3067	4.612	4.485	3.88	4.69	1	1	0.454	45.84	-0.37	-0.73	-0.02	4.0
1	195.445	-0.112	3.7	...	...	...	1	2	0.160	45.17	-0.16	-0.41	0.09	20.0
1	196.534	3.940	6.016	...	...	...	1	1	0.031	44.93	-0.69	-0.75	-0.61	< 0.1
1	196.652	46.4961	...	3.065	2.76	3.23	2	1	0.055	44.53	-0.26	-0.53	0.06	8.0
1	197.434	57.6389	...	2.905	2.67	3.25	1	1	0.068	44.69	...	...	-0.64	< 0.1
1	198.217	42.4716	3.181	2.945	2.75	3.3	1	1	0.072	44.81	-0.66	-0.82	-0.52	< 0.1
1	199.322	1.1538	...	3.4	3.275	3.525	1	1	0.090	44.84	-0.59	-0.94	-0.20	0.1
1	201.424	11.477	...	4.6	4.3	4.9	2	2	0.071	45.03	0.01	-0.33	0.4	50.0
1	201.828	29.1482	...	3.675	3.6	4.08	1	1	0.030	44.45	-0.97	-0.99	-0.53	< 0.1
1	202.916	11.2840	...	2.755	2.21	3.03	1	1	0.057	44.53	-0.56	-0.68	-0.40	< 0.1
1	203.593	-1.4221	3.827	3.775	3.01	4.33	1	1	0.032	44.51	-0.51	-0.90	-0.34	0.1
1	203.612	-1.4816	...	2.905	2.57	3.26	1	1	0.074	44.69	-0.66	-0.94	-0.54	< 0.1
1	206.078	-0.511	3.070	...	...	...	1	1	0.060	44.57	-0.64	-0.84	-0.51	< 0.1
1	207.739	60.1377	...	3.285	3.05	3.95	1	1	0.110	44.89	-0.68	-0.75	-0.63	< 0.11
1	208.211	33.4822	...	2.755	2.32	3.07	1	1	0.056	44.54	-0.462	-0.57	-0.30	0.1
1	212.767	52.2988	...	2.815	2.66	3.13	1	1	0.097	44.99	-0.42	-0.48	-0.36	0.1
1	214.224	44.6294	...	2.795	2.52	3.12	1	1	0.134	44.94	-0.54	-0.66	-0.43	< 0.1
1	214.424	53.0886	...	3.495	3.15	4.37	1	1	0.037	44.49	-0.75	-0.85	-0.61	< 0.1
1	214.852	53.5323	...	3.535	3.41	3.9	1	1	0.185	45.20	-0.74	-0.95	-0.47	< 0.1
1	215.150	47.2415	3.237	2.905	2.71	3.26	1	1	0.300	45.32	-0.75	-0.90	-0.58	< 0.1
1	215.771	24.0856	4.112	4.165	3.36	4.54	1	2	0.032	44.58	-0.26	-0.54	0.01	14.0
1	216.071	22.8406	...	3.675	3.58	4.06	1	1	0.734	45.83	-0.60	-0.64	-0.56	< 0.1
1	216.447	35.455	3.53	...	...	...	1	1	0.053	44.65	-0.56	-0.66	-0.41	< 0.1
1	218.114	-1.160	...	3.3	3.0	3.6	2	1	0.079	44.76	-0.41	-0.56	-0.28	0.1
1	219.502	3.6388	3.306	3.285	2.92	4.08	1	1	0.058	44.62	-0.58	-0.68	-0.48	< 0.1
1	219.633	3.641	...	3.275	3.05	3.5	1	1	0.070	44.70	-0.81	-0.89	-0.72	< 0.1
1	219.665	3.6288	3.194	3.205	2.88	3.94	1	1	0.040	44.44	-0.68	-0.77	-0.56	< 0.1
1	220.857	58.8995	...	2.905	2.68	3.22	1	1	0.030	44.32	-0.84	-0.96	-0.35	0.1
1	221.308	-0.4237	3.142	3.065	2.68	3.36	1	1	0.058	44.58	-0.24	-0.54	N	10.0
1	225.083	22.7196	3.268	3.475	3.18	4.21	1	1	0.051	44.56	-0.79	-0.97	-0.41	< 0.1
1	230.194	52.9896	3.385	3.495	3.15	4.35	1	1	0.060	44.66	-0.63	-0.83	-0.34	< 0.1
1	230.897	28.6609	...	2.715	2.44	3.02	1	1	0.062	44.56	-0.61	-0.72	-0.48	< 0.1

1	240.652	42.5518	3.889	4.125	3.27	4.46	1	1	0.045	44.72	-0.82	N	-0.71	< 0.1
1	244.028	47.2661	...	3.205	2.92	3.97	1	1	0.058	44.60	-0.58	-0.95	0.01	0.1
1	258.269	61.3793	3.150	3.005	2.76	3.33	1	1	0.126	44.91	...	...	-0.89	< 0.1
1	258.956	63.246	...	3.6	3.5	3.7	1	1	0.139	45.09	-0.61	-0.86	-0.27	< 0.1
1	260.072	26.5628	3.057	3.145	2.77	3.5	1	1	0.053	44.51	-0.85	-0.95	-0.71	< 0.1
1	340.945	-9.6855	...	4.125	3.36	4.56	1	1	0.078	44.97	-0.71	-0.88	-0.48	< 0.1
1	359.354	0.6643	...	3.285	2.98	4.19	1	1	0.039	44.45	...	...	-0.75	< 0.1
2	149.543	1.9537	...	2.951	2.91	3.01	2	2	0.024	44.28	0.49	0.32	0.79	80.0
2	149.624	1.8854	...	2.264	2.1	3.86	1	1	0.007	43.98	...	...	-0.34	< 3.0
2	149.690	2.2641	...	...	>3.0	...	...	2	0.031	45.46	0.22	-0.17	0.53	50.0
2	149.669	2.1677	3.089	3.094	2.75	3.21	2	2	0.018	44.21	-0.04	-0.18	0.10	22.0
2	149.736	2.1799	4.255	4.245	4.23	4.26	1	1	0.014	44.40	-0.41	-0.59	-0.23	0.1
2	149.742	2.5354	...	2.942	2.9	3.01	2	2	-0.015	44.30	...	0.31	...	≥55.0
2	149.761	2.4358	...	3.647	3.64	3.66	1	2	0.023	44.46	-0.16	-0.39	-0.11	22.0
2	149.771	2.3658	...	3.447	3.35	3.53	2	2	0.002	43.38	...	...	0.73	< 1000.0
2	149.782	2.4713	...	3.246	3.23	3.26	1	2	-0.014	44.334	...	-0.05	...	≥25.0
2	149.783	2.4521	5.07	1.939	1.9	1.98	2	2	0.007	44.31	...	...	0.11	< 75.0
2	149.797	2.2897	...	...	>3.0	...	...	2	-0.002	44.33	...	0.69	...	< 1000.0
2	149.803	2.1417	...	2.838	2.24	3.09	1	2	0.009	43.87	-0.37	-0.58	-0.12	1.5
2	149.804	2.1189	...	3.791	1.59	4.58	2	2	0.004	43.68	...	...	0.60	< 300.0
2	149.807	1.8105	...	2.382	2.33	3.260	1	2	0.006	43.79	-0.22	-0.65	0.20	11.0
2	149.808	2.3148	...	3.471	3.41	3.79	2	1	0.025	44.44	-0.34	-0.46	-0.23	4.0
2	149.812	2.2830	...	3.297	3.24	3.35	1	1	0.009	43.95	...	...	-0.69	0.1
2	149.814	2.7348	...	...	>3.0	...	...	2	0.021	45.29	...	...	0.51	< 85
2	149.823	2.5398	...	...	>3.0	...	...	2	-0.010	44.97	...	0.52	...	> 85
2	149.845	2.4817	...	3.375	3.36	3.39	1	1	0.007	43.87	...	...	-0.498	< 0.1
2	149.851	2.2764	3.371	3.317	3.3	3.33	1	1	0.012	44.09	-0.53	-0.70	-0.35	0.1
2	149.851	2.4269	...	3.35	3.16	3.58	2	2	0.004	43.69	0.33	0.15	0.52	68.0
2	149.858	2.4093	...	4.108	3.68	4.29	2	2	0.049	44.91	-0.27	-0.34	-0.21	11.0
2	149.860	2.3876	...	2.949	2.33	3.97	1	2	0.002	43.51	0.22	-0.13	0.57	65.0
2	149.869	2.2941	3.345	3.4	3.39	3.41	1	2	0.024	44.42	0.06	-0.02	0.15	37.0
2	149.874	2.3615	...	6.88	6.88	7.0	2	2	0.002	44.10	...	...	0.74	< 1000.0

2	149.879	2.2258	3.65	3.647	3.64	3.66	1	1	0.018	44.35	-0.41	-0.54	-0.28	0.1
2	149.882	2.5051	...	3.1	3.02	3.19	2	2	0.046	44.60	-0.22	-0.29	-0.16	10.0
2	149.886	2.2759	3.335	3.277	3.26	3.3	2	2	-0.004	43.83	...	0.29	...	> 65.0
2	149.889	1.9662	...	3.053	2.2	3.12	2	1	0.004	43.47	...	...	-0.32	< 5.0
2	149.894	2.4330	3.382	3.393	3.38	3.41	1	2	0.003	43.43	-0.19	-0.70	0.31	14.0
2	149.897	2.3244	...	2.998	2.9	3.16	2	2	0.006	43.72	...	...	0.45	< 75.0
2	149.908	2.5723	...	...	>3.0	...	...	2	0.004	43.64	...	...	0.88	< 1000.0
2	149.909	2.6199	...	2.569	2.13	4.23	1	1	0.006	44.02	...	...	-0.29	< 6.0
2	149.910	1.8996	...	3.063	2.585	3.194	2	2	0.002	43.24	...	...	0.62	< 200.0
2	149.911	1.8427	...	3.295	2.81	3.45	2	...	-0.003	43.50	...	...	...	...
2	149.913	2.2465	...	...	>3.0	...	...	2	0.010	44.02	0.46	0.23	0.52	71.0
2	149.919	2.3454	3.021	3.043	3.03	3.05	1	1	0.009	43.85	...	...	-0.69	< 0.1
2	149.924	1.8441	...	2.936	1.79	3.05	2	2	0.004	43.55	...	...	-0.21	< 13.0
2	149.931	2.3519	...	...	>3.0	...	...	2	0.004	43.62	...	0.87	...	1000.0
2	149.944	1.7404	...	2.044	2.0	3.66	1	1	0.006	43.88	...	...	-0.28	< 6.0
2	149.952	2.6514	3.08	3.083	3.07	3.09	2	2	-0.011	44.16	...	0.411	...	> 70.0
2	149.966	2.4325	...	2.893	2.23	3.3	2	2	-0.013	44.33	...	0.753	...	> 1000.0
2	149.969	2.3048	3.155	3.099	3.076	3.13	1	2	0.014	44.12	0.06	-0.07	0.19	32.0
2	149.972	1.9415	...	2.843	2.63	3.06	2	1	0.013	44.02	-0.26	-0.41	-0.12	7.0
2	149.981	2.3150	...	3.003	2.97	3.03	2	2	0.023	44.28	-0.06	-0.15	0.04	22.0
2	149.990	2.2973	3.026	2.97	2.93	3.05	2	1	0.009	43.87	...	...	-0.72	< 0.1
2	149.998	1.9745	...	2.911	2.88	3.01	2	1	0.013	44.02	...	...	-0.78	< 0.1
2	150.004	2.0389	3.515	3.5	3.49	3.51	1	1	0.018	44.31	-0.41	-0.54	-0.28	0.1
2	150.007	1.9180	...	...	>3.0	...	...	2	0.006	43.76	0.60	0.33	0.78	150.0
2	150.007	2.1489	...	2.851	2.77	3.43	1	2	0.005	43.78	0.17	-0.03	0.37	48.0
2	150.009	1.8526	...	4.032	4.02	4.05	2	1	0.008	44.11	...	...	-0.63	< 0.1
2	150.017	2.4979	...	2.914	2.5	3.26	2	1	0.009	43.95	...	...	-0.71	< 0.1
2	150.025	2.0038	...	3.124	2.67	3.17	2	2	-0.006	43.93	...	0.48	...	≥1000.0
2	150.042	1.8722	3.371	3.338	3.32	3.35	1	2	0.008	43.94	-0.32	-0.58	-0.06	5.0
2	150.046	2.3674	...	2.313	1.94	3.1	2	1	0.004	43.50	...	...	-0.39	0.1
2	150.048	2.4816	...	...	>3.0	...	...	2	0.004	43.64	...	...	0.86	1000.0
2	150.062	1.7226	...	3.033	2.91	3.41	2	2	0.008	43.84	0.06	-0.21	0.33	32.0

2	150.063	2.4219	...	3.087	3.02	3.25	2	2	-0.006	43.93	...	0.48	...	> 80.0
2	150.063	1.7774	...	3.426	1.21	3.84	2	2	-0.009	44.17	...	0.32	...	> 50.0
2	150.064	2.1910	...	2.887	1.53	3.06	1	2	0.025	44.35	0.11	0.03	0.19	35.0
2	150.067	2.0843	...	3.01	2.99	3.03	1	1	0.006	43.66	...	...	-0.57	< 0.1
2	150.086	2.139	...	5.045	4.73	5.14	1	2	0.003	43.99	0.25	0.01	0.49	100.0
2	150.091	1.9292	...	2.864	2.84	3.23	1	2	-0.007	44.04	...	0.54	...	> 90.0
2	150.096	2.0215	3.546	3.362	3.33	3.39	2	1	0.006	43.81	...	...	-0.59	< 0.1
2	150.099	2.1527	...	2.844	2.6	3.06	2	1	0.008	43.81	...	...	-0.67	< 0.1
2	150.101	2.4194	4.66	4.545	4.53	4.56	1	2	0.009	44.33	-0.27	-0.49	-0.05	14.0
2	150.107	1.7592	4.16	3.949	3.93	3.96	1	2	0.006	44.01	0.01	-0.28	0.3	43.0
2	150.133	2.4574	3.189	3.111	3.08	3.15	2	1	0.006	43.71	...	...	-0.494	< 0.1
2	150.152	2.3079	3.175	3.163	3.08	3.24	2	2	0.003	43.55	0.42	0.24	0.60	75.0
2	150.164	2.1793	...	2.82	2.75	3.15	1	2	-0.004	43.57	...	0.407	...	27.0
2	150.176	2.5697	...	3.144	3.09	3.24	2	2	0.005	43.61	...	...	0.65	< 5000.0
2	150.180	2.0760	3.01	3.015	3.0	3.03	1	1	0.011	43.94	...	...	-0.77	< 0.1
2	150.192	2.2199	3.09	3.077	3.07	3.09	1	2	0.007	43.76	-0.15	-0.39	0.1	15.0
2	150.199	1.7312	...	2.821	2.66	3.45	2	2	0.004	43.68	0.18	-0.10	0.47	50.0
2	150.205	1.7360	...	2.929	2.4	4.19	1	2	0.006	44.02	0.04	-0.22	0.30	48.0
2	150.205	2.5029	...	3.072	3.06	3.09	1	2	0.014	44.07	-0.08	-0.28	0.12	20.0
2	150.208	2.4819	3.333	3.378	3.37	3.39	1	1	0.024	44.37	-0.49	-0.62	-0.35	0.1
2	150.209	2.4385	3.715	3.563	3.55	3.57	1	1	0.010	44.09	...	...	-0.717	< 0.1
2	150.210	2.3915	3.095	3.085	3.07	3.1	1	2	0.009	43.88	-0.17	-0.35	0.02	13.0
2	150.214	2.4750	...	3.075	3.06	3.09	1	2	0.020	44.24	-0.07	-0.17	0.03	20.0
2	150.214	2.5827	5.3	5.201	5.15	5.28	2	2	0.009	44.42	...	...	0.36	< 500.0
2	150.225	1.7999	...	3.264	3.12	3.46	1	2	0.004	43.63	0.36	0.16	0.55	68.0
2	150.247	2.4422	3.029	2.992	2.97	3.02	1	2	0.023	44.31	0.10	0.02	0.18	35.0
2	150.259	2.3761	3.717	2.673	2.66	2.68	1	1	0.008	44.03	...	...	-0.68	< 0.1
2	150.260	2.1180	...	...	>3.0	...	...	...	-0.009	43.97	...	...	...	...
2	150.261	1.7316	...	3.126	3.08	3.55	2	2	-0.005	43.67	...	...	0.51	> 65.0
2	150.267	1.7009	...	3.412	3.33	3.46	1	1	0.014	44.17	...	...	-0.45	< 0.1
2	150.268	1.7891	...	...	>3.0	...	...	2	0.010	44.02	0.72	0.48	0.87	1000.0
2	150.271	1.6139	...	3.466	3.44	3.5	2	2	0.011	44.14	0.24	N	0.49	60.0

2	150.284	1.8183	...	...	>3.0	...	...	2	0.011	44.06	-0.033	-0.18	0.25	12.0
2	150.285	2.309	...	2.897	2.42	3.0	2	1	0.011	43.94	-0.38	-0.56	-0.20	1.2
2	150.288	1.6511	...	3.871	3.13	3.95	1	1	0.018	44.40	...	...	-0.48	< 0.1
2	150.297	2.1489	3.328	3.459	3.45	3.47	1	2	0.005	43.74	-0.11	-0.42	0.20	20.0
2	150.299	1.6878	...	2.976	2.67	3.14	1	1	0.008	43.83	...	...	-0.24	< 9.0
2	150.300	2.3007	3.498	3.434	3.41	3.46	2	2	0.003	43.55	...	...	0.70	< 1000.0
2	150.304	1.8242	...	2.949	2.49	3.35	1	1	0.006	43.79	...	...	-0.47	< 0.1
2	150.306	1.7616	...	3.265	3.24	3.29	2	2	0.003	43.46	...	...	0.77	< 1000.0
2	150.310	2.5045	...	...	>3.0	...	...	2	0.005	43.75	0.33	0.09	0.48	68.0
2	150.315	2.3369	...	4.216	3.85	4.44	2	2	0.002	43.47	...	...	0.76	< 1000.0
2	150.317	2.0050	...	3.428	3.38	3.49	2	2	0.007	43.86	...	...	0.03	< 30.0
2	150.318	2.2477	...	...	>3.0	...	...	2	0.008	43.88	0.06	-0.13	0.18	11.0
2	150.333	2.4415	...	2.481	2.12	3.07	2	1	0.015	44.09	-0.54	-0.76	-0.33	0.1
2	150.334	1.7882	...	2.683	2.34	3.02	1	1	0.005	43.60	...	...	-0.24	< 8.0
2	150.344	1.6361	...	3.805	3.74	3.85	2	2	0.019	44.41	...	...	-0.08	< 30.0
2	150.345	1.9579	...	3.065	2.98	3.17	2	2	0.010	43.93	0.18	-0.07	0.25	45.0
2	150.356	2.2242	...	2.701	2.51	3.09	2	2	-0.008	44.02	...	0.56	...	> 75.0
2	150.359	2.0737	4.917	1.991	1.96	2.01	2	2	0.008	44.30	...	...	0.27	< 70.0
2	150.364	2.1438	3.328	3.361	3.35	3.37	1	1	0.025	44.40	-0.26	-0.38	-0.14	8.0
2	150.379	1.8761	...	3.33	3.02	3.44	2	2	0.009	43.96	-0.18	-0.44	0.06	14.0
2	150.380	2.0995	...	4.498	4.43	4.56	2	2	-0.008	44.39	...	0.514	...	> 200.0
2	150.383	2.0748	...	3.852	3.83	3.88	2	2	0.003	43.62	0.40	0.13	0.68	90.0
2	150.398	2.2709	...	...	>3.0	...	...	2	0.005	43.72	0.46	0.24	0.61	200.0
2	150.415	1.9342	...	3.681	1.28	3.75	1	1	0.011	44.15	...	...	-0.54	< 0.1
2	150.415	2.3648	...	2.423	2.24	3.29	1	1	0.003	43.47	...	...	-0.29	< 6.0
2	150.425	2.3120	...	3.092	2.98	3.29	2	2	0.003	43.42	0.21	-0.05	0.48	48.0
2	150.455	1.9674	3.485	3.493	3.46	3.52	1	1	0.007	43.89	...	...	-0.46	< 0.1
2	150.467	2.5315	...	4.45	4.43	4.47	2	1	0.014	44.46	...	...	-0.563	< 0.1
2	150.485	2.4135	...	2.949	2.57	3.51	2	2	-0.006	44.04	...	0.14	...	> 25.0
2	150.486	2.4281	...	3.464	2.95	3.61	2	2	-0.005	43.77	...	0.07	...	32.0
2	150.546	2.2243	...	3.506	3.35	3.66	2	2	0.029	44.53	-0.08	-0.21	0.03	25.0
2	150.551	2.1400	...	3.028	2.97	3.07	2	2	-0.024	44.50	...	0.67	...	≥1000.0

---

2    150.647    2.4182    ...    3.034    2.6    3.32    1    2    -0.052    44.84    ...    0.69    ...     $\geq 1000.0$

## Appendix B

B1. Properties of the  $z \approx 1$  AGN sample (Chapter 4).

RA	DEC	type	$z$	$L_{\text{Bol}}^{12}$	$L_{\text{rad}}^{13}$	cont. <sup>14</sup>	$M_{\text{BH}}^{15}$	$L_{\text{FIR}}^{16}$
219.686	62.199	RLQ	1.094	46.20±0.01	27.168	N	9.28±0.14	45.44±0.77
127.792	37.703	RLQ	0.919	46.02±0.01	27.320	Y	8.90±0.07	45.55±0.05
247.324	44.581	RLQ	1.033	46.23±0.01	25.744	N	8.85±0.05	45.64±0.39
116.073	37.888	RLQ	1.067	46.69±0.01	27.561	N	9.57±0.06	45.40±0.07
205.555	60.362	RLQ	0.965	46.51±0.01	27.337	N	9.00±0.24	45.80±0.03
207.394	53.688	RLQ	0.979	46.67±0.01	26.936	Y	9.29±0.06	45.97±0.03
197.763	55.232	RLQ	0.924	46.43±0.01	26.186	Y	9.33±0.66	46.00±0.01
248.512	39.000	RLQ	1.085	46.46±0.01	27.013	Y	8.39±0.10	45.81±0.05
257.455	30.550	RLQ	1.043	46.00±0.01	25.522	N	8.42±0.09	45.52±0.06
241.317	31.606	RLQ	1.028	45.99±0.01	25.939	N	8.74±0.31	45.55±0.36
127.151	50.807	RLQ	0.929	46.17±0.01	25.710	Y	8.68±0.11	45.63±0.02
127.255	37.302	RLQ	0.934	45.78±0.01	25.372	N	7.52±0.36	46.17±0.01
170.097	54.074	RLQ	0.923	45.86±0.01	26.353	Y	8.88±0.04	44.91±0.01
177.835	54.626	RLQ	0.975	47.37±0.01	25.673	N	9.48±0.06	46.53±0.02
248.259	39.408	RLQ	1.024	47.08±0.01	25.930	N	9.25±0.04	45.93±0.19
204.457	55.017	RLQ	1.099	46.54±0.01	26.545	Y	8.81±0.10	45.91±0.02
152.431	5.498	RLQ	0.942	46.78±0.01	25.917	N	9.62±0.02	46.00±0.01
146.686	41.718	RLQ	1.018	46.34±0.01	25.706	N	8.11±0.05	45.45±0.23
148.113	50.814	RLQ	1.091	46.66±0.01	25.742	Y	9.09±0.05	45.69±0.12
186.041	50.032	RLQ	1.066	46.77±0.04	25.443	N	8.87±0.12	46.15±0.04
212.617	46.139	RLQ	1.016	45.93±0.01	26.497	N	9.05±0.06	45.54±0.07
250.226	31.725	RLQ	0.958	45.89±0.01	25.670	N	8.95±0.08	45.46±0.07
225.391	61.626	RLQ	0.910	45.53±0.02	25.490	N	7.92±0.09	45.32±0.06
254.930	37.906	RLQ	1.038	46.07±0.01	25.701	N	8.94±0.13	45.56±0.34
181.484	10.715	RLQ	1.088	47.03±0.01	26.764	N	9.59±0.05	46.18±0.05
231.484	59.283	RLQ	0.955	46.33±0.01	26.292	N	9.54±0.05	45.60±0.02
146.916	51.916	RLQ	1.063	46.00±0.01	26.382	N	9.14±0.39	45.22±0.20
242.305	53.908	RLQ	0.992	46.45±0.01	25.698	N	9.30±0.12	45.01±0.18
222.156	50.247	RLQ	1.074	46.03±0.01	27.002	N	7.86±0.13	45.85±0.03
161.426	52.853	RLQ	1.058	46.40±0.01	26.626	N	9.15±0.22	45.73±0.04
123.836	27.605	RLQ	0.908	47.04±0.01	24.643	N	9.20±0.05	45.82±0.03
135.427	42.942	RLQ	1.014	46.17±0.01	25.166	N	9.09±0.03	45.50±0.04
137.051	51.784	RLQ	1.002	46.41±0.01	25.918	N	9.05±0.02	45.49±0.21
236.316	43.498	RLQ	0.903	46.53±0.01	24.852	N	9.32±0.09	45.94±0.14
221.364	39.355	RLQ	0.965	45.48±0.02	25.329	Y	8.20±0.11	45.67±0.38
249.104	36.249	RLQ	0.909	45.75±0.03	24.817	N	8.45±0.15	45.75±0.04
119.868	30.175	RLQ	1.002	46.63±0.01	26.119	N	8.97±0.08	45.72±0.05
202.288	48.019	RLQ	0.928	46.99±0.01	25.726	N	9.71±0.37	45.55±0.05
256.700	32.240	RLQ	1.070	47.14±0.01	26.329	N	9.59±0.18	45.62±0.09
254.833	37.726	RLQ	1.025	45.99±0.01	25.671	N	8.48±0.25	45.17±0.21
219.444	44.550	RLQ	0.944	46.42±0.01	25.048	N	8.86±0.10	45.47±0.06
226.996	2.015	RLQ	1.083	47.18±0.01	25.721	N	9.36±0.03	46.55±0.015
152.419	46.924	RLQ	1.013	45.71±0.01	26.013	Y	8.55±0.06	45.49±0.46
246.472	43.787	RLQ	1.048	46.37±0.01	25.440	N	8.18±0.07	46.28±0.01

<sup>12</sup>The logarithmic bolometric luminosity in units of  $\text{erg s}^{-1}$  with the associated  $1\sigma$  errors.

<sup>13</sup>The logarithmic 325 MHz radio luminosity in units of  $\text{W Hz}^{-1} \text{sr}^{-1}$  with the associated  $1\sigma$  errors.

<sup>14</sup>Synchrotron contamination at the FIR bands

<sup>15</sup>The logarithmic black hole mass in units of  $M_{\odot}$  with the associated  $1\sigma$  errors.

<sup>16</sup>The logarithmic FIR luminosity in units of  $\text{erg s}^{-1}$  with the associated  $1\sigma$  errors.

135.158	55.055	RLQ	0.947	46.11±0.01	24.816	N	8.52±0.06	45.87±0.04
137.292	1.360	RLQ	1.024	46.79±0.01	26.957	Y	9.15±0.06	46.66±0.01
137.546	46.605	RLQ	1.020	46.88±0.01	26.076	N	8.84±0.04	45.75±0.07
130.118	32.542	RLQ	1.099	46.30±0.01	25.533	N	9.03±0.08	45.63±0.06
244.526	42.426	RLQ	0.934	46.40±0.01	25.189	Y	8.16±0.09	45.07±0.28
238.521	46.186	RLQ	1.004	45.50±0.04	25.610	Y	8.58±0.12	45.30±0.19
128.202	42.417	RLQ	1.051	46.30±0.01	26.687	Y	8.56±0.11	45.40±0.23
125.053	43.233	RLQ	1.073	46.60±0.01	25.213	Y	8.98±0.05	45.52±0.10
185.914	46.189	RLQ	1.013	46.60±0.01	26.243	N	8.54±0.17	45.57±0.03
192.913	54.466	RLQ	1.066	46.13±0.01	26.012	N	9.14±0.05	45.41±0.08
128.109	34.571	RLQ	1.005	45.93±0.01	25.742	N	8.75±0.10	45.49±0.06
205.990	57.912	RLQ	0.933	46.12±0.01	25.862	N	8.82±0.15	45.55±0.03
180.364	9.011	RLQ	1.016	46.98±0.01	25.294	N	9.77±0.20	45.80±0.05
214.512	41.826	RLQ	1.042	46.00±0.01	25.207	N	9.05±0.11	46.31±0.01
139.840	50.815	RLQ	0.921	46.43±0.01	25.683	N	9.32±0.04	45.94±0.04
225.132	48.613	RLQ	1.028	47.06±0.01	25.348	N	9.46±0.06	45.96±0.04
238.569	51.539	RLQ	0.907	46.32±0.01	25.094	N	9.02±0.38	45.35±0.06
117.064	22.017	RLQ	1.059	47.31±0.01	24.960	N	9.41±0.05	45.55±0.18
143.386	41.829	RLQ	0.933	45.73±0.01	25.441	N	7.98±0.10	45.35±0.55
128.531	35.787	RLQ	1.087	45.78±0.01	25.535	N	8.09±0.12	45.72±0.07
232.457	39.753	RLQ	1.081	46.24±0.01	26.375	N	8.25±0.22	45.69±0.21
244.016	46.540	RLQ	0.950	45.87±0.01	25.403	Y	8.41±0.15	45.44±0.06
122.316	32.178	RLQ	0.915	45.63±0.01	24.885	N	8.15±0.08	45.30±0.07
128.313	35.113	RLQ	1.098	46.04±0.01	25.483	Y	9.01±0.16	45.55±0.46
217.125	44.664	RLQ	1.050	46.21±0.01	25.534	N	9.10±0.09	45.39±0.12
188.249	51.568	RLQ	0.986	45.95±0.01	25.035	N	8.67±0.14	45.23±0.15
218.224	46.062	RLQ	1.077	46.88±0.01	24.840	N	9.38±0.09	45.53±0.11
239.375	33.080	RLQ	0.953	46.37±0.01	26.098	N	8.62±0.04	45.74±0.01
160.486	59.603	RLQ	1.100	45.72±0.01	24.500	N	8.27±0.31	45.52±0.11
183.873	53.599	RLQ	1.069	46.45±0.01	27.584	N	9.28±0.20	45.36±0.17
114.510	38.521	RQQ	1.023	46.97±0.01	23.819	N	8.92±0.07	46.23±0.02
257.523	64.812	RQQ	1.008	46.52±0.01	23.803	N	9.13±0.06	46.20±0.02
239.210	39.762	RQQ	0.942	46.54±0.01	23.730	N	9.15±0.08	46.09±0.04
151.877	5.162	RQQ	0.920	45.54±0.01	23.706	N	7.23±1.07	46.00±0.04
176.751	62.002	RQQ	1.041	46.87±0.01	23.838	N	8.97±0.12	46.10±0.05
194.250	4.460	RQQ	1.025	47.26±0.01	23.822	N	9.54±0.05	46.13±0.05
144.497	54.408	RQQ	1.067	45.76±0.01	23.864	N	8.18±0.16	46.05±0.03
127.816	42.555	RQQ	0.931	46.41±0.01	23.718	N	9.04±0.07	45.94±0.05
228.836	0.794	RQQ	0.951	46.30±0.01	23.741	N	8.68±0.10	45.88±0.05
259.270	28.234	RQQ	1.078	47.33±0.01	23.876	N	9.39±0.12	46.07±0.04
155.956	52.364	RQQ	0.955	46.89±0.01	23.746	N	9.07±0.04	45.73±0.07
258.376	64.715	RQQ	1.051	46.62±0.01	23.848	N	9.00±0.05	45.96±0.08
223.764	1.703	RQQ	1.053	45.83±0.01	23.850	N	7.75±0.18	45.88±0.05
163.537	4.447	RQQ	1.085	46.80±0.01	23.882	N	9.15±0.07	45.98±0.07
253.130	35.604	RQQ	0.928	45.92±0.01	23.715	N	8.47±0.57	45.63±0.09
140.741	44.781	RQQ	1.077	46.53±0.01	23.875	N	8.35±0.09	45.89±0.08
159.624	58.868	RQQ	0.935	45.76±0.01	23.723	N	8.40±0.11	45.58±0.09
215.353	42.501	RQQ	1.000	46.50±0.01	23.795	N	8.20±0.07	45.72±0.08
158.447	9.678	RQQ	1.028	46.95±0.01	23.825	N	9.40±0.03	45.73±0.08
260.793	59.852	RQQ	0.990	46.09±0.01	23.784	N	8.40±0.09	45.70±0.09
259.387	59.796	RQQ	1.060	46.25±0.01	23.857	N	8.84±0.18	45.71±0.10
135.473	6.988	RQQ	1.082	47.00±0.01	23.879	N	9.38±0.06	45.73±0.08
204.389	59.106	RQQ	1.087	46.99±0.01	23.885	N	9.36±0.02	45.69±0.12
238.651	32.069	RQQ	1.058	46.80±0.01	23.855	N	9.14±0.04	45.61±0.12
158.854	58.060	RQQ	0.964	46.01±0.01	23.756	N	8.43±0.11	45.44±0.14

206.646	41.942	RQQ	0.902	46.02±0.01	23.685	N	8.87±0.20	45.63±0.08
143.264	46.078	RQQ	1.090	46.50±0.01	23.887	N	9.07±0.06	45.69±0.12
142.597	40.520	RQQ	1.097	46.38±0.01	23.894	N	8.92±0.07	45.74±0.15
152.276	2.599	RQQ	1.100	47.00±0.01	23.897	N	9.08±0.02	45.43±0.14
202.488	54.085	RQQ	0.949	46.96±0.01	23.739	N	9.39±0.07	45.62±0.24
161.407	48.821	RQQ	0.942	45.28±0.05	23.731	N	8.54±0.29	45.51±0.11
248.275	40.296	RQQ	0.974	45.76±0.01	23.767	N	8.46±0.07	45.46±0.10
223.775	56.493	RQQ	1.038	46.73±0.01	23.836	N	9.22±0.03	45.73±0.13
251.572	36.753	RQQ	0.958	45.59±0.02	23.749	N	8.11±0.32	45.43±0.11
155.025	3.552	RQQ	0.936	46.94±0.01	23.724	N	9.43±0.03	45.62±0.52
187.749	10.274	RQQ	1.056	46.13±0.01	23.854	N	9.33±0.28	45.35±0.19
170.823	5.301	RQQ	1.000	46.99±0.01	23.795	N	9.25±0.05	45.59±0.23
131.848	1.170	RQQ	1.081	46.40±0.01	23.879	N	9.31±0.08	45.59±0.16
177.613	66.980	RQQ	1.035	46.96±0.01	23.832	N	9.40±0.02	45.43±0.16
340.498	14.349	RQQ	0.954	46.52±0.01	23.744	N	8.57±0.04	45.33±0.16
160.981	59.515	RQQ	0.909	45.49±0.03	23.692	N	8.12±0.22	45.47±0.17
328.924	12.472	RQQ	1.064	46.92±0.01	23.862	N	9.12±0.05	45.68±0.33
260.379	58.735	RQQ	1.000	46.36±0.01	23.795	N	9.03±0.20	45.65±0.16
162.399	55.831	RQQ	1.056	46.41±0.01	23.853	N	9.39±0.10	45.46±0.10
147.049	55.291	RQQ	1.034	45.69±0.02	23.831	N	8.58±0.39	45.35±0.20
159.730	57.971	RQQ	0.956	46.19±0.01	23.747	N	8.90±0.12	45.35±0.19
160.665	58.542	RQQ	0.998	46.11±0.01	23.793	N	8.23±0.09	45.35±0.23
249.878	41.004	RQQ	1.052	46.39±0.01	23.849	N	9.03±0.13	45.40±0.24
162.249	56.947	RQQ	1.014	46.33±0.01	23.810	N	8.61±0.05	45.52±0.14
141.973	5.610	RQQ	1.062	46.49±0.01	23.860	N	9.31±0.05	45.73±0.23
248.107	41.314	RQQ	0.909	46.26±0.01	23.692	N	8.71±0.14	45.28±0.19
152.149	51.658	RQQ	1.085	46.36±0.01	23.882	N	8.78±0.25	45.52±0.24
248.536	33.212	RQQ	1.007	46.33±0.01	23.802	N	9.13±0.11	45.22±0.28
138.070	42.054	RQQ	1.077	45.56±0.02	23.875	N	8.17±0.16	45.53±0.18
155.298	61.238	RQQ	0.931	45.55±0.01	23.719	N	8.14±0.13	45.06±0.47
160.309	59.039	RQQ	1.094	45.91±0.01	23.891	N	8.49±1.00	45.29±0.41
162.377	59.342	RQQ	1.011	46.12±0.01	23.807	N	8.34±0.09	45.45±0.29
118.095	27.640	RQQ	1.057	46.98±0.01	23.854	N	9.34±0.06	45.77±0.66
7.942	13.775	RQQ	1.007	45.89±0.01	23.803	N	8.38±0.10	45.25±0.37
257.940	60.222	RQQ	0.980	46.28±0.01	23.774	N	8.82±0.20	45.13±0.14
217.072	50.454	RQQ	1.013	46.85±0.01	23.809	N	9.22±0.02	45.31±0.29
204.304	61.130	RQQ	0.926	45.62±0.01	23.713	N	8.79±0.20	45.04±0.48
38.920	0.178	RQQ	0.948	45.69±0.01	23.738	N	8.27±0.15	45.31±1.02
209.600	2.229	RQQ	0.957	47.41±0.01	23.748	N	9.46±0.05	45.31±0.68
187.137	60.626	RQQ	1.040	45.55±0.02	23.837	N	8.63±0.16	45.15±0.39
118.416	25.027	RQQ	0.943	45.92±0.01	23.732	N	9.56±0.42	45.25±0.26
161.747	57.516	RQQ	1.026	46.21±0.01	23.823	N	8.94±0.06	45.07±0.16
117.743	42.271	RQQ	0.938	45.73±0.01	23.726	N	8.39±1.21	45.07±0.06
229.841	53.978	RQQ	1.026	45.61±0.02	23.823	N	8.04±0.85	45.18±1.34
125.624	44.452	RQQ	1.057	46.84±0.01	23.854	N	9.25±0.04	45.33±1.53
116.871	43.769	RQQ	1.086	45.73±0.01	23.884	N	7.91±0.08	45.20±0.48
142.124	50.810	RQQ	1.034	46.33±0.01	23.831	N	9.04±0.05	45.39±0.94
2.128	36.364	LERG	0.911	44.78±0.29	25.993	N	8.92	44.85±0.89
3.451	34.949	LERG	0.926	45.14±0.13	25.526	N	8.44	45.11±0.20
3.879	36.205	HERG	0.968	45.74±0.05	26.034	N	9.08	45.29±0.04
12.734	51.201	HERG	0.936	46.81±0.01	27.470	?	9.37	-45.26±0.75
22.873	39.716	HERG	0.929	44.80±0.33	26.661	?	8.25	45.15±0.10
24.169	48.873	LERG	1.029	44.69±0.70	26.520	N	7.85	45.41±0.62
32.570	32.826	HERG	1.073	45.68±0.07	26.618	N	8.91	45.02±0.10
108.520	14.606	HERG	0.920	45.58±0.09	27.371	?	8.73	45.38±0.85

---

114.851	70.386	HERG	0.994	45.61±0.11	27.571	?	8.97	45.58±0.11
123.247	26.863	HERG	0.936	45.81±0.06	26.219	N	7.93	44.53±0.10
123.411	29.275	HERG	1.098	45.64±0.12	26.456	N	8.20	44.88±0.04
124.445	29.364	LERG	0.918	45.28±0.17	26.096	N	8.98	45.07±0.30
126.428	24.673	HERG	0.992	46.04±0.04	26.094	N	8.41	45.87±0.16
146.578	39.738	LERG	1.035	46.08±0.03	26.729	N	8.31	45.13±0.30
153.554	36.288	HERG	1.042	45.91±0.05	26.739	N	8.28	45.39±0.05
155.167	36.951	HERG	1.053	45.86±0.05	26.862	N	8.21	44.89±0.13
155.730	39.147	LERG	0.923	45.18±0.26	26.760	N	8.35	45.18±0.01
173.148	36.905	HERG	1.060	45.74±0.06	26.870	N	8.31	45.64±0.05
180.100	73.012	HERG	0.970	45.69±0.06	27.78	?	7.48	45.01±0.08
183.736	37.814	LERG	0.950	45.10±0.16	26.713	N	8.35	45.25±0.51
185.041	36.485	HERG	1.088	45.33±0.15	26.856	N	8.45	45.65±0.03
194.241	47.339	HERG	0.996	46.71±0.01	27.819	?	8.35	45.33±0.18
194.775	36.533	HERG	1.070	46.01±0.04	26.937	N	9.04	45.67±0.05
194.875	36.284	HERG	1.004	45.68±0.06	26.639	N	8.72	45.11±0.18
206.363	49.775	HERG	0.967	46.27±0.02	27.501	?	9.10	45.35±0.13
248.641	62.760	HERG	0.988	46.59±0.01	27.733	?	8.78	-45.30±0.56
261.079	50.961	HERG	1.079	46.44±0.02	27.534	N	8.75	45.210±0.08

B2. SMA observations of the 44 RLQs candidates for synchrotron contamination (Chapter 4).

name	Atmospheric opacity ( $\tau$ )	Dates	Observed frequency (GHz)	Number of antennas	$S_{1300\mu\text{m}}$ (mJy)
SDSS075928.3+301028.3	0.05	150130	225.436	3	$< 4 \times 3.8$
	0.12	150219	225.435	6	$6.94 \pm 2.90$
	0.20	150220	219.137	6	$6.01 \pm 1.80$
SDSS080915.9+321041.6	0.05	150130	225.436	3	$5.13 \pm 3.4$
	0.12	150219	225.435	6	$7.13 \pm 3.00$
	0.20	150220	219.137	6	$3.79 \pm 1.80$
SDSS081520.6+273617.0	0.05	150130	225.436	3	$10.08 \pm 4.90$
	0.12	150219	225.435	6	$6.20 \pm 2.20$
	0.20	150220	219.137	6	$6.40 \pm 1.80$
SDSS082012.6+431358.5	0.06	150209	219.178	5	$6.21 \pm 3.30$
SDSS082836.4+504826.5	0.06	150209	219.178	5	$37.9 \pm 3.3$
SDSS082901.3+371806.1	0.06	150209	219.178	5	$6.90 \pm 3.40$
SDSS083226.1+343414.3	0.10	150216	226.143	5	$3.40 \pm 2.4$
SDSS083248.4+422459.5	0.10	150216	226.143	5	$10.64 \pm 2.40$
SDSS083315.1+350647.3	0.10	150216	226.143	5	$3.50 \pm 2.20$
SDSS083407.6+354712.0	0.10	150216	226.143	5	$< 4 \times 2.6$
SDSS090142.4+425631.0	0.12	150219	225.435	6	$2.87 \pm 3.10$
SDSS091011.0+463617.8	0.12	150219	225.435	6	$< 4 \times 2.3$
SDSS091921.6+504855.4	0.12	150219	225.435	6	$2.49 \pm 2.30$
SDSS094740.0+515456.8	0.12	150219	225.435	6	$< 4 \times 2.3$
SDSS100940.5+465525.0	0.12	150219	225.435	6	$4.9 \pm 3.3$
SDSS104542.2+525112.6	0.09	150201	226.133	6	$6.5 \pm 1.6$
SDSS112023.2+540427.1	0.15	150202	225.215	6	$42.16 \pm 3.40$
SDSS120556.1+104253.9	0.09	150201	226.133	6	$5.02 \pm 1.50$
SDSS122339.3+461118.7	0.12	150225	225.476	5	$23.43 \pm 2.70$
SDSS123259.8+513404.5	0.12	150225	225.476	5	$3.83 \pm 2.80$
SDSS125139.1+542758.1	0.12	150225	225.476	5	$< 4 \times 2.8$
SDSS131103.2+551354.4	0.05	150208	235.509	5	$63.1 \pm 2.5$
	0.12	150219	225.435	6	$77.5 \pm 2.5$
SDSS132909.3+480109.7	0.05	150208	235.509	5	$3.95 \pm 2.40$
	0.12	150219	225.435	6	$4.56 \pm 2.40$
SDSS133749.6+550102.2	0.05	150208	235.509	5	$97.0 \pm 2.4$
	0.12	150219	225.435	6	$114.5 \pm 2.5$
SDSS134213.3+602142.8	0.05	150208	235.509	5	$2.23 \pm 2.50$
	0.12	150219	225.435	6	$< 3.52 \times 2.50$
SDSS134934.6+534117.0	0.05	150208	235.509	5	$205.7 \pm 2.7$
SDSS141028.2+460821.0	0.10	140524		7	$5.3 \pm 1.5$
SDSS142829.9+443949.8	0.10	140524		7	$< 4 \times 1.8$
SDSS143844.8+621154.5	0.10	140524		7	$8.8 \pm 3.1$
SDSS144527.4+392117.0	0.12	150219	225.435	6	$11.54 \pm 2.50$
SDSS144837.5+501448.9	0.10	140524		7	$12.5 \pm 2.8$
SDSS150133.9+613733.8	0.05-0.1	140530		7	$2.7 \pm 1.3$
SDSS152556.2+591659.5	0.05-0.1	140530		7	$< 4 \times 1.3$
SDSS155405.0+461107.5	0.05-0.1	140530		7	$5.4 \pm 1.1$
SDSS155416.5+513218.9	0.05-0.1	140530		7	$< 4 \times 1.3$
SDSS155729.9+330446.9	0.12	150219	225.435	6	$18.95 \pm 2.40$

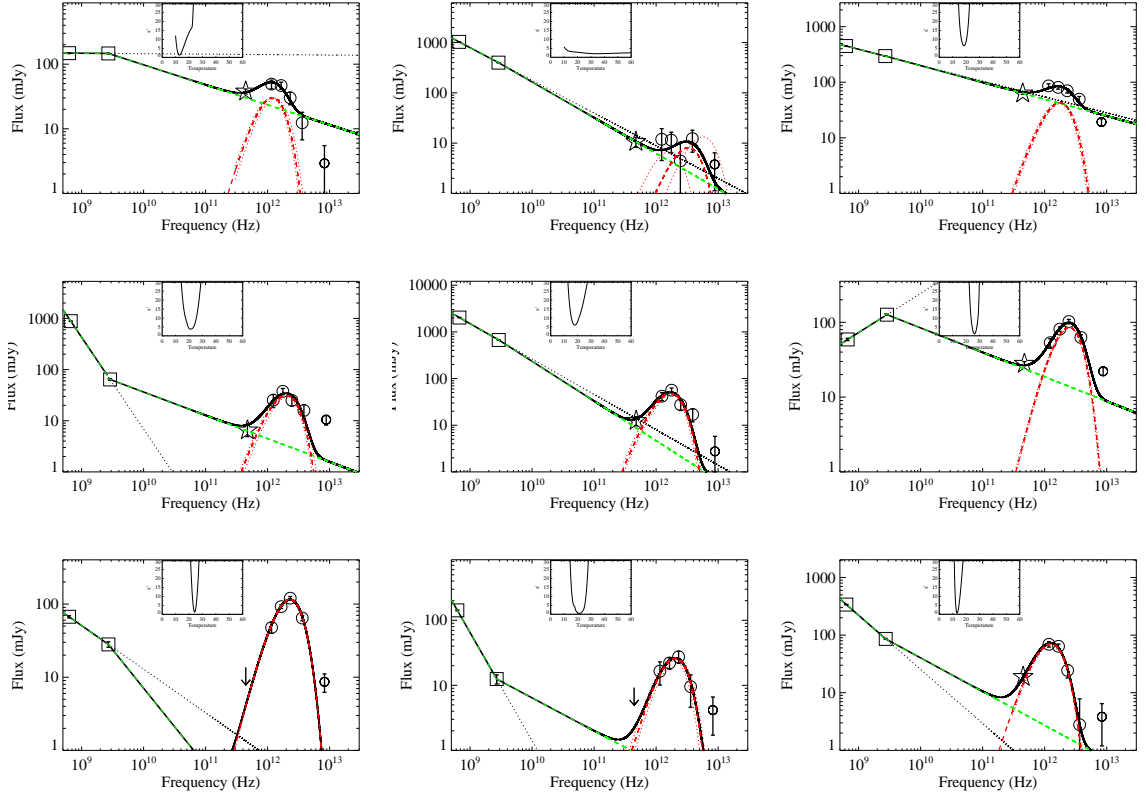


FIGURE A.1: Radio to FIR spectral energy distribution (SEDs, solid black) for representative RLQs observed with SMA. Open squares show the 325 (WENSS) and 1400 MHz (FIRST) radio photometry, open stars the 1300  $\mu\text{m}$  SMA photometry (arrow indicated the  $4\sigma$  upper limit) and open circles the SPIRE and 160  $\mu\text{m}$  PACS photometry. The 70  $\mu\text{m}$  PACS photometry is shown with a smaller circle and is not used for the SED fitting. Error bars correspond to  $1\sigma$  photometric uncertainties. The radio photometry has been fitted with a broken power-law from 325 to 1400 MHz and from 1400 MHz to 230 GHz (or 1300  $\mu\text{m}$ ; green dashed line) and the FIR photometry with an optically thin modified blackbody component (red dashed line). The dotted black line shows the radio spectrum based on WENSS and FIRST radio observations only. The dotted red lines show the  $1\sigma$  blackbody fitting uncertainty. The inner plot show the blackbody fitting  $\chi^2$  value as a function of dust temperature. The SED plot are arrange in terms of non-thermal contamination at 1300  $\mu\text{m}$ , from top to bottom. The top panel show RLQs that have been rejected from our sample, the middle and bottom panels RLQs without significant synchrotron contamination at the FIR band while the bottom panel RLQs that the 1300  $\mu\text{m}$  emission is dominated by the thermal component.

# Bibliography

- Ahn C. P. et al., 2014, *ApJS*, 211, 17
- Aird J. et al., 2013, *ApJ*, 775, 41
- Aird J. et al., 2010, *MNRAS*, 401, 2531
- Akritas M. G., Siebert J., 1996, *MNRAS*, 278, 919
- Alexander D. M. et al., 2011, *ApJ*, 738, 44
- Alexander D. M., Bauer F. E., Chapman S. C., Smail I., Blain A. W., Brandt W. N., Ivison R. J., 2005, *ApJ*, 632, 736
- Alexander D. M., Brandt W. N., Hornschemeier A. E., Garmire G. P., Schneider D. P., Bauer F. E., Griffiths R. E., 2001, *AJ*, 122, 2156
- Alexander D. M. et al., 2008, *ApJ*, 687, 835
- Alexander D. M., Hickox R. C., 2012, *Nar*, 56, 93
- Alexandroff R. et al., 2013, *MNRAS*, 435, 3306
- Alonso-Herrero A., Pérez-González P. G., Rieke G. H., Alexander D. M., Rigby J. R., Papovich C., Donley J. L., Rigopoulou D., 2008, *ApJ*, 677, 127
- Amblard A. et al., 2010, *A&A*, 518, L9
- Antonucci R., 1993, *ARA&A*, 31, 473
- Arav N., Moe M., Costantini E., Korista K. T., Benn C., Ellison S., 2008, *ApJ*, 681, 954
- Archibald E. N., Dunlop J. S., Hughes D. H., Rawlings S., Eales S. A., Ivison R. J., 2001, *MNRAS*, 323, 417
- Arnouts S., Ilbert O., 2011, *LePHARE: Photometric Analysis for Redshift Estimate*. Astrophysics Source Code Library
- Baldry I. K., Glazebrook K., Brinkmann J., Ivezić Ž., Lupton R. H., Nichol R. C., Szalay A. S., 2004, *ApJ*, 600, 681
- Baldwin J. A., Phillips M. M., Terlevich R., 1981, *PASP*, 93, 5
- Ballantyne D. R., 2008, *ApJ*, 685, 787
- Ballantyne D. R., Shi Y., Rieke G. H., Donley J. L., Papovich C., Rigby J. R., 2006, *ApJ*, 653, 1070

- Barger A. J., Cowie L. L., Mushotzky R. F., Yang Y., Wang W.-H., Steffen A. T., Capak P., 2005, *AJ*, 129, 578
- Barr J. M., Bremer M. N., Baker J. C., Lehnert M. D., 2003, *MNRAS*, 346, 229
- Barthel P., Haas M., Leipski C., Wilkes B., 2012, *ApJ*, 757, L26
- Barthel P. D., 1989, *ApJ*, 336, 606
- Barthel P. D., Arnaud K. A., 1996, *MNRAS*, 283, L45
- Barvainis R., Lehár J., Birkinshaw M., Falcke H., Blundell K. M., 2005, *ApJ*, 618, 108
- Becker R. H., White R. L., Helfand D. J., 1995, *ApJ*, 450, 559
- Beifiori A., Courteau S., Corsini E. M., Zhu Y., 2012, *MNRAS*, 419, 2497
- Best P. N., Heckman T. M., 2012, *MNRAS*, 421, 1569
- Best P. N., Kaiser C. R., Heckman T. M., Kauffmann G., 2006, *MNRAS*, 368, L67
- Best P. N., Kauffmann G., Heckman T. M., Brinchmann J., Charlot S., Ivezić Ž., White S. D. M., 2005, *MNRAS*, 362, 25
- Best P. N., Ker L. M., Simpson C., Rigby E. E., Sabater J., 2014, *MNRAS*, 445, 955
- Best P. N., Longair M. S., Rottgering H. J. A., 1996, *MNRAS*, 280, L9
- Bicknell G. V., Sutherland R. S., van Breugel W. J. M., Dopita M. A., Dey A., Miley G. K., 2000, *ApJ*, 540, 678
- Bîrzan L., McNamara B. R., Nulsen P. E. J., Carilli C. L., Wise M. W., 2008, *ApJ*, 686, 859
- Blandford R. D., McKee C. F., 1982, *ApJ*, 255, 419
- Blandford R. D., Rees M. J., 1974, *MNRAS*, 169, 395
- Blandford R. D., Znajek R. L., 1977, *MNRAS*, 179, 433
- Bonfield D. G. et al., 2011, *MNRAS*, 416, 13
- Boroson T., 2005, *AJ*, 130, 381
- Bournaud F. et al., 2012, *ApJ*, 757, 81
- Bower R. G., McCarthy I. G., Benson A. J., 2008, *MNRAS*, 390, 1399
- Boyle B. J., Shanks T., Croom S. M., Smith R. J., Miller L., Loaring N., Heymans C., 2000, *MNRAS*, 317, 1014
- Boyle B. J., Terlevich R. J., 1998, *MNRAS*, 293, L49
- Brandt W. N., Hasinger G., 2005, *ARA&A*, 43, 827
- Brusa M. et al., 2010, *ApJ*, 716, 348
- Brusa M. et al., 2009, *ApJ*, 693, 8

- Brusa M. et al., 2003, *A&A*, 409, 65
- Buat V. et al., 2010, *MNRAS*, 409, L1
- Bundy K. et al., 2006, *ApJ*, 651, 120
- Bundy K. et al., 2008, *ApJ*, 681, 931
- Burlon D., Ajello M., Greiner J., Comastri A., Merloni A., Gehrels N., 2011, *ApJ*, 728, 58
- Caccianiga A. et al., 2004, *A&A*, 416, 901
- Calzetti D., Armus L., Bohlin R. C., Kinney A. L., Koornneef J., Storchi-Bergmann T., 2000, *ApJ*, 533, 682
- Canalizo G., Stockton A., 2001, *ApJ*, 555, 719
- Cappelluti N. et al., 2009, *A&A*, 497, 635
- Carr B. J., Hawking S. W., 1974, *MNRAS*, 168, 399
- Casali M. et al., 2007, *A&A*, 467, 777
- Cattaneo A., Best P. N., 2009, *MNRAS*, 395, 518
- Cavagnolo K. W., McNamara B. R., Nulsen P. E. J., Carilli C. L., Jones C., Bîrzan L., 2010, *ApJ*, 720, 1066
- Chapman S. C., Blain A. W., Smail I., Ivison R. J., 2005, *ApJ*, 622, 772
- Chen C.-T. J. et al., 2015, *ApJ*, 802, 50
- Chen Y.-M., Kauffmann G., Heckman T. M., Tremonti C. A., White S., et al., 2013, *MNRAS*, 429, 2643
- Cimatti A., Daddi E., Renzini A., 2006, *A&A*, 453, L29
- Cirasuolo M., Celotti A., Magliocchetti M., Danese L., 2003a, *MNRAS*, 346, 447
- Cirasuolo M., Magliocchetti M., Celotti A., Danese L., 2003b, *MNRAS*, 341, 993
- Civano F. et al., 2011, *ApJ*, 741, 91
- Civano F., Comastri A., Brusa M., 2005, *MNRAS*, 358, 693
- Civano F. et al., 2012, *ApJS*, 201, 30
- Cleary K., Lawrence C. R., Marshall J. A., Hao L., Meier D., 2007, *ApJ*, 660, 117
- Clements D. L., McDowell J. C., Shaked S., Baker A. C., Borne K., Colina L., Lamb S. A., Mundell C., 2002, *ApJ*, 581, 974
- Cohen A. S., Lane W. M., Cotton W. D., Kassim N. E., Lazio T. J. W., Perley R. A., Condon J. J., Erickson W. C., 2007, *AJ*, 134, 1245
- Comastri A., Brunetti G., Dallacasa D., Bondi M., Pedani M., Setti G., 2003, *MNRAS*, 340, L52

- Comastri A. et al., 2011, *A&A*, 526, L9
- Condon J. J., Cotton W. D., Greisen E. W., Yin Q. F., Perley R. A., Taylor G. B., Broderick J. J., 1998, *AJ*, 115, 1693
- Condon J. J., Kellermann K. I., Kimball A. E., Ivezić Ž., Perley R. A., 2013, *ApJ*, 768, 37
- Cool R. J. et al., 2008, *ApJ*, 682, 919
- Coppin K. et al., 2006, *MNRAS*, 372, 1621
- Coppin K. E. K. et al., 2008, *MNRAS*, 389, 45
- Corral A., Barcons X., Carrera F. J., Ceballos M. T., Mateos S., 2005, *A&A*, 431, 97
- Cowie L. L., Barger A. J., Bautz M. W., Brandt W. N., Garmire G. P., 2003, *ApJ*, 584, L57
- Cowie L. L., Songaila A., Hu E. M., Cohen J. G., 1996, *AJ*, 112, 839
- Croft S. et al., 2006, *ApJ*, 647, 1040
- Croom S. M. et al., 2009, *MNRAS*, 399, 1755
- Croton D. J. et al., 2006, *MNRAS*, 365, 11
- Cui J., Xia X.-Y., Deng Z.-G., Mao S., Zou Z.-L., 2001, *AJ*, 122, 63
- Curran S. J., 2000, *A&AS*, 144, 271
- Daddi E. et al., 2007, *ApJ*, 670, 173
- Daddi E. et al., 2010, *ApJ*, 713, 686
- Dai Y. S. et al., 2014, *ApJ*, 791, 113
- Dalton G. et al., 2012, in *Society of Photo-Optical Instrumentation Engineers (SPIE) Conference Series*, Vol. 8446, *Society of Photo-Optical Instrumentation Engineers (SPIE) Conference Series*, p. 84460P
- Damen M., Labbé I., Franx M., van Dokkum P. G., Taylor E. N., Gawiser E. J., 2009, *ApJ*, 690, 937
- Davies R. I., Maciejewski W., Hicks E. K. S., Tacconi L. J., Genzel R., Engel H., 2009, *ApJ*, 702, 114
- De Breuck C., Downes D., Neri R., van Breugel W., Reuland M., Omont A., Ivison R., 2005, *A&A*, 430, L1
- Del Moro A. et al., 2013, *A&A*, 549, A59
- Delvecchio I. et al., 2014, *MNRAS*, 439, 2736
- Dey A., van Breugel W., Vacca W. D., Antonucci R., 1997, *ApJ*, 490, 698
- Di Matteo T., Colberg J., Springel V., Hernquist L., Sijacki D., 2008, *ApJ*, 676, 33

- Di Matteo T., Croft R. A. C., Springel V., Hernquist L., 2003, *ApJ*, 593, 56
- Di Matteo T., Springel V., Hernquist L., 2005, *Nature*, 433, 604
- DiPompeo M. A., Myers A. D., Hickox R. C., Geach J. E., Hainline K. N., 2014, *MNRAS*, 442, 3443
- Donley J. L., Rieke G. H., Pérez-González P. G., Rigby J. R., Alonso-Herrero A., 2007, *ApJ*, 660, 167
- Donoso E., Best P. N., Kauffmann G., 2009, *MNRAS*, 392, 617
- Donoso E., Yan L., Stern D., Assef R. J., 2014, *ApJ*, 789, 44
- Dotan C., Shaviv N. J., 2011, *MNRAS*, 413, 1623
- Douglas J. N., Bash F. N., Bozayan F. A., Torrence G. W., Wolfe C., 1996, *AJ*, 111, 1945
- Downes D., Eckart A., 2007, *A&A*, 468, L57
- Draper A. R., Ballantyne D. R., 2010, *ApJ*, 715, L99
- Drouart G. et al., 2014, ArXiv e-prints
- Dubois Y., Devriendt J., Slyz A., Teyssier R., 2012, *MNRAS*, 420, 2662
- Dunlop J. S., McLure R. J., Kukula M. J., Baum S. A., O’Dea C. P., Hughes D. H., 2003, *MNRAS*, 340, 1095
- Dunlop J. S., Taylor G. L., Hughes D. H., Robson E. I., 1993, *MNRAS*, 264, 455
- Dunn J. P. et al., 2010, *ApJ*, 709, 611
- Dunne L., Eales S. A., 2001, *MNRAS*, 327, 697
- Dunne L. et al., 2011, *MNRAS*, 417, 1510
- Dye S. et al., 2010, *A&A*, 518, L10
- Dye S. et al., 2006, *MNRAS*, 372, 1227
- Eales S. et al., 2010, *PASP*, 122, 499
- Eales S. A., 1985, *MNRAS*, 217, 149
- Elbaz D. et al., 2007, *A&A*, 468, 33
- Elbaz D. et al., 2011, *A&A*, 533, A119
- Elbaz D., Jahnke K., Pantin E., Le Borgne D., Letawe G., 2009, *A&A*, 507, 1359
- Elitzur M., 2012, *ApJ*, 747, L33
- Elitzur M., Shlosman I., 2006, *ApJ*, 648, L101
- Ellingson E., Yee H. K. C., Green R. F., 1991, *ApJ*, 371, 49

- Elvis M., 2000, *ApJ*, 545, 63
- Elvis M. et al., 2009, *ApJS*, 184, 158
- Elvis M., Risaliti G., Zamorani G., 2002, *ApJ*, 565, L75
- Evans A. S., Mazzarella J. M., Surace J. A., Frayer D. T., Iwasawa K., Sanders D. B., 2005, *ApJS*, 159, 197
- Faber S. M. et al., 2007, *ApJ*, 665, 265
- Fabian A. C., 1999, *MNRAS*, 308, L39
- Fabian A. C., Barcons X., Almaini O., Iwasawa K., 1998, *MNRAS*, 297, L11
- Fabricant D. et al., 2005, *PASP*, 117, 1411
- Falcke H., Sherwood W., Patnaik A. R., 1996, *ApJ*, 471, 106
- Falder J. T. et al., 2010, *MNRAS*, 405, 347
- Fan L., Fang G., Chen Y., Li J., Lv X., Knudsen K. K., Kong X., 2014, *ApJ*, 784, L9
- Fan X. et al., 2001, *AJ*, 121, 31
- Fanaroff B. L., Riley J. M., 1974, *MNRAS*, 167, 31P
- Fanidakis N. et al., 2012, *MNRAS*, 419, 2797
- Feigelson E. D., Nelson P. I., 1985, *ApJ*, 293, 192
- Feltre A. et al., 2013, *MNRAS*, 434, 2426
- Fernandes C. A. C. et al., 2015, *MNRAS*, 447, 1184
- Fernandes C. A. C. et al., 2011, *MNRAS*, 411, 1909
- Ferrarese L., 2002, *ApJ*, 578, 90
- Ferrarese L., Merritt D., 2000, *ApJ*, 539, L9
- Feruglio C., Maiolino R., Piconcelli E., Menci N., Aussel H., Lamastra A., Fiore F., 2010, *A&A*, 518, L155
- Filippenko A. V., Terlevich R., 1992, *ApJ*, 397, L79
- Fiore F. et al., 2003, *A&A*, 409, 79
- Floyd D. J. E. et al., 2010, *ApJ*, 713, 66
- Fontanot F., De Lucia G., Monaco P., Somerville R. S., Santini P., 2009, *MNRAS*, 397, 1776
- Fragile P. C., Murray S. D., Anninos P., van Breugel W., 2004, *ApJ*, 604, 74
- Franceschini A., Vercellone S., Fabian A. C., 1998, *MNRAS*, 297, 817

- Freeman P., Doe S., Siemiginowska A., 2001, in Society of Photo-Optical Instrumentation Engineers (SPIE) Conference Series, Vol. 4477, Society of Photo-Optical Instrumentation Engineers (SPIE) Conference Series, Starck J.-L., Murtagh F. D., eds., pp. 76–87
- Gabor J. M., Bournaud F., 2013, *MNRAS*, 434, 606
- Gabor J. M. et al., 2009, *ApJ*, 691, 705
- Gaibler V., Khochfar S., Krause M., Silk J., 2012, *MNRAS*, 425, 438
- Garmire G. P., Bautz M. W., Ford P. G., Nousek J. A., Ricker, Jr. G. R., 2003, in Society of Photo-Optical Instrumentation Engineers (SPIE) Conference Series, Vol. 4851, X-Ray and Gamma-Ray Telescopes and Instruments for Astronomy., Truemper J. E., Tananbaum H. D., eds., pp. 28–44
- Garofalo D., Evans D. A., Sambruna R. M., 2010, *MNRAS*, 406, 975
- Gebhardt K. et al., 2000a, *ApJ*, 539, L13
- Gebhardt K. et al., 2000b, *ApJ*, 539, L13
- Genzel R. et al., 2010, *MNRAS*, 407, 2091
- Georgakakis A. et al., 2009, *MNRAS*, 397, 623
- Georgakakis A., Nandra K., 2011, *MNRAS*, 414, 992
- Georgantopoulos I., Akylas A., Georgakakis A., Rowan-Robinson M., 2009, *A&A*, 507, 747
- Gilli R., Comastri A., Hasinger G., 2007, *A&A*, 463, 79
- Glikman E., Djorgovski S. G., Stern D., Dey A., Jannuzi B. T., Lee K.-S., 2011, *ApJ*, 728, L26
- Gofford J. et al., 2011, *MNRAS*, 414, 3307
- Goldschmidt P., Kukuła M. J., Miller L., Dunlop J. S., 1999, *ApJ*, 511, 612
- Gonçalves T. S., Steidel C. C., Pettini M., 2008, *ApJ*, 676, 816
- González-Solares E. A. et al., 2011, *MNRAS*, 416, 927
- Goudfrooij P., de Jong T., 1995, *A&A*, 298, 784
- Goulding A. D., Alexander D. M., 2009, *MNRAS*, 398, 1165
- Graham A. W., Scott N., 2013, *ApJ*, 764, 151
- Granato G. L., Silva L., Monaco P., Panuzzo P., Salucci P., De Zotti G., Danese L., 2001, *MNRAS*, 324, 757
- Green P. J. et al., 2009, *ApJ*, 690, 644
- Green P. J., Myers A. D., Barkhouse W. A., Aldcroft T. L., Trichas M., Richards G. T., Ruiz Á., Hopkins P. F., 2011, *ApJ*, 743, 81

- Green P. J., Myers A. D., Barkhouse W. A., Mulchaey J. S., Bennert V. N., Cox T. J., Aldcroft T. L., 2010, *ApJ*, 710, 1578
- Green R. F., Yee H. K. C., 1984, *ApJS*, 54, 495
- Greene J. E., Zakamska N. L., Ho L. C., Barth A. J., 2011, *ApJ*, 732, 9
- Griffin M. J. et al., 2010, *A&A*, 518, L3
- Griffith M. R., Wright A. E., Burke B. F., Ekers R. D., 1995, *ApJS*, 97, 347
- Grogin N. A. et al., 2005, *ApJ*, 627, L97
- Haas M. et al., 2003, *A&A*, 402, 87
- Hambly N. C. et al., 2008, *MNRAS*, 384, 637
- Hao H. et al., 2014, *ArXiv e-prints*
- Hardcastle M. J. et al., 2013, *MNRAS*, 429, 2407
- Hardcastle M. J., Evans D. A., Croston J. H., 2006, *MNRAS*, 370, 1893
- Hardcastle M. J., Evans D. A., Croston J. H., 2007, *MNRAS*, 376, 1849
- Hardcastle M. J. et al., 2010, *MNRAS*, 409, 122
- Häring N., Rix H.-W., 2004, *ApJ*, 604, L89
- Harrison C. M. et al., 2012, *ApJ*, 760, L15
- Harrison F. A. et al., 2013, *ApJ*, 770, 103
- Hasinger G., 2008, *A&A*, 490, 905
- Hasinger G. et al., 2001, *A&A*, 365, L45
- Hasinger G., Miyaji T., Schmidt M., 2005, *A&A*, 441, 417
- Hatch N. A., Overzier R. A., Röttgering H. J. A., Kurk J. D., Miley G. K., 2008, *MNRAS*, 383, 931
- Hatziminaoglou E. et al., 2008, *MNRAS*, 386, 1252
- Hatziminaoglou E., Fritz J., Jarrett T. H., 2009, *MNRAS*, 399, 1206
- Hatziminaoglou E. et al., 2010, *A&A*, 518, L33
- Healey S. E., Romani R. W., Taylor G. B., Sadler E. M., Ricci R., Murphy T., Ulvestad J. S., Winn J. N., 2007, *ApJS*, 171, 61
- Heckman T. M., 1980, *A&A*, 87, 152
- Heckman T. M., Best P. N., 2014, *ARA&A*, 52, 589
- Heckman T. M., Kauffmann G., Brinchmann J., Charlot S., Tremonti C., White S. D. M., 2004, *ApJ*, 613, 109

- Heinz S., Merloni A., Schwab J., 2007, *ApJ*, 658, L9
- Heisler C. A., Lumsden S. L., Bailey J. A., 1997, *Nature*, 385, 700
- Helou G., Soifer B. T., Rowan-Robinson M., 1985, *ApJ*, 298, L7
- Hennawi J. F. et al., 2006, *ApJ*, 651, 61
- Herbert P. D., Jarvis M. J., Willott C. J., McLure R. J., Mitchell E., Rawlings S., Hill G. J., Dunlop J. S., 2010, *MNRAS*, 406, 1841
- Herbert P. D., Jarvis M. J., Willott C. J., McLure R. J., Mitchell E., Rawlings S., Hill G. J., Dunlop J. S., 2011, *MNRAS*, 410, 1360
- Hewett P. C., Warren S. J., Leggett S. K., Hodgkin S. T., 2006, *MNRAS*, 367, 454
- Hickox R. C. et al., 2007, *ApJ*, 671, 1365
- Hickox R. C. et al., 2009, *ApJ*, 696, 891
- Hickox R. C., Mullaney J. R., Alexander D. M., Chen C.-T. J., Civano F. M., Goulding A. D., Hainline K. N., 2014, *ApJ*, 782, 9
- Hickox R. C. et al., 2011, *ApJ*, 731, 117
- Hildebrand R. H., 1983, *QJRAS*, 24, 267
- Hill G. J., Lilly S. J., 1991, *ApJ*, 367, 1
- Hill G. J., Rawlings S., 2003, *nature*, 47, 373
- Hiner K. D., Canalizo G., Lacy M., Sajina A., Armus L., Ridgway S., Storrie-Lombardi L., 2009, *ApJ*, 706, 508
- Hiroi K., Ueda Y., Akiyama M., Watson M. G., 2012, *ApJ*, 758, 49
- Ho L. C., 2002, *ApJ*, 564, 120
- Ho L. C., 2008, *ARA&A*, 46, 475
- Ho L. C., Filippenko A. V., Sargent W. L. W., 1997, *ApJ*, 487, 579
- Ho P. T. P., Moran J. M., Lo K. Y., 2004, *ApJ*, 616, L1
- Hodgkin S. T., Irwin M. J., Hewett P. C., Warren S. J., 2009, *MNRAS*, 394, 675
- Hooper E. J., Impey C. D., Foltz C. B., Hewett P. C., 1995, *ApJ*, 445, 62
- Hopkins A. M., Beacom J. F., 2006, *ApJ*, 651, 142
- Hopkins P. F., Hernquist L., Cox T. J., Di Matteo T., Robertson B., Springel V., 2005, *ApJ*, 630, 716
- Hopkins P. F., Hernquist L., Cox T. J., Di Matteo T., Robertson B., Springel V., 2006, *ApJS*, 163, 1

- Hopkins P. F., Hernquist L., Cox T. J., Kereš D., 2008, *ApJS*, 175, 356
- Hopkins P. F., Richards G. T., Hernquist L., 2007, *ApJ*, 654, 731
- Hopkins P. F., Younger J. D., Hayward C. C., Narayanan D., Hernquist L., 2010, *MNRAS*, 402, 1693
- Hoyle F., Fowler W. A., 1963, *MNRAS*, 125, 169
- Hughes S. A., Blandford R. D., 2003, *ApJ*, 585, L101
- Hyvönen T., Kotilainen J. K., Örndahl E., Falomo R., Uslenghi M., 2007, *A&A*, 462, 525
- Ibar E., Ivison R. J., Biggs A. D., Lal D. V., Best P. N., Green D. A., 2009, *MNRAS*, 397, 281
- Ibar E. et al., 2010, *MNRAS*, 409, 38
- Ikeda H. et al., 2011, *ApJ*, 728, L25
- Ilbert O. et al., 2009, *ApJ*, 690, 1236
- Impey C., Petry C., 2001, *ApJ*, 547, 117
- Inskip K. J., Best P. N., Longair M. S., Röttgering H. J. A., 2005, *MNRAS*, 359, 1393
- Inskip K. J., Villar-Martín M., Tadhunter C. N., Morganti R., Holt J., Dicken D., 2008, *MNRAS*, 386, 1797
- Isaak K. G., Priddey R. S., McMahon R. G., Omont A., Peroux C., Sharp R. G., Withington S., 2002, *MNRAS*, 329, 149
- Ishibashi W., Fabian A. C., 2012, *MNRAS*, 427, 2998
- Isobe T., Feigelson E. D., Akritas M. G., Babu G. J., 1990, *ApJ*, 364, 104
- Ivezić Ž. et al., 2002, *AJ*, 124, 2364
- Ivezić Z. et al., 2004, in *Astronomical Society of the Pacific Conference Series*, Vol. 311, *AGN Physics with the Sloan Digital Sky Survey*, Richards G. T., Hall P. B., eds., p. 347
- Iwasawa K., Sanders D. B., Evans A. S., Trentham N., Miniutti G., Spoon H. W. W., 2005, *MNRAS*, 357, 565
- Jansen F. et al., 2001, *A&A*, 365, L1
- Jarvis M. J., McLure R. J., 2002, *MNRAS*, 336, L38
- Jarvis M. J., McLure R. J., 2006, *MNRAS*, 369, 182
- Jarvis M. J., Rawlings S., 2000, *MNRAS*, 319, 121
- Jarvis M. J., Rawlings S., Eales S., Blundell K. M., Bunker A. J., Croft S., McLure R. J., Willott C. J., 2001a, *MNRAS*, 326, 1585

- Jarvis M. J., Rawlings S., Willott C. J., Blundell K. M., Eales S., Lacy M., 2001b, MNRAS, 327, 907
- Jarvis M. J. et al., 2010, MNRAS, 409, 92
- Jiang L. et al., 2009, AJ, 138, 305
- Jiang L., Fan X., Ivezić Ž., Richards G. T., Schneider D. P., Strauss M. A., Kelly B. C., 2007, ApJ, 656, 680
- Johnston R., Vaccari M., Jarvis M., Smith M., Giovannoli E., Häußler B., Prescott M., 2015, MNRAS, 453, 2540
- Juneau S. et al., 2014, ApJ, 788, 88
- Juneau S., Dickinson M., Alexander D. M., Salim S., 2011, ApJ, 736, 104
- Kalfountzou E., Jarvis M. J., Bonfield D. G., Hardcastle M. J., 2012, MNRAS, 427, 2401
- Kalfountzou E. et al., 2014a, MNRAS, 442, 1181
- Kalfountzou E. et al., 2014b, MNRAS, 442, 1181
- Kalfountzou E., Trichas M., Rowan-Robinson M., Clements D., Babbedge T., Seiradakis J. H., 2011, MNRAS, 413, 249
- Karouzos M. et al., 2014, ApJ, 784, 137
- Kartaltepe J. S. et al., 2012, ApJ, 757, 23
- Kaspi S., Smith P. S., Netzer H., Maoz D., Jannuzi B. T., Giveon U., 2000, ApJ, 533, 631
- Kauffmann G. et al., 2003, MNRAS, 346, 1055
- Keel W. C., 1983, ApJ, 269, 466
- Kellermann K. I., Sramek R., Schmidt M., Shaffer D. B., Green R., 1989, AJ, 98, 1195
- Kelly B. C., Vestergaard M., Fan X., 2009, ApJ, 692, 1388
- Kennicutt R. C., Evans N. J., 2012, ARA&A, 50, 531
- Kennicutt, Jr. R. C., 1998, ApJ, 498, 541
- Kewley L. J., Dopita M. A., Sutherland R. S., Heisler C. A., Trevena J., 2001, ApJ, 556, 121
- Kewley L. J., Groves B., Kauffmann G., Heckman T., 2006, MNRAS, 372, 961
- Khachikian E. Y., Weedman D. W., 1974, ApJ, 192, 581
- Khochfar S., Silk J., 2011, MNRAS, 410, L42
- Kim M. et al., 2007, ApJS, 169, 401
- Kocevski D. D. et al., 2012, ApJ, 744, 148

- Kodama T. et al., 2004, *MNRAS*, 350, 1005
- Koekemoer A. M. et al., 2004, *ApJ*, 600, L123
- Körding E. G., Jester S., Fender R., 2008, *MNRAS*, 383, 277
- Kormendy J., Bender R., 2013, *ApJ*, 769, L5
- Kormendy J., Richstone D., 1995, *ARA&A*, 33, 581
- Koss M., Mushotzky R., Veilleux S., Winter L. M., Baumgartner W., Tueller J., Gehrels N., Valencic L., 2011, *ApJ*, 739, 57
- Kuiper E. et al., 2011, *MNRAS*, 415, 2245
- Kukula M. J., Dunlop J. S., McLure R. J., Miller L., Percival W. J., Baum S. A., O'Dea C. P., 2001, *MNRAS*, 326, 1533
- Kurucz R., 1993, *ATLAS9 Stellar Atmosphere Programs and 2 km/s grid*. Kurucz CD-ROM No. 13. Cambridge, Mass.: Smithsonian Astrophysical Observatory, 1993., 13
- Kurucz R. L., 1979, *ApJS*, 40, 1
- La Franca F. et al., 2005, *ApJ*, 635, 864
- La Franca F., Melini G., Fiore F., 2010, *ApJ*, 718, 368
- Lacy M., Laurent-Muehleisen S. A., Ridgway S. E., Becker R. H., White R. L., 2001, *ApJ*, 551, L17
- Lacy M., Sajina A., Petric A. O., Seymour N., Canalizo G., Ridgway S. E., Armus L., Storrie-Lombardi L. J., 2007, *ApJ*, 669, L61
- Lacy M. et al., 2004, *ApJS*, 154, 166
- Lagos C. D. P., Padilla N. D., Cora S. A., 2009, *MNRAS*, 395, 625
- Laing R. A., Riley J. M., Longair M. S., 1983, *MNRAS*, 204, 151
- Laird E. S. et al., 2009, *ApJS*, 180, 102
- Lal D. V., Shastri P., Gabuzda D. C., 2011, *ApJ*, 731, 68
- Lanzuisi G. et al., 2013, *MNRAS*, 431, 978
- Laor A., 2000, *ApJ*, 543, L111
- Laor A., Behar E., 2008, *MNRAS*, 390, 847
- Lavalley M., Isobe T., Feigelson E., 1992, in *Astronomical Society of the Pacific Conference Series, Vol. 25, Astronomical Data Analysis Software and Systems I*, Worrall D. M., Biemesderfer C., Barnes J., eds., p. 245
- Lawrence A., 1987, *PASP*, 99, 309
- Lawrence A., Elvis M., 1982, *ApJ*, 256, 410

- Lawrence A., Elvis M., 2010, *ApJ*, 714, 561
- Lawrence A. et al., 2007, *MNRAS*, 379, 1599
- Ledlow M. J., Owen F. N., 1996, *AJ*, 112, 9
- Leeuw L. L., Sansom A. E., Robson E. I., Haas M., Kuno N., 2004, *ApJ*, 612, 837
- Lehmann I. et al., 2001, *A&A*, 371, 833
- Lehmer B. D. et al., 2007, *ApJ*, 657, 681
- Leipski C. et al., 2013, *ApJ*, 772, 103
- Lilly S. J. et al., 2009, *ApJS*, 184, 218
- Lilly S. J. et al., 2007, *ApJS*, 172, 70
- Lindner C. C., Fragile P. C., 2007, in *Bulletin of the American Astronomical Society*, Vol. 39, American Astronomical Society Meeting Abstracts, p. 810
- Liu Y. T., Shapiro S. L., 2010, *Phys. Rev. D*, 82, 123011
- Lonsdale C. J. et al., 2003, *PASP*, 115, 897
- Lutz D. et al., 2010, *ApJ*, 712, 1287
- Lutz D. et al., 2011, *A&A*, 532, A90
- Lutz D. et al., 2008, *ApJ*, 684, 853
- Lyutikov M., Pariev V. I., Gabuzda D. C., 2005, *MNRAS*, 360, 869
- Maccacaro T., Gioia I. M., Wolter A., Zamorani G., Stocke J. T., 1988, *ApJ*, 326, 680
- Madau P., Dickinson M., 2014, *ARA&A*, 52, 415
- Maddox N., Hewett P. C., Warren S. J., Croom S. M., 2008, *MNRAS*, 386, 1605
- Magliocchetti M. et al., 2004, *MNRAS*, 350, 1485
- Magorrian J. et al., 1998, *AJ*, 115, 2285
- Maia M. A. G., Machado R. S., Willmer C. N. A., 2003, *AJ*, 126, 1750
- Mainieri V. et al., 2011, *A&A*, 535, A80
- Maiolino R. et al., 2012, *MNRAS*, 425, L66
- Maiolino R., Rieke G. H., 1995, *ApJ*, 454, 95
- Maiolino R., Ruiz M., Rieke G. H., Papadopoulos P., 1997, *ApJ*, 485, 552
- Malkan M. A., Gorjian V., Tam R., 1998, *ApJS*, 117, 25
- Marconi A., Axon D. J., Maiolino R., Nagao T., Pastorini G., Pietrini P., Robinson A., Torricelli G., 2008, *ApJ*, 678, 693

- Marconi A., Hunt L. K., 2003, *ApJ*, 589, L21
- Marconi A., Risaliti G., Gilli R., Hunt L. K., Maiolino R., Salvati M., 2004, *MNRAS*, 351, 169
- Markwardt C. B., 2009, in *Astronomical Society of the Pacific Conference Series*, Vol. 411, *Astronomical Data Analysis Software and Systems XVIII*, Bohlender D. A., Durand D., Dowler P., eds., p. 251
- Martínez-Sansigre A., Taylor A. M., 2009, *ApJ*, 692, 964
- Mas-Hesse J. M., Rodríguez-Pascual P. M., de Córdoba L. S. F., Mirabel I. F., 1994, *ApJS*, 92, 599
- Mason B. S., Weintraub L., Sievers J., Bond J. R., Myers S. T., Pearson T. J., Readhead A. C. S., Shepherd M. C., 2009, *ApJ*, 704, 1433
- Massardi M., Bonaldi A., Negrello M., Ricciardi S., Raccanelli A., de Zotti G., 2010, *MNRAS*, 404, 532
- Matt G., 2000, *A&A*, 355, L31
- Matthews T. A., Sandage A. R., 1963, *ApJ*, 138, 30
- Mauch T., Klöckner H.-R., Rawlings S., Jarvis M., Hardcastle M. J., Obreschkow D., Saikia D. J., Thompson M. A., 2013, *MNRAS*, 435, 650
- McConnell N. J., Ma C.-P., 2013, *ApJ*, 764, 184
- McLure R. J., Dunlop J. S., 2001, *MNRAS*, 321, 515
- McLure R. J., Dunlop J. S., 2004, *MNRAS*, 352, 1390
- McLure R. J., Jarvis M. J., 2002, *MNRAS*, 337, 109
- McLure R. J., Jarvis M. J., 2004, *MNRAS*, 353, L45
- McLure R. J., Jarvis M. J., Targett T. A., Dunlop J. S., Best P. N., 2006, *Astronomische Nachrichten*, 327, 213
- McLure R. J., Kucula M. J., Dunlop J. S., Baum S. A., O’Dea C. P., Hughes D. H., 1999, *MNRAS*, 308, 377
- Medling A. M. et al., 2015, *ApJ*, 803, 61
- Menci N., Fiore F., Lamastra A., 2013, *ApJ*, 766, 110
- Menci N., Fontana A., Giallongo E., Grazian A., Salimbeni S., 2006, *ApJ*, 647, 753
- Merloni A., 2004, *MNRAS*, 353, 1035
- Merloni A. et al., 2010, *ApJ*, 708, 137
- Merloni A. et al., 2014, *MNRAS*, 437, 3550
- Merloni A., Heinz S., 2008, *MNRAS*, 388, 1011

- Metcalf R. B., Magliocchetti M., 2006, MNRAS, 365, 101
- Miller J. S., Goodrich R. W., Mathews W. G., 1991, ApJ, 378, 47
- Miller L., Peacock J. A., Mead A. R. G., 1990, MNRAS, 244, 207
- Miller P., Rawlings S., Saunders R., 1993, MNRAS, 263, 425
- Miyaji T. et al., 2015, ApJ, 804, 104
- Moran E. C., Barth A. J., Kay L. E., Filippenko A. V., 2000, ApJ, 540, L73
- Morrissey P. et al., 2007, ApJS, 173, 682
- Mortlock D. J., Webster R. L., Francis P. J., 1999, MNRAS, 309, 836
- Muñoz Marín V. M., González Delgado R. M., Schmitt H. R., Cid Fernandes R., Pérez E., Storchi-Bergmann T., Heckman T., Leitherer C., 2007, AJ, 134, 648
- Mulchaey J. S., Wilson A. S., Tsvetanov Z., 1996, ApJ, 467, 197
- Mullaney J. R., Alexander D. M., Goulding A. D., Hickox R. C., 2011a, MNRAS, 414, 1082
- Mullaney J. R., Alexander D. M., Goulding A. D., Hickox R. C., 2011b, MNRAS, 414, 1082
- Mullaney J. R., Alexander D. M., Huynh M., Goulding A. D., Frayer D., 2010, MNRAS, 401, 995
- Mullaney J. R. et al., 2012a, MNRAS, 419, 95
- Mullaney J. R. et al., 2012b, MNRAS, 419, 95
- Myers A. D., Brunner R. J., Nichol R. C., Richards G. T., Schneider D. P., Bahcall N. A., 2007, ApJ, 658, 85
- Myers A. D., Richards G. T., Brunner R. J., Schneider D. P., Strand N. E., Hall P. B., Blomquist J. A., York D. G., 2008, ApJ, 678, 635
- Nagar N. M., Falcke H., Wilson A. S., Ulvestad J. S., 2002, A&A, 392, 53
- Nandra K. et al., 2007, ApJ, 660, L11
- Nandra K., Pounds K. A., 1994, MNRAS, 268, 405
- Nardini E., Risaliti G., Watabe Y., Salvati M., Sani E., 2010, MNRAS, 405, 2505
- Neistein E., Netzer H., 2014, MNRAS, 437, 3373
- Nenkova M., Sirocky M. M., Nikutta R., Ivezić Ž., Elitzur M., 2008, ApJ, 685, 160
- Nesvadba N. P. H. et al., 2010, A&A, 521, A65
- Nesvadba N. P. H., De Breuck C., Lehnert M. D., Best P. N., Binette L., Proga D., 2011, A&A, 525, A43

- Nesvadba N. P. H., Lehnert M. D., Eisenhauer F., Gilbert A., Tecza M., Abuter R., 2006, *ApJ*, 650, 693
- Netzer H., 2009, *MNRAS*, 399, 1907
- Netzer H. et al., 2007, *ApJ*, 666, 806
- Nguyen H. T. et al., 2010, *A&A*, 518, L5
- Noterdaeme P. et al., 2012, *A&A*, 547, L1
- Oliver S. J. et al., 2012, *MNRAS*, 424, 1614
- Oliver S. J. et al., 2010, *A&A*, 518, L21
- Oshlack A. Y. K. N., Webster R. L., Whiting M. T., 2002, *ApJ*, 576, 81
- Osterbrock D. E., Koski A. T., 1976, *MNRAS*, 176, 61P
- Ott S., 2010, in *Astronomical Society of the Pacific Conference Series*, Vol. 434, *Astronomical Data Analysis Software and Systems XIX*, Mizumoto Y., Morita K.-I., Ohishi M., eds., p. 139
- Owen F. N., Laing R. A., 1989, *MNRAS*, 238, 357
- Padovani P., 1993, *MNRAS*, 263, 461
- Padovani P., Miller N., Kellermann K. I., Mainieri V., Rosati P., Tozzi P., 2011, *ApJ*, 740, 20
- Padovani P., Urry C. M., 1992, *ApJ*, 387, 449
- Page M. J., Stevens J. A., Ivison R. J., Carrera F. J., 2004, *ApJ*, 611, L85
- Page M. J., Stevens J. A., Mittaz J. P. D., Carrera F. J., 2001, *Science*, 294, 2516
- Page M. J. et al., 2012, *Nature*, 485, 213
- Panessa F., Bassani L., 2002, *A&A*, 394, 435
- Pannella M. et al., 2009, *ApJ*, 698, L116
- Papadopoulos P. P., van der Werf P., Isaak K., Xilouris E. M., 2010, *ApJ*, 715, 775
- Pâris I. et al., 2014, *A&A*, 563, A54
- Park T., Kashyap V. L., Siemiginowska A., van Dyk D. A., Zezas A., Heinke C., Wargelin B. J., 2006, *ApJ*, 652, 610
- Pascale E. et al., 2011, *MNRAS*, 415, 911
- Penston M. V., Perez E., 1984, *MNRAS*, 211, 33P
- Peterson B. M., 1993, *PASP*, 105, 247
- Pilbratt G. L. et al., 2010, *A&A*, 518, L1

- Podigachoski P. et al., 2015, *A&A*, 575, A80
- Poglitsch A. et al., 2010, *A&A*, 518, L2
- Polletta M. et al., 2007, *ApJ*, 663, 81
- Popesso P. et al., 2012, *ArXiv e-prints*
- Priddey R. S., Isaak K. G., McMahon R. G., Omont A., 2003a, *MNRAS*, 339, 1183
- Priddey R. S., Isaak K. G., McMahon R. G., Omont A., 2003b, *MNRAS*, 339, 1183
- Priddey R. S., Isaak K. G., McMahon R. G., Robson E. I., Pearson C. P., 2003c, *MNRAS*, 344, L74
- Priddey R. S., Ivison R. J., Isaak K. G., 2008, *MNRAS*, 383, 289
- Puccetti S. et al., 2009, *ApJS*, 185, 586
- Punsly B., Coroniti F. V., 1990, *ApJ*, 354, 583
- Rafferty D. A., Brandt W. N., Alexander D. M., Xue Y. Q., Bauer F. E., Lehmer B. D., Luo B., Papovich C., 2011, *ApJ*, 742, 3
- Ramos Almeida C. et al., 2012, *MNRAS*, 419, 687
- Rawlings S., Eales S., Lacy M., 2001, *MNRAS*, 322, 523
- Rees M. J., 1984, *ARA&A*, 22, 471
- Rees M. J., 1989, *MNRAS*, 239, 1P
- Rengelink R. B., Tang Y., de Bruyn A. G., Miley G. K., Bremer M. N., Roettgering H. J. A., Bremer M. A. R., 1997, *A&AS*, 124, 259
- Richards G. T. et al., 2005, *MNRAS*, 360, 839
- Richards G. T. et al., 2002, *AJ*, 123, 2945
- Richards G. T. et al., 2011, *AJ*, 141, 167
- Richards G. T. et al., 2009, *ApJS*, 180, 67
- Richards G. T. et al., 2006a, *AJ*, 131, 2766
- Richards G. T. et al., 2006b, *AJ*, 131, 2766
- Rigby E. E., Argyle J., Best P. N., Rosario D., Röttgering H. J. A., 2015, *A&A*, 581, A96
- Rigby E. E., Best P. N., Brookes M. H., Peacock J. A., Dunlop J. S., Röttgering H. J. A., Wall J. V., Ker L., 2011, *MNRAS*, 416, 1900
- Rodighiero G. et al., 2010, *A&A*, 518, L25
- Rosario D. J. et al., 2013, *ApJ*, 763, 59
- Rosario D. J. et al., 2012, *A&A*, 545, A45

- Roseboom I. G. et al., 2012, *MNRAS*, 419, 2758
- Roseboom I. G. et al., 2010, *MNRAS*, 409, 48
- Ross N. P. et al., 2013, *ApJ*, 773, 14
- Ross N. P. et al., 2012, *ApJS*, 199, 3
- Rovilos E. et al., 2012, *A&A*, 546, A58
- Rowan-Robinson M., 1977, *ApJ*, 213, 635
- Rowan-Robinson M., 1995, *MNRAS*, 272, 737
- Rowan-Robinson M. et al., 2008, *MNRAS*, 386, 697
- Rowan-Robinson M. et al., 2010, *MNRAS*, 409, 2
- Ruiz A., Miniutti G., Panessa F., Carrera F. J., 2010, *A&A*, 515, A99
- Salpeter E. E., 1955, *ApJ*, 121, 161
- Salpeter E. E., 1964, *ApJ*, 140, 796
- Salvato M. et al., 2009, *ApJ*, 690, 1250
- Salvato M. et al., 2011, *ApJ*, 742, 61
- Salviander S., Shields G. A., Gebhardt K., Bonning E. W., 2007, *ApJ*, 662, 131
- Sánchez S. F. et al., 2004, *ApJ*, 614, 586
- Sanders D. B., Mirabel I. F., 1996, *ARA&A*, 34, 749
- Sanders D. B., Phinney E. S., Neugebauer G., Soifer B. T., Matthews K., 1989, *ApJ*, 347, 29
- Santini P. et al., 2010, *A&A*, 518, L154
- Santini P. et al., 2012, *A&A*, 540, A109
- Sargent B. A., Patel N. A., Meixner M., Otsuka M., Riebel D., Srinivasan S., 2013, *ApJ*, 765, 20
- Sargent M. T. et al., 2010, *ApJS*, 186, 341
- Sądowski A., Abramowicz M., Bursa M., Kluźniak W., Lasota J.-P., Róžańska A., 2011, *A&A*, 527, A17
- Schmidt M., 1963, *Nature*, 197, 1040
- Schmidt M., Green R. F., 1983, *ApJ*, 269, 352
- Schmidt M. et al., 1998, *A&A*, 329, 495
- Schmidt M., Olsen E. T., 1968, *The Astronomical Journal Supplement*, 73, 117

- Schmidt M., Schneider D. P., Gunn J. E., 1995, *AJ*, 110, 68
- Schneider D. P. et al., 2005, *AJ*, 130, 367
- Schneider D. P. et al., 2010, *AJ*, 139, 2360
- Schreiber C. et al., 2015, *A&A*, 575, A74
- Schwartz D. A., Ku W. H.-M., 1983, *ApJ*, 266, 459
- Schweitzer M. et al., 2006, *ApJ*, 649, 79
- Seymour N. et al., 2007, *ApJS*, 171, 353
- Seymour N. et al., 2011, *MNRAS*, 413, 1777
- Shabala S. S., Godfrey L. E. H., 2013, *ApJ*, 769, 129
- Shakura N. I., Sunyaev R. A., 1973, *A&A*, 24, 337
- Shankar F., 2010, in *IAU Symposium*, Vol. 267, *IAU Symposium*, pp. 248–253
- Shankar F., Salucci P., Granato G. L., De Zotti G., Danese L., 2004, *MNRAS*, 354, 1020
- Shao L. et al., 2010, *A&A*, 518, L26
- Shen Y. et al., 2011a, *ApJS*, 194, 45
- Shen Y. et al., 2011b, *ApJS*, 194, 45
- Shi Y., Rieke G., Donley J., Cooper M., Willmer C., Kirby E., 2008, *ApJ*, 688, 794
- Shi Y. et al., 2005, *ApJ*, 629, 88
- Shupe D. L. et al., 2008, *AJ*, 135, 1050
- Sikora M., Stawarz Ł., Lasota J.-P., 2007, *ApJ*, 658, 815
- Silk J., Nusser A., 2010a, *ApJ*, 725, 556
- Silk J., Nusser A., 2010b, *ApJ*, 725, 556
- Silk J., Rees M. J., 1998, *A&A*, 331, L1
- Silverman J. D. et al., 2005, *ApJ*, 618, 123
- Silverman J. D. et al., 2008a, *ApJ*, 679, 118
- Silverman J. D. et al., 2008b, *ApJ*, 679, 118
- Silverman J. D. et al., 2011, *ApJ*, 743, 2
- Silverman J. D. et al., 2009, *ApJ*, 696, 396
- Silverman J. D. et al., 2008c, *ApJ*, 675, 1025
- Silverman J. D. et al., 2010, *ApJS*, 191, 124

- Skrutskie M. F. et al., 2006, *AJ*, 131, 1163
- Smith A. J. et al., 2012a, *MNRAS*, 419, 377
- Smith D. J. B., 2015, ArXiv e-prints
- Smith D. J. B. et al., 2012b, *MNRAS*, 427, 703
- Smith D. J. B. et al., 2011, *MNRAS*, 416, 857
- Smith D. J. B. et al., 2013, *MNRAS*, 436, 2435
- Smith E. P., Heckman T. M., Bothun G. D., Romanishin W., Balick B., 1986, *ApJ*, 306, 64
- Smith R. J., Boyle B. J., Maddox S. J., 2000, *MNRAS*, 313, 252
- Smolčić V. et al., 2009, *ApJ*, 696, 24
- Somerville R. S., Hopkins P. F., Cox T. J., Robertson B. E., Hernquist L., 2008, *MNRAS*, 391, 481
- Spergel D. N. et al., 2003, *ApJS*, 148, 175
- Springel V., Di Matteo T., Hernquist L., 2005, *MNRAS*, 361, 776
- Steidel C. C., Giavalisco M., Pettini M., Dickinson M., Adelberger K. L., 1996, *ApJ*, 462, L17
- Steidel C. C., Hunt M. P., Shapley A. E., Adelberger K. L., Pettini M., Dickinson M., Giavalisco M., 2002, *ApJ*, 576, 653
- Stern D., Djorgovski S. G., Perley R. A., de Carvalho R. R., Wall J. V., 2000, *AJ*, 119, 1526
- Stern D. et al., 2005, *ApJ*, 631, 163
- Stern J., Laor A., 2012, *MNRAS*, 426, 2703
- Stevens J. A., Hannikainen D. C., Wu K., Hunstead R. W., McKay D. J., 2003, *MNRAS*, 342, 623
- Stevens J. A., Jarvis M. J., Coppin K. E. K., Page M. J., Greve T. R., Carrera F. J., Ivison R. J., 2010, *MNRAS*, 405, 2623
- Stevens J. A., Page M. J., Ivison R. J., Carrera F. J., Mittaz J. P. D., Smail I., McHardy I. M., 2005, *MNRAS*, 360, 610
- Stevens J. A., Page M. J., Ivison R. J., Smail I., Carrera F. J., 2004, *ApJ*, 604, L17
- Stocke J. T., Morris S. L., Gioia I. M., Maccacaro T., Schild R., Wolter A., Fleming T. A., Henry J. P., 1991, *ApJS*, 76, 813
- Strateva I. et al., 2001, *AJ*, 122, 1861
- Strittmatter P. A., Serkowski K., Carswell R., Stein W. A., Merrill K. M., Burbidge E. M., 1972, *ApJ*, 175, L7

- Symeonidis M., Rosario D., Georgakakis A., Harker J., Laird E. S., Page M. J., Willmer C. N. A., 2010, MNRAS, 403, 1474
- Tacconi L. J. et al., 2013, ApJ, 768, 74
- Tasse C., Best P. N., Röttgering H., Le Borgne D., 2008, A&A, 490, 893
- Tozzi P. et al., 2006, A&A, 451, 457
- Tran H. D., 2001, ApJ, 554, L19
- Tran H. D., 2003, ApJ, 583, 632
- Treister E. et al., 2009, ApJ, 706, 535
- Treister E., Schawinski K., Urry C. M., Simmons B. D., 2012, ApJ, 758, L39
- Treister E., Schawinski K., Volonteri M., Natarajan P., Gawiser E., 2011, Nature, 474, 356
- Treister E., Urry C. M., 2006, ApJ, 652, L79
- Tremonti C. A., Moustakas J., Diamond-Stanic A. M., 2007, ApJ, 663, L77
- Trichas M., Georgakakis A., Rowan-Robinson M., Nandra K., Clements D., Vaccari M., 2009, MNRAS, 399, 663
- Trichas M. et al., 2013, ApJ, 778, 188
- Trichas M. et al., 2012, ApJS, 200, 17
- Trichas M. et al., 2010, MNRAS, 405, 2243
- Tristram K. R. W. et al., 2007, A&A, 474, 837
- Trouille L., Barger A. J., Tremonti C., 2011, ApJ, 742, 46
- Ueda Y., Akiyama M., Hasinger G., Miyaji T., Watson M. G., 2014, ApJ, 786, 104
- Ueda Y., Akiyama M., Ohta K., Miyaji T., 2003, ApJ, 598, 886
- Urry C. M., Padovani P., 1995, PASP, 107, 803
- Urry M., 2003, in *Astronomical Society of the Pacific Conference Series*, Vol. 290, *Active Galactic Nuclei: From Central Engine to Host Galaxy*, Collin S., Combes F., Shlosman I., eds., p. 3
- van Breugel W., Fragile C., Anninos P., Murray S., 2004, in *IAU Symposium*, Vol. 217, *Recycling Intergalactic and Interstellar Matter*, Duc P.-A., Braine J., Brinks E., eds., p. 472
- van Haarlem M. P. et al., 2013, A&A, 556, A2
- Vardoulaki E. et al., 2010, MNRAS, 401, 1709
- Venemans B. P. et al., 2007, A&A, 461, 823
- Vestergaard M., Peterson B. M., 2006, ApJ, 641, 689

- Vignali C., Brandt W. N., Schneider D. P., 2003, *AJ*, 125, 433
- Villforth C. et al., 2014, *MNRAS*, 439, 3342
- Virdee J. S. et al., 2013, *MNRAS*
- Vito F. et al., 2014, *ArXiv e-prints*
- Vito F. et al., 2013, *MNRAS*, 428, 354
- Vlahakis C., Dunne L., Eales S., 2005, *MNRAS*, 364, 1253
- Wagner A. Y., Bicknell G. V., Umemura M., 2012, *ApJ*, 757, 136
- Wall J. V., Jackson C. A., Shaver P. A., Hook I. M., Kellermann K. I., 2005, *A&A*, 434, 133
- Wang J.-G. et al., 2009, *ApJ*, 707, 1334
- Wang J.-M., Chen Y.-M., Ho L. C., McLure R. J., 2006, *ApJ*, 642, L111
- Wardlow J. L. et al., 2011, *MNRAS*, 415, 1479
- Warner C., Hamann F., Dietrich M., 2004, *ApJ*, 608, 136
- Warren S. J., Hewett P. C., Foltz C. B., 2000, *MNRAS*, 312, 827
- Weisskopf M. C., Brinkman B., Canizares C., Garmire G., Murray S., Van Speybroeck L. P., 2002, *PASP*, 114, 1
- Weisskopf M. C., Tananbaum H. D., Van Speybroeck L. P., O'Dell S. L., 2000, in *Society of Photo-Optical Instrumentation Engineers (SPIE) Conference Series*, Vol. 4012, *X-Ray Optics, Instruments, and Missions III*, Truemper J. E., Aschenbach B., eds., pp. 2–16
- White N. E., Swank J. H., Holt S. S., 1983, *ApJ*, 270, 711
- White R. L. et al., 2000, *ApJS*, 126, 133
- White R. L., Helfand D. J., Becker R. H., Glikman E., de Vries W., 2007, *ApJ*, 654, 99
- Whittam I. H. et al., 2013, *MNRAS*, 429, 2080
- Whittam I. H., Riley J. M., Green D. A., Jarvis M. J., Vaccari M., 2015, *MNRAS*, 453, 4244
- Willott C. J. et al., 2010, *AJ*, 139, 906
- Willott C. J., Rawlings S., Blundell K. M., Lacy M., 1998, *MNRAS*, 300, 625
- Willott C. J., Rawlings S., Blundell K. M., Lacy M., 1999, *MNRAS*, 309, 1017
- Willott C. J., Rawlings S., Blundell K. M., Lacy M., Eales S. A., 2001, *MNRAS*, 322, 536
- Wilson A. S., Colbert E. J. M., 1995, *ApJ*, 438, 62
- Wold M., Lacy M., Lilje P. B., Serjeant S., 2001, *MNRAS*, 323, 231
- Woo J.-H., Urry C. M., 2002a, *ApJ*, 579, 530

- Woo J.-H., Urry C. M., 2002b, *ApJ*, 581, L5
- Worsley M. A., Fabian A. C., Barcons X., Mateos S., Hasinger G., Brunner H., 2004, *MNRAS*, 352, L28
- Worsley M. A. et al., 2005, *MNRAS*, 357, 1281
- Wright E. L. et al., 2010, *AJ*, 140, 1868
- Wu X.-B., Hao G., Jia Z., Zhang Y., Peng N., 2012, *AJ*, 144, 49
- Wu X.-B., Jia Z., 2010, *MNRAS*, 406, 1583
- Wu X.-B., Zhang W., Zhou X., 2004, *ChjAA*, 4, 17
- Xue Y. Q. et al., 2010, *ApJ*, 720, 368
- Xue Y. Q. et al., 2011, *ApJS*, 195, 10
- York D. G. et al., 2000, *AJ*, 120, 1579
- Young M., Elvis M., Risaliti G., 2010, *ApJ*, 708, 1388
- Zirbel E. L., Baum S. A., 1995, *ApJ*, 448, 521